Many-Body Physics in an Optical Lattice Clock

by

Sarah L. Bromley

MPhys., University of St. Andrews, 2012

M.S., University of Colorado, 2017

A thesis submitted to the

Faculty of the Graduate School of the

University of Colorado in partial fulfillment

of the requirements for the degree of

Doctor of Philosophy

Department of Physics

2018

This thesis entitled:
Many-Body Physics in an Optical Lattice Clock
written by Sarah L. Bromley
has been approved for the Department of Physics

Jun Ye

Ana Maria Rey

Date

The final copy of this thesis has been examined by the signatories, and we find that both the content and the form meet acceptable presentation standards of scholarly work in the above mentioned discipline.

Bromley, Sarah L. (Ph.D., Physics)

Many-Body Physics in an Optical Lattice Clock

Thesis directed by Prof. Jun Ye

In this work we study the effect of interactions in an optical lattice clock based on fermionic Sr atoms. In current one-dimensional lattice clocks nuclear spin-polarized atoms are known to have contact interactions of p-wave character and collective in nature. Here we focus on interactions that will influence the design of future optical lattice clocks. We study the case where atoms are no longer confined to a single nuclear spin state. By using samples of atoms with different distributions among the ten nuclear spin states of Sr we show that these interactions are SU($\mathcal{N}$) symmetric up to a 3% uncertainty in our measurements. Through these measurements we are also able to determine all the s-wave and p-wave scattering lengths.

We also study the case of nuclear spin-polarized interacting atoms that are allowed to tunnel between different lattice sites where the electronic spin and the motion of these atoms become coupled. We observe spectroscopically the precession of the collective magnetization and evolution of spin locking effects arising from the interplay between p-wave interactions and interactions induced by the spin-orbit coupling. The many-body dynamics are captured by a spin model that describes a broad class of condensed matter systems ranging from superconductors to quantum magnets.

By loading a dense sample of atoms into a magneto-optical trap we are able to observe long-range dipole-dipole interactions between our Sr atoms. These interactions will be important for atomic clocks based on a three dimensional lattice, such as the one recently demonstrated in our lab. In these clocks it is possible to remove the contact interactions between the atoms by loading only one atom per lattice site. In this case the dominant interactions will be from the long-range dipole-dipole interactions that will take place between the atoms.

Dedication

To my parents for supporting me when I moved across the world and to Corielyn who agreed to move back across the world with me.

Acknowledgements

When I first moved to Colorado I was surrounded by new things and new people. It took me a while to get my bearings, but I did so with the help of a few awesome people: Clarissa, Carl, Eric, Susanna, Jimmy, Effie, & Adam. For the first time I felt able to be completely myself around friends and for your kindness and friendship I thank you.

Once I had my bearings my next task was to find myself a research group. I was persistent in wanting to join Jun's group and was excited when he gave me the chance to join the Strontium Team. I thank him for always pushing me to get the best out of myself. It can be annoying how he always seem to be right about everything, but it has meant he was able to teach me a lot about physics for which I am eternally grateful.

I have had the opportunity to work with an amazing Strontium Team over the last 5ish years and I thank you all for being so great! When I first joined the group I was shown the ropes of the Sr1 experiment by graduate student Mike Bishof and postdoc Xibo Zhang. Mike, Xibo, and I spent many late nights together in the lab for both the initial clock comparison between our two Sr experiments and our SU($\mathcal{N}$) work. They both taught me a lot about the running of the experiments and the need to really know the everyday running of the experiment well.

On the Sr1 experiment we were quickly joined by Toby Bothwell and I have had the pleasure to work with him for the majority of my PhD. He has helped tremendously to make improvements to the control of the experiment and in leading the design of the next generation of the experiment. I was also lucky to have a large overlap with postdoc Shimon Kolkowitz. Together we made a very productive team and Shimon is one of the nicest and friendliest people I have met, as well as being

a great physicist. Recently we have been joined on the experiment by Dhruv Kedar and postdoc Colin Kennedy. They are both extremely friendly and hard-working people and I am sad that I don't have the oportunity to work with them both longer. Together with Toby they are already making an awesome team and I can't wait to see what they do next.

At the same time we have always worked closely with the Sr2 experiment. When I first joined the experiment, Travis Nicholson, Ben Bloom, and Sara Campbell were all working hard to measure and improve their clock systematics. Travis always had such a great passion for the work he was doing. Sara was always the bubbly, curious, and enthusiastic member of the team. She was the "organizer" of the group and would take it upon herself to organize the yearly ski trip and even some Ye lab t-shirts.

More recent additions to the Sr2 team include Ross Hutson and postdocs Ed Marti and Aki Goban. Ross joined the Sr team a few months after I did and he was instrumental in implementing LabRad into the new SrQ experiment. He is also investigating brilliant new ways for improving our clocks. Ed is an incredibly clever individual and always willing to sit down and explain something to you when you ask him questions. Aki is an incredibly hard worker and such a friendly person to be around in lab.

I would also like to thank the stable lasers team as they help make our experiments better by maintaining and improving our clock laser system. Wei Zhang has so much knowledge about these stable lasers and he can still be found in the evenings at JILA. It is still unclear to me if he actually still works at JILA or he just drops by to help out. Lindsay Sonderhouse somehow managed to repair and keep the old frequency comb working for such a long time and now she is rewarded with a shiny new comb that can free up her time to work with the Sr atoms. John Robinson briefly worked on the Sr1 experiment before joining the stable lasers teams and he is such a thoughtful scientist who is making awesome next generation laser systems. Erik Oelker recently joined the team as a posdoc and is already doing great work in the lab and leading the search for dark matter with our clocks.

Ana Maria Rey has worked with our experimental team on almost all of the work described

in this thesis and has been a great collaborator. She has helped us understand our observations and taught us so much about what we are observing. As well as working closely with Ana Maria, we have also worked closely with her group. In particular, I would like to thank Bihui Zhu, Johannes Schachenmayer, Michael Wall, and Arghavan Safavi-Naini for answering my many questions.

I would also like to thank everyone else who works at JILA that I have not already mentioned. JILA has such a great community of scientists, administrative staff, custodians, and technicians which all contribute to the success of JILA. The different shops provide invaluable technical support and guidance, and the administrative staff and custodians deal with all the different things going on in the backgound and keep things running smoothly.

And lastly, I thank my family. To my parents I thank them for supporting my decision to move so far away from home and their continued love and support even from a distance. I would not have had the strength to move so far from home without their strong, loving upbringing. I would also like to thank my brother and sister who have always been there for me whenever I needed them. To the newest member of my family, Corielyn - I can't believe I found you. Your love, strength, and support inspires me to work hard and be the best person I can be. I know that whatever the future holds as long as you are by my side life will be good.

Contents

Chapter

Tables

Table

Figures

Figure

Chapter 1

Introduction to Optical Lattice Clocks

1.1 A History of Time, in Brief

From the beginning of civilization time has been important for people. Time can bring with it changes in nature such as the seasons which can be important for reasons such as harvesting food. With astronomical events, such as the seeming motion of the stars around the earth, occuring once per year astronomical events become natural measures of time. The motion of the earth around the sun or of the moon around the earth therefore give a natural system of time. For example, the ancient egyptians used the rising of the star Sirius, that was absent from the sky for approximately 70 days per year, to mark the start of the year which they then split into 12 months of 30 days each with an extra 5 days per year to make up a 365 day year [1].

The splitting of the day into 24 hours was first initiated by the Egyptians. Some of the oldest clocks ever found are from Egypt dating back to 2000 BC [2]. These early clocks were water clocks and sundials and these types of clocks are still used around the world today. As time progressed, the hour was split into 60 units of time (minutes) by the Babylonians. This splitting of time into smaller and smaller units is a natural progression as the need to measure smaller and smaller time intervals is needed. Clocks have progressed from early clocks described above to clocks such as pendulum clocks, and quartz crystal oscillator based clocks. However, such clocks are not good frequency standards as their resonance frequencies depend on the physical parameters of the oscillator such as the size and shape of the quartz crystal. The frequency of such clocks can also vary with time with aging.

Oscillators derived from frequency transitions in atoms do not have such problems. All atoms of the same element, and isotope, have identical transitions such that atoms are ideal frequency standards. All transition frequencies have a central frequency ν_0 with a linewidth $\Delta\nu_0$ where we can define a quality factor

$$Q = \frac{\nu_0}{\Delta\nu_0} \tag{1.1}$$

Oscillators with higher Q can lead to more stable and accurate clocks meaning higher frequencies and narrower transition linewidths are better for clocks. With some of the latest clocks based on atoms the need for more accurate and precise clocks is still necessary for applications such as the global positioning system (GPS). In each of these satellites that we use every day to navigate there are multiple atomic clocks which are required for location positioning.

1.2 Atomic Clocks

Atomic clocks are currently used to define time. The second is currently defined as 9,192,631,770 oscillations of the ground state hyperfine transition of cesium, and has been so since 1967 [3]. In the same way that having more ticks on a ruler is a more precise way to measure distance, the higher the frequency of the atomic transition the more precisely and accurately we can measure time. For this reason, atomic clocks based on optical transitions with higher frequencies make better clocks than microwave transitions which are lower frequencies that have a lower quality factor.

Atomic clocks are not only important for defining the unit of time but are also used in the definition of other units in the international system (SI). The SI units of meter, candela, and ampere also depend on the definition of the second. For example, the meter is defined as the length of the path travelled by light in vacuum during a time interval of $1/c$ of a second, where c is the speed of light.

All time and frequency standards have several components in common. All are referenced to a periodic event that repeats at a constant rate. The clock then measures this periodicity. To make an atomic clock the atoms are laser cooled to reduce motional broadening of the transition. For the

case of optical lattice atomic clocks, the atoms are then confined in an optical lattice formed by a standing wave of light. The clock transition frequency is the periodic event, or oscillator, that the clock is referenced to and needs to be measured as accurately and precisely as possible. In order to do this, we need to understand all the different factors that change this transition frequency such as electric and magnetic fields and even the interactions between the atoms themselves. Understanding all these different frequency changes is vital for a clock and the environment for the clock needs to be well controlled to limit the systematic uncertainties associated with the environmental changes. In order to measure the frequency of the atomic transition a laser is stabilized to the atomic transition and the frequency of the laser can then be measured. The ability to measure optical frequencies is made possible due to the invention of the frequency comb, which earned Hall and Hänsch a share of the 2005 Nobel prize for physics.

During the preceding paragraphs the terms "accuracy" and "precision" have been thrown around without being specifically defined. It is important to understand these important concepts. The accuracy of an atomic clock is how far away the measured value is from the true value. The

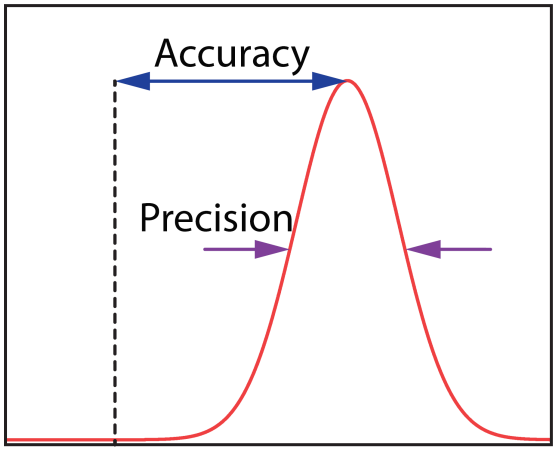

Figure 1.1: Accuracy, precision, and systematic uncertainty. A measurement will have a distribution of values (red line). The accuracy of a measurement is how far the center of the distribution is from the true value (dashed, line). The precision of the measurement is related to the width of the distribution where the narrower the width the more precise the measurement. The systematic uncertainty of the measurement is related to how well the center of the distribution of measurements can be determined.

precision of the measurement is the measure of the spread of values. The systematic uncertainty is related to how well we can determine center of the distribution of measurements. Figure 1.1 is a cartoon showing these concepts of accuracy, precision, and systematic uncertainty. Technically speaking accuracy should only be used when referring to a Cs atomic clock reference as that is how time is defined for now, this will change when in the foreseeable future the definition of time changes to be based upon on optical transitions. With other atomic frequencies the term systematic uncertainty is employed instead.

1.3 Clock Stability

The precision of a clock is also known as the clock stability. In practice it is important to be able to measure the systematic uncertainties in a reasonable amount of time and it is important that a clock is stable in order to do this. The stability measures the noise of a clock where the noisier the clock the longer it will take to average away this noise. The stability is most commonly described in terms of an Allan deviation which gives the fractional frequency instability as a function of the averaging time, τ_{av}. The Allan deviation involves a large number of measurements of the clock frequency and compares these frequencies. The Allan deviation, $\sigma_y(\tau_{av})$ can be written mathematically by

$$\sigma_y(\tau_{av}) = \left[\frac{1}{2(j-1)}\sum_{i=1}^{j-1}(y_{i+1}-y_i)^2\right]^{1/2} \tag{1.2}$$

where j is the total number of measured values y_i. If the cycle time of the experiment is T_{cycle} then every $4T_{cycle}$ we get an independent measurement of the transition frequency by measuring on either side of the $m_F = \pm 9/2$ states as discussed in more detail in chapter 3. Overlapping measurements of the transition frequency are routinely used which can give a new measurement of the transition frequency every $2T_{cycle}$. Due to the overlapping nature of the measurements any uncertainty measured in this way needs a correction factor as the measurements will not be statistically independent [4].

For the overlapping Allan deviation where a measurement of y_i made every $2T_{cycle}$, we get

an Allan deviation of $\sigma_y(2T_{cycle})$. By taking an average of every two measurements a new Allan deviation can be calculated, $\sigma_y(4T_{cycle})$, where the time between these measurements is now $4T_{cycle}$. This can be repeated in the same way to get the Allan deviation at times of multiples of $2^n 2T_{cycle}$ for n an integer. For white noise sources this Allan deviation will keep decreasing linearly with time. Due to the discrete nature of the measurements that are being made here, the high frequency noise of the local oscillator is aliased by the slow sampling rate to frequencies close to the signal, resulting in false frequency shifts in the clock. This effect is known as the Dick effect and limits clock stability. The fundamental limit to the stability of the clock is quantum projection noise which is discussed in the next section.

1.4 Quantum Projection Noise

The most fundamental limit to the atomic frequency measurements in optical lattice clocks is the quantum projection noise (QPN) which is also referred to as atom shot noise. For a clock operating at an average excitation fraction p_e, and using uncorrelated atoms the number of atoms found in the excited state follows a binomial, or coin toss, distribution. When tossing coins, the probability of getting a head or tails is each $p_e = 0.5$. When several coins are tossed at once, the proportion that land on heads will fluctuate about 0.5 each time another toss is made. If the number of coins is increased, the percentage that land on heads will fluctuate less. In a similar way, more atoms leads to less QPN.

From fluctuation in the excited state atom number follows Binomial statistics and it follows that the variance of the measured excited state fraction is

$$\sigma^2 [p_e] = \frac{p_e (1 - p_e)}{N} \tag{1.3}$$

where N is the atom number. This is the key reason that multi-atom atomic lattice clocks have an advantage over single ion clocks: as the number of atoms increases the noise decreases. Typically, clocks are operated with $p_e = 0.5$ as this is where the slope of the excitation probability with

respect to frequency is maximized, giving a more sensitive measurement.

Since QPN is a white noise process, the noise amplitude averages down with the square root of the number of points averaged. For an averaging time of τ_{av} and a cycle time of T_{cycle}, the number of points averaged is $\tau_{av}/2T_{cycle}$, and the clock stability due to QPN is [5]

$$\sigma_{QPN} = \frac{\chi'}{\pi Q}\frac{1}{S/N}\sqrt{\frac{2T_{cycle}}{\tau_{av}}} = \frac{\chi'}{\pi Q}\sqrt{\frac{(1-p_e)}{Np_e}}\sqrt{\frac{T_{cycle}}{\tau_{av}}} = \frac{\chi'}{\pi Q}\sqrt{\frac{T_{cycle}}{N\tau_{av}}} \tag{1.4}$$

where $Q = \nu_0/\delta\nu$ is the transition line quality factor, $p_e = 1/2$, and χ' is a constant of order unity that accounts for the details of spectroscopy. For Ramsey spectroscopy (see section 6.3) χ'=1, but experimentally we tend to use Rabi spectroscopy with only a single excitation from the clock laser. This discussion of QPN has assumed that the states of the atom are uncorrelated and does not apply for squeezed clock states for example.

1.5 Thesis Outline

The outline of this thesis is as follows. We will start by discussing the experimental setup, strontium structure, and cooling schemes employed in our one dimensional optical lattice clock in chapter 2. We will then move on to discuss the two systematic evaluations of our JILA Sr 1 clock, that have taken place during my time at JILA, in chapter 3. We will discuss how the frequency of the clock transition changes due to different systematic effects and the methods used to compare the clocks. We will then move on to discuss some of the different experiments we have undertaken to understand the interactions that can take place in our optical lattice clock that will be important for designing future generations of optical lattice clocks, as well as being interesting in their own way. In chapter 4 we will discuss collective atomic scattering that takes place in a dense sample of ^{88}Sr atoms. For this chapter the atoms are not trapped within a lattice but we look at interactions in the dense magneto-optical trap. The interactions that take place are dipole-dipole interactions that are long range in nature and will be important for future generations of clocks such as in a 3D optical lattice clocks [6]. In such clocks the atoms can be prepared one atom per lattice site

such that contact interactions can be prohibited. In this case the dominant interactions will then be from these long-range dipole-dipole interactions.

In chapter 5 we will briefly discuss the theory model developed by the group of Rey et al that describes the interactions in our one dimensional optical lattice clock for atoms in the same nuclear spin state and without tunneling taking place between the different lattice sites. In chapters 6 and 7 we will extend upon this model. In chapter 6 we will extend the model to include the case where atoms can also be in different nuclear spin states and see how this changes how the atoms interact with each other. In chapter 7 we will see how the interactions change when the atoms are allowed to tunnel between the different lattice sites and the spin and motion become coupled and how this affects observables such as the contrast and the frequency shift in the clock spectroscopy signal.

Chapter 2

Strontium Cooling and Trapping

2.1 Introduction

The same vacuum chamber and basic setup has been used successfully in our lab for more than ten years. In this chapter, we will give an overview of how we prepare strontium atoms for our experiments. In the majority of these experiments we cool the only stable fermionic isotope of strontium, ^{87}Sr, and load them into either a horizontal or a vertical optical lattice before manipulating them using the ultra-narrow clock laser transition at 698 nm. During one of our experiments we use the bosonic ^{88}Sr isotope as this allows large dense samples of Strontium to be prepared. The different laser systems that we use for cooling, trapping, and probing the atoms have all been upgraded during the last few years and the new setups will be described in this chapter.

2.1.1 Chapter Outline

This chapter focusses on the preparation of the atoms ready for the more interesting physics experiments to take place. In section 2.2 we will discuss the overall layout of the main experiment including the location of the different lasers beams and which vacuum viewports are used for the different beams. In section 2.3 the relevant energy levels of Sr are discussed including the particular transitions needed for the cooling and probing of the strontium atoms. In section 2.3.1 we zoom in and look at the hyperfine structure of the ^{1}P$_1$ and ^{3}P$_1$ electronic levels that are used to cool the atoms.

We will then move on in section 2.4 to discuss the laser setup for cooling the atoms in the first

stage blue magneto-optical trap (MOT) based on the $^1S_0 - ^1P_1$ transition. As described in previous theses [7, 8] the cooling light was derived from a 922 nm diode and tapered amplifier (TA) system. This 922 nm light was then frequency doubled using two home-built setups using $KNbO_3$ crystals. This frequency doubled system was old and required long warm up times of several hours every day. In 2015 we therefore upgraded to a diode based system that had been tested out previously by the JILA Sr 2 experiment in our lab. The system uses one 461 nm ECDL laser to seed three 150 mW diode lasers.

In section 2.5 we discuss the laser setup for the second stage red MOT based on the $^1S_0 - ^3P_1$ transition. This system was also upgraded from using a heatpipe to lock to the Sr resonance at 689 nm, to using a cavity based setup. The cavities used in this setup were from older laser setups that were used to create the clock laser and gives us $\sim$ Hz level linewidths and $\sim$ kHz level drifts per day. This laser is shared between the two Sr experiments in our lab and is used to seed the four slave lasers used by the two experiments.

We will then discuss the loading of the atoms into the optical lattice at 813 nm that allows us to trap the atoms in section 2.6. Commercial narrow linewidth Ti:Sapphire lasers have recently become available and therefore during the last few years we have also upgraded from a TA system of producing the lattice light that gave us $\sim$ 300 mW of light at the atoms to now have over 3 W of light available at the atoms. This new Ti:Sapphire laser also has the advantage of not having the noise pedestal associated with amplified spontaneous emission from a TA system. We will also discuss in this section how we detect atoms and determine the fraction of atoms in each clock state and how we can do further in lattice cooling that can be seen by scanning the clock laser

2.2 The Experimental Apparatus

A solidworks drawing of our experimental vacuum chamber is shown in Figure 2.1. The oven was last replaced in December 2010 with 15 grams of strontium being placed inside. Under typical operating conditions the oven is heated to 375°C and the nozzle of the oven is heated to 575°C to stop strontium buildup. The atomic beam leaving the oven is collimated using a stage of transverse

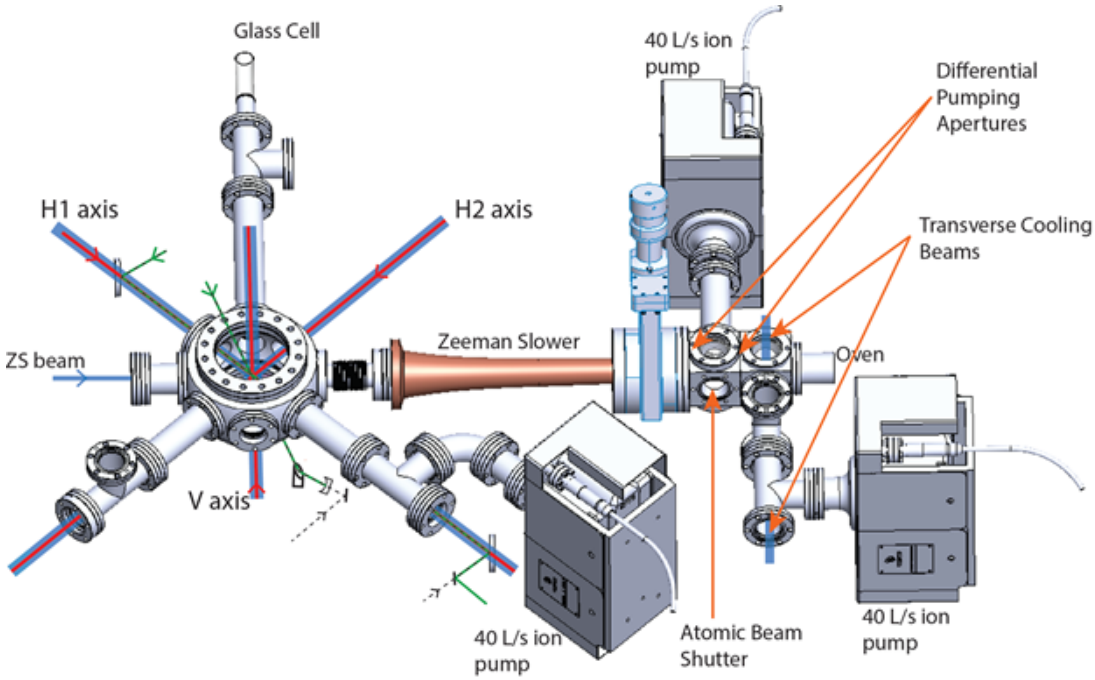

Figure 2.1: Vacuum chamber showing the position of the different laser beams. As the atomic beam exits the oven it is collimated using a stage of transverse cooling before being slowed using Zeeman slowing with a varying magnetic field and a counter-propagating laser beam. The atoms are captured at the center of the spherical octagon in a magneto-optical trap (MOT) based on the $^1S_0 - ^1P_1$ transition before being transferred to a MOT based on the $^1S_0 - ^3P_1$ transition for cooling to μK temperatures. The blue cooling light is shown in blue and the overlapped red cooling light and repumps are shown in red. The atoms are then usually transferred to a lattice, shown here in green, that is either Horizontal (H1 axis) or close to vertical (V axis). The atoms can then be probed with the clock laser, shown here as dashed lines, along the axis of the lattice. We also alternatively probe along the H2 axis to measure the radial temperature

cooling that typically increases the atom number in the magneto-optical trap (MOT) by a factor of ~ 2. The atoms then pass through two differential pumping apertures before passing through a gate valve and entering the σ^- Zeeman slower.

The atoms are slowed using a Zeeman slower beam detuned 1040 MHz below the $^1S_0 - ^1P_1$ transition and kept in resonance as the atoms slow by the spatially varying magnetic field produced by the Zeeman slower. The atoms are then captured in a MOT based on the $^1S_0 - ^1P_1$ transition

2.3 Strontium Level Structure

Strontium is an alkaline-earth atom and therefore contains two valence electrons. This leads to the formation of singlet and triplet states where transitions between them are weakly forbidden due to the need for an electron spin to flip during such a transition. The lower lying energy levels of strontium are shown in Fig. 2.2. The energy levels are shown to scale and are split to show the

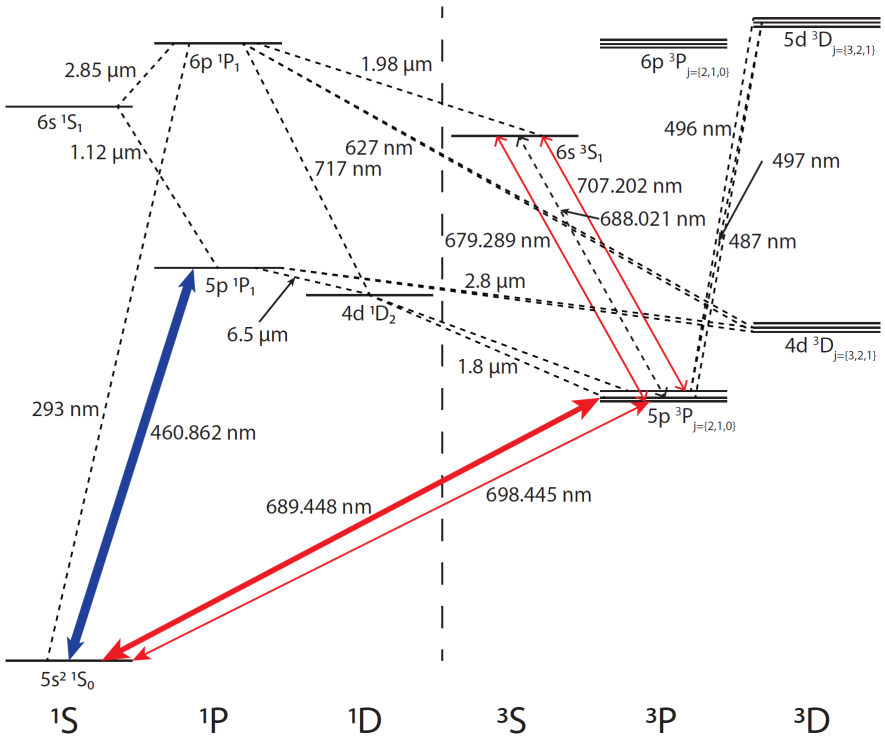

Figure 2.2: Low lying enercy levels of strontium. The transitional energies are drawn to scale and split into singlet (left) and triplet (right) states

singlet states on the left and triplet states on the right.

Figure 2.3 shows the relevant cooling transitions that we use to cool and trap strontium. The broad ($\Gamma/(2\pi) = 32$ MHz) $^1S_0$–$^1P_1$ transition is used to cool the atoms in a MOT to mK temperatures. A small percentage of atoms (2×10^{-5} branching ratio) leak out of the blue MOT cooling transition to the $^1D_2$ state [9]. The atoms in the $^1D_2$ state then decay to either the $^3P_1$ or $^3P_2$ state. Those that decay to the $^3P_1$ state can decay back quickly to the $^1S_0$ state but those that decay to the long-lived $^3P_2$ state need to be repumped to the ground state using the 707 nm transition to the $^3S_1$ state where atoms can decay to any of the ^3P_j levels meaning a second repump laser at 679 nm is also required to remove atoms that become trapped in the $^3P_0$ clock state. For further cooling to μK temperatures the weaker $\Gamma/(2\pi) = 7.5$ kHz linewidth transition is used. For ^{87}Sr cooling the hyperfine structure of the atom needs to also be taken into account.

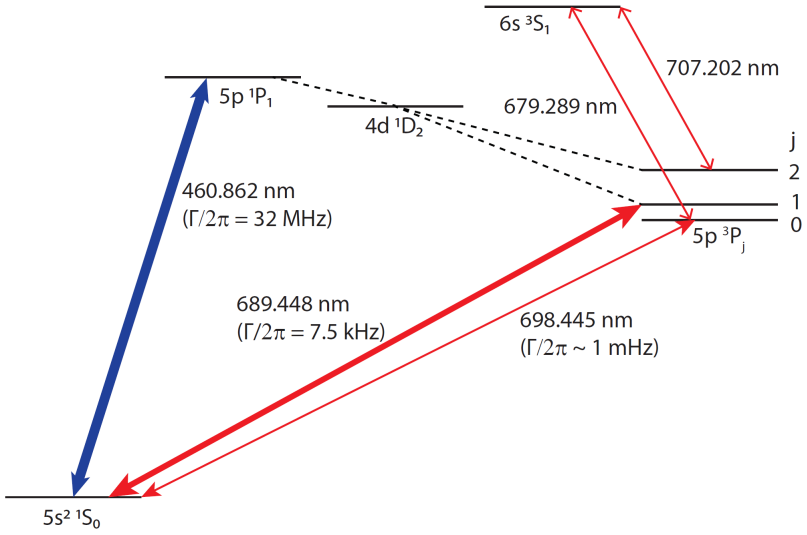

Figure 2.3: Relevant transitions for cooling and probing Sr. The broad 32 MHz linewidth transition ($^1S_0$–$^1P_1$) is used for slowing and cooling the atoms to mK temperatures. This transition is not completely closed and atoms decay via the $^1D_2$ to the $^3P_1$ state and the long-lived $^3P_2$ state. The repump laser at 707 nm removes atoms from this long-lived state to the $^3S_1$ state where they decay to all ^3P_j levels. An additional repump laser is needed at 679 nm to remove atoms from the $^3P_0$ clock state. Atoms are further cooled using the narrow 7.5 kHz natural linewidth transition down to μK temperatures. The ultra-narrow clock transition at 698 nm that is used for probing the atoms is also indicated above.

2.3.1 Hyperfine Structure

The $^1P_1$ energy level structure for ^{88}Sr and ^{87}Sr are shown in Fig. 2.4. The isotope shift for this transition is 49.2 MHz [10]. For the ^{87}Sr isotope there are three hyperfine levels. The shift away from the central value is calculated using the equation

$$\Delta E_{HF} = \frac{A_{HFS}}{2}K + \frac{B_{Quad}}{2}\frac{\frac{3}{4}K(K+1) - I(I+1)J(J+1)}{I(2I-1)J(2J-1)} \tag{2.1}$$

where

$$K = F(F+1) - J(J+1) - I(I+1) \tag{2.2}$$

with A_{HFS} the magnetic dipole hyperfine constant and B_{Quad} the electric quadrupole coupling constant, F, J, and I are the quantum numbers associated with the total angular momentum, the total electronic angular momentum and the nuclear angular momentum respectively.

For the $^1P_1$ state of ^{87}Sr we have the quantum numbers $J = 1$, $I = 9/2$, $F = \{11/2, 9/2, 7/2\}$ and coupling constants $A_{HFS} = -3.4$ and $B_{Quad} = 39$ [11] to give the energy shifts shown in Fig.

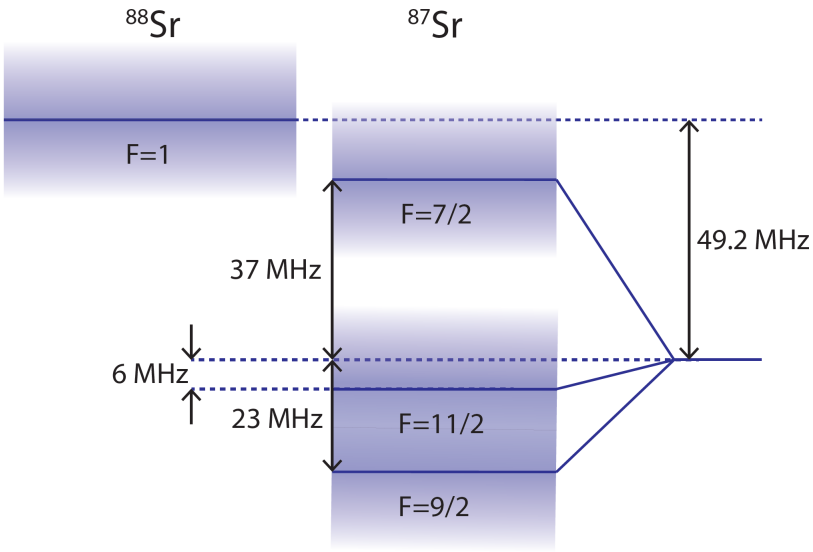

Figure 2.4: Hyperfine structure of the 5p $^1P_1$ energy levels of strontium drawn to scale. For bosonic ^{88}Sr (left) the nuclear spin I =0 leads to only a single hyperfine energy level. For fermionic ^{87}Sr (right) the nuclear spin $I = 9/2$ leads to three hyperfine levels with splittings given above. The natural linewidth is indicated by the width of the lines and is $\Gamma = 2\pi \times 32$ MHz for this state.

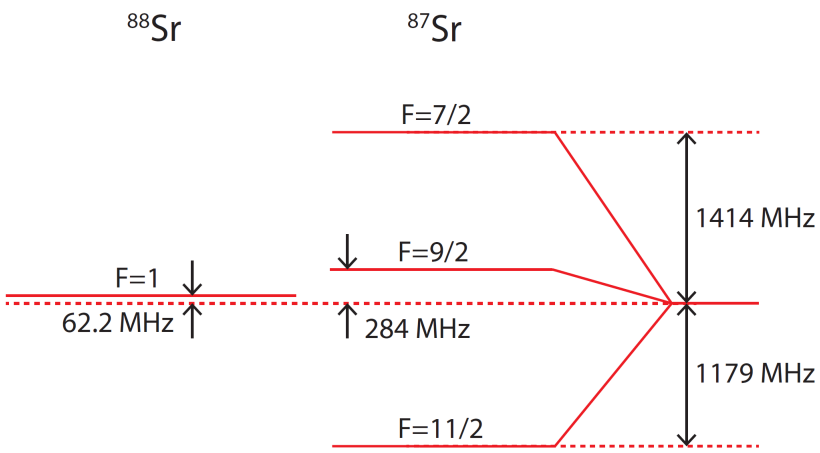

Figure 2.5: Hyperfine structure of the 5p $^3P_1$ energy levels of strontium drawn to scale. For bosonic ^{88}Sr (left) the nuclear spin I =0 leads to only a single hyperfine energy level. For fermionic ^{87}Sr (right) the nuclear spin I =9/2 leads to three hyperfine levels with splittings given above. The $\Gamma = 2\pi \times 7.5$ kHz natural linewidth is narrower than the width of the lines.

2.4. The $^3P_1$ energy level structure for ^{88}Sr and ^{87}Sr are shown in Fig. 2.5. The isotope shift for this transition is 62.2 MHz [12]. For the ^{87}Sr isotope there are again three hyperfine levels. For the $^3P_1$ state of ^{87}Sr we have the quantum numbers $J = 1$, $I = 9/2$, $F = \{11/2, 9/2, 7/2\}$ and coupling constants $A_{HFS} = -260.084$ and $B_{Quad} = -35.658$ [13] to give the energy shifts shown in Fig. 2.5.

2.4 Blue MOT cooling

The optical laser setups for the $^1S_0$–$^1P_1$ cooling transition are shown in Figs. 2.6, 2.7, and 2.8. The master laser setup is shown in Fig. 2.6. A single mode master laser (Newport, Vortex Plus TLB 6800) is split between the locking setup shown in Fig. 2.7 and between the slave diode lasers in Fig. 2.8. A small amount of light is also sent to the wavemeter for coarsely setting the frequency of the master laser via piezo and current tuning of the master laser.

For the spectrometer setup $\sim$ 6.5 mW of light from the blue master laser is output from a fiber launch with the power being monitored by a pickoff shortly after the output. The rest of the light passes through an acousto-optic modulator (AOM) giving a frequency shift of $\omega_{AOM1} = 2\pi \times 80$ MHz, which provides an overall offset of the blue master laser from the Sr transition. The light is

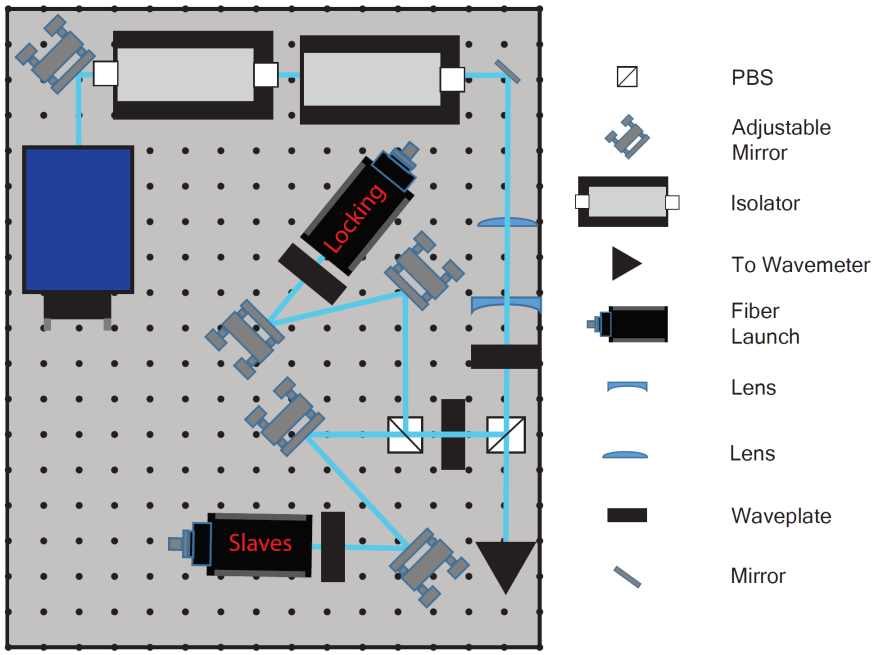

Figure 2.6: The optical setup of the 461nm master laser. The laser (Newport, Vortex Plus TLB 6800) pass through a double isolator setup (60 dB attenuation) before being shaped and split between two different paths. The first path goes to the spectrometer to lock the laser to the strontium transition and the second path goes to the slave laser setup for injection locking the three diodes.

then split between the pump and probe beams. The probe beam passes through a $\omega_{EOM} = 2\pi \times 19$ MHz EOM which adds sidebands to the laser for locking [14]. The pump beam passes through a species dependent AOM, with frequency $\omega_{Sr87/88}$, where magnetic mirrors are used to switch between cooling ^{87}Sr and ^{88}Sr. The spectroscopy cell used is a hollow cathode lamp (Hamamatsu L2783-38NE-SR) and uses Doppler-free spectroscopy for locking.

The main principle behind Doppler-free spectroscopy is velocity selection. There will be only a small subset of atoms with velocities that can interact with both the pump and probe beams. If both pump and probe beams are at the same frequency then only atoms with near zero velocity, along the beam propagation direction, can interact with both beams. Given that the absorption profile in the rest frame of the atoms has a natural linewidth Γ_0 we should expect the frequency range of the laser that can interact with the atoms to be approximately $\omega_0 \pm \Gamma_0/2$. This means

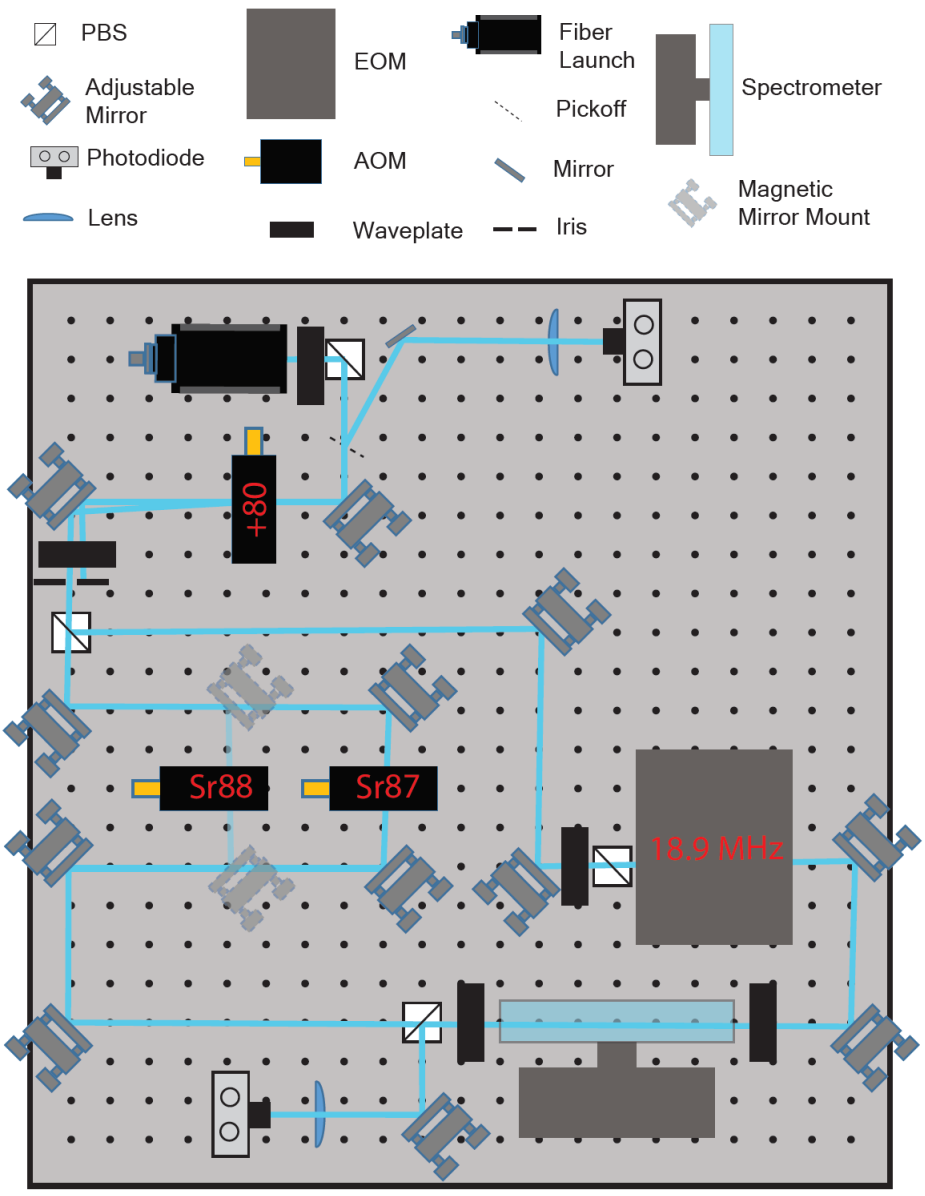

Figure 2.7: Some of the light from the blue master laser is fiber coupled to the setup shown above for locking to the strontium transition. An AOM is used to give an overall offset of +82.2 MHz from the ^{88}Sr transition. The light is then split between two paths. The probe path passes through the EOM before passing through the strontium cell and onto the photodiode. The second path passes through a species dependent AOM to add an additional offset for the pump beam. Magnetic mirror mounts are used to switch between the two strontium isotopes with the ^{88}Sr AOM at a frequency of +80 MHz and the ^{87}Sr AOM at a frequency of +175.7 MHz.

that we can ignore the increased linewidth due to Doppler motion.

In our experimental setup, the pump laser is sent through an isotope-dependent AOM before going through the vapor cell. The pump laser frequency thus experiences a shift of $+\omega_{Sr87/88}$ such that $\omega_{pump} = \omega_{probe} + \omega_{Sr87/88}$. To find the central velocity at which both the pump and the probe beams are resonant with the atoms we need to consider how the frequency of each beam is shifted due to the Doppler effect. Let ω'_{probe} and ω'_{pump} be the frequencies of the two lasers in the rest frame of the atom. In terms of the frequencies in the lab frame they are given by

$$\omega'_{probe} = \omega_{probe}\left(1 - \frac{v_z}{c}\right) \tag{2.3}$$

$$\omega'_{pump} = \left(\omega_{probe} + \omega_{Sr87/88}\right)\left(1 + \frac{v_z}{c}\right) \tag{2.4}$$

In the rest frame of the atom, on resonance, $\omega'_{probe} = \omega'_{pump} = \omega_0$. Solving these 2 equations for velocity gives

$$v_z = -\frac{c\omega_{Sr87/88}}{\omega_{Sr87/88} + 2\omega_{probe}} \tag{2.5}$$

Putting this expression for v_z back into the equation for ω'_{pump} and setting $\omega'_{pump} = \omega_0$ gives us the frequency we are locking from resonance as

$$\omega_{probe} = \frac{\omega_0 - \omega_{Sr87/88}}{2} + \frac{\sqrt{\omega_0^2 + \omega_{Sr87/88}^2}}{2} \sim \omega_0 - \frac{\omega_{Sr87/88}}{2} \tag{2.6}$$

$$\Rightarrow \omega_{pump} = \omega_0 + \frac{\omega_{Sr87/88}}{2} \tag{2.7}$$

making the approximation at the end because $\omega_0 \sim 2\pi \times 400$ THz and $\omega_{Sr87/88} \sim 2\pi \times 100$ MHz

We therefore know that we are locking our Blue Master laser $\left(-\nu_{AOM1} - \nu_{Sr87/88}\right)$ below the ^{88}Sr resonance. In both cases this is -120 MHz below the resonance of the species we wish to probe with ^{87}Sr ∼48 MHz below ^{88}Sr which agrees with the detuning shown in 2.4.

The rest of the master light, that is not sent to the spectrometer, is used to injection lock three different 150 mW laser diodes (Nichia, NDB4216E) with different offset frequencies. One of these injection locked diodes is used for the MOT beams with an overall offset from atomic resonance of -40 MHz. This light is sent via a polarization maintaining fiber splitter (1 : 3 fiber splitter, Evanescent Optics) to the experiment. The second of these diodes is used for Zeeman

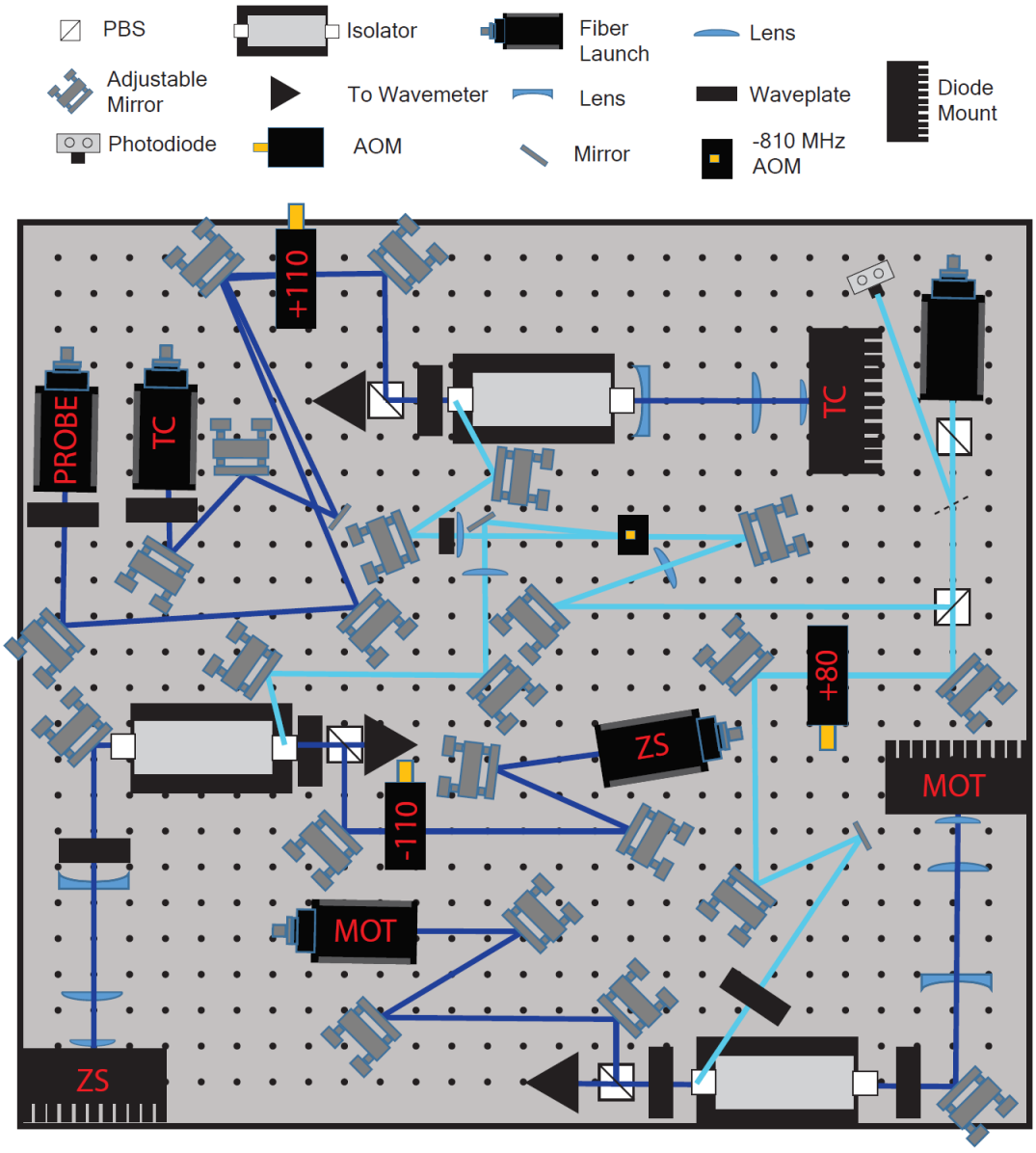

Figure 2.8: The slave diode setup at 461 nm. Light from the 461 nm master laser (cyan) is used to injection lock three diodes (Nichia NDB4216E). The diode light is shown in blue with the light being sent to different parts of the experiment. One diode is used for the blue MOT beams and is offset by −40 MHz from atomic resonance. Another diode is used for the Zeeman slower slowing beam and is offset from atomic resonance by -1040 MHz. The third diode is used for both transverse cooling and probing the atoms. The probe beam has an offset of −10 MHz and the transverse cooling beam passes through another +110 MHz AOM after the fiber to give the same offset frequency.

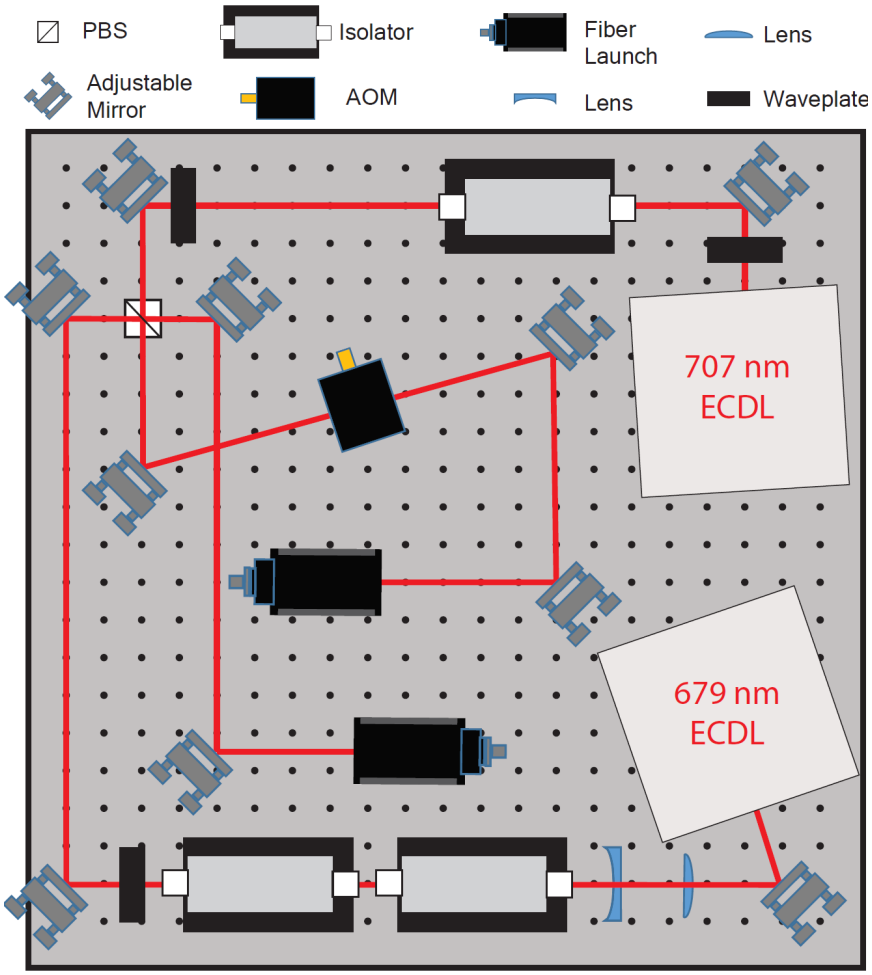

Figure 2.9: The 707 nm and 679 repump lasers remove atoms that become stuck in the long lived $^3P_2$ and $^3P_0$ states to allow further blue MOT cooling to take place. The two lasers are combined on a polarizing beam splitter before passing through an AOM and enter the fiber to the experiment with orthogonal polarizations. An alternative path takes the laser light to the wavemeter.

slowing the atoms that exit our strontium oven. The overall offset from resonance is -1040 MHz from resonance. The third diode is used for both transverse cooling of the atoms (with a AOM after the fiber) and probing the atoms both with a detuning of -10 MHz at the atoms. Each diode also sends a small amount of light to the wavemeter to check the mode of the laser is single mode after locking.

The optical setup of the repump lasers required for cooling on the $^1S_0$–$^1P_1$ transition are shown in Fig. 2.9. Both of the 707 nm and 679 nm lasers required for repumping are combined

on a polarizing beam splitter (PBS) before passing through an AOM in order to switch the beam quickly on and off. This also means that the two beams are orthogonally polarized going into the fiber with one aligned to the fast-axis of the fiber and the other to the slow-axis. The repump lasers are not locked but are set to the correct wavelength using the wavemeter and then optimized using the atomic signal from the MOT that is measured using a photodiode. The laser currents and piezos are swept for both ECDLs which allows the lasers to address all hyperfine structure and remain on resonance for many hours at a time.

2.5 Red MOT cooling

After blue MOT cooling to ∼mK temperatures the atoms are transferred to a broadband red MOT based on the $^1S_0{-}^3P_1$ transition. The blue lasers and repump lasers are switched off and the magnetic field gradient is quickly reduced from 50 G/cm to 4 G/cm and the lasers are modulated to increase their bandwidth and are broadened by $\sim$ 1 MHz. The gradient is held constant for $\sim$ 100 ms and then the gradient is ramped over $\sim$ 100 ms to 11 G/cm to the single frequency red MOT and at the same time the modulation is turned off.

The red master laser setup is shown in Fig. 2.10. The laser is stabilized with a prestabilization cavity and a master cavity (not shown) to give a linewidth of ∼1 Hz. This is of course unnecessary, but this cavity provides an excellent long-term stability so that our red MOT is reproducible every day. A 300 MHz AOM is used to set the frequency of the master laser to a detuning of +40 MHz compared to the ^{88}Sr $^1S_0{-}^3P_1$ transition. This red master laser is used to phase lock the lasers needed for the red MOT transition, shown in Fig. 2.11.

The $J = 0$ $^1S_0$ state has a small Landé g-factor compared to the excited state. The splitting of the different states by the applied magnetic field is large enough that not all of the magnetic sublevels are trapped. In order to get around this problem we use an additional laser to mix the states of the atoms so they can be continually cooled [7]. We refer to the MOT trapping laser as laser B which works on the $F = 9/2 \rightarrow F = 11/2$ transition and Laser A is used to interrogate the $F = 9/2 \rightarrow F = 9/2$ transition which mixes the states. DDSs are used to lock the lasers with

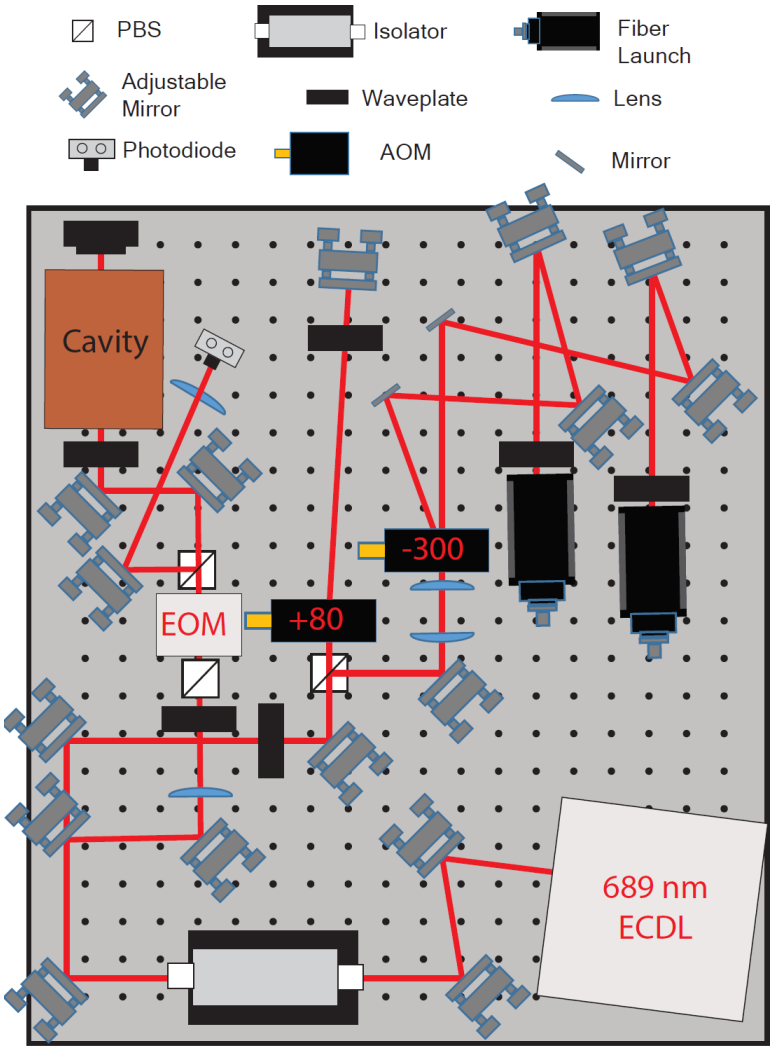

Figure 2.10: Setup of the 689 nm red master laser. The 689 nm light from the extended cavity diode laser (ECDL) is split after the isolator with $\sim$ 10 % of the light being used to lock to a prestabilization cavity. The rest of the light then double passes through an 80 MHz AOM before being split into two paths using a 300 MHz AOM. The -1 order is sent to the experiment and the $0th$ order is sent to another high finesse master cavity for further stabilization.

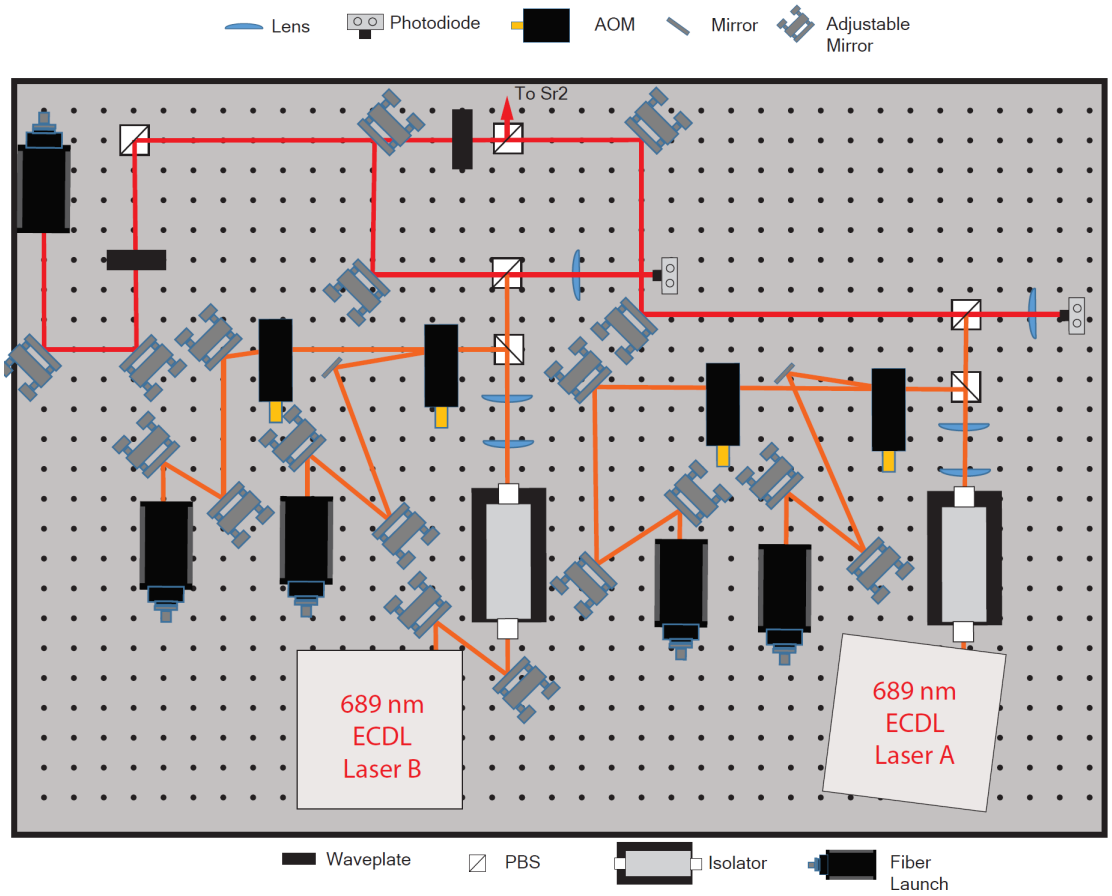

Figure 2.11: Two 689 nm lasers are needed to operate the $^1S_0 - ^3P_1$ MOT. The $F = 11/2$ transition is probed using Laser B which is the trapping laser of the MOT. The $F = 9/2$ state is probed with Laser A which is used as a stirring laser with a further AOM that is used for nuclear-spin polarizing the atoms. Laser B also has an AOM that can be used for on resonance probing of the atoms. The AOMs are all ~ 80 MHz with those for laser B using the -1 order and those for laser A using the $+1$ order. The lasers are locked using phase locks with different offset frequencies from the red Master laser (red lines).

appropriate offsets. For cooling ^{88}Sr the lack of hyperfine structure means that it is possible to operate the red MOT using just one trapping laser and no additional stirring lasers.

2.6 The Optical lattice

After cooling the atoms in the blue and red MOTs to μK temperatures, the atoms are then transferred to a one-dimensional optical lattice. In our case the lattice is on during the whole cooling sequence, and when the red lasers are switched off the atoms are transferred to the lattice. In most of the experiments discussed in this thesis the lattice is a vertical lattice (offset by 18°) to suppress tunneling between the different lattice sites. For our spin-orbit coupling work discussed in chapter 7 a horizontal lattice is used to study the tunneling effects.

When a magnetic field is applied to the atoms the 10 nuclear spin states of Sr can be resolved spectroscopically as shown in Fig. 2.12 using π-polarized clock light with the propagation axis of the clock beam aligned with the direction of the lattice. The different heights of the unpolarized

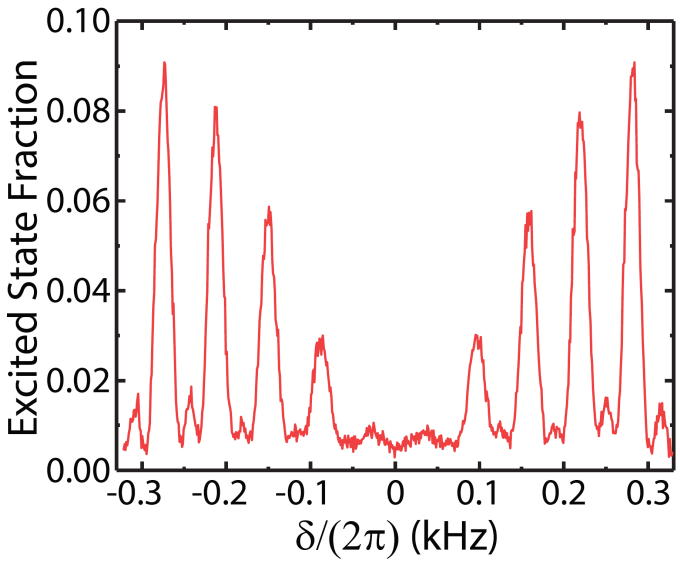

Figure 2.12: Unpolarized clock scan with a magnetic field using π-polarized clock light The ten nuclear spin states can be seen, along with Rabi sidepeaks, and are equally populated after MOT cooling. The different heights of the excited peaks are due to different Clebsch-Gordon coefficients for the different m_F states.

carrier clock transitions are caused by the different Clebsch-Gordon coefficients even though the population, after the MOT cooling, is an incoherent mixture with the same number of atoms in each state.

To determine the normalized fraction of atoms in each of the clock states we measure both the number of atoms in the ground clock state and the excited clock state. Once atoms are prepared in a superposition or mixture of clock states the number of atoms in the ground state can be determined by slashing on a $^1S_0 - ^1P_1$ blue probe laser beam which causes the atoms to fluoresce and heat up and they are removed from the trap by this heating. The fluorescence signal is measured using a photomultiplier tube (PMT). The number of atoms in the excited clock state can be measured by using the repump lasers to move the atoms back down to the ground clock state where they can be measured again using a blue probe beam. By also making a measurement of the background fluorescence the fraction of atoms in the excited state can then be found.

While trapped in the lattice the atoms can be spin-polarized using a magnetic field along the

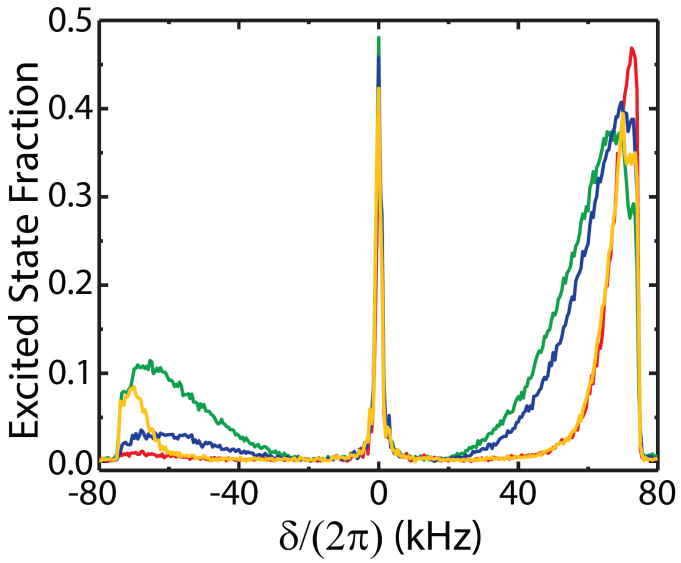

Figure 2.13: Axial sideband scans under different conditions. The green scan shows the axial sideband scan without any in lattice cooling. With only sideband cooling the sideband scan is shown in blue. With only radial cooling the sideband scan is shown in yellow. With sideband and radial cooling the sideband scan is shown in red.

$H2$ axis (see Fig. 2.1) and a polarizing beam using the $^1S_0 - ^3P_1$ $F = 9/2 \rightarrow F = 9/2$ transition along the same axis. The atoms can be cooled in the lattice both axially and radially. For the axial sideband cooling a component of the axial beam needs to be along the lattice axis and the frequency can be set roughly using the known axial trapping frequency. The fine tuning of the frequency is set by making the red detuned lattice sideband as low as possible. For the radial cooling the MOT trapping beams are used as molasses cooling and the frequencies are set by either reducing the width of the radial profile of the trapped atoms or equivalently by reducing the width of the axial sidebands. Figure 2.13 shows the effect of cooling on the axial sideband scan. Without any in lattice cooling the sideband scan is shown by the green line. When radial cooling is applied (yellow line) the width of the axial sidebands are reduced due to axial radial coupling. If only axial cooling is applied then the height of the red detuned sideband is reduced (blue line). With both axial and radial cooling (red line) both the width of the sidebands and the height of the red sideband are reduced. The clock laser that we use to probe the clock transition has been used since before I joined the strontium team in 2013. The cavity and setup is described in detail in [7] and has been an extremely reliable tool.

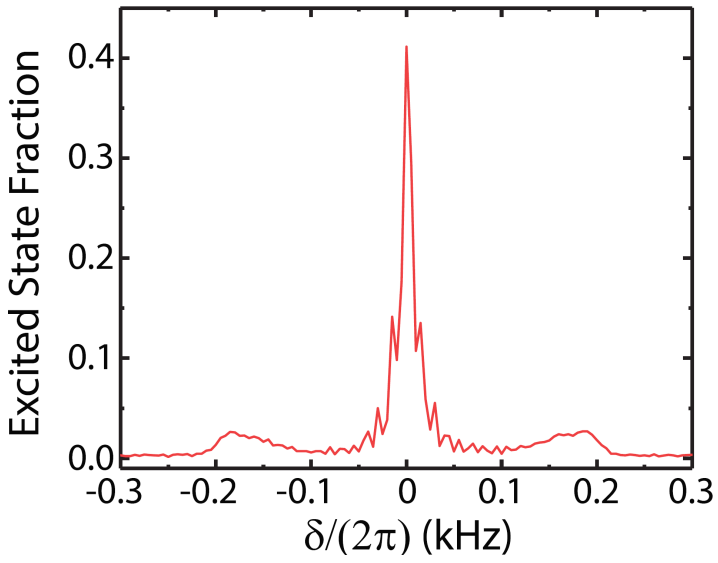

Figure 2.14: A radial sideband scan with $\nu_R = 190$ Hz. The axial trapping frequency in this case is $\nu_Z = 43$ kHz.

As well as the axial sidebands the radial sidebands can be measured to determine the radial trapping frequency. To measure the radial sidebands the clock beam needs to be misaligned from the lattice axis and an example of a radial sideband scan is shown in Fig. 2.14.

The lattice wavelength is set to the "magic wavelength" at 813 nm. This magic wavelength occurs where the polarizability of the two clock states is the same meaning the two states are shifted in frequency by the same amount. Figure 2.15 shows the scalar polarizability of the two clock states in the wavelength range $700-900$ nm. The vector polarizability is cancelled when $m_F = +9/2$ and $m_F = -9/2$ states are interrogated (see section 3.2.2).

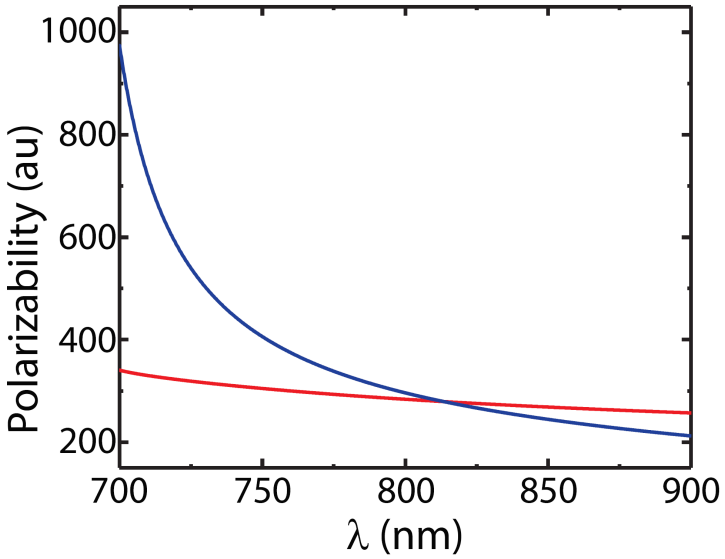

Figure 2.15: The scalar polarizability of the two different clock state $^1S_0$ (red) and $^3P_0$ (blue). The magic wavelength at 813 nm occurs when the polarizability of the two clock states are the same.

Chapter 3

Strontium Clock Evaluations

3.1 Introduction

In order to evaluate the frequency of our $^1S_0 - ^3P_0$ strontium clock transition we need to understand and measure all effects that shift the frequency of this transition. These effects are all due to the environment in which the atom is located such as from electromagnetic fields, interactions between different atoms, and the motion of atoms.

The basic principle around measuring these shifts is the same for most of these effects - we must vary one parameter with all other conditions constant and measure how the frequency of the transition varies. The way we do this is by preparing atoms in our optical lattice, applying a magnetic field, and alternate preparing atoms in the $m_F = \pm 9/2$ nuclear spin states as well as changing the parameter of interest. For some shifts, for example the density dependent frequency shift, it is possible to just probe one of the stretched nuclear spin states to measure the shift which means the measurement can be made faster.

For the case of alternating between probing each of the stretched nuclear spin states, to determine the resonance frequency the center of both stretched states are measured individually. To do this one measurement of the excitation fraction is made on either side of each lineshape. The difference between the two measured excitation fractions can then be used to predict where the center frequency of the lineshape is. By doing this measurement for both $m_F = \pm 9/2$ states the center frequency can be determined (see Fig. 3.1). Once the center frequency is determined from this measurement, digital feedback is used to change the clock laser probing frequencies to

stabilize them at 50% excitation fraction frequencies. This can be repeated for different conditions such as different lattice intensities. By alternating high and low lattice intensities and measuring a resonance frequency for both lattice depths a shift in the resonance frequency can be measured and be used to correct the transition frequency. To measure the center frequency using the stretched states four measurements are needed for each condition so we refer to this method of locking the laser as an "8 point lock".

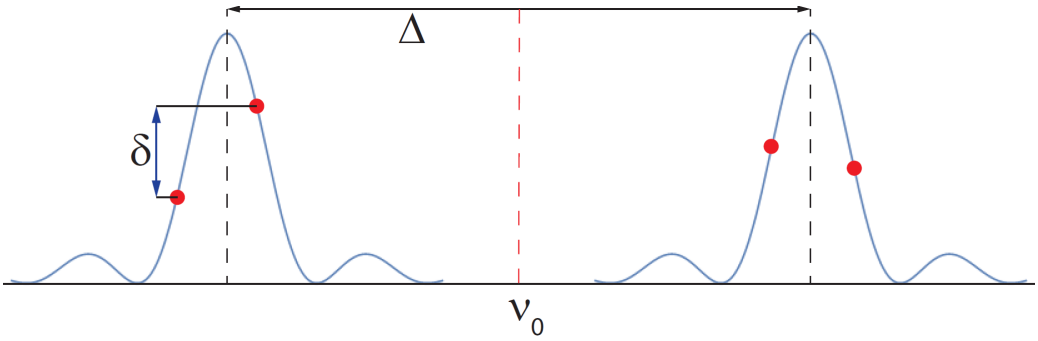

Figure 3.1: Determining the strontium resonance frequency. Both the $\pm 9/2$ nuclear spin states are probed on each side of the lineshape (red circles). Using the difference δ between the measured excitation fractions the center of each lineshape is determined, and half way in frequency between the two is the resonance frequency of Sr ν_0. A digital servo uses the measured splitting and center frequency to feedback for the frequencies used to probe the next measurement of ν_0.

After many measurements of a frequency shift the distribution of measured shifts is Gaussian in nature. An example measurement is shown in Fig. 3.2. We can see the distribution is Gaussian and is peaked at $-0.118 * 10^{-15}$, where we use fractional frequency units $\Delta\nu/\nu_0$, where ν_0 is the resonance frequency of the clock transition. As more measurements are taken the systematic uncertainty in how well we can determine the center frequency is reduced.

3.1.1 Chapter Outline

In this chapter we will discuss in detail some of the major causes of frequency shifts in optical lattice clocks along with the comparison of different clocks. In section 3.2.1 we will discuss the frequency shift that arises from contact interactions between the atoms that are trapped within

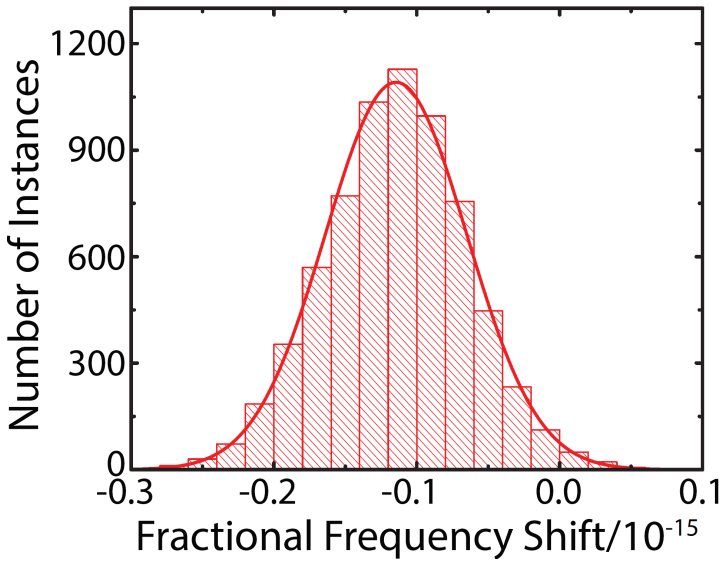

Figure 3.2: An example measurement of a density dependent frequency shift. After many measurements the distribution is Gaussian and the peak indicates the frequency shift. The systematic uncertainty in the frequency shift is related to how well we can determine this center frequency.

the optical lattice. In section 3.2.2 we will discuss the effect the lattice light used to hold the atoms has on the clock transition frequency. In section 3.2.3 we will discuss the dc Stark Shift which can be caused by patch charges located on vacuum viewports, cavity mirrors, or other dielectric materials that are in close proximity to the atoms. In section 3.2.4 we will discuss the effect that magnetic fields, that we need to apply to split the different nuclear spin states, have on the transition frequency. In section 3.2.5 we will discuss the frequency shift caused by the surrounding temperature environment of the atoms. This frequency shift can be large and it is important to measure the temperature accurately and precisely in order to make a strontium optical lattice clock with low 10^{-18} fractional frequency uncertainty. In section 3.2.6 we will give a brief summary of other known frequency shifts that effect the clock transition frequency for optical lattice clocks.

We will then move on in section 3.4 to discuss the two different clock comparisons that we have undertaken during the last six years. The first of these clock comparisons (see section 3.3.1) took place in 2013 where we compared both of the strontium clocks within our own lab. In section 3.3.2 we discuss the second of these clock comparisons which is ongoing and involves our colleagues

at the National Institute of Standards and Technology (NIST). In this comparison we are comparing our Sr optical lattice clock to both a Yb optical lattice clock and an Al^+ ion clock.

3.2 Measuring Systematic Uncertainties

3.2.1 Density Shift

The more atoms that we load into our optical lattice the more atoms we have to measure the transition frequency. During a measurement each atom will collapse from a superposition state into either the excited or the ground clock states and the more atoms we have the better understanding of the initial superposition we will have. However, by having more atoms we are also loading more atoms per lattice site. The atoms can then interact with each other via contact interactions that we investigate further in chapter 6 for the case of atoms loaded into different nuclear spin states, and in chapter 7 for the case of nuclear spin polarized atoms when tunneling is allowed. In chapter 4 we also look at interactions that are not caused by contact interactions but instead caused by dipole-dipole interactions between atoms.

While these studies will be important for the design of future clocks, in our current setup the interactions that take place have been studied previously in detail [15, 16, 17]. Experimentally the atom number can be calibrated in multiple ways as discussed in Appendix A. The density per particle of the atoms in the lattice is given by

$$n(\mathbf{r}) = \frac{N_{site}}{(2\pi)^{3/2}\sigma_x\sigma_y\sigma_z} e^{-\frac{x^2}{\sigma_x^2}-\frac{y^2}{\sigma_y^2}-\frac{z^2}{\sigma_z^2}} \tag{3.1}$$

where N_{site} is the number of atoms per lattice site, and σ_α are the $1/e$ widths of the atomic cloud. For a thermal distribution of atoms, the widths in the lattice are given by [18]

$$\sigma_\alpha = \sqrt{\frac{\hbar}{2\pi M\nu_\alpha}} \times \sqrt{2\langle n_\alpha\rangle + 1} \tag{3.2}$$

where

$$\langle n_\alpha\rangle = \frac{1}{e^{\frac{\hbar\omega}{k_B T_\alpha}} - 1} \tag{3.3}$$

is the average vibrational quantum number along the α direction. The average density of a lattice site is given by the density-weighted density

$$\bar{n} = \frac{1}{N_{site}} \int n(\mathbf{r})^2 d\mathbf{r} \tag{3.4}$$

$$= \frac{N_{site}}{(2\pi)^{3/2}\sigma_x\sigma_y\sigma_z} \tag{3.5}$$

For the axial direction the atoms are cooled such that $\langle n_z \rangle \approx 0$ giving $\sigma_z = \sqrt{\frac{\hbar}{2\pi M \nu_z}}$. In the radial direction, under standard clock operating conditions, we can approximate the exponential term in $\langle n_\alpha \rangle$ and write $\sigma_x = \sigma_y = \sigma_R = \sqrt{\frac{2k_B T}{(2\pi\nu_R)^2 M}}$.

During the 2013 clock comparison our clock operating conditions were $\nu_z \approx 46$ kHz and $\nu_R = 240$ Hz and the total number of atoms $N = 700$ atoms, where $N = N_{site} \times L$ for L the number of lattice sites. For the 2017/18 comparison the lattice beam was expanded to reduce the density shift and we had the operating conditions of $\nu_z \approx 46$ kHz and $\nu_R = 90$ Hz and $N = 1000$. Comparing these two different lattice configurations we expect a ratio of the density shifts to be

$$\frac{\Delta\nu_\rho(2017/18)}{\Delta\nu_\rho(2013)} = \frac{N_{2017/18}}{N_{2013}} \frac{\sqrt{\nu_{z,2017/18}} \times \nu_{R,2017/18}}{\sqrt{\nu_{z,2013}} \times \nu_{R,2013}} = 0.20 \tag{3.6}$$

The actual measurments gave a ratio of 0.17 ± 0.03 consistent with the expected ratio (see Table 3.3.2)

3.2.2 Lattice ac Stark Shift

During clock spectroscopy, the transition frequency is perturbed by electromagnetic fields. This means that even the light used to trap the atoms in the optical lattice causes perturbations to the transition frequency. To avoid this, as mentioned in chapter 2, a "magic wavelength" optical lattice is used that moves the two clock states in the same way. The differential ac Stark shift between the two clock states, $\Delta\nu_{ac}$, is given by

$$\Delta\nu_{ac} = U_0\{\Delta\kappa_s + \Delta\kappa_v m_F \xi \hat{\mathbf{k}} \cdot \hat{\mathbf{B}} + [3m_F^2 - F(F+1)(3|\hat{\epsilon} \cdot \hat{\mathbf{B}}|^2 - 1)\Delta\kappa_t]\} \tag{3.7}$$

where U_0 is the lattice trap depth, $\hat{\epsilon}$ and $\hat{\mathbf{k}}$ are the polarization and wavevector of the lattice, ξ is

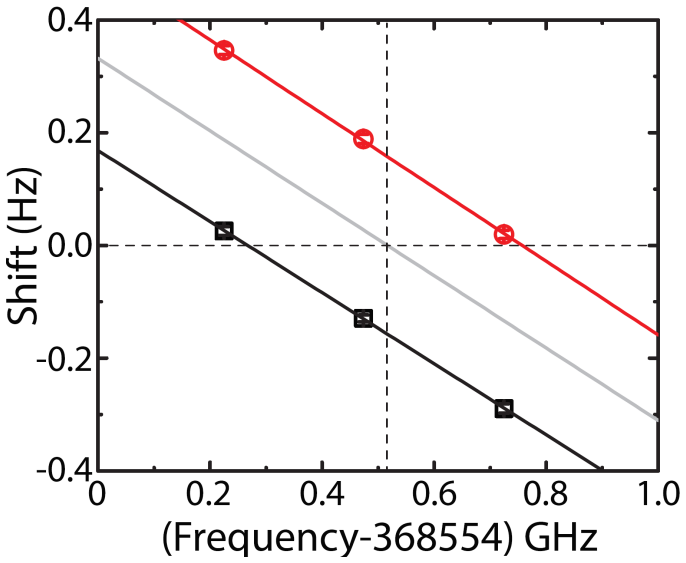

Figure 3.3: Measurement of the magic wavelength using $m_F = +9/2$ (black) and $m_F = -9/2$ (red). The splitting of the two m_F states indicates the presence of a residual vector Stark shift.

the ellipticity of the lattice polarization, $\hat{\mathbf{B}}$ is the direction of the applied bias field, and $\Delta\kappa_s$, $\Delta\kappa_v$, and $\Delta\kappa_t$ are the coefficients of the differential scalar, vector, and tensor shifts, respectively. The equation also uses the quantum numbers F and m_F which are the total angular momentum and the total angular momentum projection along the quantization axis given by the magnetic field. For our lattice we use linearly polarized light, $\xi = 0$, with $\hat{\mathbf{k}} \cdot \hat{\mathbf{B}} = 0$ $\hat{\epsilon} \cdot \hat{\mathbf{B}} = 1$. Doing this doubly suppresses the vector Stark shift and by probing both the $m_F = \pm 9/2$ states we can remove all contributions from the vector Stark shift. The "magic wavelength" we use is therefore where the scalar and tensor components of the differential Stark shift cancel for $m_F = \pm 9/2$.

To find this magic wavelength experimentally we vary the lattice intensity to change the depth of the lattice and find the frequency shift for both $m_F = \pm 9/2$. Such a measurement is shown in Fig. 3.3. As can be seen there is a residual vector shift which makes the shifts for the two states different. The magic wavelength is then the frequency of the lattice half way between where the frequency shift is zero for the $+9/2$ state and for the $-9/2$ state. This measurement gives roughly the magic wavelength and by performing an 8point lock (see section 3.1) with $\pm 9/2$ and by varying the lattice depth again between two values. Any residual lattice ac Stark shift can

be measured and if needed the frequency can be further tuned.

It is important to note that during the ac Stark shift measurement the density shift will be different between the two lattice depths. The density shifts at each lattice depth therefore need to be measured and taken into account in order to determine the true lattice ac Stark shift. Also, during each of our clock evaluations the lattice ac Stark shift was found to drift with time. In 2013, a tapered amplifier (TA) system was used to create the optical lattice. These TA systems are known to have a spectral noise pedestal due to amplified spontaneous emission (ASE). Even with the use of a spectral filter the shift was found to drift linearly with time by $\sim 12 \times 10^{-17}$ in 35 days. During our second clock comparison it was thought that upgrading our lattice light source from a TA system to a lattice based on a Ti:Sapphire laser would reduce this problem and a filter would not be required. Without any filtering a drift in the lattice ac Stark shift was still measured and thought to be due to a poorly performing pump laser of the Ti:Sapphire laser. By adding in two volume bragg gratings the frequency shift was found to be consistent over time, and also consistent with the first ac Stark measurement before the power in the laser started to deteriorate.

The lattice light may become a limiting factor for our optical lattice clock in the near future. The recently built 3D optical lattice clock in our lab has measured an excited state lifetime of < 20 s where the predicted lifetime should be ~ 160 s. The lattice light is believed to be causing Raman transitions from $^3P_0$ to $^3P_1$ allowing the atoms to decay to the ground state quickly. Other schemes involving lower lattice intensities and larger lattice spacings may be required for future clocks to take advantage of the full excited state lifetime [19] .

3.2.3 dc Stark Shift

The dc Stark shift in an optical lattice clock was first seen by Lodewyck et al [20] and was found to be caused by a charge on an in-vacuum cavity mirror that was used to form the optical lattice. Due to the close proximity of the mirrors the fractional frequency shift was found to be at the 10^{-13} fractional frequency shift level. This shift was removed by illuminating the mirrors with UV radiation for two days. Even without an in vacuum cavity the vacuum chamber windows can

be close enough to measure a large frequency shift, especially as atomic clocks are pushed to better levels of accuracy.

In 2014, Bloom et al [21] reported a 1.3×10^{-16} shift caused by a charge on one of the vacuum viewports that was removed by filling the vacuum chamber with nitrogen gas. During the 2013 evaluation of the systematic uncertainties on our experiment no dc Stark shift was observed. However, during the 2017/18 systematic evaluation a large frequency shift was measured, and then removed, that will be discussed in more detail later in this section.

The dc Stark effect induces a frequency shift given by

$$\Delta\nu_{dc} = -\frac{1}{2}\Delta\alpha_0 E^2 \tag{3.8}$$

where E is the dc electric field and $\Delta\alpha_0$ is the difference in the dc polarizability between the two clock states. The quadratic nature of the shift means that by reversing the direction of the electric field will have no effect on the magnitude of the shift. However, when a static patch charge, producing an electric field E_p, is present then the frequency shift for two opposite applied electric fields, E_a are given by

$$\Delta\nu_{\pm} = -\frac{1}{2}\Delta\alpha_0 (E_a \pm E_p)^2 \tag{3.9}$$

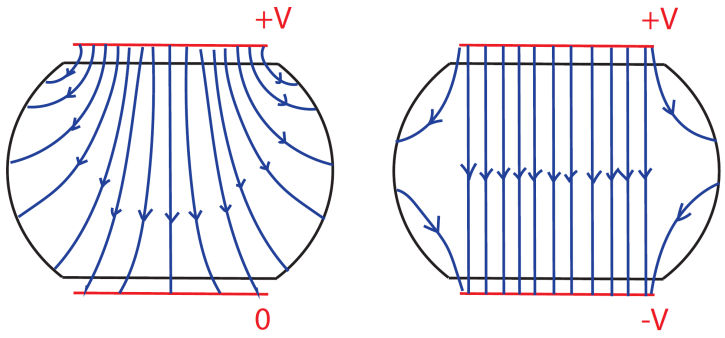

Figure 3.4: Cartoon of the dc Stark measurement. On the left is a cartoon of the electric field when one electrode is charged and the other is grounded. Due to the grounded chamber it can be difficult to measure perpendicular axes. When equal and opposite voltages are applied to the electrodes, the electric field can be more easily measured for perpendicular axes, due to less fringe effects.

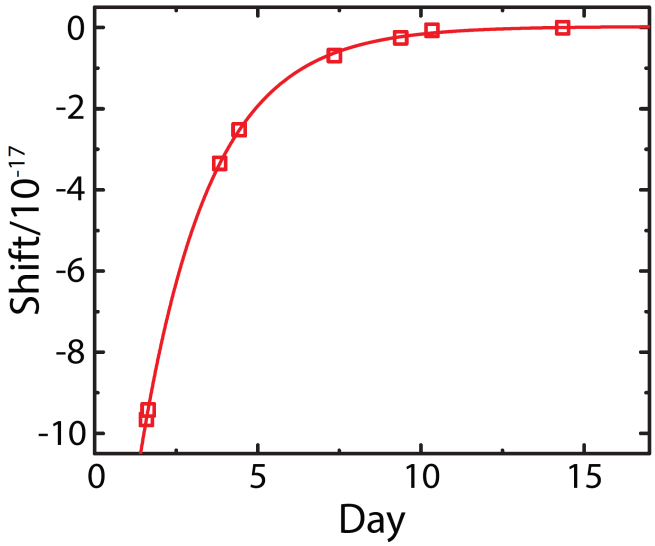

Figure 3.5: Drift of the dc Stark shift with time. A Large dc Stark shift was measured and is seen to discharge with time to below the 10^{18} fractional frequency level.

The difference between these two, $\Delta\nu_+ - \Delta\nu_-$, is proportional to $4E_aE_p$. We can then get the frequency shift by using

$$\Delta\nu_{dc} = \frac{(\nu_+ - \nu_-)^2}{16V_a} \tag{3.10}$$

where V_a is the applied voltage on the electrodes, where one has voltage V_a and the other $-V_a$. It is important to use equal and opposite voltages on the two electrodes used in order to easily apply orthogonal electric fields. The reason for this is shown in the cartoon in Fig. 3.4.

On the left of the figure shows the case when one electrode has a voltage and the other is grounded. The electric field can be reversed by changing the voltage on the top plate from $+V$ to $-V$ but overall the electric field does not go straight from one plate to the other due to the grounded vacuum chamber. When the electrodes have equal and opposite voltages applied (right) then the electric field is straighter and it is easier to apply orthogonal electric fields at the atoms.

When measuring the dc Stark shift it is convenient to use quadrant electrodes similar to those discussed in [22]. Due to the asymmetry of our chamber the top and bottom viewports are much closer than the other viewports. This means that it is easier to place the electrodes close to the atoms and their large size enables us to not block the laser beam access. These quadrant

electrodes allow us to apply perpendicular electric fields to the atoms to measure the dc Stark shift in all directions.

During our 2013 systematic evaluation no dc Stark shift was measured at the 10^{-18} level for the Sr1 experiment. For the 2017/18 evaluation a large shift was measured that varied in time as shown in Fig. 3.5. The shift was measured over 17 days and was seen to exponentially decay to below the 10^{-18} level over 15 days. The shift is believed to have occured due to charging a dielectric material used between the electrodes and the thermistors on the viewports when the voltage was applied for a long time. By alternating the measurements between $\pm V$ and ground every cycle of the experiment we were able to stop charging them up.

To cancel the electric field we can apply a voltage to the electrodes that will cancel the field. We can check that the field is cancelled by adding in an additional $\pm V$ to the electrodes. An example of a cancelled dc Stark shift is shown in Fig. 3.6. It is seen to be parabolic as expected from Equation 3.8 We note that even though voltages required to cancel the field are small, they are reversed during atom preparation to avoid any build-up of charge.

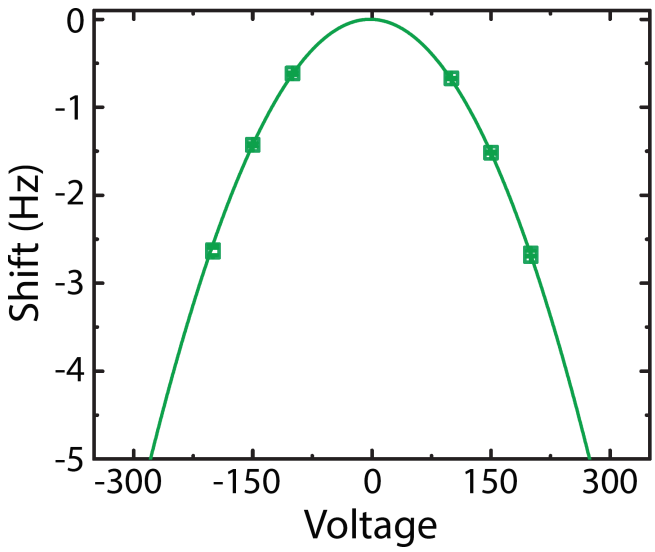

Figure 3.6: A cancelled dc Stark shift measurement.

3.2.4 Zeeman Shifts

A magnetic field is applied in order to spin polarize the atoms into a single nuclear spin state. Having the atoms in a single nuclear spin state has the advantages of suppressing s-wave collisions and also gives a better signal to noise ratio during clock spectroscopy as all atoms can be interrogated. The Zeeman shift has two components the first order Zeeman shift and the second order Zeeman shift. The resulting Zeeman shift is shown in Fig. 3.7 for the 10 nuclear spin states.

The first order Zeeman shift is caused by a differential g-factor δg between the two clock states. This first order shift for π-transitions is given by

$$\delta\nu^{(1)} = -m_F B \delta g \mu_0 / h \tag{3.11}$$

where B is the magnetic field, μ_0 is the Bohr Magneton, and h is Planck's constant, with $\delta g \mu_0 / h = -108.4$ Hz/Gauss. This differential g-factor arises from state mixing of the $^3\mathrm{P}_0$ clock state with other states due to hyperfine interaction mixing of states [8]. This shift is cancelled out when both spin states are interrogated. However a residual first-order shift can remain due to any small changes in the magnetic field strength which changes the measured center frequency from the true center frequency.

For the second-order Zeeman shift, the frequency shift is proportional to B^2 and is dominated by the interaction between the $^3\mathrm{P}_0$ and $^3\mathrm{P}_1$ states [8]. The shift is given by

$$\delta\nu^{(2)} = -A_{B2} B^2 \tag{3.12}$$

where $A_{B2} = 0.233$ Hz/G^2. Equivalently the shift can also be written in terms of the splitting between the $m_F = +9/2$ and $m_F = -9/2$ states $\mathcal{S}$ as

$$\delta\nu^{(2)} = -B_{B2} \mathcal{S}^2 \tag{3.13}$$

where the coefficient is measured to be $B_{B2} = 0.248(2) \times 10^{-6}$ Hz^{-1}[21].

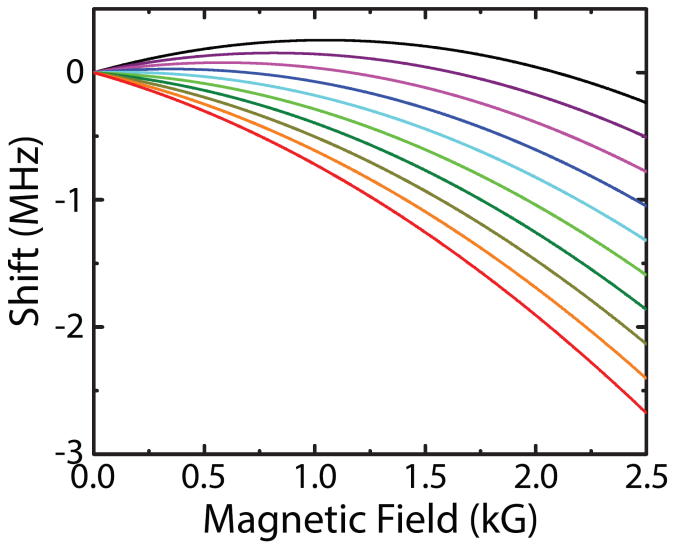

Figure 3.7: First- and second-order Zeeman frequency shifts for π-transitions of the different nuclear spin states. The nuclear spin states are in order from $m_F = -9/2$ (red line) to $m_F = +9/2$ (black).

3.2.5 Blackbody Radiation Shift

The blackbody radiation (BBR) shift arises from the environment in which the atoms are located. The effect is similar to the lattice ac Stark shift but arises from the interaction of the atoms with thermal BBR radiation instead of the optical lattice light. The BBR shift is the largest of the clock shifts under our usual operating conditions and strontium has the biggest BBR shift for the optical atomic clocks currently being studied and therefore this systematic is particularly important for us. Whereas other systematic uncertainties are measured using the locking method discussed in the introduction to this chapter, with the BBR shift we rely on measuring the temperature and the homogeneity of the environment. It should be pointed out that some other groups have been able to systematically vary the temperature environment to check the measurements are agreeing with the theoretical model [23].

The BBR Shift, $\delta\nu_{BBR}$, can be written in terms of two components as

$$\delta\nu_{BBR} = \Delta\nu_{stat}\left(\frac{T}{300\text{K}}\right)^4 + \Delta\nu_{dyn}\left(\frac{T}{300\text{K}}\right)^6 \tag{3.14}$$

where the first term is a static shift and the second is a dynamic part. The static shift is from an effective dc electric field experienced by the atoms and the dynamic part is a correction to this first term. The static coefficient was measured by Middleman et al to be $\Delta\nu_{stat} = -2.13023(6)$ Hz. For the dynamic coefficient, before 2015 there were two calculated values from Middleman et al [24] $\Delta\nu_{dyn} = -147.6(23)$ mHz and from Safronova et al [25] $\Delta\nu_{dyn} = -149.2(16)$ mHz. For our 2013 clock evaluation we therefore took a weighted mean of the two values and used $\Delta\nu_{dyn} = (-148.3 \pm 1.6)$ mHz where the error is the difference between the two calculated values.

In 2015 Nicholson et al were able to improve upon the uncertainty of the calculated value of $\Delta\nu_{dyn}$. The reason for this relates to a proposal in by Safronova et al [25] who proposed a solution to improving upon the uncertainty in the calculated value of this coefficient by measuring the lifetime of the $^3\text{D}_1$ state of Sr. The reason for this is that the oscillator strength of the 2.6 μm $^3\text{D}_1$–$^3\text{P}_0$ transition is the dominant source of uncertainty in the calculation of $\Delta\nu_{dyn}$ due to its significant overlap with the room temperature BBR spectrum [26]. From this new measurement the value of

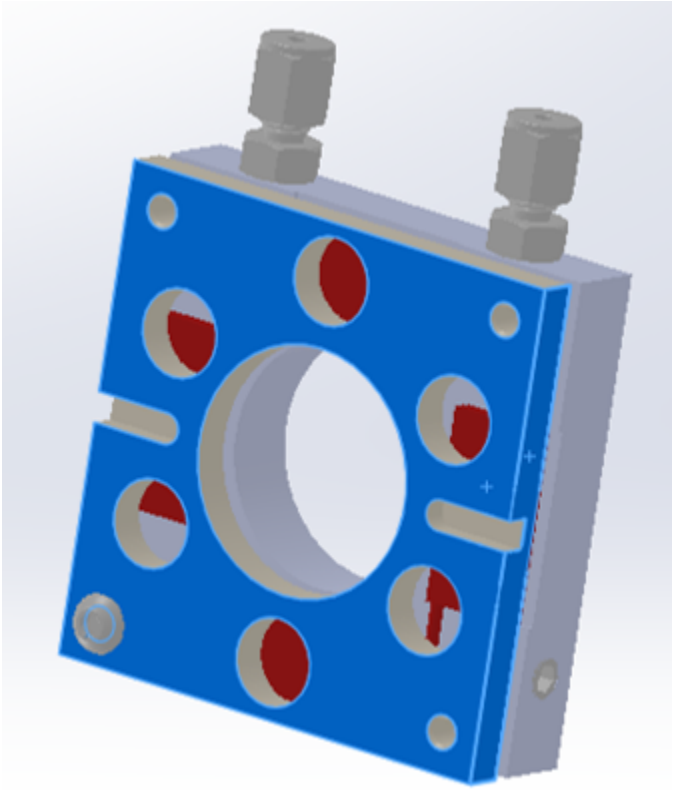

Figure 3.8: Temperature stabilization of the vacuum viewport. At least two thermistors are used for each viewport. One of the thermistors is used in-loop to control the viewport temperature and the others are used as witnesses. Peltier coolers are used to control the temperature to $\sim 22\,^{\circ}\mathrm{C}$ and water lines are attached at the top to circulate water for removing any excess heat.

$\Delta\nu_{dyn}$ used during our 2017/18 clock evaluation was changed to (-148.7 ± 0.7) mHz. The remaining uncertainty in the blackbody radiation therefore comes from the measurement of the temperature. The uncertainties of $\delta\nu_{BBR}$ will also be temperature dependent ($\propto T^3$ for the static contribution and $\propto T^5$ for the dynamic contribution) meaning that cryogenic clocks have the prospect of leading to more accurate clocks. For the 2013 evaluation we used 8 thermistors to record an emissivity weighted average of the temperature around the vacuum chamber with the uncertainty related to the drift of this average with time. For this same clock evaluation the second Sr experiment Sr2 took the approach of using in-vacuum temperature sensors combined with a BBR shielding box around the vacuum chamber. One of these sensors was attached to a bellows and moveable in

order to measure how the temperature distribution changed and to check the agreement with the temperature model [4]. With the use of these in vacuum temperature sensors Sr2 were able to show for the first time a total systematic uncertainty at the low 10^{-18} level. The temperature stabilization of the vacuum viewports also allows the whole vacuum chamber to thermalize more easily.

During our 2017/18 systematic evaluation we wanted to test the limits of a room temperature clock without in vacuum temperature sensors. For this approach we also built a BBR shielding box around the whole chamber with the majority of the laser light being brought through optical fibers into the box. In order to keep the BBR environment as uniform as possible we chose to temperature stabilize each of the vacuum viewports. The reason that we care in particular about the vacuum viewports is that they have a much higher emissivity than the rest of the vacuum chamber. The emissivity gives the ratio of heat emitted compared to a perfect blackbody such that a low emissivity surface does not emit as much BBR radiation and thus we care less about its temperature.

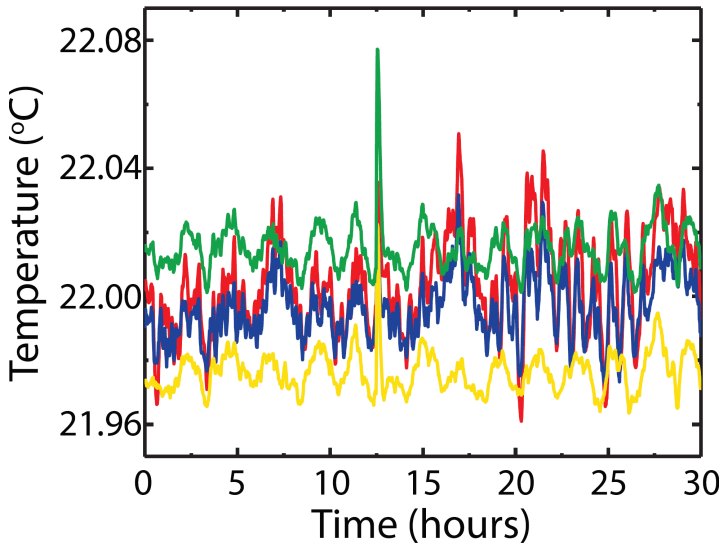

Figure 3.9: Temperature measurements of the top (green and yellow) and bottom (red and blue) vacuum viewports. These viewports have the highest emissivity weighted solid angle and hence contribute most to the BBR shift and uncertainty. They are stable to within ±50 mK with the large spike during hour 12 during a break in the experimental data.

The temperature stabilization uses both Peltier coolers and water cooling to remove any excess heat from the Peltier cooler. An example of the cooling setup is shown in Fig. 3.8 and fits over the vacuum viewport. Great effort was taken to control the temperature of the vacuum chamber[1] and an example of the temperature during clock operation is shown in Fig. 3.9. As can be seen the temperature is stable to within ±50 mK and combined with the temperature uncertainty of the thermistors the total uncertainty from BBR radiation was reduced by more than an order of magnitude compared to our Sr1 2013 evaluation to $\sim 6 \times 10^{-18}$. The work on reducing the BBR uncertainty is ongoing and is continuing to be improved upon during the writing of this thesis.

3.2.6 Other Frequency Shifts

In this section we will briefly summarize some of the other frequency shifts that affect optical lattice atomic clocks. In the same way that the light forming the optical lattice can cause frequency shifts, the clock light used to probe the atoms also causes a frequency shift. This can be measured by using π-pulses of varying length and comparing how the clock transition frequency changes. It is important when measuring this shift to take into account shifts associated with the AOM used for fiber noise cancellation. This AOM is switched on and off to create the probe pulse which causes a phase chirp due to the heating of the AOM crystal which also leads to the amplitude modulation of the clock light used for fiber noise cancellation [27].

As well as collisions between the different Sr atoms within the lattice, the Sr atoms can also collide with any other atoms or molecules that are within the vacuum chamber. This shift can be calculated based on the methods discussed in Gibble et al [28]. For this measurement the lifetime of the atoms in the vacuum needs to be known, and the measurement is shown in Fig. 3.10 and shows a lifetime in the optical lattice of 6.6 s. This will be a lower limit on vacuum lifetime of the atoms and gives a shift and uncertainty below the 10^{-18} level. The movement of the atoms in the lattice can also lead to Doppler shifts of the clock transition frequency. The first order doppler

[1] The majority of this work was undertaken by Toby Bothwell and Dhruv Kedar.

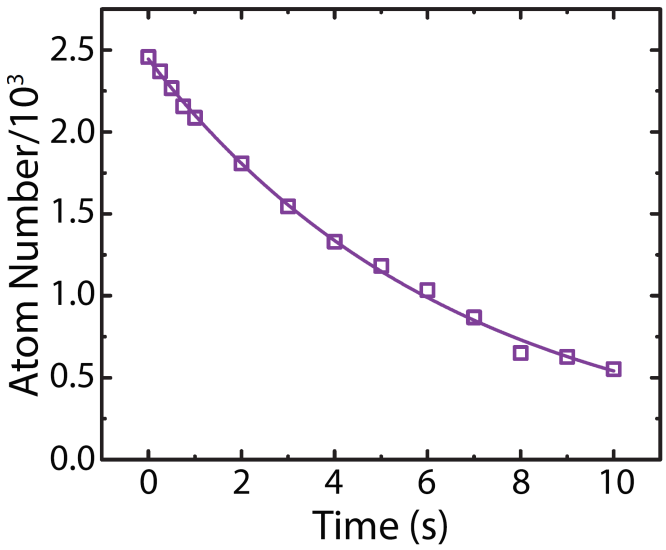

Figure 3.10: Measurement of the vacuum lifetime measured in the optical lattice.

shifts are removed by referencing the probing clock laser to the mirror that retroreflects the lattice. Second order Doppler shifts are calculated to not be important at the current level of systematic uncertainty but could become important as the accuracy of clocks increases. Another important effect that needs to be taken into account is the gravitational redshift. The frequency difference between two clocks with a height difference of Δh can be written as a fractional frequency difference as

$$\frac{\delta\nu}{\nu_0} = \frac{g\Delta h}{c^2} \tag{3.15}$$

where g is the local acceleration due to gravity and c is the speed of light. The equation assumes only small changes in height close to the earth's surface. For our 2013 systematic evaluation the clocks were located on adjacent optical tables and a relative height difference between the two clocks can be measured easily to the cm level. For the 2017/18 evaluation the two clocks are located ~ 1 mile apart and so the height difference is measured by a geodetic survey conducted by the National Geodetic Survey team.

3.3 Uncertainty Tables

3.3.1 2013 Sr-Sr comparison

The full uncertainty table for the 2013 systematic evaluation is shown in Table 3.3.1. On the left are the nominal shifts and their uncertainties for the Sr1 experiment and on the right shows the nominal shifts and their uncertainties for the Sr2 experiment. As can be seen the main sources of uncertainty that are different are the BBR radiation shifts, the AOM phase chirp and the density shift. The main differences between the two Sr clocks are the use of in vacuum temperature sensors which allow for the temperature uncertainty to be reduced. The Sr2 experiment also uses

Source of shift	$\Delta\nu_{Sr1}$	σ_{Sr1}	$\Delta\nu_{Sr2}$	σ_{Sr2}
BBR static	-4,832	45	-4,962.9	1.8
BBR dynamic	-332	6	-345.7	3.7
Density shift	-84	12	-4.7	0.6
Lattice Stark	-279	11	-461.5	3.7
Probe beam a.c. Stark	8	4	0.8	1.3
First-order Zeeman	0	<0.1	-0.2	1.1
Second-order Zeeman	-175	1	-144.5	1.2
Residual lattice vector shift	0	<0.1	0	<0.1
Line pulling and tunneling	0	<0.1	0	<0.1
d.c. Stark	-4	4	-3.5	2.1
Background gas collisions	0	0.07	0	0.6
AOM phase chirp	-7	20	0.6	0.4
Second-order Doppler	0	<0.1	0	<0.1
Servo error	1	4	0.4	0.6
Totals	-5,704	53	-5,921.2	6.4

Table 3.1: The uncertainties for the two experiments are quoted as 1σ standard errors and all shifts and uncertainties are in fractional frequency units multiplied by 10^{-18}.

a lattice based on Ti:sapphire laser and a build-up cavity to create the optical lattice compared to the TA system used by our Sr1 experiment for this evaluation. The high powered and more spectrally pure Ti:sapphire laser allows for a more stable lattice ac Stark shift as well as the ability to create a bigger lattice waist which reduces the density shift for a constant atom number. For this comparison the density shift for our Sr1 experiment is quoted for our working condition of ~ 700

atoms and the Sr2 experiment used a few thousand atoms.

The BBR shift is calculated at 298 K for Sr1 and the box around the Sr2 experiments heats up the box to be at a higher temperature of 300 K. For Sr1 the applied bias field leads to a splitting of 550 Hz whereas the Sr2 experiment worked at a lower magnetic field and also suffered from a drifting magnetic field that needed to be servoed and caused a residual first order Zeeman shift. For both experiments a 160 ms pulse was used.

3.3.2 2017/18 JILA-NIST comparison

Source of shift	$\Delta\nu_{2013}$	σ_{2013}	$\Delta\nu_{2017/18}$	$\sigma_{2017/18}$
BBR static	-4,832	45	-4,640.3	4.5
BBR dynamic	-332	6	-313.2	1.5
Density shift	-84	12	-14.5	1
Lattice Stark	-279	11	-16.1	3.0
Probe beam a.c. Stark	8	4	0.9	0.7
First-order Zeeman	0	<0.1	0	0.5
Second-order Zeeman	-175	1	-178	1.4
Residual lattice vector shift	0	<0.1	0	<0.1
Line pulling and tunneling	0	<0.1	0	<0.1
d.c. Stark	-4	4	0	0.6
Background gas collisions	0	0.07	0	0.1
AOM phase chirp	-7	20	-3	1
Second-order Doppler	0	<0.1	0	<0.1
Servo error	1	4	6.4	0.9
Totals	-5,705	53	-5169.7	∼6

Table 3.2: Systematic evaluation table for Sr1 comparing the 2013 evaluation to the 2017/18 systematic evaluation. The uncertainties for the two experiments are quoted as 1σ standard errors and all shifts and uncertainties are in fractional frequency units multiplied by 10^{-18}. It should be noted that these numbers are from 2017 and are preliminary. Further improvement of these systematic uncertainties is already reaching the low 10^{-18} level.

During our 2017/18 systematic evaluation our Sr1 experiment was able to make an improvement of almost an order of magnitude upon our 2013 systematic evaluation. Table 3.3.2 compares the two systematic evaluations for our Sr1 experiment. It should be noted that the measured systematics are from 2017 and they are constantly being improved upon. The majority of this comes from the improvement of the BBR shifts by more than an order of magnitude. During the second

evaluation the temperature control of the chamber was improved as discussed in section 3.2.5 with the temperature of the vacuum viewports servoed to 22°C.

The volume of the lattice was also increased with the waist increasing from 32 μm to $\sim 85\,\mu$m allowing for a lower density shift measurement along with longer pulses of 500 ms, and a carefully measured AOM phase chirp.

3.4 Comparing Clocks

It is important to compare different clocks as this allows us to check the agreement between two clocks and can allow us to see if we are not accounting properly for any systematic offsets. Comparing the frequencies of clocks depends on whether they are the same atom or not and can also depend on where they are located relative to each other.

For our 2013 clock comparison [21] we compared two Sr optical lattice clocks that were located within the same lab. The same clock laser is used to probe both sets of atoms and there is only one AOM that is different between the two experiments. In this case to compare frequencies all that is needed is to measure the final frequency of each AOM and, after all corrections are considered, these two frequencies are all that need to be considered.

For our 2017/18 clock comparison our Sr optical lattice clock is being compared with two other clocks at NIST $\sim$ 1 mile away. The two clocks that we are comparing to are the NIST Yb optical lattice clock and the Al^+ single ion clock. For this clock comparison the frequency differences between the two clocks are more complicated and are shown in Fig. 3.11. This only shows the relevant frequencies at JILA and there are more frequency offsets at NIST where the atom-stabilized light for all clocks are measured using two independent frequency combs.

An example of some comparison data is shown in Fig. 3.12. The Allan deviation (see section 1.3) showing the stability of the two clocks is shown in (a) where the averaging of a single clock is shown to be 3.4×10^{-16} at one second. Figure 3.12 (b) shows the frequency difference of the two clocks over the course of the month long measurement. The data shows agreement of the two frequencies at the -2.8×10^{-17} level which is within the systematic uncertainty of the two clocks,

which is dominated by the systematic uncertainty of the Sr1 experiment. As of the writing of this thesis the comparisons between our strontium optical lattice clock at JILA and the clocks at NIST are still ongoing, but statistics indicate the Sr-Al clock's frequency ratio is stable at the 1×10^{-18} level.

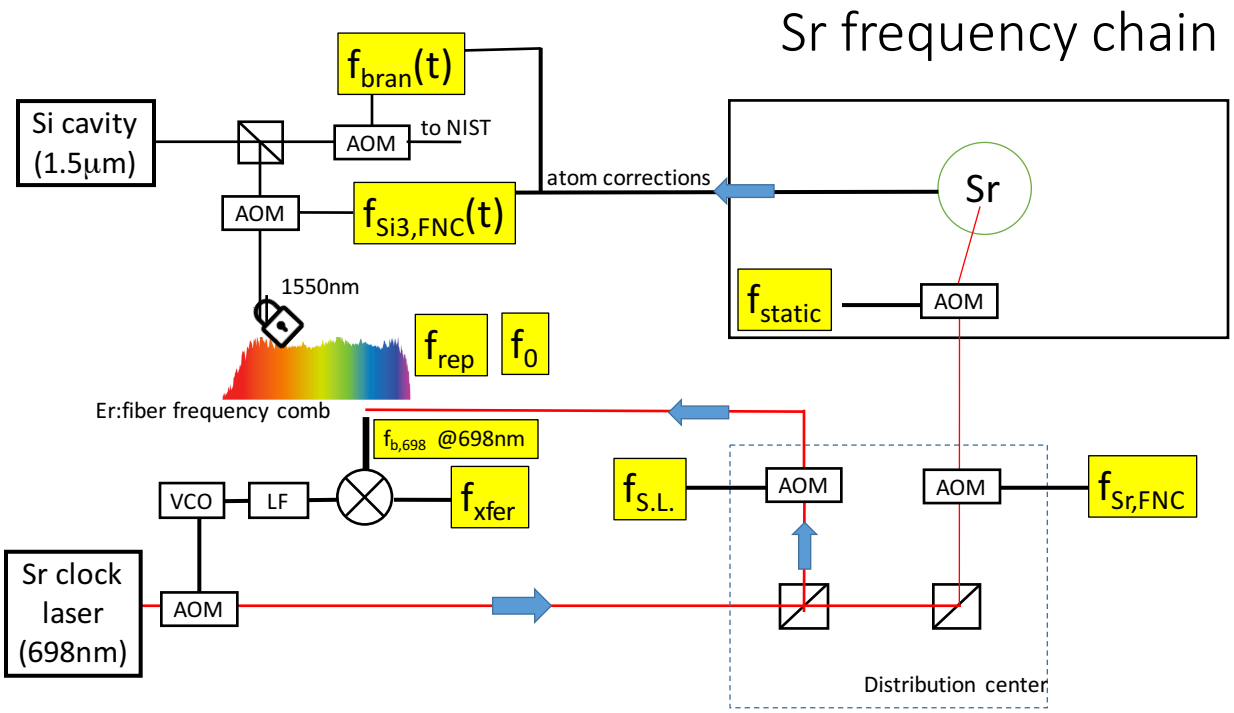

Figure 3.11: The strontium frequency chain for sending atom stabilized light to NIST via the BRAN fiber link. Highlighted in yellow are the relevant frequencies that need to be measured to calculate any frequency offsets that are needed for the absolute frequency measurement by the NIST frequency combs. Schematic courtesy of John Robinson.

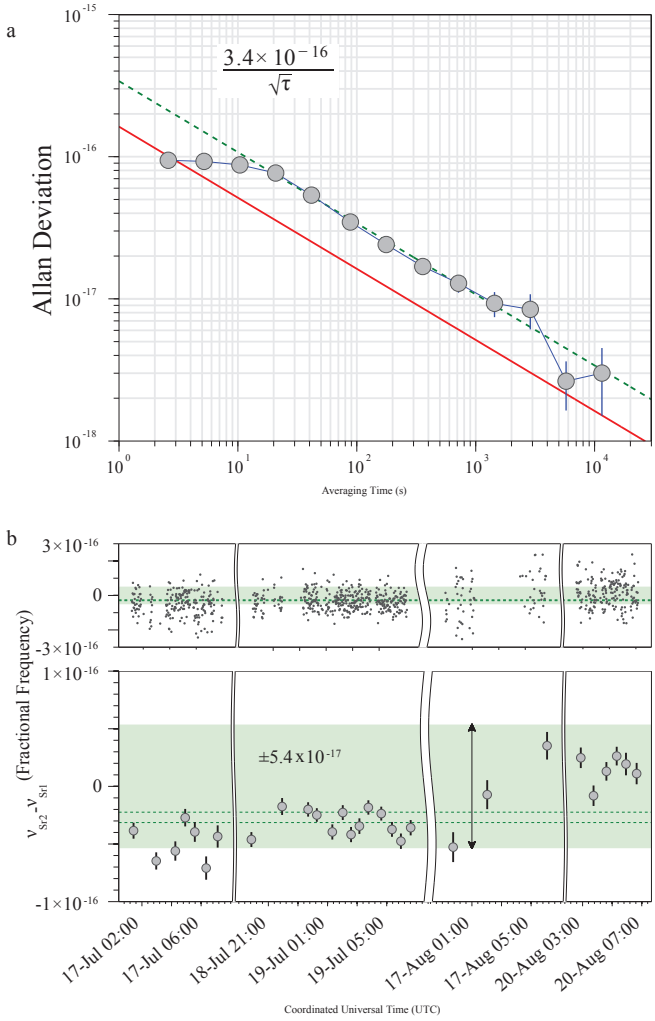

Figure 3.12: **(a)** Allan deviation of the Sr1 and Sr2 comparison divided by $\sqrt{2}$ to reflect the performance of a single clock. The red solid line is the calculated quantum projection noise for this comparison. The green dashed line is a fit to the data, showing the worst case scenario for the averaging of a single clock of 3.4×10^{-16} at one second. **b)** The absolute agreement between Sr1 and Sr2 recorded at the indicated Coordinated Universal Time. The light-green region denotes the 1σ combined systematic uncertainty for the two clocks under the running conditions at that time. The top panel shows the frequency record binned at 60 s; in the bottom panel each solid circle represents 30 min of averaged data. The green dashed lines represent the 1σ standard error inflated by the square root of the reduced chi-squared, $\sqrt{\chi^2_\nu}$, for the weighted mean of these binned comparison data. The final comparison over 52,000 s of data showed agreement at $-2.7(5) \times 10^{-17}$ ($\sqrt{\chi^2_\nu}$ =10.5) for the 30-min averaging time and $-2.8(2) \times 10^{-17}$ ($\sqrt{\chi^2_\nu}$ =3.5) for the 60-s averaging time. Reproduced from [21].

Chapter 4

Collective atomic scattering in a dense sample of ^{88}Sr

4.1 Introduction

Understanding interactions between light and matter in a dense atomic medium is a long-standing problem in physical science [29, 30] since the seminal work of Dicke [31]. In addition to their fundamental importance in optical physics, such interactions play a central role in enabling a range of new quantum technologies including optical lattice atomic clocks[21] and quantum networks [32].

The key ingredient in a dense sample is dipole-dipole interactions that arise from the exchange of virtual photons with dispersive and radiative contributions, with their relative magnitude varying between the near-field and far-field regimes. The dispersive (real) part of these dipole-dipole interactions is responsible for collective level shifts and the radiative (imaginary) part gives rise to line broadening and collective superradiant emission [33, 34, 35]. Intense theoretical efforts have been undertaken over many years to treat the complex interplay between the dispersive and radiative dynamics [36, 37, 38, 39, 40, 41, 42, 43, 44, 45]. However, experimental demonstrations that provide a complete picture to clarify these interactions have been elusive.

Collective level shifts and line broadening arising from the real and imaginary parts of dipole-dipole interactions have recently been observed in both atomic [46, 47, 48, 49, 50] and condensed matter [51] systems. The modification of radiative decay dynamics at low excitation levels has also been observed using short probe pulses [52, 53, 54, 55], and interaction effects were manifested in coherent backscattering [56, 57]. While simple models of incoherent radiation transport

have often been used to describe light propagation through opaque media [58, 59] and radiation trapping in laser cooling of dense atomic samples [60], coherent effects arising from atom-atom interactions, which are necessary to capture correlated many-body quantum behavior induced by dipolar exchange, are beginning to play a central role. For example, the dipole-dipole interaction is responsible for the observed dipolar blockade and collective excitations in Rydberg atoms [61, 62, 63, 64, 65, 66, 67, 68]; it may also place a limit to the accuracy of an optical lattice clock and will require non-trivial lattice geometries to overcome the resulting frequency shift [69]. Previous theoretical efforts have already shown that physical conditions such as finite sample size, sample geometry, and the simultaneous presence of dispersive and radiative parts can play crucial roles in atomic emission [36, 37, 39, 40, 70, 71, 72] .

In this work we use millions of Sr atoms in optically thick ensembles, taking advantage of the unique level structure of Sr to address motional effects, to study these radiative and dispersive parts simultaneously. We demonstrate that a single, self-consistent, microscopic theory model can provide a unifying picture for the majority of our observations. These understandings can help underpin emerging applications based on many-body quantum science, such as lattice-based optical atomic clocks [21, 73, 74], quantum nonlinear optics [66], quantum simulations [75], and atomic ensemble-based quantum memories [76].

4.1.1 Chapter Outline

The outline of this chapter is as follows. In section 4.2 we will present the experimental details of the system used to measure the collective effects in ^{88}Sr. We will then discuss the experimental results in section 4.3 which we shall separate into three different sections. Section 4.3.1 will discuss the intensity measurements that we have made for both the blue and red transitions. Section 4.3.2 will discuss the linewidth broadening observations, again for both transitions. Section 4.3.3 will compare the measured density dependent frequency shifts of the blue transition to a prior measurement of the frequency shift of the red transition [77]. In section 4.4 we will discuss in detail the coupled dipole model which can be used to model the majority of our experimental observations.

4.2 Experimental Details

4.2.1 Strontium 88

We choose to use bosonic ^{88}Sr, whereas in the rest of the work described in this thesis we use fermionic ^{87}Sr and there are a number of reasons we choose to do this. First of all ^{88}Sr contains zero nuclear spin giving a relatively simple energy level structure compared to both ^{87}Sr and to alkali metal atoms. This simple structure makes bosonic ^{88}Sr, and other zero nuclear spin alkaline-earth atoms, easier to model and to interpret the experimental observations. This simple structure alongside the large natural abundance of the ^{88}Sr isotope makes cooling large dense samples of atom to μK temperatures possible.

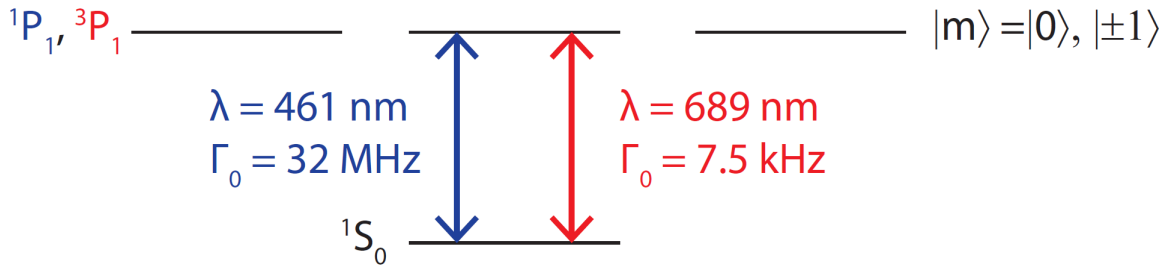

Figure 4.1: A schematic diagram of the four-level atomic structure shared by both the $^1S_0$ – $^1P_1$ blue transition and the $^1S_0$ – $^3P_1$ red transition in bosonic ^{88}Sr.

Bosonic ^{88}Sr also has the advantage that we can study the effects of motion on the collective emission from a dense sample of atoms. It contains both a strong $^1S_0$ – $^1P_1$ blue transition ($\lambda = 461$ nm) and a spin-forbidden $^1S_0$ – $^3P_1$ red transition ($\lambda = 689$ nm) with a strict four-level geometry as shown in Fig. 4.1. Throughout this chapter we will refer to these two transitions as the "blue" and "red" transitions respectively. The reason we can measure the effects of motion on the collective emission can be seen by considering the Doppler broadening for both of these transitions. The full width at half maximum of the Doppler broadening is given by

$$\Delta\nu_D = \frac{1}{\lambda}\sqrt{\frac{8k_BT\ln 2}{M}} = \Delta_D\sqrt{8\ln 2} \tag{4.1}$$

where k_B is the Boltzmann constant, M is the mass of an atom, T is the atomic temperature, λ

is the wavelength of the transition, and Δ_D is the Gaussian standard deviation of the frequency broadening.

When the atoms are cooled to a typical temperature of $T = 1.3\,\mu$K then the Doppler broadening of the blue transition is $\Delta\nu_D = 57$ kHz. This is almost three orders of magnitude smaller than the natural linewidth of the blue transition, $\Gamma_0 = 32$ MHz. This means that to an excellent approximation, atomic motion is negligible and the atoms do not move between when they absorb and when they emit a blue photon. On the contrary, the Doppler broadening of the red transition is $\Delta\nu_D = 38$ kHz which is ~ 5 times larger than the natural linewidth, $\Gamma_0 = 7.5$ kHz. This means that the red transition is strongly affected by atomic motion. By comparing the behaviors of the same atomic ensemble when probing the red and blue transition, we can thus collect clear signatures of motional effects on collective scattering.

4.2.2 Experimental Setup

In the experiment up to 2×10^7 atoms are cooled to $\sim 1\mu$K temperatures in our two-stage magneto-optical trap (MOT), the first based on the blue transition and the second based on the red transition. The atomic cloud is then released from the MOT and allowed to expand for a variable time of flight (TOF), as discussed in section 4.2.3.2. This allows us to control the optical depth (OD) and density of the atomic ensemble while keeping the atom number, N, constant. The atoms are then illuminated for $50(100)\,\mu$s using a weak probe beam that is large compared to the size of the atomic cloud and resonant with the blue (red) transition.

A simplified schematic of the experimental setup is shown in Fig. 4.2. Two detectors measure the resulting light scattered by the atoms. One detector is along the forward direction (detector D_F) and the other along the transverse direction (detector D_T, offset by $\sim 10^\circ$). For a short TOF, the atomic cloud is anisotropic and has an approximately Gaussian distribution with an aspect ratio $\sigma_x : \sigma_y : \sigma_z = 2 : 2 : 1$, where σ_α are the root-mean-squared (r.m.s) radii.

We can use this same basic setup to perform a comprehensive set of measurements of fluorescence intensity emitted by a dense sample of ^{88}Sr atoms. We vary the atomic density, cloud

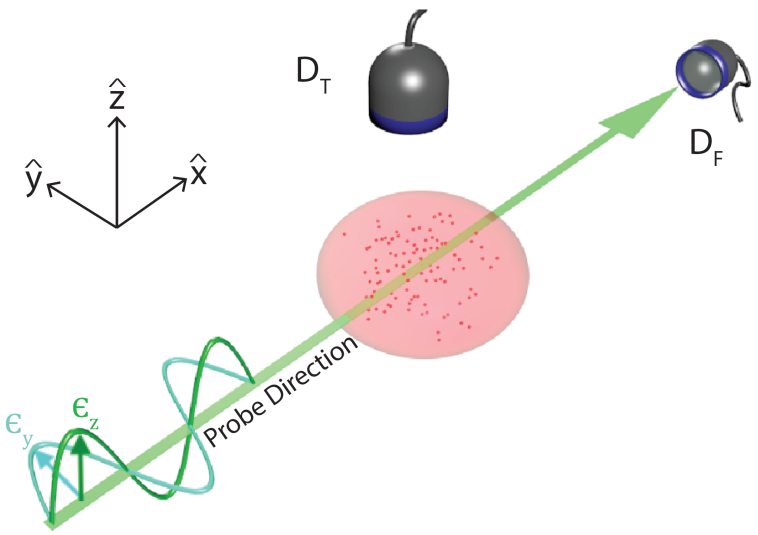

Figure 4.2: The atomic ensemble is weakly excited using a laser beam larger than the size of the atomic cloud and propagating along the $\hat{x}$ with polarization along either $\hat{y}$ or $\hat{z}$. The atomic fluorescence is then collected simultaneously with two detectors: one in the forward direction, $\hat{x}$, and the other offset by $\sim 10^{\circ}$ from the perpendicular direction, $\hat{z}$.

geometry, observation direction, and polarization of the probe laser and characterize the three key parameters: the peak intensity, the linewidth broadening, and the linecenter shift.

4.2.3 System Parameters

A number of different system calibrations need to take place in order to know the initial conditions of our experiment and to obtain universal scaling parameters such as density and optical depth that can be compared between different experiments both in our lab and by others. In this section we will describe how certain experimental parameters such as atom number and temperature are calibrated and how they can be related to these universal parameters.

4.2.3.1 Atom Number

The atom number is calibrated using a method of transfer efficiencies [78] (see Appendix A). The atom number in the blue MOT is found by measuring the lifetime of the blue MOT when the repump lasers are blocked. Using the known branching ratios this measurement tells us the fraction of time each atom spends in the $^1P_1$ state and thus how many photons are emitted per atom. Once the atom number in the blue MOT is known the transfer efficiency to the broad-band red MOT can be calculated by comparing the PMT signal for the blue MOT and broadband red MOT when the MOT beams are flashed on. Typically, this transfer efficiency is 48%.

The blue probe beam can then be used to calculate the transfer efficiency from broad-band red MOT to single-frequency Red MOT in the same way. We note that for dense ensembles of atoms the intensity can depend on the TOF due to the collective effects. In this case the transfer efficiency is calculated for longer time of flights where the intensity tends to peak. For these measurements this was typically 15 ms and gives a transfer efficiency for this stage of 65%.

4.2.3.2 Temperature

Unlike in most of our other experiments where we measure the temperature of the atoms using the ratio of the areas of the different axial sidebands of the lattice, here we do not have a lattice

and thus measure the temperature using the free expansion of the atomic cloud. This temperature

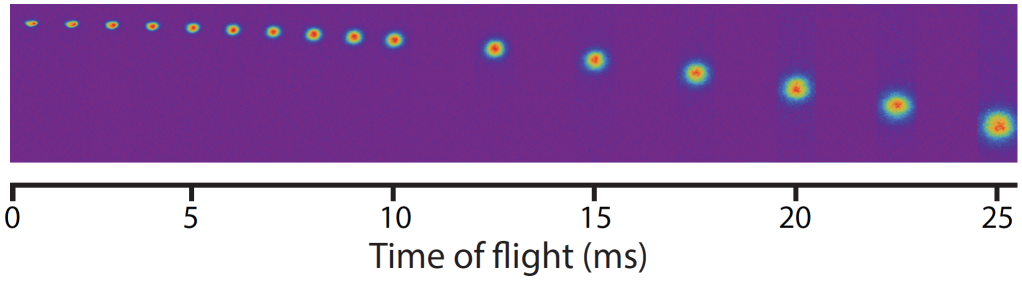

Figure 4.3: Time of flight fluorescence images showing the expansion of the atomic cloud after releasing the atoms from the magneto-optical trap.

calibration is performed at low density and in order to calibrate the temperature of the atoms the pixel size of the camera that we are using (forward detector D_F) needs to be calibrated too. In fact, the pixel size can be calibrated in the same measurement and then this allows us to determine the size of the atomic cloud needed to obtain the temperature.

To perform this measurement, for different TOF, pictures of the atomic cloud are taken as in Fig. 4.3. The vertical centers of each of these images is used to get the pixel size by knowing the displacement of the atoms with time whilst falling under the influence of gravity

$$z - z_0 = v_0 t + \frac{1}{2} a t^2 \tag{4.2}$$

with z_0 the initial vertical position of the cloud, z the final position of the cloud after a TOF t, v_0 the initial velocity of the cloud, and a the acceleration of the cloud. We let this fitting function vary v_0, z, and a and from the extracted value of a we know our pixel size to be a/g where $g = 9.81$ ms^{-2} is the acceleration due to gravity. The pixel size of our camera is found to be (20.6 ± 0.2) μm which is consistent with the expected size of $\sim 20\,\mu$m from the actual $10\,\mu$m pixels demagnified by a factor of two.

The Gaussian root-mean-squared radius of the velocity distribution, σ_{v_α}, in the $\alpha = \{x, y, z\}$ direction is associated with the temperature T_α of the cloud by

$$T_\alpha = \frac{M}{k_B} \sigma_{v_\alpha}^2 \tag{4.3}$$

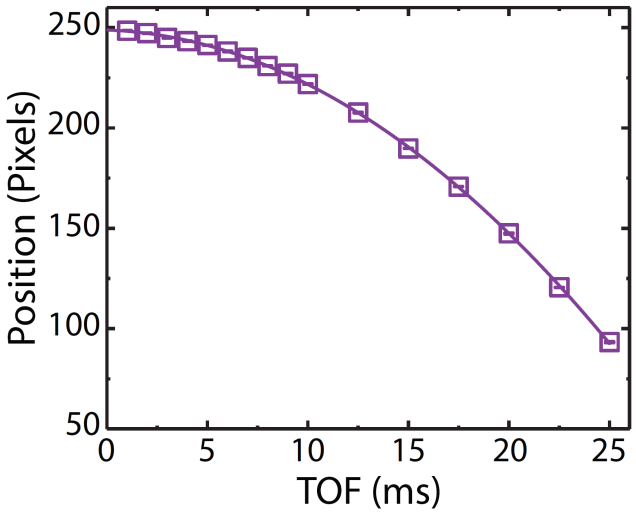

Figure 4.4: The vertical center position of the atomic cloud is measured (purple, squares) versus time-of-flight in order to calculate the pixel size which is found by fitting the data to Eq. 4.2 (purple, line) to be (20.6 ± 0.2) μm.

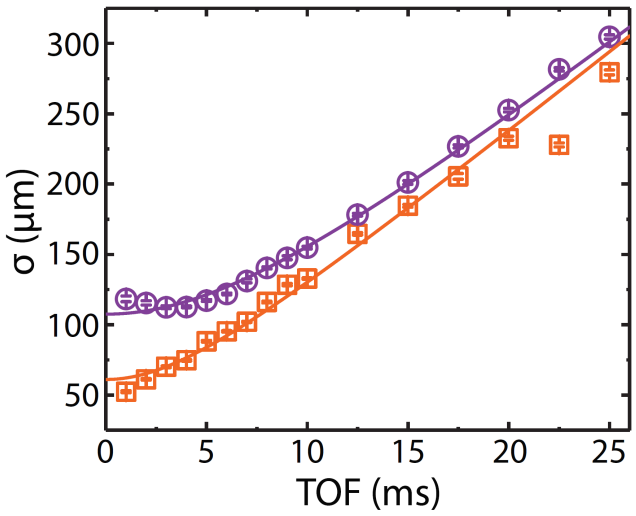

Figure 4.5: An example measurement of the cloud temperature in the $\hat{y}$ (purple, circles) and $\hat{z}$ (orange, squares) directions. The plotted Gaussian fitted r.m.s radii versus time-of-flight are fitted with Eq. 4.4 (solid lines) to extract the atomic cloud temperatures to be $T_z = 1.4\mu$K and $T_y = 1.3\mu$K.

where the Gaussian radius of the freely expanding cloud is related by the equation

$$\sigma_\alpha(t) = \sqrt{\sigma_{\alpha,0} + \sigma_{v_\alpha}^2 t^2} \tag{4.4}$$

where $\sigma_{\alpha,0}$ is the initial Gaussian radius at time $t = 0$. Fitting Eq. 4.4 to the Gaussian radii as a function of time can then be used to extract the temperature of the atomic cloud as shown in Fig. 4.5 giving typical temperatures of $1.3\,\mu$K.

4.2.3.3 Optical Depth and Density

In order to convert the measured atom numbers and cloud sizes into a more experimentally comparable quantity such as density and optical depth we need to know how they scale with each quantity. The distribution of atoms in our atomic cloud is approximately Gaussian and given by the distribution

$$n\left(x,y,z\right) = n_0 e^{-\frac{x^2}{2\sigma_x^2}} e^{-\frac{y^2}{2\sigma_y^2}} e^{-\frac{z^2}{2\sigma_z^2}} \tag{4.5}$$

where n_0 is the peak density which satisfies the equation $\int dxdydzn\left(x,y,z\right) = N$ to give the peak density,

$$n_0 = \frac{N}{\left(2\pi\right)^{3/2}\sigma_x\sigma_y\sigma_z}. \tag{4.6}$$

For the case of optical depth the scaling with atomic cloud size is different. Throughout this chapter we will define the OD as the on resonance optical depth of the cloud. The optical depth can be written as

$$OD = n\sigma_{scatt}L \tag{4.7}$$

where n is the atomic density found by integrating the density distribution given in Eq. 4.5, $\sigma_{scatt} = \frac{3\lambda^2}{2\pi}$ is the resonant scattering cross section for a Lorentzian lineshape and L is the length of the medium through which the probe light travels. The addition of motion will reduce the peak cross section and hence optical depth. If we consider the optical depth along the $\hat{x}$ direction

(direction of the probe beam, see Fig. 4.2) we can rewrite the OD as

$$\begin{aligned} OD &= \frac{N}{V}\frac{3\lambda^2}{2\pi}L \\ &= \frac{N}{\int\int\int dxdydz e^{-\frac{x^2}{2\sigma_x^2}} e^{-\frac{y^2}{2\sigma_y^2}} e^{-\frac{z^2}{2\sigma_z^2}}} \int dx e^{-\frac{x^2}{2\sigma_x^2}} \frac{3\lambda^2}{2\pi} \\ &= \frac{3N}{2k^2\sigma_y\sigma_z} \\ &= \frac{3N}{2\left(k\sigma_\perp\right)^2} \end{aligned} \tag{4.8}$$

where k is the wave vector of the light and we have defined $\sigma_\perp$ as the radius perpendicular to the direction of observation. This radius depends on the direction of observation and is given by $\sigma_{\perp,T} = \sigma_x = \sigma_y$ and $\sigma_{\perp,F} = (\sigma_y\sigma_z)^{1/2}$, for the transverse and forward direction respectively.

As we can see the density and the OD scale differently with the cloud radii. The different experimental data that we will show in the next three sections will be scaled to either OD or density where the choice is dependent on the appropriate scaling of the quantity as determined by the coupled dipole model (see section 4.4).

4.3 Experimental Observations

4.3.1 Intensity

The coherent effects manifest themselves most clearly in the fluorescence intensity in the forward direction, which is the direction along which the probe beam is travelling. The probe beam synchronizes the dipoles so that in the forward direction the radiation from the different dipoles interfere constructively to give a strong forward intensity peak. However, the forward direction also has the experimental difficulty that we need to separate the probe beam from the fluorescence emitted by the atoms. When measuring the intensity in the forward direction we use the additional setup shown in Fig. 4.6 for this separation.

The probe beam is focused with a lens (L_1, focal length $f_1 = 15$ cm) after passing through the atomic cloud and exiting the vacuum chamber. The probe beam is then blocked using a razor blade which can be translated perpendicular to the probe beam. The same lens (L_1) also collimates

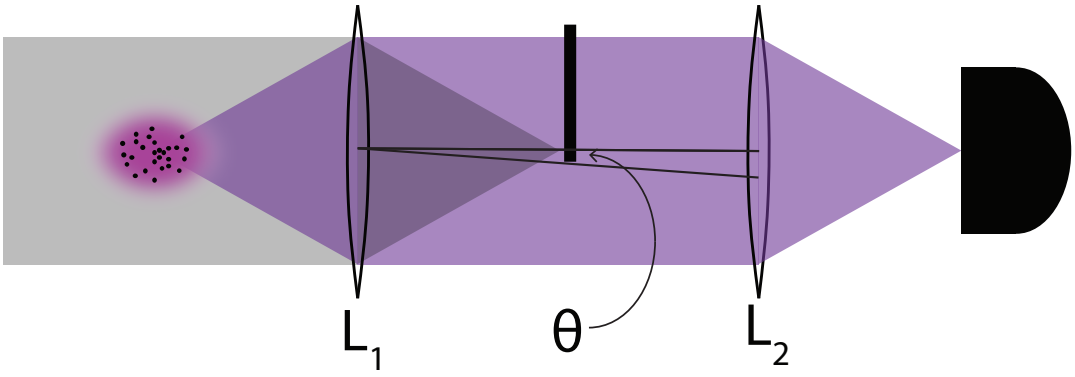

Figure 4.6: Setup for measuring the forward intensity. A lens (L_1, focal length $f_1 = 15$ cm) just outside the vacuum chamber focusses the probe beam onto a razor blade that can be translated perpendicular to the direction of the probe beam to change the angle θ. This same lens collimates the fluorescence emitted by the atomic ensemble and a second lens (L_2 , focal length $f_2 = 15$ cm) images the fluorescence onto a detector

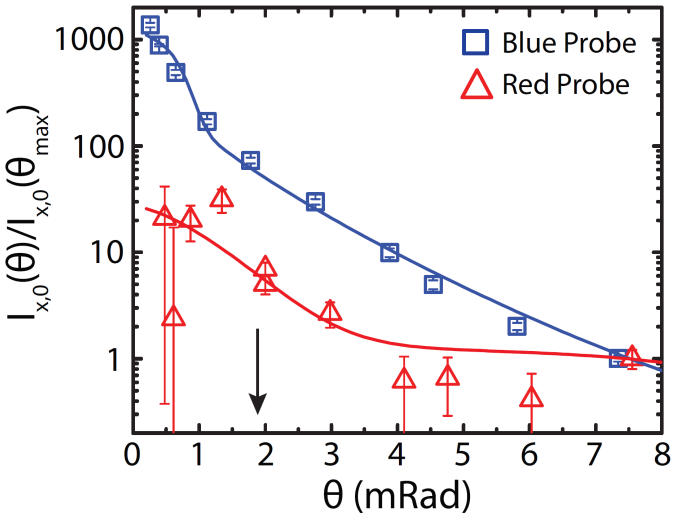

Figure 4.7: The enhancement of the intensity in the forward direction. The intensity in the forward direction is measured for the blue transition (blue, squares) and red transition (red, squares) by using the setup shown in 4.6 with the intensity normalized to the intensity at ~ 7.5 mRad. The enhancement of the intensity for the red transition is reduced due to motional effects. Solid lines are theory fits using the coupled dipole model. The black arrow indicates the angle that the data in Fig. 4.9 is taken.

the atomic fluorescence so that it can be imaged using a further lens (L_2, focal length $f_2 = 15$ cm) onto the forward detector, D_F. The position of the razor blade can therefore be used to vary the angular range of the detected fluorescence whilst at the same time blocking the probe beam.

We should note that in reality the setup is slightly more complicated than that shown in Fig. 4.6. The reason for this is that the forward CCD detector used for collecting the blue fluorescence is actually insensitive to the red fluorescence. After the light is focused, using L_2, the light is spatially filtered using an iris and then the blue and red fluorescence split using a dichroic. The blue fluorescence is still collected using the CCD camera used for the rest of the blue forward measurements and the red fluorescence is collected using a photon counter.

4.3.1.1 Forward Intensity Enhancement

The angular distribution of the fluorescence in the forward direction can be characterized by the angle $\theta = \arctan \frac{\Delta x}{15\text{cm}}$ which is the angle between $\hat{x}$ and the edge of the razor blade. This angle is changed by translating the razor blade edge from the center of the probe beam by Δx. Figure 4.7 shows the intensity of the forward emission for the blue probe (blue, squares) and red probe (red, triangles) at different angles of theta which are normalized to that collected at $\theta_{max} \approx 7.5$ mRad. The measurements at each position of the razor blade are averaged over multiple cycles of the experiment where we interleave both the blue and red probe beam and in each case compare the fluorescence with and without atoms to remove any background noise.

For the case of the blue probe beam in the forward direction we see over a factor of 1000 enhancement in the normalized intensity for $\theta < 0.5$ mRad. The enhancement is also present for the red transition, but is reduced by almost two orders of magnitude at small θ due to motional effects. However, the longer wavelength of the red transition leads to a wider angular area of enhancement.

A close look at Fig. 4.7 reveals that the angles θ for the two transition are actually offset from each other, even though they are measured at the same razor blade positions. The reason for this is that the two probe beams are offset from each other by $33\,\mu$m (~ 0.2 mRad) as shown in Fig. 4.8, giving different $\hat{x}$ directions for the two probe beams and hence different angle θ.

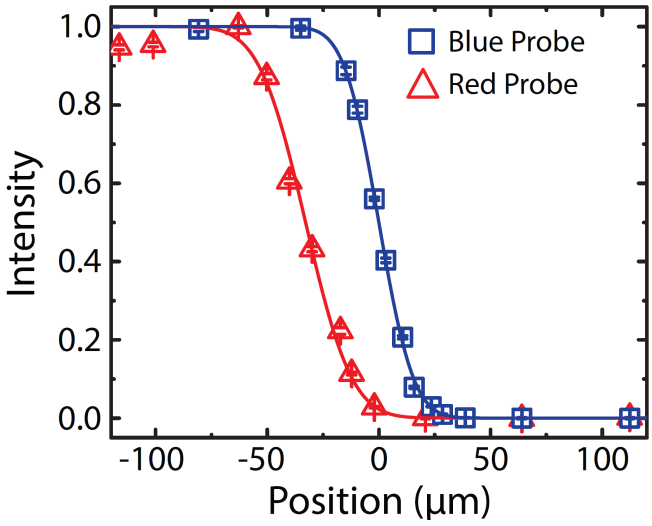

Figure 4.8: Focused Probe Beam Calibration. The normalized intensity of the probe beams are plotted as the razor blade is scanned across the focus for both the blue (blue, squares) and red (red, triangles) probe beams. The fits (solid, lines) are Gaussian cumulative distribution functions given by Eq. 4.9. From these measurements we can see that the probe beams are offset by $\sim 33\,\mu$m. The focused r.m.s radius of the Gaussian probe beams is extracted from the fit to be $12.2\,\mu$m ($16.4\,\mu$m) for the blue (red) probe beam.

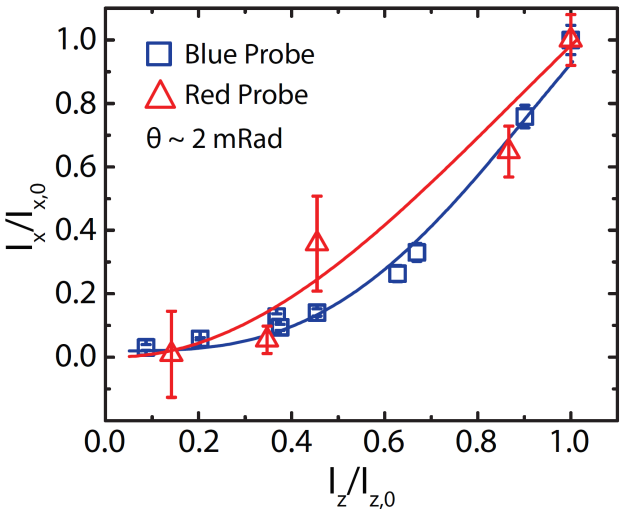

Figure 4.9: Intensity in the forward ($\hat{x}$) and transverse ($\hat{z}$) directions for the blue (blue, squares) and red (red, triangles) probe beams as the atom number is changed taken at $\theta = 2$ mRad as indicated by the arrow in Fig. 4.7. The transverse intensity scales approximately with atom number N, meaning that the forward intensity scales $\propto N^2$.

Figure 4.8 shows the intensity of the probe beam measured as the razor blade is translated across the focus. The intensity is then fit with a Gaussian cumulative distribution function

$$G_{CDF} = \frac{1}{2}\left(1 + \mathrm{erf}\left[\frac{x_0 - x}{\sqrt{2}\sigma_p}\right]\right) \tag{4.9}$$

where x_0 is the center position of the beam, and σ_p is the root-mean-square radius of the Gaussian probe beam. The difference between the two values of x_0 for the fits to the different probe beam intensities gives the offset of the two beams. For the blue probe beam the extracted value of $\sigma_p = 12.2\,\mu$m and for the red probe beam $\sigma_p = 16.4\,\mu$m.

4.3.1.2 Forward N^2 Intensity dependence

The observed forward intensity depends strongly on the atom number due to the constructive interference of the dipole emission in that direction. In Fig. 4.9 we present measurements of the forward intensity I_x versus the transverse intensity I_z at a fixed angle of $\theta = 2$ mRad (indicated by the arrow in Fig. 4.7).

The intensities in each direction are normalized to the peak atom number used in Fig. 4.7. To the first-order approximation, the transverse intensity scales linearly with atom number. Hence, the forward intensity of both the blue and red transitions scale approximately with the atom number squared. The exact scaling for both transitions is reduced from N^2 due to multiple scattering events (see section 4.4.4).

4.3.1.3 Transverse Polarization Dependent Intensity

Whereas the forward emission has no dependence on the probe beam polarization due to symmetry arguments, the transverse fluorescence (along $\hat{z}$) should be highly sensitive to the probe polarization and it is even classically forbidden if the probe beam is $\hat{z}$-polarized. However, multiple scattering processes with dipolar interactions can completely modify this picture by redistributing the atomic population in the three excited $|m\rangle$ states and thus scrambling the polarization of the emitted fluorescence.

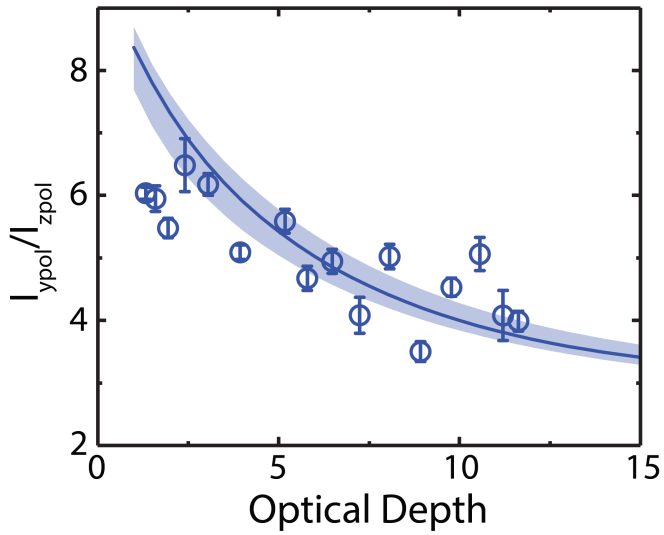

Figure 4.10: Blue transition intensity ratio for $\hat{y}$- and $\hat{z}$-polarization in the transverse direction. The classically forbidden intensity I_{zpol} increases with OD due to multiple scattering events. Solid line is a theory prediction using the coupled dipole model, where the shaded area takes into account the uncertainty in the atom number.

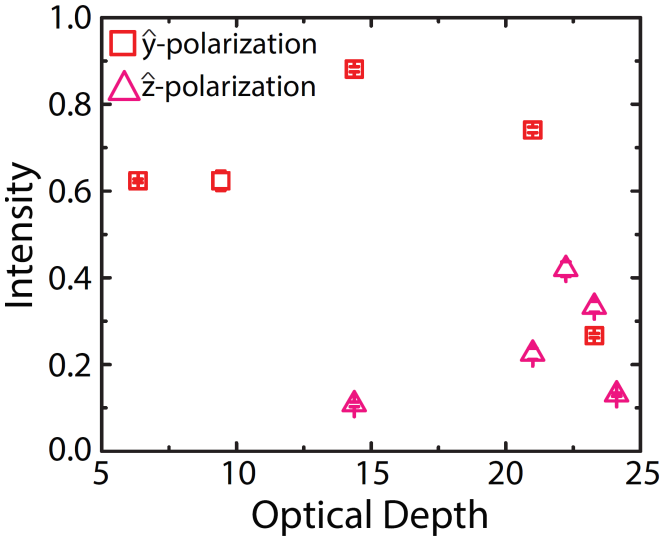

Figure 4.11: On resonance intensity for the red transition for $\hat{y}$-polarization (red, squares) and $\hat{z}$-polarization (pink, triangles) in the transverse direction. The classically forbidden intensity I_{zpol} increases with OD due to multiple scattering events. For $OD > 22.5$ the intensity decreases for both polarizations.

Measuring the fluorescence directly along $\hat{z}$ is also technically challenging in our setup. First, as mentioned earlier our detector is offset by $\sim 10^{\circ}$ from the vertical direction and this is due to the fact we cannot block the vertical MOT beam path. The second is that it is only exactly along $\hat{z}$ that the fluorescence is classically forbidden but we need to take into account that the detector lens also has a finite size. However, we still expect to see differences between the forward and transverse directions due to the non-symmetrical intensity distribution of each radiating dipole.

The prediction of increasing transverse intensity with OD for $\hat{z}$-polarized light is shown in Fig. 4.10 for the blue transition and Fig. 4.11 for the red transition. Figure 4.10 shows the on resonance intensity ratio of the two orthogonal intensities I_{ypol}/I_{zpol} of the blue transition and it can be seen that this ratio decreases significantly with an increasing OD indicating the rapidly rising fluorescence with a $\hat{z}$-polarized probe as OD increases. For the red transition, Fig. 4.11 shows how the intensity of the classically forbidden polarization (pink, triangles) increases with OD. For $OD > 22.5$, the intensity of both polarizations decreases. It is possible that this is an effect related to the atomic cloud moving away from the detector.

4.3.2 Linewidth Broadening

4.3.2.1 Blue Transition

For the blue transition, we have also investigated the linewidth broadening in both the forward and transverse direction. The frequency of the blue probe beam is scanned across resonance to extract the fluorescence linewidth of the atoms simultaneously using both forward and transverse detectors. In this case the razor blade is not present and instead a half-inch mirror at 45° is used to pick off the probe beam and monitor the power. For this case of the blue probe beam, which is unaffected by motion, the expected lineshape is a Lorentzian

$$\mathcal{L}(\nu) = \frac{1}{\pi} \frac{\frac{\Gamma}{2}}{(\nu - \nu_0)^2 + \left(\frac{\Gamma}{2}\right)^2} \tag{4.10}$$

where Γ is the linewidth and ν_0 is the resonance frequency. The fluorescence data at different OD is then fitted using Eq. 4.10 with a varying amplitude. From this fit we can extract both the center

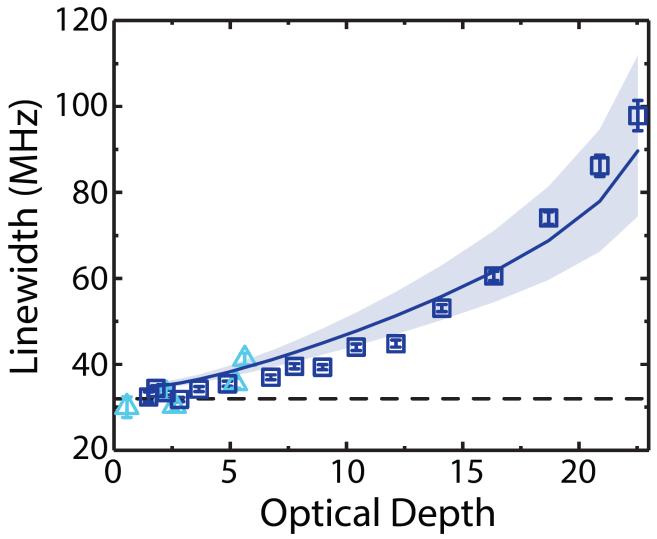

Figure 4.12: Linewidth broadening in the forward direction $\hat{x}$ under two different atom numbers N (blue, squares) and $N/4$ (cyan, triangles).

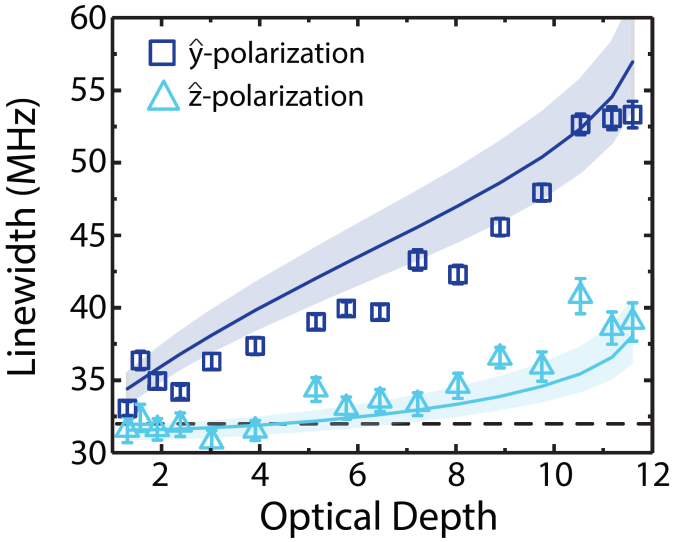

Figure 4.13: Linewidth broadening in the transverse direction $\hat{z}$ using two orthogonal polarizations $\hat{y}$ (blue, squares) and $\hat{z}$ (cyan, triangles) which is classically forbidden.

frequency ν_0 and the linewidth Γ.

The fluorescence linewidth in the forward direction, which is determined primarily by the OD of the atomic cloud, is plotted in Fig. 4.12. We show data for two different atom numbers $N = 1.7\,(2) \times 10^7$ (blue, squares) and $N/4$ (cyan, triangles). To an excellent approximation the linewidth data are observed to collapse to the same curve when plotted as a function of OD. At the same time that we measure the linewidth broadening in the forward direction we can also measure the linewidth broadening in the transverse direction using a separate detector. As mentioned earlier the fluorescence scattering in the transverse direction is highly dependent on polarization. In the transverse direction, $\hat{z}$, we can measure the linewidth broadening for both $\hat{y}$ and $\hat{z}$ polarization under the same experimental conditions by interleaving scans with each polarization and the results for the blue probe are shown in Fig. 4.13. The classically allowed polarization $\hat{y}$ (blue, squares) shows a similar trend to the forward linewidth broadening, whereas the classically forbidden polarization $\hat{z}$ gives rise to a much lower broadening for the same OD. For the classically allowed polarization, even though the data are taken under the same conditions as in Fig. 4.12 due to the anisotropic

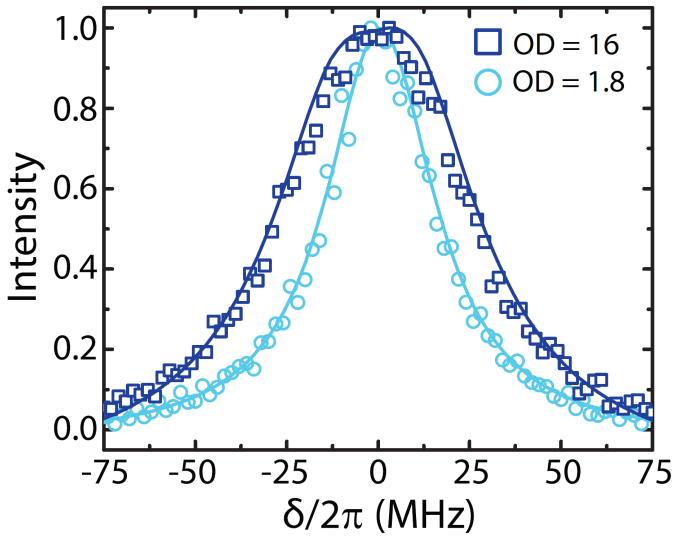

Figure 4.14: Measured lineshapes of the blue transition for different OD. At low OD (cyan, circles) the lineshape is Lorentzian. As the OD increases (blue, squares) the lineshape flattens out around the center.

size of the atomic cloud the OD in the transverse direction is smaller than in the forward direction (see Section 4.2.3.3).

For the forward direction where we are able to reach higher OD, for the range of $0 < OD < 15$ the lineshape is Lorentzian as shown in Fig. 4.14 (cyan, circles) for $OD = 1.8$. However, for larger $OD = 16$ (blue, squares) the lineshape starts to flatten out near the center.

4.3.2.2 Red Transition

For the red transition, the importance of Doppler broadening requires the lineshape data to be fitted with a Voigt profile which is a convolution between the Lorentzian natural lineshape and the Gaussian Doppler broadened lineshape. It can be written in terms of the complementary error function, $\mathrm{erfc}\,[x]$, as

$$V(\nu) \propto e^{\frac{[-i(\nu-\nu_0)+\Gamma/2]^2}{2\Delta_D^2}} \mathrm{erfc}\left[\frac{[-i(\nu-\nu_0)+\Gamma/2]}{\sqrt{2}\Delta_D}\right] + C.C. \tag{4.11}$$

where C.C. is the complex conjugate.

To fit using the Voigt function we fix the Gaussian linewidth, $\Delta\nu_D = \Delta_D\sqrt{8\ln 2} = 38$ kHz from our measured temperature and the resulting Lorentzian linewidth as a function of OD is shown in Fig. 4.15 for $\hat{y}$-polarized probe light and shows a strong increase of the linewidth with OD. When the red data is taken a large magnetic field is turned on to separate the different $|m\rangle$ states. The reason for this is because the shift of the line resonance for the red transition is larger than that for the blue transition when compared to the natural linewidth of the transition. By only probing one state we are therefore able to remove any additional broadening that may occur due to stray magnetic fields.

4.3.3 Frequency Shift

Whereas the transverse linewidth broadening is similar for the red and blue transition, this behavior is in stark contrast to the shift of the transition center frequency. Figure 4.17 shows the linecenter frequency shift observed for the blue transition (blue, squares) and the red transition

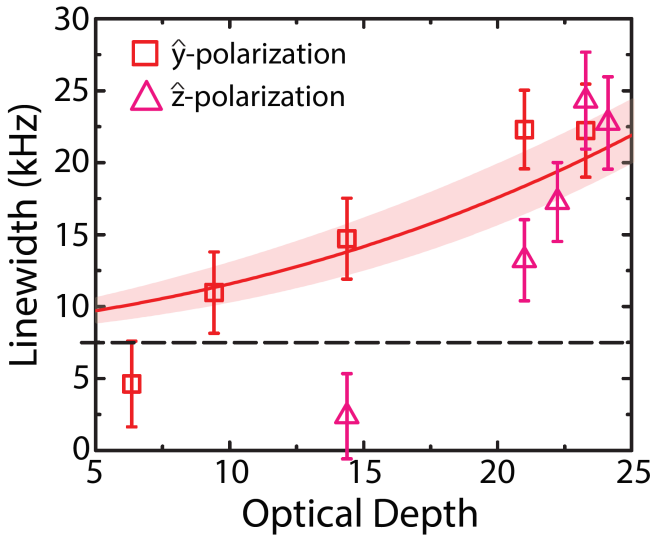

Figure 4.15: Red Linewidth Broadening in the transverse ($\hat{z}$) direction for $\hat{y}$-polarization (red, squares) and $\hat{z}$-polarization (pink, triangles).

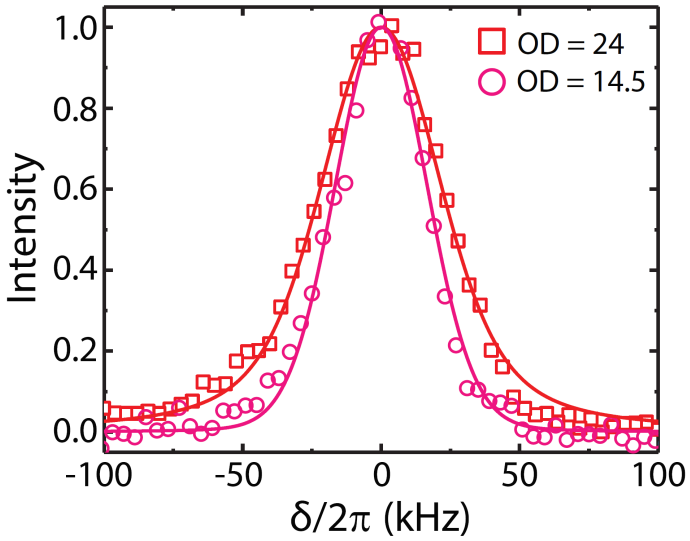

Figure 4.16: Red transition resonance fluorescence lineshape scans.

(red, triangles). The blue frequency shift data is taken by extracting the center frequency from the same Lorentzian lineshapes used to extract the linewidth data.

However, the red data is taken from [77] and measured under similar conditions to those presented here. Two counter-propagating probe beams are used and the frequency of the red probe laser is measured using a frequency comb which was not the case for the red line broadening data shown in Fig. 4.15. The frequency of this red laser can easily wander around on the 1 kHz level[1] which is $\sim 0.1\Gamma_{0,red}$. On the contrary the frequency stability of the blue lasers is < 1 MHz which is $\sim 0.03\Gamma_{0,blue}$.

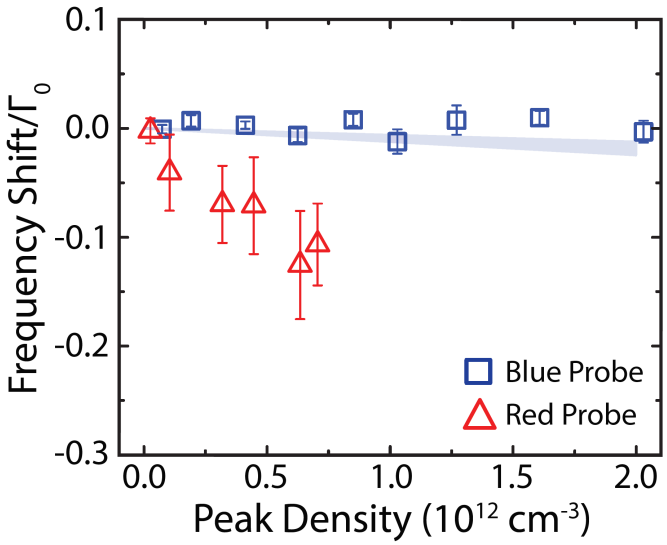

Figure 4.17: Comparison of frequency shifts normalized to the corresponding natural linewidth for the blue (blue, squares) and red (red, triangles) transitions. The blue frequency shift is consistent with 0-0.004 of Γ_0 at an atomic density of 10^{12} cm^{-3}. The red data shows more than $0.1\Gamma_0$ shift at densities up to 0.7×10^{12} cm^{-3}

For densities up to 10^{12} cm^{-3} the frequency shift of the blue transition is below the frequency stability of our probe laser and hence consistent with a zero shift. For the red transition the shift relative to the natural linewidth is more than $0.1\Gamma_{0,red}$ at an atom density of 0.7×10^{12} cm^{-3}. The density-related frequency shift significantly exceeds the predicted value based on general S-matrix

[1] This data was taken using an older red master laser which is locked to the Strontium transition using a heatpipe and not the currently in use version based on a cavity resonance.

calculations of s-wave collisions [77]. These frequency shifts are relevant for future 3D optical lattice clocks [6]. Even though the 3D optical lattice clocks can work with one atom per lattice site which will prevent collisional shifts, the long-range dipolar interactions will then be the most relevant density dependent frequency shift.

4.4 Theoretical Model - The Coupled Dipole Model

Before we turn to a microscopic model to obtain a full and consistent understanding of all these related experimental observations, we note that semiclassical models [79] treating the atomic cloud as a continuous medium of an appropriate refractive index can give an intuitive explanation of the linewidth broadening in the forward direction. Classically, an incoming electric field is attenuated as it propagates through the medium according to the Beer–Lambert law and the forward fluorescence intensity is determined by the same mechanism. This simple semiclassical model recovers the linear dependence of the forward width for small OD and predicts a nonlinear dependence of the linewidth for large OD and a flattening of the line centre. However, we find that this semiclassical approach cannot provide explanations for most aspects of the experimental observations.

The Coupled Dipole model[2] is a microscopic model that describes a system of N atoms that are driven by a uniform electromagnetic field. Here, we consider the particular case of four-level atoms that are each treated as discrete radiating dipoles located at frozen spatial positions, and driven by a weak incident laser beam, where the atoms are coupled by retarded dipole radiation. We will consider the simple four state model consisting of three degenerate upper levels and a single ground state as shown in Fig. 4.1.

The Hamiltonian describing the system can be written in terms of an atomic part $\hat{H}_a$, a part

[2] Also referred to as the coherent dipole model

that describes the field $\hat{H}_f$, and one that describes the interaction between the two $\hat{H}_{af}$

$$\begin{aligned}\hat{H}_{CD} &= \hat{H}_a + \hat{H}_f + \hat{H}_{af} \\ \hat{H}_{CD} &= \hbar\omega_0 \sum_j \hat{\mathbf{b}}_j^\dagger \cdot \hat{\mathbf{b}}_j + \sum_\lambda \hbar\omega_\lambda \hat{a}_\lambda^\dagger \hat{a}_\lambda + i\hbar \sum_j \sum_\lambda \mathbf{g}^\lambda \cdot \left(\hat{a}_\lambda^\dagger e^{-i\mathbf{k}_\lambda \cdot \mathbf{r_j}} - \hat{a}_\lambda e^{i\mathbf{k}_\lambda \cdot \mathbf{r_j}}\right)\left(\hat{\mathbf{b}}_j + \hat{\mathbf{b}}_j^\dagger\right)\end{aligned} \tag{4.12}$$

where $\hat{\mathbf{b}}_j^\dagger \left(\hat{\mathbf{b}}_j\right)$ are the vector transition operators, or coherences, for the jth atom with transition frequency ω_0 and at position $\mathbf{r}_j$, $\hat{a}_\lambda^\dagger \left(\hat{a}_\lambda\right)$ are the photon creation (annihilation) operators for a photon with wavevector $\mathbf{k}_\lambda$ and frequency ω_λ. The vector $\mathbf{g}^\lambda$ is given by

$$\mathbf{g}^\lambda = \left(\frac{p^2\omega_\lambda}{2\epsilon_0 V\hbar}\right)^{1/2} \boldsymbol{\epsilon}^\lambda \tag{4.13}$$

where p is the electric dipole matrix element, $\boldsymbol{\epsilon}^\lambda$ is the unit polarization vector of the light, ϵ_0 is the vacuum permittivity and V is the quantization volume of the electromagnetic field.

4.4.1 Coherences

In order to derive the equation of motion describing the evolution of the coherences we can first consider the equation of motion for some general atomic variable described by the operator $\hat{A}$. The Heisenberg equation of motion for this operator is then given by

$$\frac{d\hat{A}}{dt} = \frac{i}{\hbar}\left[\hat{H}_{CD}, \hat{A}\right] = \frac{i}{\hbar}\left[\hat{H}_a, \hat{A}\right] + \frac{i}{\hbar}\left[\hat{H}_f, \hat{A}\right] + \frac{i}{\hbar}\left[\hat{H}_{af}, \hat{A}\right]. \tag{4.14}$$

The first two terms are relatively simple and give, for the atomic Hamiltonian

$$\frac{i}{\hbar}\left[\hat{H}_a, \hat{A}\right] = i\omega_0 \sum_j \left[\hat{\mathbf{b}}_j^\dagger \cdot \hat{\mathbf{b}}_j, \hat{A}\right] \tag{4.15}$$

and for the electromagnetic field Hamiltonian we get

$$\frac{i}{\hbar}\left[\hat{H}_f, \hat{A}\right] = \sum_\lambda \omega_\lambda \left[\hat{a}_\lambda^\dagger \hat{a}_\lambda, \hat{A}\right] = 0 \tag{4.16}$$

where we have used the fact that an atomic operator $\hat{A}$ commutes with the electromagnetic field operators. The equation of motion for the Hamiltonian that couples the atom and the electromagnetic field is given by

$$\frac{i}{\hbar}\left[\hat{H}_{af}, \hat{A}\right] = -\sum_j \sum_\lambda \mathbf{g}^\lambda \cdot \left(e^{i\mathbf{k}_\lambda \cdot \mathbf{r}_j}\left[\hat{A}, \hat{\mathbf{s}}_j\right]\hat{a}_\lambda - e^{-i\mathbf{k}_\lambda \cdot \mathbf{r}_j}\left[\hat{A}, \hat{\mathbf{s}}_j\right]\hat{a}_\lambda^\dagger\right). \tag{4.17}$$

where we define $\hat{\mathbf{s}}_j \equiv \left(\hat{\mathbf{b}}_j + \hat{\mathbf{b}}_j^\dagger\right)$.

In order to simplify Eq. 4.17 further we can follow the method of Lehmberg [44] and James [45] and first consider the equation of motion for $\hat{a}_\lambda$. By again using the Heisenberg equation of motion we end up with the result

$$\frac{d\hat{a}_\lambda}{dt} = -i\omega_\lambda \hat{a}_\lambda + \sum_j \mathbf{g}^\lambda \cdot e^{-i\mathbf{k}_\lambda \cdot \mathbf{r}_j} \hat{\mathbf{s}}_j. \tag{4.18}$$

The solution to Eq. 4.18 can be shown to be given by

$$\hat{a}_\lambda(t) = \hat{a}_\lambda(0)\, e^{-i\omega_\lambda t} + \sum_j \mathbf{g}^\lambda \cdot e^{-i\mathbf{k}_\lambda \cdot \mathbf{r}_j} \int_0^t dt' \hat{\mathbf{s}}_j\left(t'\right) e^{-i\omega_\lambda (t-t')}. \tag{4.19}$$

where to further simplify this solution, we need to make the assumption [80] that we can decompose the coherence operators into

$$\hat{\mathbf{b}}(t) = \hat{\mathbf{B}} e^{-i\omega t} \tag{4.20}$$

where $\hat{\mathbf{B}}$ is an unknown operator whose time variation compared with $e^{-i\omega_0 t}$ is slow enough that we can remove it from the integral in Eq. 4.19. This leads to the solution of Eq 4.19 becoming

$$\hat{a}_\lambda(t) = \hat{a}_\lambda(0)\, e^{-i\omega_\lambda t} - i \sum_j \mathbf{g}^\lambda \cdot e^{-i\mathbf{k}_\lambda \cdot \mathbf{r}_j} \left[\hat{\mathbf{b}}_j \zeta^*(\omega_\lambda - \omega_0) + \hat{\mathbf{b}}_j^\dagger \zeta^*(\omega_\lambda + \omega_0)\right]. \tag{4.21}$$

where $\zeta^*(\omega)$ is the Heitler zeta function [81] defined by

$$-i\zeta^*(\omega) \equiv -i\frac{P}{\omega} + \pi\delta(\omega) \tag{4.22}$$

with P the Cauchy principal part and $\delta(\omega)$ the Dirac delta function.

Now we can consider the $\hat{a}_\lambda$ term in equation 4.17 (ignoring the $\hat{a}_\lambda^\dagger$ term), which gives us

$$\begin{aligned} -\sum_j \sum_\lambda \mathbf{g}^\lambda \cdot e^{i\mathbf{k}_\lambda \cdot r_j} \left[\hat{A}, \hat{\mathbf{s}}_j\right] \hat{a}_\lambda = &-\sum_j \sum_\lambda \mathbf{g}^\lambda \cdot e^{i\mathbf{k}_\lambda \cdot r_j} \left[\hat{A}, \hat{\mathbf{s}}_j\right] \hat{a}_\lambda(0)\, e^{-i\omega_\lambda t} \\ &+ i \sum_{j,m} \sum_\lambda \mathbf{g}^\lambda \cdot e^{+i\mathbf{k}_\lambda \cdot \mathbf{r}_{jm}} \left[\hat{A}, \hat{\mathbf{s}}_j\right] \left[\hat{\mathbf{b}}_m \zeta^*(\omega_\lambda - \omega_0) + \hat{\mathbf{b}}_m^\dagger \zeta^*(\omega_\lambda + \omega_0)\right] \end{aligned} \tag{4.23}$$

with $\mathbf{r}_{jm} = \mathbf{r}_j - \mathbf{r}_m$. We will consider the two terms in Eq. 4.23 separately. The first term can be simplified using the rotating wave approximation to give

$$-\sum_j \sum_\lambda \mathbf{g}^\lambda \cdot e^{i\mathbf{k}_\lambda \cdot \mathbf{r}_j} \left[\hat{A}, \hat{\mathbf{s}}_j\right] \hat{a}_\lambda (0)\, e^{-i\omega_\lambda t} = +\frac{ip}{\hbar} \sum_j \left[\hat{A}, \hat{\mathbf{b}}_j^\dagger\right] \hat{\boldsymbol{E}}_0^+ (\mathbf{r}_{j,t}) \tag{4.24}$$

where $\hat{\boldsymbol{E}}_0^+ (\mathbf{r}_j, t)$ represents the positive frequency part of the vacuum field and is defined as

$$\hat{\boldsymbol{E}}_0^+ (\mathbf{r}_j, t) = \sum_\lambda i \left(\frac{\hbar\omega_\lambda}{2\epsilon_0 V}\right)^{1/2} \boldsymbol{\epsilon}^\lambda \hat{a}_\lambda e^{i(\mathbf{k}_\lambda \cdot r_j - \omega_\lambda t)} \tag{4.25}$$

For the second part of Eq. 4.23 we allow the volume $V \to \infty$ which converts the summation over λ into the integral

$$\sum_\lambda \to \frac{V}{(2\pi c)^3} \int_0^\infty \omega^2 d\omega \oint d\Omega_{\hat{k}} \sum_{\hat{\epsilon}=1}^{2} \tag{4.26}$$

The seond integral can be written as

$$\frac{V}{(2\pi c)^3} \oint d\Omega_{\hat{k}} \sum_{\hat{\epsilon}=1}^{2} e^{i\mathbf{k}_\lambda \cdot r_{jm}} \left(\mathbf{g}^\lambda\right)^2 = \frac{1}{4\pi\epsilon_0} \frac{\omega p^2}{\pi c^3 \hbar} \frac{4}{3\Gamma} f(k_0 r_{jm}) = -\frac{\omega}{\pi\omega_0^3} f(k r_{jm}) \tag{4.27}$$

where

$$f(k r_{jm}) = -\frac{3\Gamma}{4} \left(\left[1 - (\hat{p} \cdot \hat{r}_{jm})^2\right] \frac{\sin(k r_{jm})}{k r_{jm}} + \left[1 - 3(\hat{p} \cdot \hat{r}_{jm})^2\right] \left(\frac{\cos(k r_{jm})}{(k r_{jm})^2} - \frac{\sin(k r_{jm})}{(k r_{jm})^3} \right) \right] \tag{4.28}$$

We can now write the second term in Eq. 4.23 as

$$\begin{aligned} &+i \sum_{j,m} \sum_\lambda \mathbf{g}^\lambda \cdot e^{+i\mathbf{k}_\lambda \cdot r_{jm}} \left[\hat{A}, \hat{\mathbf{s}}_j\right] \left[\hat{\mathbf{b}}_m \zeta^*(\omega_\lambda - \omega_0) + \hat{\mathbf{b}}_{\mathbf{m}}^\dagger \zeta^*(\omega_\lambda + \omega_0)\right] \\ &\quad = \sum_{j,m} \left(\left(-i\Omega_{jm}^- - f(k_0 r_{jm})\right) \left[\hat{\mathbf{b}}_j^\dagger, \hat{A}\right] \hat{\mathbf{b}}_m - i\Omega_{jm}^+ \left[\hat{\mathbf{b}}_j, \hat{A}\right] \hat{\mathbf{b}}_m^\dagger \right) \end{aligned} \tag{4.29}$$

where

$$\Omega_{jm}^\pm = \frac{\Gamma}{\omega_0^3 \pi} P \int_0^\infty d\omega \frac{\omega^3}{\omega \pm \omega_0} f(k_0 r_{jm}) \tag{4.30}$$

A similar method can be used to rewrite the $\hat{a}_\lambda^\dagger$ term in Eq. 4.17 to give

$$\begin{aligned}\frac{i}{\hbar}\left[\hat{H}_{af},\hat{A}\right] &= \sum_{j,m}\left(\left(-i\Omega_{jm}^{-}-f\left(k_0 r_{jm}\right)\right)\left[\hat{\mathbf{b}}_\mathbf{j}^\dagger,\hat{A}\right]\hat{\mathbf{b}}_\mathbf{m}-i\Omega_{jm}^{+}\left[\hat{\mathbf{b}}_\mathbf{j},\hat{A}\right]\hat{\mathbf{b}}_\mathbf{m}^\dagger\right)\\ &\quad+\sum_{j,m}\left(\left(+i\Omega_{jm}^{+}-f\left(k_0 r_{jm}\right)\right)\hat{\mathbf{b}}_\mathbf{m}^\dagger\left[\hat{A},\hat{\mathbf{b}}_j\right]+i\Omega_{jm}^{-}\hat{\mathbf{b}}_m^\dagger\left[\hat{A},\hat{\mathbf{b}}_j\right]\right)\\ &= -i\sum_{\substack{jm\\ j\neq m}}g_{jm}\left[\hat{A},\hat{\mathbf{b}}_j^\dagger\hat{\mathbf{b}}_m\right]-\sum_{j,m}f\left(k_0 r_{jm}\right)\left(\hat{\mathbf{b}}_j^\dagger\left[\hat{A},\hat{\mathbf{b}}_\mathbf{m}\right]+\left[\hat{\mathbf{b}}_j^\dagger,\hat{A}\right]\hat{\mathbf{b}}_m^\dagger\right)\end{aligned} \tag{4.31}$$

where we have defined

$$g_{jm}=\frac{3\Gamma}{4}\left(-\left[1-(\hat{p}\cdot\hat{r_{jm}})^2\right]\frac{\cos\left(k_0 r_{jm}\right)}{k_0 r_{jm}}+\left[1-3\left(\hat{p}\cdot\hat{r_{jm}}\right)^2\right]\left(\frac{\cos\left(k_0 r_{jm}\right)}{\left(k_0 r_{jm}\right)^2}-\frac{\sin\left(k_0 r_{jm}\right)}{\left(k_0 r_{jm}\right)^3}\right)\right) \tag{4.32}$$

The Ω_{jj} terms have been removed from the equation and absorbed into the resonance frequency of the single atom. This self-interaction term is known as the Lamb shift and cannot be calculated non-relativistically. The term g_{jm} is the frequency shift due to the interaction between different dipoles j and m.

This gives us a simplified version of the first term in Eq. 4.17. The second term can be found in a similar way to give

$$\begin{aligned}\frac{d\hat{A}}{dt} &= i\omega_0\sum_j\left[\hat{\mathbf{b}}_\mathbf{j}^\dagger\cdot\hat{\mathbf{b}}_j,\hat{A}\right]+\frac{ip}{\hbar}\sum_j\left(\left[\hat{A},\hat{\mathbf{b}}_j^\dagger\right]\hat{\boldsymbol{E}}_0^{+}\left(\mathbf{r}_j,t\right)+\hat{\boldsymbol{E}}_0^{-}\left(\mathbf{r}_j,t\right)\left[\hat{A},\hat{\mathbf{b}}_j\right]\right)\\ &\quad-i\sum_{\substack{jm\\ j\neq m}}g_{jm}\left[\hat{A},\hat{\mathbf{b}}_j^\dagger\hat{\mathbf{b}}_m\right]-\sum_{j,m}f\left(k_0 r_{jm}\right)\left(\hat{\mathbf{b}}_j^\dagger\left[\hat{A},\hat{\mathbf{b}}_\mathbf{m}\right]+\left[\hat{\mathbf{b}}_\mathbf{j}^\dagger,\hat{A}\right]\hat{\mathbf{b}}_m^\dagger\right)\end{aligned} \tag{4.33}$$

For the four level configuration exhibited by ^{88}Sr we now label the $J=0$ ground state $|g\rangle = |0,0\rangle$ and the excited $J=1$ states using a Cartesian basis $|e^z\rangle = |1,0\rangle$, $|e^x\rangle = \left(|1,-1\rangle - |1,+1\rangle\right)/\sqrt{2}$ and $|e^y\rangle = i\left(|1,-1\rangle + |1,+1\rangle\right)/\sqrt{2}$ with states labelled $|J,m\rangle$ in the standard angular momentum basis. In the Cartesian basis we can now write the vector transition operators as $\hat{\mathbf{b}}_j = \hat{x}\hat{b}_j^x + \hat{y}\hat{b}_j^y + \hat{z}\hat{b}_j^z$

with $\hat{b}_j^\alpha = |g\rangle_j \langle e^\alpha|$. In this basis Eq. 4.37 becomes

$$\begin{aligned}\frac{db_j^\alpha}{dt} &= \left(i\Delta^\alpha - \frac{\Gamma}{2}\right) b_j^\alpha - \frac{i}{2}\Omega_j \delta_{\alpha,\kappa} - i \sum_{\substack{m\neq j \\ \beta}} \left(g_{jm}^{\alpha\beta} + i f_{jm}^{\alpha\beta}\right) b_m^\beta \\ &= \left(i\Delta^\alpha - \frac{\Gamma}{2}\right) b_j^\alpha - \frac{i}{2}\Omega_j \delta_{\alpha,\kappa} - i \sum_{\substack{m\neq j \\ \beta}} G_{jm}^{\alpha\beta} b_m^\beta.\end{aligned} \tag{4.34}$$

These two expressions can also be related as they are the Real and Imaginary parts of the dipole-dipole interaction term

$$G_{jm}^{\alpha\beta} = \frac{3\Gamma}{4} \frac{e^{ik_0 r}}{k_0 r} \left[\delta_{\alpha,\beta} C\left(r_{jm}\right) + \hat{\mathbf{r}}_{jm}^\alpha \hat{\mathbf{r}}_{jm}^\beta D\left(r_{jm}\right)\right] \tag{4.35}$$

with

$$C\left(r\right) = -1 - i\frac{1}{k_0 r} + \frac{1}{\left(k_0 r\right)^2} \tag{4.36}$$

$$D\left(r\right) = 1 + \frac{3i}{k_0 r} - \frac{3}{\left(k_0 r\right)^2} \tag{4.37}$$

We can solve Eq. 4.34 to find the steady state solutions which have the form

$$b_j^\alpha = \frac{\Omega_j \delta_{\alpha,\kappa}/2}{\Delta^\alpha + i\Gamma/2} + \sum_{\substack{m\neq j \\ \beta}} \frac{G_{jm}^{\alpha\beta}}{\Delta^\alpha + i\Gamma/2} b_m^\beta \tag{4.38}$$

We can solve this equation perturbatively assuming the interactions are weak using as an expansion parameter $\mathcal{G} \equiv \sum_{j\neq m,\alpha,\beta} |G_{jm}^{\alpha\beta}|/(N\Gamma) << 1$ [82, 83] giving for Eq. 4.38 the form $b_j^\alpha = b_j^{\alpha(0)} + b_j^{\alpha(1)} + b_j^{\alpha(2)} + ...$, where the zeroth and first order terms are given by

$$b_j^{\alpha(0)} = \frac{\Omega^\kappa e^{i\mathbf{k}\cdot\mathbf{r}_j} \delta_{\alpha,\kappa}/2}{\Delta^\alpha + i\Gamma/2} \tag{4.39}$$

$$b_j^{\alpha(1)} = \frac{\Omega^\kappa \delta_{\alpha,\kappa}/2}{i(\Delta^\alpha + i\Gamma/2)^2} K_{\alpha,\beta}^j e^{i\mathbf{k}\cdot\mathbf{r}_j} \tag{4.40}$$

where $K_{\alpha,\kappa}^j = \sum_{m\neq j} G_{jm}^{\alpha\beta} e^{\mathbf{k}\cdot\mathbf{r}_{jm}}$.

4.4.2 Scattered Fluorescence

The electic field scattered by a dense sample of atoms in the far field can be written as [44, 45]

$$\hat{\mathbf{E}}^{+}\left(\hat{\mathbf{r}}_s, t\right) \approx \frac{\Gamma_0}{2p} \sum_j \frac{\hat{\mathbf{r}}_s \times \left[\hat{\mathbf{r}}_s \times \hat{\mathbf{b}}_j\left(t'\right)\right]}{\left|\hat{\mathbf{r}}_j - \hat{\mathbf{r}}_s\right|} \tag{4.41}$$

where $t' = t - \left|\hat{\mathbf{r}}_j - \hat{\mathbf{r}}_s\right|/c$. By using the vector identity $\mathbf{u} \times (\mathbf{v} \times \mathbf{w}) = (\mathbf{u} \cdot \mathbf{w})\mathbf{v} - (\mathbf{u} \cdot \mathbf{v})\mathbf{w}$ the intensity is then given by

$$\begin{aligned} I\left(\hat{\mathbf{r}}_s, t\right) &= \left\langle \hat{\mathbf{E}}^{+}\left(\hat{\mathbf{r}}_s, t\right) \hat{\mathbf{E}}^{-}\left(\hat{\mathbf{r}}_s, t\right) \right\rangle \\ &\approx \frac{\Gamma_0^2}{4p^2 r^2} \sum_{j,m} \left[\mathbf{b}_j \cdot \mathbf{b}_m^* - (\mathbf{b}_j \cdot \hat{\mathbf{r}}_s)(\mathbf{b}_m^* \cdot \hat{\mathbf{r}}_s)\right] e^{-i\mathbf{k}_s \cdot (\mathbf{r}_j - \mathbf{r}_m)} \\ &\approx \frac{\Gamma_0^2}{4p^2 r^2} \sum_{j,m} e^{-i\mathbf{k}_s \cdot \mathbf{r}_{jm}} \sum_{\alpha,\beta} \left[\delta_{\alpha,\beta} - \hat{\mathbf{r}}_s^{\alpha} \hat{\mathbf{r}}_s^{\beta}\right] b_j^{\alpha} b_m^{\beta *} \end{aligned} \tag{4.42}$$

where $\hat{\mathbf{r}}^{\alpha}$ is the component of the unit vector $\hat{\mathbf{r}}$ along the $\alpha = x, y$ or z direction. The intensity can be found by splitting the summation over j and m into the two cases where $j = m$ and $j \neq m$. By using the zeroth order solution to Eq. 4.38, the scattered intensity is driven only by the external field and this leads to the intensity

$$I \propto \frac{1}{\Delta^2 + \Gamma_0^2/4} \left(N + N^2 e^{-|\mathbf{k}_s - \mathbf{k}_0|^2 \sigma_{\perp}}\right) \tag{4.43}$$

The overall intensity distribution is Lorentzian with an amplitude dependent on atom number N. The $j = m$ term of Eq. 4.42 corresponds to the incoherent sum of single atom intensities to give the first term in Eq. 4.43. The $j \neq m$ term is an interference term and in our case of coherently driven dipole moments this term is responsible for the build of of intensity $\propto N^2$ in Eq. 4.43. The phase coherence is restricted to a narrow angular region $\delta\theta \sim 1/(k_0\sigma) = \lambda/\sigma$ in the direction of the probe beam and the constructive interference is quickly reduced due to the random positions of the atoms. The wavelength dependence of the angular region is consistent with the data shown in Fig. 4.7 where the red transition shows a larger angular region of forward enhancement.

Including the first order corrections the intensity of the scattered light in the transverse direction is given by

$$I \propto \frac{N\Omega^2}{(\Delta - \Gamma_0 \mathrm{Re}[\bar{G}])^2 + (\Gamma_0 + 2\Gamma_0 \mathrm{Im}[\bar{G}])^2/4} \tag{4.44}$$

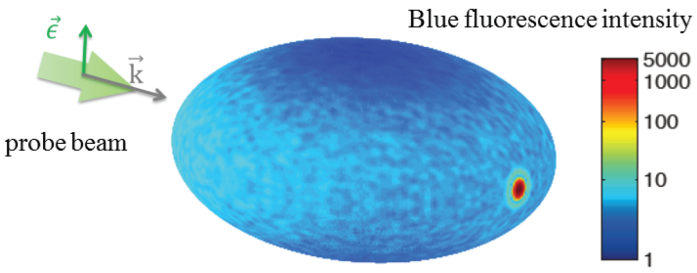

Figure 4.18: Three dimensional intensity prediction from the coupled dipole model. The intensity is peaked in the forward direction due to the constructive interference of the synchronized dipoles. The intensity in the direction of the polarization is classically forbidden but finite due to multiple scattering events. The speckled pattern is due to randomly positioned atoms and can be removed by averaging over multiple atom configurations.

where $\bar{G} = \sum_{j \neq m} G^{\alpha\alpha}_{jm} e^{-i\mathbf{k}_0 \cdot \mathbf{r}_{jm}}/(N\Gamma)$. For the forward direction the factor of N is replaced by N^2. We can see that the lineshape is still Lorentzian with modifications to the center frequency and linewidth which are caused by the dipole-dipole interactions. For a relatively dilute cloud with average interparticle distance $\bar{r} \gg 1/k$, the far field interactions dominate and all terms beyond $1/r$ can be neglected. In this limit analytic expressions for the frequency shift and line broadening are found to be

$$2\Gamma_0 \mathrm{Im}[\bar{G}] = \frac{OD}{4}\Gamma_0 \tag{4.45}$$

$$\Gamma_0 \mathrm{Re}[\bar{G}] = -\frac{3\sqrt{2}\pi n_0}{16 k_0^3}\Gamma_0 \tag{4.46}$$

This first-order approximation provides an intuitive picture about the role of dipolar effects on the lineshape. We can see that for lower densities the frequency shift scales with density and arises from the real part of the dipole-dipole interactions. We can also see that the linewidth scales with OD, whch is seen experimentally (see Section 4.3.2), and arises from the imaginary part of the dipole-dipole interactions.

4.4.3 Motional Effects

The motional effects in the red transition are taken into account by introducing a random detuning $\delta\nu$ for each atom which can be sampled according to a Gaussian thermal distribution. Assuming non-interacting and two-level atoms the zeroth order coherence given in Eq. 4.39 is modified to become

$$b_j^{(0)} = \frac{\Omega e^{i\mathbf{k}\cdot\mathbf{r}_j}}{(\Delta + \delta\nu_j) + i\Gamma_0/2} \tag{4.47}$$

We can now use this to determine the incoherent scattering in the forward direction to be

$$I_{incoh} = \frac{1}{\sqrt{2\pi}\Delta_D} \int d(\delta\nu_j)|b_j|^2 e^{-\frac{\delta\nu_j^2}{2\Delta_D^2}} \tag{4.48}$$

and the coherent part to be

$$I_{coh} = \frac{1}{2\pi\Delta_D^2} \int\int d(\delta\nu_j)d(\delta\nu_m)b_j b_m^* e^{-\frac{\delta\nu_j^2}{2\Delta_D^2}} e^{-\frac{\delta\nu_m^2}{2\Delta_D^2}} \tag{4.49}$$

evaluating the integrals in Eq. 4.48 and Eq. 4.49 for the on resonance case gives us

$$\frac{I_{coh}}{I_{incoh}} = \frac{\sqrt{\frac{\pi}{2}} e^{\frac{1}{8\Delta_D^2/\Gamma_0^2}} \operatorname{erfc}\left[\frac{1}{2\sqrt{2}\Delta_D/\Gamma_0}\right]}{2\Delta_D/\Gamma_0} \tag{4.50}$$

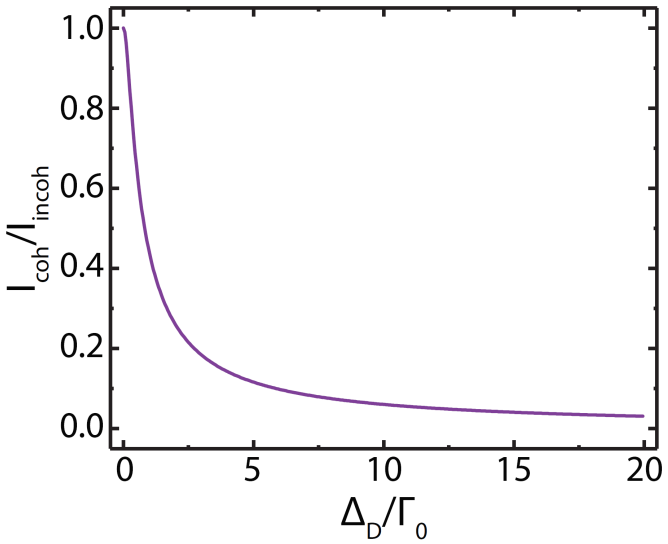

Figure 4.19: Suppression of the forward enhancement peak with motion.

This ratio, that is plotted in Fig. 4.19 tells us how the motion will suppress the forward interference and depends on Δ_D/Γ_0. For the blue transition $\Delta_D/\Gamma_0 \sim 0$ and for the red transition $\Delta_D/\Gamma_0 \sim 2$ which qualitatively explains the suppression of the forward enhancement for the red transition.

4.4.4 Multiple Scattering Processes

For an atomic cloud with an increasingly large OD, dipolar interactions are stronger and multiple scattering processes become relevant. The first order perturbative analysis then breaks down and the full solution of Eq. 4.38 becomes necessary to account for multiple scattering processes. The first signatures arise from the forward fluorescence intensity, where its naive N^2 scaling is reduced with an increasing atom number as a consequence of multiple scattering processes. The effect is observed in both the red and blue transitions, and is expected to be more pronounced on the red transition due to its longer wavelength. However, atomic motion leads to a lower effective OD, which tends to suppress multiple scattering processes and thus helps to partially recover the collective enhancement. The theory lines in Fig. 4.7 and Fig. 4.9 represent such quantitative theory calculations for both transitions, which agree with the experiment.

Meanwhile, for the linewidth broadening observed in the forward direction, it becomes evident that the scaling of the linewidth versus OD turns nonlinear at large values of OD. The experimental data falls within the shaded area in Fig. 4.12, which represents the full solution with a 20% uncertainty in the experimental atom number. Multiple scattering processes are also key to the explanation of the measured fluorescence along the transverse direction, especially for the classically forbidden polarization $\hat{z}$. Indeed, for both intensity and linewidth broadening observed in the transverse direction, under either $\hat{y}$ or $\hat{z}$ probe polarization, the full model (shown as shaded areas in both Fig. 4.10 and Fig. 4.13) reproduces well the experimental results on the blue transition. Taking into account motional dephasing, the transverse broadening for the red transition is also well reproduced as shown in Fig. 4.15.

4.4.5 Frequency Shifts

From above we have found that the frequency shift arising from the dipolar coupling is expected to scale with atomic density, which includes both a collective Lamb shift and the Lorentz-Lorenz shift [84, 85]. For our experimental density this frequency shift, normalized to Γ_0, is $\lesssim 10^{-3}$, which is consistent with the observed frequency shift for the blue transition. In contrast for the red transition the measured density shift (normalized to Γ) is significantly larger than what is predicted from the current treatment of interacting dipoles; it is also much bigger than the unitarity limit of s-wave scattering. Qualitatively, we expect that as the atoms move and approach each other, the long-lived ground-excited state coherence in the red transition can be significantly modified by the collisional process and open higher partial wave channels. We can thus expect a larger collisional phase shift. This process can be further complicated by atomic recoil, light forces and Doppler dephasing [86].

4.5 Conclusions

We have shown clear experimental observations of collective emission from a dense sample of ^{88}Sr atoms. These observations can be understood by treating the atoms as coherently coupled dipoles where the key ingredient to understanding our observations is the dipole-dipole interactions between the atoms. The probing laser beam synchronizes the dipoles such that the constructive interference of the emitted fluorescence in the direction of the probe beam shows strong constructive interference. This is seen experimentally as both an enhancement of intensity in the forward direction and an N^2 scaling of the intensity.

By probing the $^1S_0 - {}^1P_1$ blue transition and comparing to the $^1S_0 - {}^3P_1$ red transition we are able to clearly see the effects of motion that are present for the red transition. The atomic motion reduces the observed constructive interference. The linewidth broadening, caused by the imaginary part of the dipole-dipole interactions, for both transition is similar with no major differences brought about by the atomic motion. This is in contrast to the large difference in the frequency shift,

caused by the real part of the dipole-dipole interactions. For the blue transition the frequency shift is consistent with the predictions of the coupled dipole model. For the red transition the frequency shift is significantly larger than predicted by the coupled dipole model although it should be noted that this measurement was taken under different conditions than the rest of the measurements in this chapter.

Chapter 5

Many-body interactions in an optical lattice clock

5.1 Introduction

In this chapter we will provide a theoretical framework for studying the interactions of Strontium atoms in a one-dimensional optical lattice clock, based on the work of Martin et al [15] and Rey et al [87]. We will consider the case of nuclear spin polarized fermions in a deep lattice which is the most relevant case for current optical lattice clocks. This model is the basis for the interactions discussed in Chapter 6 and Chapter 7 which may become important for the operation of future optical lattice clocks. In each of these chapters the spin model derived here will be generalized to the cases under study, namely the case of interactions between spin mixtures and the interactions between atoms when tunneling is allowed.

5.1.1 Chapter Outline

In section 5.2 we will start out with the Hamiltonian that describes the nuclear spin polarized fermions in a one-dimensional optical lattice clock. We will the re-write this Hamiltonian in terms of a spin model (section 5.3). We will then discuss the interaction parameters in more detail (section 5.4) before discussing the temperature dependence of these parameters (section 5.5).

5.2 Hamiltonian

The simplest case of interactions in our one-dimensional lattice is the case of atoms trapped within a deep lattice (tunneling, $J = 0$) and where all atoms are in the same nuclear spin state.

We denote the ground clock state ($^1S_0$) as g and the excited clock state ($^3P_0$) e. The Hamiltonian describing the system can be written as

$$\hat{H} = \hat{H}_0 + \hat{H}_{\text{int}} + \hat{H}_L \tag{5.1}$$

$$\hat{H}_0 = \sum_\alpha \int d^3\mathbf{R}\hat{\Psi}^\dagger_\alpha(\mathbf{R}) \left(\frac{\hbar^2}{2M}\nabla^2 + V_{ext}(\mathbf{R})\right) \hat{\Psi}_\alpha(\mathbf{R}) \tag{5.2}$$

$$+ \frac{1}{2}\int d^3\mathbf{R}\left[\hat{\Psi}^\dagger_e(\mathbf{R})\hat{\Psi}_e(\mathbf{R}) - \hat{\Psi}^\dagger_g(\mathbf{R})\hat{\Psi}_g(\mathbf{R})\right]$$

$$\hat{H}_L = -\frac{\hbar\Omega_0}{2}\int d^3\mathbf{R}\left[\hat{\Psi}^\dagger_e(\mathbf{R})e^{-i(\omega_L t - \mathbf{k_L}\cdot\mathbf{r})}\hat{\Psi}_g(\mathbf{R}) + h.c.\right] \tag{5.3}$$

Where $\hat{\Psi}_\alpha(\mathbf{R})$ is a fermionic field operator at position $\mathbf{R}$ for atoms with mass M in electronic state $\alpha = \{g, e\}$. These fermionic field operators obey the fermionic anti-commutator relations $\{\Psi^\dagger_j(\mathbf{x}), \Psi_k(\mathbf{x}')\} = \delta(\mathbf{x}-\mathbf{x}')\delta_{jk}$. The Hamiltonian, $\hat{H}_L$, takes into account the interrogation of the atoms by the clock laser with Rabi frequency Ω_0 that has frequency ω_L and wavevector $\mathbf{k_L}$ and is detuned from atomic resonance by $\delta = \omega_L - \omega_0$.

For the interaction Hamiltonian, $\hat{H}_{\text{int}}$, we consider only two possible partial wave interactions, s-wave and p-wave, as these dominate at our μK temperatures. Since we are considering spin-polarized fermions, that are in a symmetric nuclear state, we have one s-wave scattering length a^-_{eg} describing collisions between two atoms in the anti-symmetric electronic state $\frac{1}{\sqrt{2}}(|ge\rangle - |eg\rangle)$. The p-wave interaction can have three different scattering lengths b_{gg}, b_{ee}, and b^+_{eg} associated with the symmetric electronic states $|gg\rangle$, $|ee\rangle$, and $\frac{1}{\sqrt{2}}(|ge\rangle + |eg\rangle)$ respectively.

For the interaction Hamiltonian, the general expression for the interactions is written as [88]

$$\hat{H}_{\text{int}} = \frac{1}{2}\int d^3\mathbf{r}_1 d^3\mathbf{r}_2 \sum_{\alpha,\beta} \hat{\Psi}^\dagger_\alpha(\mathbf{r}_1)\hat{\Psi}^\dagger_\beta(\mathbf{r}_2)v(\mathbf{r}_1,\mathbf{r}_2)\hat{\Psi}_\beta(\mathbf{r}_2)\hat{\Psi}_\alpha(\mathbf{r}_1) \tag{5.4}$$

where $v(\mathbf{x},\mathbf{y})$ can be written as

$$v(\mathbf{x},\mathbf{y}) = V_{s\text{-wave}} + V_{p\text{-wave}} \tag{5.5}$$

where the s-wave and p-wave interaction terms are written as

$$V_{s\text{-wave}} = \frac{4\pi a_{\alpha\beta}\hbar^2}{m}\delta(\mathbf{r}) \tag{5.6}$$

$$V_{p\text{-wave}} = \frac{\pi\hbar b^3_{\alpha\beta}}{m}\overleftarrow{\nabla}_{\mathbf{r}}\delta(\mathbf{r})\frac{\partial^3}{\partial r^3}r^3\overrightarrow{\nabla}_{\mathbf{r}} \tag{5.7}$$

where the first term is for s-wave interactions and the second term is for p-wave interactions, with $\mathbf{r} = \mathbf{r}_1 - \mathbf{r}_2$ with $\mathbf{r}_j$ the position of the jth atom. The arrows above the gradient operators indicate the direction in which the operator acts and $r = |\mathbf{r}|$. By integrating over the Dirac delta functions, $\delta(\mathbf{r})$, we can rewrite $\hat{H}_{\rm int}$ as

$$\begin{aligned}\hat{H}_{\rm int} = &\frac{1}{2}\frac{4\pi\hbar^2 a_{eg}^-}{m}\sum_{\alpha\beta}(1-\delta_{\alpha\beta})\int d^3\mathbf{R}\hat{\Psi}^\dagger_\alpha(\mathbf{R})\hat{\Psi}_\alpha(\mathbf{R})\hat{\Psi}^\dagger_\beta(\mathbf{R})\hat{\Psi}_\beta(\mathbf{R}) \\ &+\frac{1}{2}\frac{6\pi\hbar^2}{m}\sum_{\alpha\beta}b^3_{\alpha\beta}\int d^3\mathbf{R}\left[\left(\nabla\hat{\Psi}^\dagger_\alpha(\mathbf{R})\right)\hat{\Psi}^\dagger_\beta(\mathbf{R}) - \hat{\Psi}^\dagger_\alpha(\mathbf{R})\left(\nabla\hat{\Psi}^\dagger_\beta(\mathbf{R})\right)\right] \\ &\cdot\left[\hat{\Psi}_\beta(\mathbf{R})\left(\nabla\hat{\Psi}_\alpha(\mathbf{R})\right) - \left(\nabla\hat{\Psi}_\beta(\mathbf{R})\right)\hat{\Psi}_\alpha(\mathbf{R})\right] \end{aligned} \tag{5.8}$$

where the delta function indicates we have explicitly added in that we only have one s-wave channel for nuclear spin-polarized fermions.

In the case of a deep lattice we can expand the field operators in a non-interacting atom harmonic oscillator basis $\hat{\Psi}(\mathbf{R}) = \phi_0^z(z)\sum_{\mathbf{n}}\hat{c}_{\alpha\mathbf{n}}\phi_{n_x}(x)\phi_{n_y}(y)$, where $\hat{c}^\dagger_{\alpha,\mathbf{n}}$ ($\hat{c}_{\alpha,\mathbf{n}}$) create (annihilate) a fermion in mode $\mathbf{n} = (n_x, n_y)$ and electronic state α. We assume all atoms are in the ground axial band of the lattice, $\phi_0^z(z)$, and are thermally populated amongst the radial modes of the lattice $\phi_{\mathbf{n}}$. We can write these harmonic oscillator modes explicitly as

$$\phi_0^z(z) = \frac{1}{\sqrt{\sqrt{\pi}a_z}}e^{-\frac{z^2}{2a_z}} \tag{5.9}$$

$$\phi_n(x) = \frac{1}{\sqrt{2^n n!\sqrt{\pi}a_r}}e^{-\frac{x^2}{2a_R^2}}\mathrm{H}_n\left[\frac{x}{a_r}\right] \tag{5.10}$$

where $\mathrm{H}_n[x]$ is the nth Hermite polynomial, $a_R = \sqrt{\hbar/(m\omega_R)}$ is the radial harmonic oscillator length with ω_R the radial trapping frequency and $a_z = \sqrt{\hbar/(m\omega_z)}$ the axial harmonic oscillator length with ω_z the axial trapping frequency.

The interaction terms in $\hat{H}_{\rm int}$ can be re-written as integrals over hermite polynomials. For the s-wave interaction term the the x integral can be written as

$$\begin{aligned}\int dx\phi_{n_{x_1}}\phi_{n_{x_2}}\phi_{n_{x_3}}\phi_{n_{x_4}} &= \sqrt{\frac{m\omega_R}{\hbar}}\left[\int\frac{d\varrho e^{-2\varrho^2}\mathrm{H}_{n_{x_1}}[\varrho]\mathrm{H}_{n_{x_2}}[\varrho]\mathrm{H}_{n_{x_3}}[\varrho]\mathrm{H}_{n_{x_4}}[\varrho]}{\pi\sqrt{2^{n_{x_1}+n_{x_2}+n_{x_3}+n_{x_4}}n_{x_1}!n_{x_2}!n_{x_3}!n_{x_4}!}}\right] \\ &\equiv \sqrt{\frac{m\omega_R}{\hbar}}s_{n_{x_1},n_{x_2},n_{x_3},n_{x_4}}\end{aligned} \tag{5.11}$$

where we have used the substitution $\varrho = x/a_r$ and defined the term $s_{n_{x_1},n_{x_2},n_{x_3},n_{x_4}}$. The y integral gives the same as the x integral and the z integral can be written explicitly as

$$\int dx\,[\phi_0^z]^4 = \frac{1}{\sqrt{2\pi}}\sqrt{\frac{m\omega_z}{\hbar}} \tag{5.12}$$

So we can now rewrite the s-wave interaction term as

$$\begin{aligned}
&\frac{1}{2}\frac{4\pi\hbar^2 a_{eg}^-}{m}\sum_{\alpha\beta}(1-\delta_{\alpha\beta})\int d^3\mathbf{R}\hat{\Psi}_\alpha^\dagger(\mathbf{R})\hat{\Psi}_\alpha(\mathbf{R})\hat{\Psi}_\beta^\dagger(\mathbf{R})\hat{\Psi}_\beta(\mathbf{R}) \\
&= \sum_{\substack{\alpha\beta \\ \mathbf{n_1},\mathbf{n_2} \\ \mathbf{n_3},\mathbf{n_4}}} \frac{\hbar}{4}(1-\delta_{\alpha\beta})4\sqrt{2\pi}\frac{a_{eg}^-}{a_r}\sqrt{\omega_R\omega_z}S_{\mathbf{n_1},\mathbf{n_2},\mathbf{n_3},\mathbf{n_4}}\hat{c}_{\alpha\mathbf{n}_1}^\dagger\hat{c}_{\beta\mathbf{n}_2}^\dagger\hat{c}_{\beta\mathbf{n}_3}\hat{c}_{\alpha\mathbf{n}_4} \\
&= \sum_{\substack{\alpha\beta \\ \mathbf{n_1},\mathbf{n_2} \\ \mathbf{n_3},\mathbf{n_4}}} \frac{\hbar}{4}(1-\delta_{\alpha\beta})uS_{\mathbf{n_1},\mathbf{n_2},\mathbf{n_3},\mathbf{n_4}}\hat{c}_{\alpha\mathbf{n}_1}^\dagger\hat{c}_{\beta\mathbf{n}_2}^\dagger\hat{c}_{\beta\mathbf{n}_3}\hat{c}_{\alpha\mathbf{n}_4}
\end{aligned} \tag{5.13}$$

where we have defined $S_{\mathbf{n_1},\mathbf{n_2},\mathbf{n_3},\mathbf{n_4}} \equiv s_{n_{x_1},n_{x_2},n_{x_3},n_{x_4}}s_{n_{y_1},n_{y_2},n_{y_3},n_{y_4}}$ and d $u \equiv 4\sqrt{2\pi}\sqrt{\omega_R\omega_z}a_{eg}^-/a_r$.

For the p-wave interaction term, the $\nabla = \hat{x}\frac{\partial}{\partial x} + \hat{y}\frac{\partial}{\partial y} + \hat{z}\frac{\partial}{\partial z}$ is the sum of derivatives in the different directions. The z derivative term evaluates to zero and the x derivative integral gives

$$\begin{aligned}
&\int dz\,[\phi_0^z]^4\int dy\phi_{n_{y_1}}\phi_{n_{y_2}}\phi_{n_{y_3}}\phi_{n_{y_4}}\int dx\left[\frac{d\phi_{n_{x_1}}}{dx}\phi_{n_{x_2}} - \phi_{n_{x_1}}\frac{d\phi_{n_{x_2}}}{dx}\right]\left[\frac{d\phi_{n_{x_3}}}{dx}\phi_{n_{x_4}} - \phi_{n_{x_3}}\frac{d\phi_{n_{x_4}}}{dx}\right] \\
&= \frac{1}{\sqrt{2\pi}}\sqrt{\frac{m\omega_z}{\hbar}}\frac{1}{a_r}s_{n_{y_1},n_{y_2},n_{y_3},n_{y_4}}\frac{1}{a_r^3}\times \\
&\left[\frac{\int d\varrho e^{-2\varrho^2}\left[\frac{d\mathrm{H}_{n_{x_1}}[\varrho]}{d\varrho}\mathrm{H}_{n_{x_2}}[\varrho] - \mathrm{H}_{n_{x_1}}[\varrho]\frac{d\mathrm{H}_{n_{x_2}}[\varrho]}{d\varrho}\right]\left[\frac{d\mathrm{H}_{n_{x_3}}[\varrho]}{d\varrho}\mathrm{H}_{n_{x_4}}[\varrho] - \mathrm{H}_{n_{x_3}}[\varrho]\frac{d\mathrm{H}_{n_{x_4}}[\varrho]}{d\varrho}\right]}{\pi\sqrt{2^{n_{x_1}+n_{x_2}+n_{x_3}+n_{x_4}}n_{x_1}!n_{x_2}!n_{x_3}!n_{x_4}!}}\right] \\
&\equiv \frac{1}{\sqrt{2\pi}}\sqrt{\frac{m\omega_z}{\hbar}}\frac{1}{a_r}s_{n_{y_1},n_{y_2},n_{y_3},n_{y_4}}\frac{1}{a_r^3}p_{n_{x_1},n_{x_2},n_{x_3},n_{x_4}}
\end{aligned} \tag{5.14}$$

where we have defined the term $p_{n_{x_1},n_{x_2},n_{x_3},n_{x_4}}$. The y integral evaluates to the same expression.

We can therefore write the p-wave term as

$$\begin{aligned}
&\frac{1}{2}\frac{6\pi\hbar^2}{m}\sum_{\alpha\beta} b_{\alpha\beta}^3 \int d^3\mathbf{R}\left[\left(\nabla\hat{\Psi}_\alpha^\dagger(\mathbf{R})\right)\hat{\Psi}_\beta^\dagger(\mathbf{R}) - \hat{\Psi}_\alpha^\dagger(\mathbf{R})\left(\nabla\hat{\Psi}_\beta^\dagger(\mathbf{R})\right)\right] \\
&\cdot\left[\hat{\Psi}_\beta(\mathbf{R})\left(\nabla\hat{\Psi}_\alpha(\mathbf{R})\right) - \left(\nabla\hat{\Psi}_\beta(\mathbf{R})\right)\hat{\Psi}_\alpha(\mathbf{R})\right] \\
&= \sum_{\substack{\alpha\beta \\ \mathbf{n_1},\mathbf{n_2} \\ \mathbf{n_3},\mathbf{n_4}}} \frac{\hbar}{4} 6\sqrt{2\pi}\sqrt{\omega_z\omega_R}\frac{b_{\alpha\beta}^3}{a_r^3} P_{\mathbf{n}_1,\mathbf{n}_2,\mathbf{n}_3,\mathbf{n}_4}\hat{c}_{\alpha\mathbf{n}_1}^\dagger\hat{c}_{\beta\mathbf{n}_2}^\dagger\hat{c}_{\beta\mathbf{n}_3}\hat{c}_{\alpha\mathbf{n}_4} \\
&= \sum_{\substack{\alpha\beta \\ \mathbf{n_1},\mathbf{n_2} \\ \mathbf{n_3},\mathbf{n_4}}} \frac{\hbar}{4} \mathrm{v}_{\alpha\beta} P_{\mathbf{n}_1,\mathbf{n}_2,\mathbf{n}_3,\mathbf{n}_4}\hat{c}_{\alpha\mathbf{n}_1}^\dagger\hat{c}_{\beta\mathbf{n}_2}^\dagger\hat{c}_{\beta\mathbf{n}_3}\hat{c}_{\alpha\mathbf{n}_4}
\end{aligned} \tag{5.15}$$

where we have defined $P_{\mathbf{n}_1,\mathbf{n}_2,\mathbf{n}_3,\mathbf{n}_4} \equiv \left(s_{n_{y_1},n_{y_2},n_{y_3},n_{y_4}} p_{n_{x_1},n_{x_2},n_{x_3},n_{x_4}} + p_{n_{y_1},n_{y_2},n_{y_3},n_{y_4}} s_{n_{x_1},n_{x_2},n_{x_3},n_{x_4}}\right)$ and $v_{\alpha\beta} \equiv 6\sqrt{2\pi}\sqrt{\omega_z\omega_R} b_{\alpha\beta}^3/a_r^3$. The full interaction Hamiltonian, $\hat{H}_{\mathrm{int}}$, can then be written in the rotating frame as

$$\hat{H}_{\mathrm{int}} = \sum_{\substack{\alpha\beta \\ \mathbf{n_1},\mathbf{n_2} \\ \mathbf{n_3},\mathbf{n_4}}} \frac{\hbar}{4}\left[(1-\delta_{\alpha\beta})uS_{\mathbf{n_1},\mathbf{n_2},\mathbf{n_3},\mathbf{n_4}} + v_{\alpha\beta}P_{\mathbf{n_1},\mathbf{n_2},\mathbf{n_3},\mathbf{n_4}}\right]\hat{c}_{\alpha\mathbf{n}_1}^\dagger\hat{c}_{\beta\mathbf{n}_2}^\dagger\hat{c}_{\beta\mathbf{n}_3}\hat{c}_{\alpha\mathbf{n}_4} \tag{5.16}$$

5.3 The Spin Model

At typical operating conditions of $\nu_R = 450$ Hz, $\nu_z = 80$ kHz, and temperatures in the μK regime, the mean interaction energy per particle is much weaker than the energy splitting between neighboring single-particle vibrational modes. Thus to first-order, only collisions between atoms that conserve the total single particle energy need to be considered. Such processes conserve the total number of particles per mode and in this case the many-body dynamics are mainly governed by the internal degrees of freedom of the atoms, i.e. their electronic and nuclear spin degree of freedom, and the motional degrees are assumed frozen.

However, in the case of a purely harmonic spectrum of energy levels mode changing collisions are allowed even under weak interactions due to (i) the linearly spaced energy levels of the harmonic oscillator and (ii) the separability of the harmonic oscillator potential along the x and y directions. Condition (i) would allow two particles in modes $\mathbf{n} = (n_x, n_y)$ and $\mathbf{m} = (m_x, m_y)$ to collide into

modes $\mathbf{n}' = (n_x + k, n_y + k')$ and $\mathbf{m}' = (m_x - k, n_y - k')$ without violating energy conservaton constraints. Condition (ii) would allow the same two particles to collide and scatter into modes $\mathbf{n}' = (n_x, m_y)$ and $\mathbf{m}' = (m_x, n_y)$.

In practice, however, the trapping potential does not give a fully harmonic trap due to the Gaussian lattice laser profile. This anharmonic, inseparable, spectrum of energy levels then prevents the processes described in (i) and (ii) and we are left with only two types of interactions that take place in the lattice:

- **Direct**: No modes are changed $\mathbf{n}' = \mathbf{n} = (n_x, n_y)$ $\mathbf{m}' = \mathbf{m} = (m_x, m_y)$
- **Exchange**: Both motional eigenstates are exchanged $\mathbf{n}' = \mathbf{m} = (m_x, m_y)$ $\mathbf{m}' = \mathbf{n} = (n_x, n_y)$

This simplifies our interaction Hamiltonian and allows us to re-write it as

$$\begin{aligned}\hat{H}_{\text{int}} = &\sum_{\substack{\alpha\beta \\ \mathbf{n_1},\mathbf{n_2}}} \frac{\hbar}{4}\left[(1-\delta_{\alpha\beta})uS_{\mathbf{n_1},\mathbf{n_2},\mathbf{n_2},\mathbf{n_1}} + v_{\alpha\beta}P_{\mathbf{n_1},\mathbf{n_2},\mathbf{n_2},\mathbf{n_1}}\right]\hat{c}^\dagger_{\alpha\mathbf{n}_1}\hat{c}^\dagger_{\beta\mathbf{n_2}}\hat{c}_{\beta\mathbf{n_2}}\hat{c}_{\alpha\mathbf{n}_1} \\ &+ \sum_{\substack{\alpha\beta \\ \mathbf{n_1},\mathbf{n_2}}} \frac{\hbar}{4}\left[(1-\delta_{\alpha\beta})uS_{\mathbf{n_1},\mathbf{n_2},\mathbf{n_1},\mathbf{n_2}} + v_{\alpha\beta}P_{\mathbf{n_1},\mathbf{n_2},\mathbf{n_1},\mathbf{n_2}}\right]\hat{c}^\dagger_{\alpha\mathbf{n}_1}\hat{c}^\dagger_{\beta\mathbf{n_2}}\hat{c}_{\beta\mathbf{n_1}}\hat{c}_{\alpha\mathbf{n_2}}\end{aligned} \tag{5.17}$$

This can be re-written using the anticommutation relations of the fermionic operators and using the symmetrization of the s-wave and p-wave coefficients, $S_{\mathbf{n_1},\mathbf{n_2},\mathbf{n_1},\mathbf{n_2}} = S_{\mathbf{n_1},\mathbf{n_2},\mathbf{n_2},\mathbf{n_1}}$ and $P_{\mathbf{n_1},\mathbf{n_2},\mathbf{n_1},\mathbf{n_2}} = -P_{\mathbf{n_1},\mathbf{n_2},\mathbf{n_2},\mathbf{n_1}}$ to give

$$\begin{aligned}\hat{H}_{\text{int}} = &\sum_{\substack{\alpha\beta \\ \mathbf{n_1}\neq\mathbf{n_2}}} \frac{\hbar}{4}\left[(1-\delta_{\alpha\beta})uS_{\mathbf{n_1},\mathbf{n_2},\mathbf{n_2},\mathbf{n_1}} + v_{\alpha\beta}P_{\mathbf{n_1},\mathbf{n_2},\mathbf{n_2},\mathbf{n_1}}\right]\hat{c}^\dagger_{\alpha\mathbf{n}_1}\hat{c}_{\alpha\mathbf{n}_1}\hat{c}^\dagger_{\beta\mathbf{n_2}}\hat{c}_{\beta\mathbf{n_2}} \\ &- \sum_{\substack{\alpha\beta \\ \mathbf{n_1}\neq\mathbf{n_2}}} \frac{\hbar}{4}\left[(1-\delta_{\alpha\beta})uS_{\mathbf{n_1},\mathbf{n_2},\mathbf{n_1},\mathbf{n_2}} - v_{\alpha\beta}P_{\mathbf{n_1},\mathbf{n_2},\mathbf{n_2},\mathbf{n_1}}\right]\hat{c}^\dagger_{\alpha\mathbf{n}_1}\hat{c}_{\beta\mathbf{n_1}}\hat{c}^\dagger_{\beta\mathbf{n_2}}\hat{c}_{\alpha\mathbf{n_2}}\end{aligned} \tag{5.18}$$

In order to be able to write the Hamiltonian as a spin model we use the spin operator

$$\hat{\mathbf{S}} = \frac{1}{2}\sum_{\alpha\beta}\hat{c}^\dagger_\alpha \boldsymbol{\sigma}_{\alpha\beta}\hat{c}_\beta \tag{5.19}$$

where $\hat{\mathbf{S}} = \left(\hat{S}^X, \hat{S}^Y, \hat{S}^Z\right)$ and $\boldsymbol{\sigma} = (\sigma^X, \sigma^Y, \sigma^Z)$, where σ^X, σ^Y, and σ^Z are the Pauli matrices

when written in the $|g\rangle$, $|e\rangle$ basis as

$$\sigma^X = \begin{pmatrix} 0 & 1 \\ 1 & 0 \end{pmatrix} = |e\rangle\langle g| + |g\rangle\langle e| \tag{5.20}$$

$$\sigma^Y = \begin{pmatrix} 0 & -i \\ i & 0 \end{pmatrix} = (|e\rangle\langle g| - |g\rangle\langle e|)/i \tag{5.21}$$

$$\sigma^Z = \begin{pmatrix} 1 & 0 \\ 0 & -1 \end{pmatrix} = |e\rangle\langle e| - |g\rangle\langle g| \tag{5.22}$$

The different components of the spin-1/2 operator can therefore be written as

$$\hat{S}^X = \sum_{j=1}^{N} \hat{S}^X_{n_{x_j}} = \sum_{j=1}^{N} (\hat{c}^\dagger_{e,n_{x_j}} \hat{c}_{g,n_{x_j}} + \hat{c}^\dagger_{g,n_{x_j}} \hat{c}_{e,n_{x_j}})/2 \tag{5.23}$$

$$\hat{S}^Y = \sum_{j=1}^{N} \hat{S}^Y_{n_{y_j}} = \sum_{j=1}^{N} (\hat{c}^\dagger_{e,n_{y_j}} \hat{c}_{g,n_{y_j}} - \hat{c}^\dagger_{g,n_{y_j}} \hat{c}_{e,n_{y_j}})/(2i) \tag{5.24}$$

$$\hat{S}^Z = \sum_{j=1}^{N} \hat{S}^Z_{n_{z_j}} = \sum_{j=1}^{N} (\hat{c}^\dagger_{e,n_{z_j}} \hat{c}_{e,n_{z_j}} - \hat{c}^\dagger_{g,n_{z_j}} \hat{c}_{g,n_{z_j}})/2 \tag{5.25}$$

The full spin Hamiltonian 5.1 can now be re-written in the rotating frame, using these spin operaotrs, as

$$\begin{aligned} \hat{H} = &-\delta \sum_{j=1}^{N} \hat{S}^Z_{\mathbf{n}_j} - \sum_{j=1}^{N} \Omega_{\mathbf{n}_j} \hat{S}^Y_{\mathbf{n}_j} + \sum_{j \neq k}^{N} \xi_{\mathbf{n}_j \mathbf{n}_k} \hat{\mathbf{S}}_{\mathbf{n}_j} \cdot \hat{\mathbf{S}}_{\mathbf{n}_k} + \chi_{\mathbf{n}_j \mathbf{n}_k} \hat{S}^Z_{\mathbf{n}_j} \hat{S}^Z_{\mathbf{n}_k} \\ &+ \sum_{j \neq k}^{N} \frac{C_{\mathbf{n}_j \mathbf{n}_k}}{2} \left(\hat{S}^Z_{\mathbf{n}_j} I_{\mathbf{n}_k} + \hat{S}^Z_{\mathbf{n}_k} I_{\mathbf{n}_j} \right) + \frac{K_{\mathbf{n}_j \mathbf{n}_k}}{4} I_{\mathbf{n}_j} I_{\mathbf{n}_k} \end{aligned} \tag{5.26}$$

where $I_{\mathbf{n}_j} = \sum_{\alpha,\beta} \hat{c}^\dagger_{\alpha,\mathbf{n}_j} \hat{c}_{\beta,\mathbf{n}_k}$ is the identity operator. The coefficients of the interaction terms can be written as

$$\xi^+_{\mathbf{n}_j \mathbf{n}_k} = \frac{V^{eg}_{\mathbf{n}_j \mathbf{n}_k} - U^{eg}_{\mathbf{n}_j \mathbf{n}_k}}{2} \tag{5.27}$$

$$\chi^+_{\mathbf{n}_j \mathbf{n}_k} = \frac{V^{ee}_{\mathbf{n}_j \mathbf{n}_k} + V^{gg}_{\mathbf{n}_j \mathbf{n}_k} - 2V^{eg}_{\mathbf{n}_j \mathbf{n}_k}}{2} \tag{5.28}$$

$$C^+_{\mathbf{n}_j \mathbf{n}_k} = \frac{V^{ee}_{\mathbf{n}_j \mathbf{n}_k} - V^{gg}_{\mathbf{n}_j \mathbf{n}_k}}{2} \tag{5.29}$$

$$K^+_{\mathbf{n}_j \mathbf{n}_k} = \frac{V^{ee}_{\mathbf{n}_j \mathbf{n}_k} + V^{gg}_{\mathbf{n}_j \mathbf{n}_k} + V^{eg}_{\mathbf{n}_j \mathbf{n}_k} + U^{eg}_{\mathbf{n}_j \mathbf{n}_k}}{2} \tag{5.30}$$

where

$$V^{\alpha\beta}_{\mathbf{n}_j\mathbf{n}_k} = v^{\alpha\beta} P_{\mathbf{n_1},\mathbf{n_2},\mathbf{n_2},\mathbf{n_1}} \equiv v^{\alpha\beta} P_{\mathbf{n_1},\mathbf{n_2}} \tag{5.31}$$

$$U^{eg}_{\mathbf{n}_j\mathbf{n}_k} = uS_{\mathbf{n_1},\mathbf{n_2},\mathbf{n_2},\mathbf{n_1}} \equiv uS_{\mathbf{n_1},\mathbf{n_2}} \tag{5.32}$$

capture the temperature dependence of the interactions.

5.3.1 Collective Spin Model

The spin Hamiltonian in Eq. 5.26 can be simplified further as we can replace the interaction parameters by their mode-averaged values due to only a weak dependence of the interaction parameters on the mode. We can also write the when the atoms are initially prepared in the totally symmetric Dicke manifold [87]. The collective spin operator can then be written as $\hat{\mathbf{S}}^{\tau=X,Y,Z} = \sum_{j=1}^{N} \hat{\mathbf{S}}^{\tau}_{\mathbf{n}_j}$. The atoms will remain in the symmetric Dicke manifold because due to the energy gap $\xi_{\mathbf{n}_j}$ which suppresses transitions between the Dicke manifolds[1] . This is the only term that has a contribution from s-wave interactions. In general, the s-wave terms will dominate due to the fact that p-wave collisions are suppressed by the centrifugal barrier.

We can now write our collective spin Hamiltonian as

$$\hat{H}/\hbar = -\delta\hat{S}^Z - \Omega\hat{S}^Y + \xi^+\hat{\mathbf{S}}\cdot\hat{\mathbf{S}} + \chi^+\left(\hat{S}^Z\right)^2 + C^+(N-1)\hat{S}^Z \tag{5.33}$$

5.4 Interaction Parameters

In order to gain more of a physical understanding of the spin model we will here consider in more detail what some of the interaction coefficients represent.

5.4.1 χ^+ - Promoting one atom from $|g\rangle$ to $|e\rangle$

To understand physically the meaning of the χ^+ term in the interaction Hamiltonian it is useful to consider an example. Let us consider the case where initially there is a total atom number

[1] In other work ξ^+ is denoted as $J^\perp$

N_T with N atoms in $|e\rangle$ and $(N_T - N)$ atoms in $|g\rangle$. We now want to consider what is the energy change when we excite one of the atoms from $|g\rangle$ to $|e\rangle$ to give $(N+1)$ atoms in $|e\rangle$ and (N_T-1-N) atoms in $|g\rangle$. This change in energy when promoting one atom from $|g\rangle$ to $|e\rangle$ is given by

$$\begin{aligned}\Delta E &= NV_{ee} + (N_T - 1 - N)V_{eg}^{+} - (N_T - 1 - N)V_{gg} - NV_{eg}^{+} \\ &= N(V_{ee} + V_{gg} - 2V_{eg}^{+}) + (N_T - 1)(V_{eg}^{+} - V_{gg}) \\ &= N(V_{ee} + V_{gg} - 2V_{eg}^{+}) + Constant\end{aligned} \tag{5.34}$$

This can be understood as the atom that was initially in $|g\rangle$ and interacted with the other $(N_T - 1 - N)$ atoms in $|g\rangle$ atoms via V_{gg} interactions. This interaction is now no longer present. The atom also used to interact with the N atoms in $|e\rangle$ via V_{eg}^{+} interactions and this interaction is also no longer present. The extra atom in $|e\rangle$ now has V_{ee} interactions with the N other atoms in $|e\rangle$ and V_{eg}^{+} interactions with the (N_T-1-N) atoms left in $|g\rangle$. So χ^{+} therefore represents the change in energy when one atom is excited from $|g\rangle$ to $|e\rangle$.

5.4.2 ξ^{+} - The exchange interaction

As shown above the ξ^{+} term corresponds to an exchange interaction. It represents that there is a difference in energy between the triplet and the singlet states. As mentioned above the atoms are initialized in the fully symmetric $|J, -J\rangle$ state (all atoms in $|g\rangle$). After a homogeneous laser excitation the atoms will still remain in the triplet manifold. The coupling between this $S = N/2$ amnifold and the $S = N/2 - 1$ manifold is prevented by an energy gap $\xi^{+}\hat{\mathbf{S}} \cdot \hat{\mathbf{S}}$. The different manifolds are connected by 2-body *ee* losses but atoms still remain in the fully symmetric state. The energy offset between the two manifolds is due to the difference in energy between the $|S = 1, m = 1\rangle$ and $|S = 1, m = 0\rangle$ states we can write the offset as

$$\xi^{+} \propto V_{eg}^{+} - U_{eg}^{-} \tag{5.35}$$

5.5 Temperature Dependence of Interactions

The thermally averaged two-body interactions are given by

$$U_{eg}^{-} = \left\langle U_{\mathbf{n}_j\mathbf{n}_k}^{eg} \right\rangle = 4\sqrt{2\pi}\sqrt{\omega_R\omega_z}\frac{a_{eg}^{-}}{a_r}\left\langle s_{\mathbf{n}_j\mathbf{n}_k}\right\rangle^2 \tag{5.36}$$

$$V_{\alpha\beta} = \left\langle V_{\mathbf{n}_j\mathbf{n}_k}^{\alpha\beta} \right\rangle = 6\sqrt{2\pi}\sqrt{\omega_z\omega_R}\frac{b_{\alpha\beta}^3}{a_r^3}2\left\langle s_{\mathbf{n}_j\mathbf{n}_k}\right\rangle\left\langle p_{\mathbf{n}_j\mathbf{n}_k}\right\rangle \tag{5.37}$$

For our 2D pancake shaped traps where the trap volume is proportional to the radial temperature and the temperature dependence of the s- and p- terms is found numerically to be [89]

$$\left\langle s_{\mathbf{n}_j\mathbf{n}_k}\right\rangle = \frac{0.281}{\widetilde{T}_r^{0.498}} \tag{5.38}$$

$$\left\langle p_{\mathbf{n}_j\mathbf{n}_k}\right\rangle = 0.564\widetilde{T}_r^{0.499} \tag{5.39}$$

where $\widetilde{T}_r$ is the radial temperature in the effective harmonic oscillator units. We can see that for the 2D traps the p-wave interactions, $V_{\alpha\beta}$, are temperature independent and the s-wave interaction term, U_{eg}^{-} depends on temperature as $1/\widetilde{T}_r$.

5.6 Extensions to the Spin Model

This model can be extended for the case of particles in different spin states which is discussed in section 6.2.1. For the case of the experiment discussed in chapter 7, the only difference between the experimental conditions discussed in this chapter and chapter 7 is the lattice depth. The derivation discussed in this chapter assumes that the atoms are trapped in a deep lattice which means we can make the assumption that the axial wavefunction is the ground state of a harmonic oscillator.

Chapter 6

Spectroscopic Observation of SU($\mathcal{N}$) physics

6.1 Introduction

Symmetries play a fundamental role in the laws of nature. A prominent example is the SU(3) symmetry of quantum chromodynamics, which governs the behavior of quarks and gluons. When generalized to large $\mathcal{N}$, SU($\mathcal{N}$) is expected to generate exotic many-body behaviors emerging from the increased degeneracy and strict conservation laws. Owing to the strong decoupling between the electronic-orbital and nuclear-spin degrees of freedom [90, 91], alkaline-earth (-like) atoms, prepared in the two lowest electronic states (clock states with zero electronic angular momenta), are predicted to exhibit nuclear spin (I) independence for their interatomic collisional parameters. This property directly leads to a SU($\mathcal{N} \leq 2I + 1$) symmetry for the interaction physics [92, 93, 94, 95]. Thanks to this symmetry, in addition to their use as ideal time keepers [21] and quantum information processors [96, 97, 98, 99], alkaline earth atoms are emerging as a unique platform for the investigation of high-energy lattice gauge theories [100], for testing orbital models used to describe transition metal oxides, heavy fermion compounds, and spin liquid phases [101], and for the observation of exotic topological phases [95, 102]. Progress towards these goals includes the production of quantum degenerate alkaline-earth gases [103, 104, 105], imaging of individual spin components [106], control of interactions [104, 107, 108], and study of many-body spin dynamics [15].

Before this work, only indirect evidence for SU($\mathcal{N}$) symmetry exists[1] , including inference

[1] After completion of this work we also became aware of two other works [109, 110]

from suppressed nuclear spin-relaxation rates [106], reduced temperatures in a Mott insulator for increased number of spin states [111], and the changing character of a strongly-interacting one-dimensional fermionic system as a function of $\mathcal{N}$ [112]. Furthermore, these observations are limited to the electronic ground state. The corresponding ground-state s-wave scattering parameter, a_{gg}, has been determined from photo-association [113] and rovibrational spectroscopy [114], but the excited state-related scattering parameters remain unknown.

In this chapter, we report a spectroscopic observation of SU($\mathcal{N}$) symmetry and two-orbital SU($\mathcal{N}$) magnetism in an ensemble of fermionic ^{87}Sr atoms at μK temperatures and confined in an array of two-dimensional (2D) disc-shaped, state-insensitive optical traps [115]. The trapping potentials are approximately harmonic, with the axial (z) trapping frequency $\nu_z \sim 80$ kHz and the radial ($x-y$) frequency ν_R of ~ 600 Hz; the slight anharmonicity makes the spacings between the energy levels uneven. Axial and radial degrees of freedom are decoupled during the initial lattice loading and cooling. Under typical temperatures ($1\ \mu\text{K} < T_R < 7\mu\text{K}$, $T_z \sim\ 2\mu$ K), atoms are cooled to the motional ground state along the z direction. In contrast, the radial modes are thermally populated. The SU($\mathcal{N}$) symmetric spin degree of freedom is encoded in the 10 nuclear spin states with quantum number m_I (Fig. 6.1(a)), and the pseudo-spin 1/2 orbital degree of freedom in the two lowest electronic (clock) states (^{1}S$_0$ and ^{3}P$_0$, henceforth $|g\rangle$ and $|e\rangle$, respectively). Under typical atomic occupancies (≤ 20 atoms per disc), temperatures and trap volume ($\propto T_R$), the mean interaction energy per particle is at least two orders of magnitude smaller than the single-particle vibrational spacing along any direction. The spectral resolution available with a laser of 1×10^{-16} stability [116] enables us to accurately probe these interactions while addressing individual nuclear spin levels.

6.1.1 Chapter Outline

In section 6.2 we will start by describing the different interactions that can take place between either two atoms in the same nuclear spin state or two atoms in different nuclear spin states. We will extend the theory model of Chapter 5 to include the case of spin mixtures. In section 6.4 we

will discuss the frequency shifts and how they manifest for both spin polarized atomic samples and spin mixtures where we will show the atoms to be SU($\mathcal{N}$) symmetric to the 3% level in section 6.5. From our measurements we will then determine the different scattering parameters 6.6. In section 6.7 we will then discuss the dynamics via measurements of the contrast for both a nuclear spin polarized sample of atoms and a nuclear spin mixture.

6.2 SU($\mathcal{N}$) spin-orbital Hamiltonian in an energy space lattice

Under our operating conditions the atomic interactions are insufficiently energetic to transfer atoms between the initially populated, slightly anharmonic motional eigenmodes, as discussed in Chapter 5. To the first order approximation atoms remain frozen in these quantized motional levels and the quantum dynamics takes place only in the internal degrees of freedom (spin and orbital) [15, 87, 117], in a way analogous to localized atoms in real-space lattice trapping potentials. This approximation greatly simplifies the modeling of our system. Here, the large energy gap between the interaction energy and the single-particle vibrational spacing, along with the anharmonicity and non-separability of the optical trapping potential provided by the Gaussian laser beam profile, lead to an energetic suppression of mode-changing collisions. Moreover, the s-wave and p-wave (Fig. 6.1(b)) interactions, which are responsible for the dynamics, provide nonlocal interactions when viewed within the energy-space lattice as they couple atoms without being overly sensitive to the thermally populated motional levels. The decoupling between motional and internal degrees of freedom combined with the sub-Hertz spectral resolution of the stable laser allows us to probe spin lattice models with effective long-range couplings in a non-degenerate Fermi gas, as schematically illustrated in Fig. 6.1(c). This system thus paves the way for study of quantum orbital magnetism beyond the ultra-cold regime.

Spin models with long-range interactions have been implemented in dipolar gases [118] or trapped ionic systems [119], but our system is further enriched by SU($\mathcal{N}$) symmetry and holds potential for addressing important open questions on many-body dynamics in spin-orbital models under the co-presence of large degeneracy [101, 120, 121] and long-range interactions. By per-

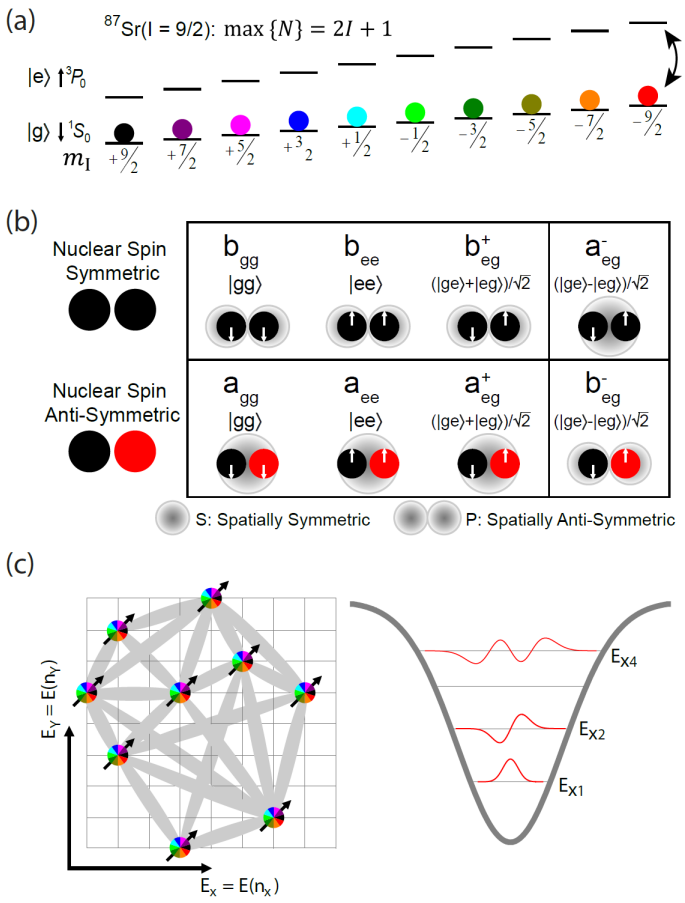

Figure 6.1: Diagram of the interacting spin lattice. **(a)** Energy levels for the two lowest electronic states ($^1S_0$ and $^3P_0$) of ^{87}Sr atoms in a magnetic field, each with ten nuclear spin states, depicted by colors. This color scheme is used throughout this chapter to denote the interrogated state. **(b)** Interactions between two fermionic atoms characterized by four s-wave ("a") and four p-wave ("b") elastic scattering parameters. The interactions are governed by symmetries in motional states (bottom labels), nuclear spins (left labels), and electronic orbitals (white arrows). **(c)** (Left panel) Schematics of the interacting electronic orbitals (spin-1/2 arrows) distributed over a lattice spanned by motional eigenenergies. In our system, the energy levels are populated according to a Boltzmann distribution and the energy spacings are slightly anharmonic; the latter is crucial for freezing atoms in their initially populated motional modes. For simplicity neither the anharmonic lattice spacing, nor the Boltzmann population of modes are reflected in the figure. The shaded connections illustrate the long-range nature of the interactions in energy space. In our theoretical approach, those interactions are calculated using the matrix element overlap of the corresponding modes. To the first order approximation, p-wave interactions can be treated collectively and can be assumed to be of all-to-all type. Thus, we can replace the values of the coupling constants with their thermal averages (27). Colored circles show the possibility of preparing statistical mixtures of $\mathcal{N}$ nuclear spin states. (Right panel) Illustration of a few occupied eigenmodes in our optical trap formed by a Gaussian beam.

forming Ramsey spectroscopy with various nuclear spin mixtures, we determine the nuclear spin independence of the s-wave and p-wave interactions. Furthermore, we probe the non-equilibrium dynamics of the orbital coherence, and the results are well reproduced by a two-orbital SU($\mathcal{N}$) spin lattice model in quantized motional eigenenergy space.

Interactions between two ^{87}Sr atoms are governed by Fermi statistics with an overall wave-function antisymmetrization under exchange in the motional, electronic, and nuclear spin degrees of freedom (Fig. 6.1(b)). Consider a pair of interacting atoms (j and k) occupying two of the quantized eigenmodes of the trapping potential, n_j and n_k. If the atoms are in a nuclear spin symmetric state they experience s-wave interactions only if their electronic state is anti-symmetric: $(|eg\rangle - |ge\rangle)/\sqrt{2}$. We denote the elastic scattering length characterizing those collisions as a_{eg}^{-}. They can collide via p-wave interactions in three possible electronic symmetric configurations $\{|gg\rangle, |ee\rangle, (|eg\rangle + |ge\rangle)/\sqrt{2}\}$, corresponding to the p-wave elastic scattering lengths $b_{gg}, b_{ee}, b_{eg}^{+}$, respectively. In contrast, if the two atoms are in an anti-symmetric nuclear spin configuration they experience s-wave collisions under these three electronic symmetric configurations, with the corresponding scattering lengths $a_{gg}, a_{ee}, a_{eg}^{+}$, respectively. Similarly, p-wave interactions occur in $(|eg\rangle - |ge\rangle)/\sqrt{2}$, corresponding to the scattering length b_{eg}^{-}. These eight parameters characterize elastic collisions at ultralow temperatures, and SU($\mathcal{N}$) symmetry predicts them to be independent of the nuclear spin configuration.

6.2.1 Expansion of the Spin Hamiltonian - Spin Mixtures

To understand the interactions of spin mixtures we can expand upon the model discussed in chapter 5 to now include the nuclear spin. Similar to the spin operators in Eq. 5.19 we introduce the spin-orbital operators

$$\mathbf{T}_j = \frac{1}{2} \sum_{\alpha,\beta m} \hat{c}_{\alpha m \mathbf{n}_j} \boldsymbol{\sigma}_{\alpha\beta} \hat{c}_{\beta m \mathbf{n}_j} \tag{6.1}$$

and the nuclear-spin permutation operators

$$S_n^m(j) = \sum_{\alpha=e,g} \hat{c}^\dagger_{\alpha n \mathbf{n}_j} \hat{c}_{\alpha m \mathbf{n}_j} \tag{6.2}$$

where $\hat{c}^\dagger_{\alpha m \mathbf{n}_j}$ ($\hat{c}_{\alpha m \mathbf{n}_j}$) creates (annihilates) a fermion in the mode $\mathbf{n}_j$, in electronic state $\alpha \in e, g$ and with a nuclear spin $m = 1, 2..., N \leq 2I + 1$. The nuclear-spin permutation operators satisfy the SU(N) algebra $[S_n^m(j), S_p^q(k)] = \delta_{j,k}(\delta_{m,p} S_n^q(j) - \delta_{n,q} S_p^m(j))$ and generate SU(N) rotations of nuclear spins. We can now expand the field operators $\hat{\Psi}^\dagger_{\alpha m}(\mathbf{R}) = \phi_0^z(z) \sum_{\mathbf{n}} \hat{c}^\dagger_{\alpha m \mathbf{n}_j} \phi_{n_X} \phi_{n_Y}$.

The Hamiltonian that governs the interactions, between atoms j and k, can be written as:

$$\hat{H}_{j,k} = \hat{\mathcal{P}}^+ \hat{H}^+ + \hat{\mathcal{P}}^- \hat{H}^- \tag{6.3}$$

$$\hat{H}^\pm = \xi^\pm_{j,k} \mathbf{T}_j \cdot \mathbf{T}_k + \chi^\pm_{j,k} \hat{T}^Z_j \hat{T}^Z_k + C^\pm_{j,k} \left(\frac{\hat{T}^Z_j + \hat{T}^Z_k}{2} \right) + K^\pm_{j,k} \mathbf{I} \tag{6.4}$$

Here, $\mathbf{I}$ is the identity matrix, $\hat{\mathcal{P}}^\pm = \frac{[\mathbf{I} \pm \sum_{n,m=1}^N \hat{S}_n^m(j) \hat{S}_m^n(k)]}{2}$ are nuclear spin projector operators into the symmetric triplets $(+)$ and anti-symmetric singlet $(-)$ nuclear spin states, respectively. The spin triplet projection operator, $\hat{\mathcal{P}}^+$, has an eigenvalue 1 when applied to a nuclear spin triplet state and 0 when applied to a nuclear spin singlet state. Similarly the nuclear spin singlet projection operator, $\hat{\mathcal{P}}^-$, has an eigenvalue 1 when applied to a nuclear spin singlet state and 0 when applied to a nuclear spin triplet one. Equation 6.3 therefore states that if the nuclear spin of the atoms is in $(+)$ or $(-)$, then they interact according to $\hat{H}^+$ or $\hat{H}^-$, respectively. The coupling constants $\xi^\pm_{j,k}, \chi^\pm_{j,k}, C^\pm_{j,k}, K^\pm_{j,k}$ depend on the scattering parameters, a_η and b_η, $\eta \in \{ee, gg, eg^+, eg^-\}$, and the wavefunction overlap of the j and k-atoms radial vibrational modes in the 2D traps.

The total spin-orbital interaction Hamiltonian is the sum over all pairs of atoms, $\hat{H}^{SO} = 1/2 \sum_{j \neq k} \hat{H}_{j,k}$, and commutes with all the SU($\mathcal{N}$) generators, $S_n^m(j)$. For the case of spin-polarized fermions the Hamiltonian reduces to 5.26. The spin-orbital Hamiltonian, $\hat{H}^{SO}$, is thus invariant under transformations from the SU($\mathcal{N}$) group (i.e., SU($\mathcal{N}$) symmetric). This implies that the number of atoms in each of the nuclear spin sublevels is conserved. The $\mathcal{N}$ is chosen by the initial state preparation of the nuclear spin distribution and can vary from 1 to $2I + 1 = 10$ in ^{87}Sr ($I = 9/2$). In this experiment we control $\mathcal{N}$ via optical pumping through another electronic state.

In addition to elastic interactions, ^{87}Sr atoms exhibit inelastic collisions. Among those however, only the $e-e$ ones have been observed to give rise to measureable losses [122]; we denote these two inelastic scattering lengths as γ_{ee} and β_{ee} for s-wave and p-wave, respectively. We set other inelastic parameters to zero based on their negligible contributions in measurements [122].

6.3 Ramsey Spectroscopy

To understand the density shift and contrast measurements undertaken in this chapter we must first look at Ramsey spectroscopy which is used to measure both of these observables. Ramsey spectroscopy can be understood in a Bloch sphere picture (see Fig. 6.2) where we consider the two poles of the Bloch sphere to be our two spin states $|g\rangle$ and $|e\rangle$. We can first consider Ramsey spectroscopy more generally for a single group of atoms, that are not interacting with each other. The atoms are initially prepared in $|g\rangle$ and an initial clock pulse, with detuning δ, rotates the Bloch vector around the $\hat{Y}$ axis of the Bloch sphere and creates a superposition of the two clock states. Here let us assume that an equal superposition of the two states is created which is to say the initial pulse has an area of $\theta_1 = \pi/2$. In the rotating frame of the laser, the atom will then evolve around the Bloch sphere with a rate proportional to the detuning between the atom and the laser.

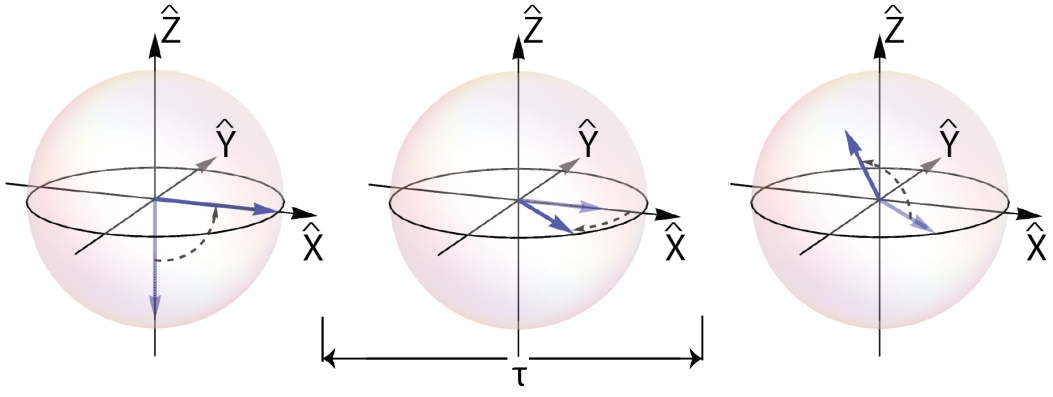

Figure 6.2: Ramsey Spectroscopy on the Bloch Sphere. An initial $\pi/2$ pulse creates a superposition of $|g\rangle$ and $|e\rangle$. During the dark time τ the atom evolves around the Bloch sphere at a rate proportional to the detuning between the laser and the atom resonance. A second $\pi/2$ pulse projects the atoms into the population of $|g\rangle$ and $|e\rangle$

A second laser pulse after a time τ, with an area $\theta_2 = \pi/2$, also around $\hat{Y}$ then rotates the Bloch vector to have a projection along the $\hat{Z}$ which can be measured as a population difference between the two clock states. By repeating this experiment many times and varying the phase difference between the two pulses the projection of the atoms will show an oscillatory behavior where the amplitude of the oscillations is known as the fringe contrast and is the projection of the length of the Bloch sphere in the $\hat{X} - \hat{Y}$ plane. When interactions are introduced, during the dark time τ the atoms will accumulate a phase shift around the Bloch sphere with respect to the case of a non-interacting sample. It is this phase shift that we refer to as a density dependent frequency shift

6.4 Density-dependent frequency shift for nuclear spin mixtures

We first test SU($\mathcal{N}$) symmetry in a two-orbital system by measuring the density-dependent frequency shift of the clock transition under various nuclear spin population distributions. We use a Ramsey sequence to measure interactions [15] under an external magnetic field that produces Zeeman splittings much larger than the interaction energy. The sequence starts with all atoms in $|g\rangle$. Only atoms in a particular nuclear spin state are coherently excited and interrogated, whereas atoms in other states (spectators) remain in $|g\rangle$. We denote the number of interrogated atoms by N_i^{tot}, the number of spectator atoms by N_S^{tot}, and define a population ratio $f = N_S^{tot}/N_i^{tot}$ and the interrogated fraction $x_i = N_i^{tot}/(N_i^{tot} + N_S^{tot})$. We control orbital excitation fraction, p_e, by varying the initial pulse area, θ_1, where $0 < \theta_1 < \pi$. After a free evolution time, $\tau = 80$ ms, the second pulse of area $\theta_2 = \pi/2$ is applied for subsequent readout of the electronic orbital distributions. The resonance frequency shift is recorded as a function of the atomic number in the trap, which can be varied in a controlled manner. We operate with highly homogeneous atom-laser coupling such that the orbital excitation is the same for all interrogated atoms. Consequently, in a fully spin-polarized sample, the s-wave interactions are suppressed and the p-wave interactions dominate the free evolution dynamics [15]. The s-wave interactions are allowed only when spectator atoms populate other nuclear spin states. The existence of SU($\mathcal{N}$) symmetry in the scattering parameters

results in an independence of the density shift with respect to both the interrogated nuclear spin state and the distribution of spectator atoms among the various spin components. Moreover, in the presence of a large magnetic field (which energetically suppresses excitation of the spectator atoms), the density shift should be only a function of N_i^{tot}, p_e, and N_S^{tot}.

In Fig. 6.3(a), we compare the fully spin-polarized case ($m_I = +9/2$) against three other scenarios with different spin mixtures under $T_R = 6 - 7\,\mu$K. The observed density shifts as a linear function of p_e, when scaled to the same number of interrogated atoms ($N_i^{tot} = 4000$), show three features: **(I)** the linear slope, l, depends only on N_i^{tot}, **(II)** the offset with respect to the polarized case increases linearly with f, and **(III)** both l and the offset are independent of how the atoms are distributed in the nuclear spin levels. The last point is verified, for example, by measuring the same shifts when interrogating 29% of the total population in either $+9/2$ or $+7/2$.

6.5 Temperature-dependent SU($\mathcal{N}$)-symmetric interactions

To determine the temperature dependence for the density shift and for additional confirmation of the observed nuclear spin independence, we interrogate other nuclear spin states, $-9/2$ or $-3/2$, at a lower $T_R \sim 2\,\mu$K, when the distribution across all spin states is nearly even (Fig. 6.3(b)). The measured density shifts scaled to $N_i^{tot} = 4000$ are again similar to each other, providing further direct experimental evidence for SU($N = 10$) symmetry. At this lower T_R, the slope still depends only on N_i^{tot}, but there is a smaller offset of the density shift relative to the polarized case when x_i varies. To quantify the T_R dependence, we plot together all measured ratios, l/l_0, where l_0 is the linear slope for the polarized case. We see that **(IV)** the ratios collapse into a single value independently of f and T_R for fixed N_i^{tot}, yielding $l/l_0 = 1.00 \pm 0.03$ (Fig. 6.4(a)). This result agrees well with the SU($\mathcal{N}$)-predicted ratio of unity and verifies this symmetry to the 3% level.

We emphasize that the test of SU($\mathcal{N}$) symmetry (at the 3% level) is based directly on the measured interactions that are independent of nuclear spin configurations, and it does not require accurate knowledge of some common-mode system calibrations. For quantum simulations of SU($\mathcal{N}$) physics, it is important to precisely test this symmetry to a level much below all relevant energy

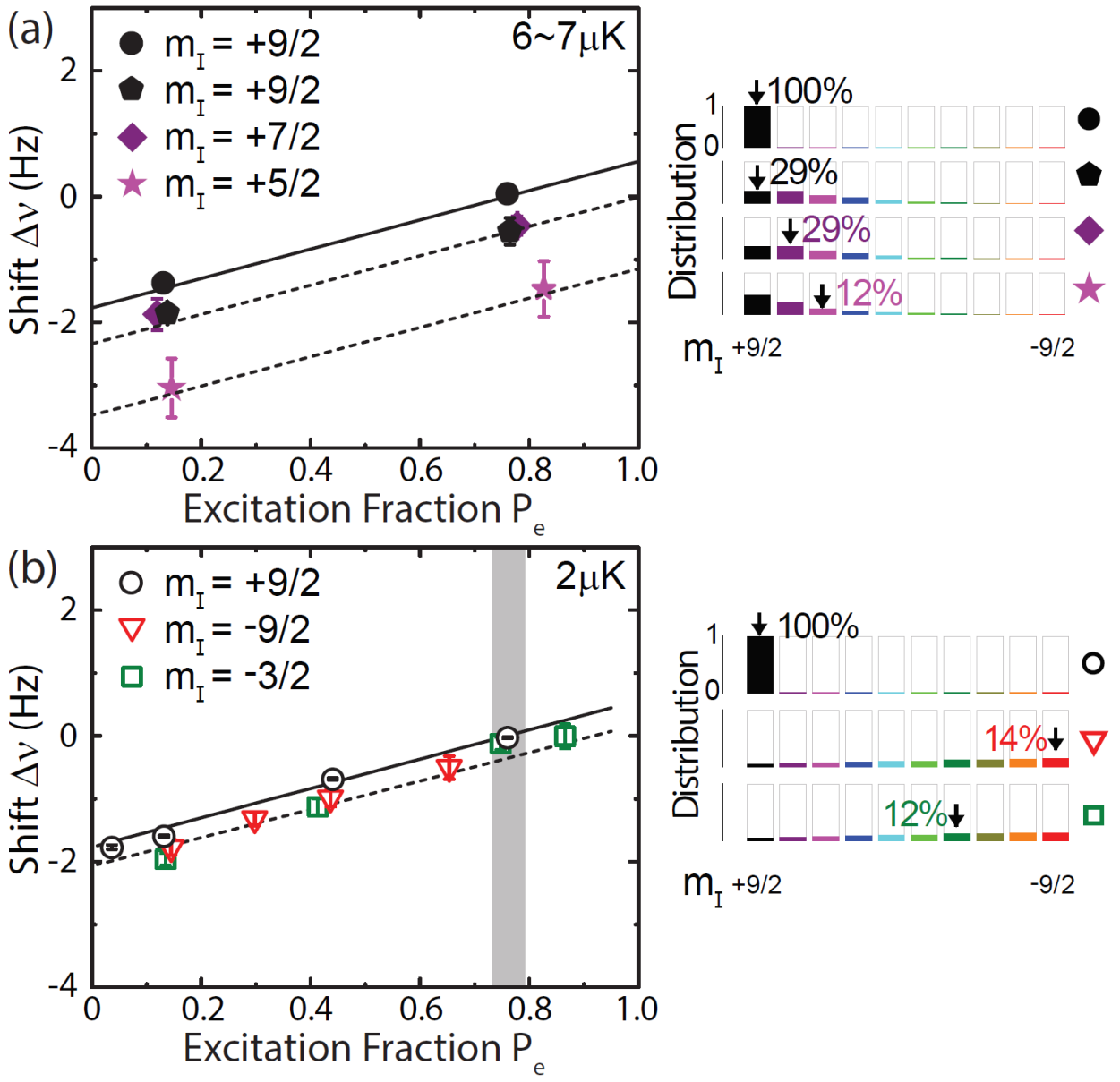

Figure 6.3: **(a)** and **(b)** (Left) Measured density shifts (symbols) and for different nuclear spin configurations at **(a)** $T_R = 6 - 7\,\mu$K and **(b)** $\sim 2\,\mu$K. (Right) Illustration of the interrogated states (black arrows) and population distributions among various nuclear spin states. For consistency, the shifts are scaled for $N_i^{tot} = 4000$. The solid and dotted lines show theory calculations for the corresponding x_i and T_R as indicated in the plots, with b_{eg}^- and a_{eg}^-. The gray band in **(b)** corresponds to p_{e0}^*, the excitation fraction for zero density shift in a polarized sample. The spectator atoms generate a temperature-dependent density shift, which is independent of p_e of the interrogated atoms and thus manifests as a net offset from the purely polarized density shift.

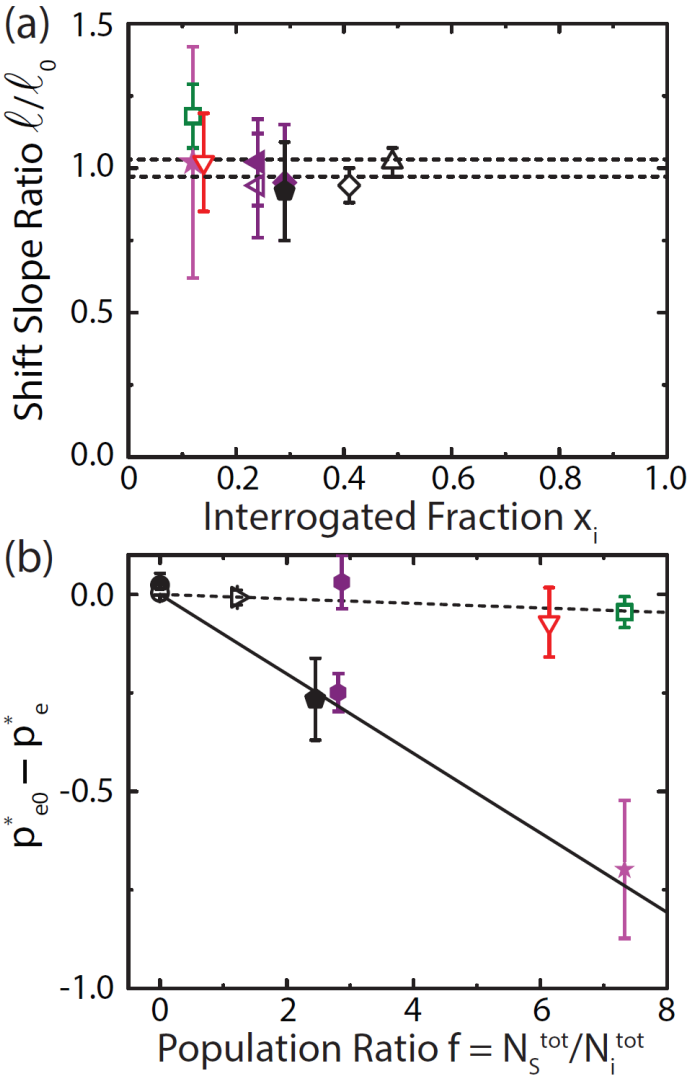

Figure 6.4: **(a)** Ratio of the slope of the frequency shift between the spin mixed and polarized samples. The dotted lines represent the standard error. **(b)** The difference in the zero-shift excitation fraction between the spin-mixed and polarized samples. The solid and dashed lines are theory fits used to determine b_{eg}^- and consequently a_{eg}^- by the analytic relations between s- and p-wave scattering parameters (see Supplementary Materials). In **(a)** and **(b)**, two values of T_R are used: 2.3(2) μK (open symbols) and 6.5(4) μK (filled symbols). In addition to conditions used for Fig. 6.3, other spin configurations are studied: open up triangles ($x_i = 49\%$), open diamond (41%), open right triangles (46%), open and filled hexagons (26%), open and filled left triangles (24%), filled pentagons (29%), and filled stars (12%).

scales. Although our measurement uncertainty (3%) has not reached the ultimate theoretical prediction (0.1%) resulting from a small admixture of the $^3P_0$ state with higher lying P states with finite electronic angular momenta [90, 91, 92], it is already sufficient for realizing a SU($\mathcal{N}$)-symmetric, unity-filling spin lattice system. Further reduction in our experimental uncertainty can be achieved by enhancing the measurement precision with improved laser stability. We observe that l decreases only by 10% when T_R is raised from $2\,\mu$K to $6\,\mu$K, verifying its insensitivity to T_R.

We also determine the excitation fraction where the shift is zero for a spin mixture, p_e^*, and compare it to that of a polarized sample, p_{e0}^* (gray band, Fig. 6.3(b)), for various interrogated spin states (colors in Fig. 6.4(b)). The difference shows the following features: **(V)** it collapses onto a single line (for a given T_R of either 2.3 or $6.5\,\mu$K) as a function of f, which provides further evidence for the spin-independence of the interactions; **(VI)** at $N_S^{tot} = 0$ (fully polarized), the two lines cross each other at the origin, as expected from the T_R-insensitivity of the p-wave interactions. The proportionality constant of $(p_{e0}^* - p_e^*)$ to f is finite for $6.5\,\mu$K (lower line), and decreases to almost zero for $T_R \sim 2.3\,\mu$K (upper line). This near zero proportionality constant for $T_R \sim 2.3\,\mu$K reflects an accidental cancellation of the spectators s- and p-wave interaction effects at this temperature.

6.6 Experimental-theory agreement and determination of the scattering parameters

In the presence of a large external magnetic field that produces differential Zeeman splittings much larger than the interaction energy, those terms in the Hamiltonian that exchange the population between the occupied spin-orbital levels are energetically suppressed and the populations of different spin-orbital levels are conserved. Hence, the Hamiltonian is dominated by Ising-type interactions that preserve the spin-orbital population. In this regime the many-body dynamics for a single trap with N atoms can be captured under a collective approximation that replaces the coupling constants with their corresponding thermal averages, $O^{\pm}_{n_j,n_k} \to O^{\pm}$ [87]. For the experimentally relevant case where only N_i atoms in spin m_I are interrogated and where N_S atoms in the other spin components remain in $|g\rangle$, the effective many-body Hamiltonian

Table 6.1: s- and p-wave scattering lengths in units of the Bohr radius

Channel	s-wave	p-wave		Determination Method
gg	96.2(1)	74.6(4)	s-wave	Two photon-associative spectroscopy(23) and rovibrational spectroscopy(24)
			p-wave	Analytic relation between s-wave and p-wave parameters (34)
eg^+	169(8)	-169(23)	s-wave	Analytic relation (34)
			p-wave	Density shift in a polarized sample (20)
eg^-	68(22)	-42^{+103}_{-22}	s-wave	Density shift in a spin mixture at different temperatures (this work)
			p-wave	Analytic relation
ee (elastic)	176(11)	-119(18)	s-wave	Analytic relation (34)
			p-wave	Density shift in a polarized sample (20)
ee (inelastic)	$\gamma_{ee} = 46^{+19}_{-32}$	$\beta_{ee} = 121(13)$	Both	Two-body loss measurement (33) and analytic relation (34)

during τ simplifies substantially. It consists of two parts, $\hat{H}^{SO} = \hat{H}_i + \hat{H}_S$. The first part, $\hat{H}_i = \chi^+(\hat{T}^Z)^2 + C^+\hat{T}^Z N_i$, describes the p-wave interactions between the interrogated atoms [15, 87], where $\hat{T}^{\alpha=X,Y,Z} = \sum_j^N \hat{S}^{m_I}_{m_I}(j)\hat{T}^{\alpha=X,Y,Z}_j$ are collective orbital operators acting on the N_i interrogated atoms. The density shift induced by these interactions, $\Delta\nu^i = N_i\,(C^+ - \cos(\theta_1)\chi^+)$, with $\chi^+ = \frac{b^3_{ee}+b^3_{gg}-2(b^+_{eg})^3}{2}\langle P\rangle_{T_R}$ and $C^+ = \frac{b^3_{ee}-b^3_{gg}}{2}\langle P\rangle_{T_R}$, depends linearly on the number of excited atoms $N_i p_e$. Here $\langle P\rangle_{T_R}$ corresponds to the thermal average of the p-wave mode overlap coefficients. Assuming a Boltzmann distribution of initially populated radial motional modes, we have $\langle P\rangle_{T_R} \propto (T_R)^0$ (insensitive to T_R) [15]. For a spin polarized sample, the observed density shifts are well reproduced by theory (solid black lines in Figs. 6.3(b) and (c)) based on the same p-wave parameters as determined in [15]. The second part, $\hat{H}_S = N_S\Lambda\hat{T}^Z$, describes the interactions between the interrogated and spectator atoms with both p- and s-wave contributions. The related density shift is $\Delta\nu^S = \Lambda N_S$, with $\Lambda = \frac{C^+ + C^- - \xi^+ - \xi^- - \chi^+ - \chi^-}{2} = \frac{a^+_{eg}+a^-_{eg}-2a_{gg}}{4}\langle S\rangle_{T_R} + \frac{(b^+_{eg})^3+(b^-_{eg})^3-2b^3_{gg}}{4}\langle P\rangle_{T_R}$. The s-wave thermal average, $\langle S\rangle_{T_R}$, decreases with T_R as $\langle S\rangle_{T_R} \propto (T_R)^{-1}$.

This model fully reproduces the experimental observations as summarized in points (**I-VI**) stated in section 6.4 and 6.5, and shown in Fig. 6.3 anf Fig. 6.4. To quantitatively compare with the experiment, we perform a Poissonian average of the atom number across the array of 2D traps

and use the average excitation fraction to account for the two-body $e-e$ losses [15, 122] during τ. The capability of the SU($\mathcal{N}$) spin lattice model to reproduce the experimental observations also enables us to determine the remaining s- and p-wave scattering parameters. For each of the four channels, $\eta \in \{ee, gg, eg^+, eg^-\}$, the s-wave and p-wave parameters relate to each other through the characteristic length, $\bar{a}_\eta$, of the van der Waals potential [123] given by

$$\bar{a}_\eta = \frac{2\pi}{\Gamma(1/4)^2}\left(\frac{2\mu C_6}{\hbar^2}\right)^{1/4}. \tag{6.5}$$

The C_6 coefficients for the $\eta = gg, ee$ and eg channels were found to be 3107(30) a.u., 5360(200) a.u., and 3880(80) a. u., respectively, where a.u.$= E_h a_0^6$, with E_h the Hartree energy and a_0 being the Bohr radius. A multichannel defect theory predicts that, for a single van der Waals potential, η, the complex scattering lengths for the s-wave interactions, $A_\eta = a_\eta - i\gamma_\eta$, and the complex scattering volumes for the p-wave interactions, $B_\eta^3 = b_\eta^3 - i\beta_\eta^3$, are related by the van der Waals length by the relation

$$\frac{A_\eta}{\bar{a}_\eta} = 1 + \left(\frac{B_\eta}{\bar{a}}\right)^3\left[\left(\frac{B_\eta}{\bar{a}}\right)^3 + 2.128\right]^{-1}. \tag{6.6}$$

Thus, after we determine $\bar{a}_\eta$ using the available van der Waals C_6 coefficients, only four elastic scattering parameters remain independent. Among those,a_{gg}, b_{ee}, b_{eg}^+ (and thus their respective p- or s-wave counterparts) are known [15], leaving only one unknown parameter associated with the eg- channel. Using the theoretical predictions and a single parameter to fit the data in Fig. 6.4(b), we extract a_{eg}^- and b_{eg}^-. Table 6.1 lists all the scattering parameters determined from the prior and current measurements.

Recently [124] the s-wave scattering lengths eg^+ and eg^- have been measured in a 3D optical lattice clock. In the eg^+ channel this was measured to be $(161 \pm 1.1)a_0$ and in the eg^- channel this was measured to be $(69.2 \pm 1.0)a_0$, where a_0 is the Bohr radius. The excellent agreement with the values we report here (in Table 6.1) shows us the validity of the analytic relations that were used to determine some of the scattering parameters in this work.

6.7 Coherent dynamic spectroscopy

We perform coherent dynamic spectroscopy to explore the development of many-body correlations as a key effect of Ising orbital magnetism, in the combined orbital and nuclear spin degrees of freedom, generated by the p-wave and s-wave interactions. This allows us to further validate the SU($\mathcal{N}$) spin-orbital model, Eq. 6.3, as a description for our system. The many-body correlations that build up during the free evolution manifest as a decay of the $e-g$ orbital coherence in the form of Ramsey fringe contrast $\mathcal{C}(\tau) = 2/N_i^{tot}\sqrt{\langle \hat{T}^X_{tot}\rangle^2 + \langle \hat{T}^Y_{tot}\rangle^2}$ that we measure as a function of τ. Here $\hat{T}^{X,Y}_{tot}$ is the sum of $\hat{T}^{X,Y}$ over the 2D traps. We extract a normalized $\mathcal{C}$ by comparing the high-atom-number raw contrast against that of the low-atom-number. This normalization removes single-particle decoherence effects. The decay of $\mathcal{C}$ during the free-evolution period has been shown to be a particularly suitable observable for characterizing the role of interactions during the dynamics [125]. For example, contrast measurements in an array of polar molecules pinned in a 3D lattice provided clear signatures of dipolar interactions and their description in terms of a spin exchange model [118, 126].

In the presence of a large magnetic field, the decay of $\mathcal{C}$ has two sources. The first arises from within the interrogated atoms: p-wave elastic interactions, two-body $e-e$ losses, higher-order interaction-induced mode-changing processes, as well as dephasing induced by the distribution of atoms across traps. All these p-wave effects are accounted for in our work using the same p-wave parameters that were determined first in Ref. [15] and then reconfirmed with our density shift measurements in this work (Fig. 6.3). The second source comes from spectators, which act on the interrogated atoms at a given site as an inhomogeneous and density-dependent effective magnetic field along z, with both s- and p-wave contributions. The effective magnetic field is static if the atoms are frozen in their motional states, but can vary with time in the presence of higher-order mode-changing processes. The p-wave interaction plays a dominant role at high $T_R = 5-6\,\mu$ K, while the s-wave interaction, which has a stronger dependence on the mode distribution, becomes important at lower T_R. We focus first on the nuclear spin polarized case (Fig. 6.5) to benchmark

our model, and then use various population distributions among nuclear spin states to investigate the interplay between orbital and spin degrees of freedom (Fig. 6.6).

6.7.1 Two-orbital dynamics in spin-polarized atoms

To understand in detail the orbital dynamics induced by p-wave interactions, we first study a nuclear spin polarized sample ($x_i = 100\%$) for $T_R = 5 - 6\,\mu$K and $\theta_1 = \pi/4$,(Fig. 6.5(b)). To separate the effects of dephasing and many-body correlation in the contrast decay, we apply a π echo pulse in the middle of the Ramsey sequence (Fig. 6.5(a), lower panel). The π echo pulse modifies the contrast decay in a θ_1-dependent way, because of the enhanced $e - e$ loss after the echo pulse (note the number normalization in $\mathcal{C}$) for $\theta_1 < \pi/2$ as well as the fact that the p-wave contribution to contrast decay contains both θ_1-independent and -dependent terms. The θ_1-independent contribution is generated by the term $C^+\hat{T}^Z N_i$. This term is responsible for the density-dependent dephasing between atoms distributed in different 2D traps. The echo pulse removes it, as well as other dephasing effects of technical origin. The θ_1-dependent contribution is generated by the term $\chi^+(\hat{T}^Z)^2$ in the Hamiltonian, and can lead to many-body orbital correlations that are not removable by echo.

For $\theta_1 = \pi/4$, the Ramsey contrast decays more slowly with an echo pulse (6.5(b)). This positive echo effect can be attributed to the suppressed dephasing from inhomogeneous atomic densities across different 2D traps (θ_1-independent contribution) and to the faster number loss with echo.

In a polarized sample where p-wave interactions dominate, the contrast decay is expected to be insensitive to T_R. This is confirmed with measurements performed at $T_R = 2.6\,\mu$K (Fig. 6.5(c)) that show similar decay behaviors to those at $5.4\,\mu$K (Fig. 6.5(b)). In addition, we find an excellent agreement between the data and the theoretical model that uses temperature-insensitive p-wave parameters. Figure 6.5(d) plots the ratio of contrasts with and without echo for different pulse areas and illustrates both the positive echo effect in suppressing contrast decay for $\theta_1 = \pi/4$, as well as the negative effect for $\theta_1 = 3\pi/4$ when the echo enhances contrast decay. The negative echo

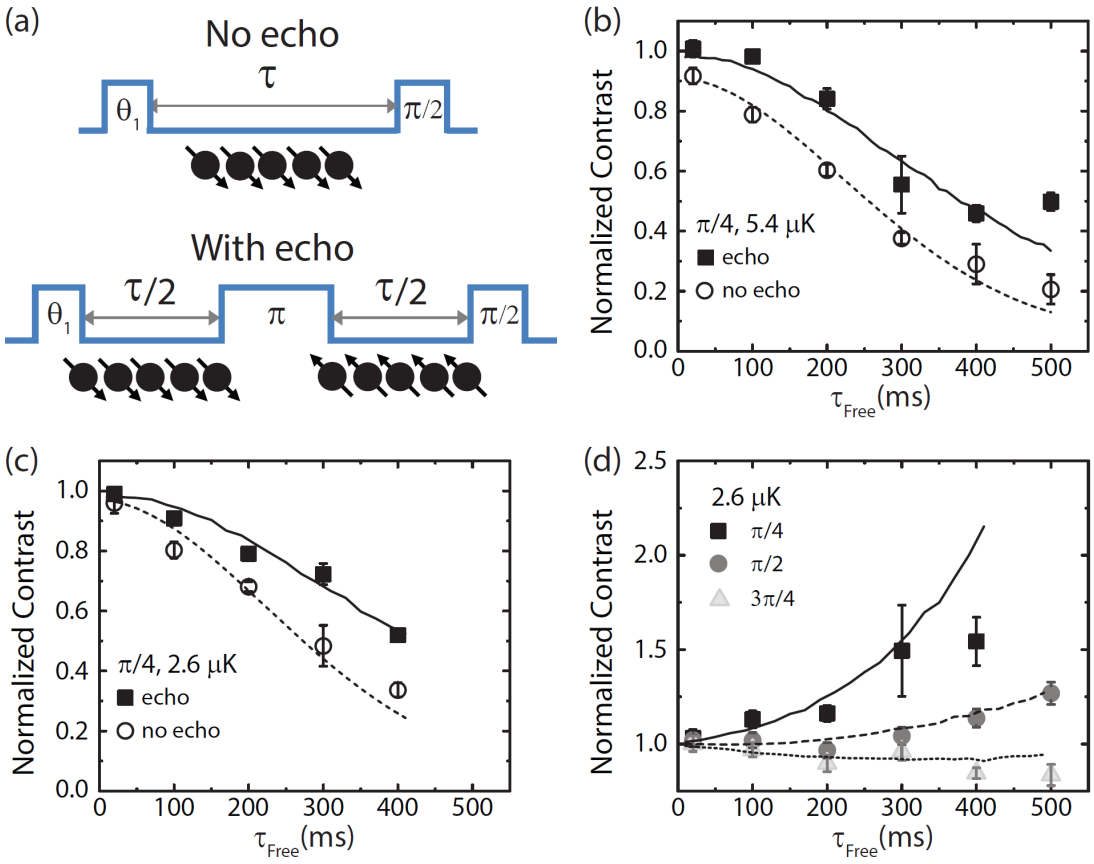

Figure 6.5: Evolution of orbital coherence in nuclear spin-polarized samples. **(a)** (Upper panel) Ramsey sequence with varying θ_1 and τ; (Lower panel) sequence with an echo (π) pulse. The group of circles illustrates the orbital configurations for interrogated atoms (black circles). (**(b)** and **(c)**) Normalized Ramsey contrasts for $\theta_1 = \pi/4$, $x_i = 100\%$, under two different radial temperatures, $T_R = 5.4\,\mu$K and $2.6\,\mu$K, respectively. The contrast is normalized by comparing the high-atom-number raw Ramsey fringe contrast, $\mathcal{C}$ (defined in the main text), against the low-atom-number raw contrast. The high total atom numbers (measured at a very short free evolution time, $\tau = 20$ ms) are in the range of $2200 \sim 3100$ for Figs. 6.5 and 6.6 (day-to-day variation over four months). However, for each specific case the data without and with echo were taken on the same day and their atom numbers are matched to within $3 \sim 7\%$. These atom numbers are recorded and serve as inputs to our theory calculation of Ramsey contrast decay. The filled symbols are for echo measurements and the empty symbols without echo. The solid and dashed lines show theory calculations with echo and without echo, respectively, using a two-orbital model with independently determined parameters (based on measurements shown in Fig. 6.4 and previous studies, see Table 6.1). Under the conditions of (**(b)** and **(c)**), the dominant source for contrast decay arises from p-wave interactions between the interrogated atoms. **(d)** Effects of echo, characterized by the ratio of contrast with echo to that without echo, for $_1 = \pi/4$ (anti-diagonal ellipse and solid line), $\pi/2$ (horizontal ellipse and short dashed line), and $3\pi/4$ (diagonal ellipse and short dotted line), under $x_i = 100\%$. Error bars represent 1σ standard error multiplied by the square root of the reduced chi-squared $\sqrt{\chi^2_{reduced}}$.

effect can be attributed to both the development of many-body orbital correlations for $\theta_1 = 3\pi/4$ [15] and the reduced $e - e$ loss after the echo. All measurements are well reproduced by our spin lattice model.

6.7.2 Spin-orbital SU($\mathcal{N}$) dynamics in spin mixtures

To investigate the interplay between orbital and spin degrees of freedom, we perform similar spectroscopic measurements in spin-mixed samples (Fig. 6.6(a)). We study the spin-mixed cases under $T_R = 5 - 6\,\mu$K, with $\theta_1 = \pi/4$ and the interrogated fraction $x_i = 14\%$ and 56%,(Figs. 6.6(b) and (c), respectively). Here, the data show similar positive effect of an echo pulse in the presence of spectator atoms. Because p-wave interactions between interrogated atoms are reduced as the interrogated fraction decreases, the overall contrast decay becomes slower. Based on the determined scattering parameters, our model predicts that spectator atoms cause almost negligible decoherence effects at this high $T_R = 5 - 6\,\mu$K.

When we decrease T_R to $\sim 2\,\mu$K, the rise of the s-wave contribution causes significant decoherence effects coming from the spectator atoms. Figure 6.6(d) illustrates the influence of spectators for the $x_i = 14\%$ minority case where contrast decay is clearly faster than in Fig. 6.6(b). The inclusion of off-resonant mode-changing collisions as higher order corrections is required for temperatures below $5\,\mu$K to accurately reproduce the experimental observations. These mode-changing collisions can be visualized as relocating pairs of atoms in the energy-space lattice shown in Fig. 6.1(c), analogous to interaction-induced tunneling processes in a real space lattice. The echo pulse suppresses the part of contrast decay arising from mode-preserving collisions between spectators and interrogated atoms, but it cannot reverse the decay due to mode-changing processes. In Fig. 6.6(d), the measured contrast decay with echo enables us to determine a single parameter characterizing the mode-changing processes.

For a further and independent test of our model, we explore another case with $x_i = 56\%$ and $T_R \sim 2\,\mu$K, so that both the interrogated atoms and spectator atoms have important contributions to the contrast decay. The data are well described by the same theory model (Fig. 6.6(e) and Fig.

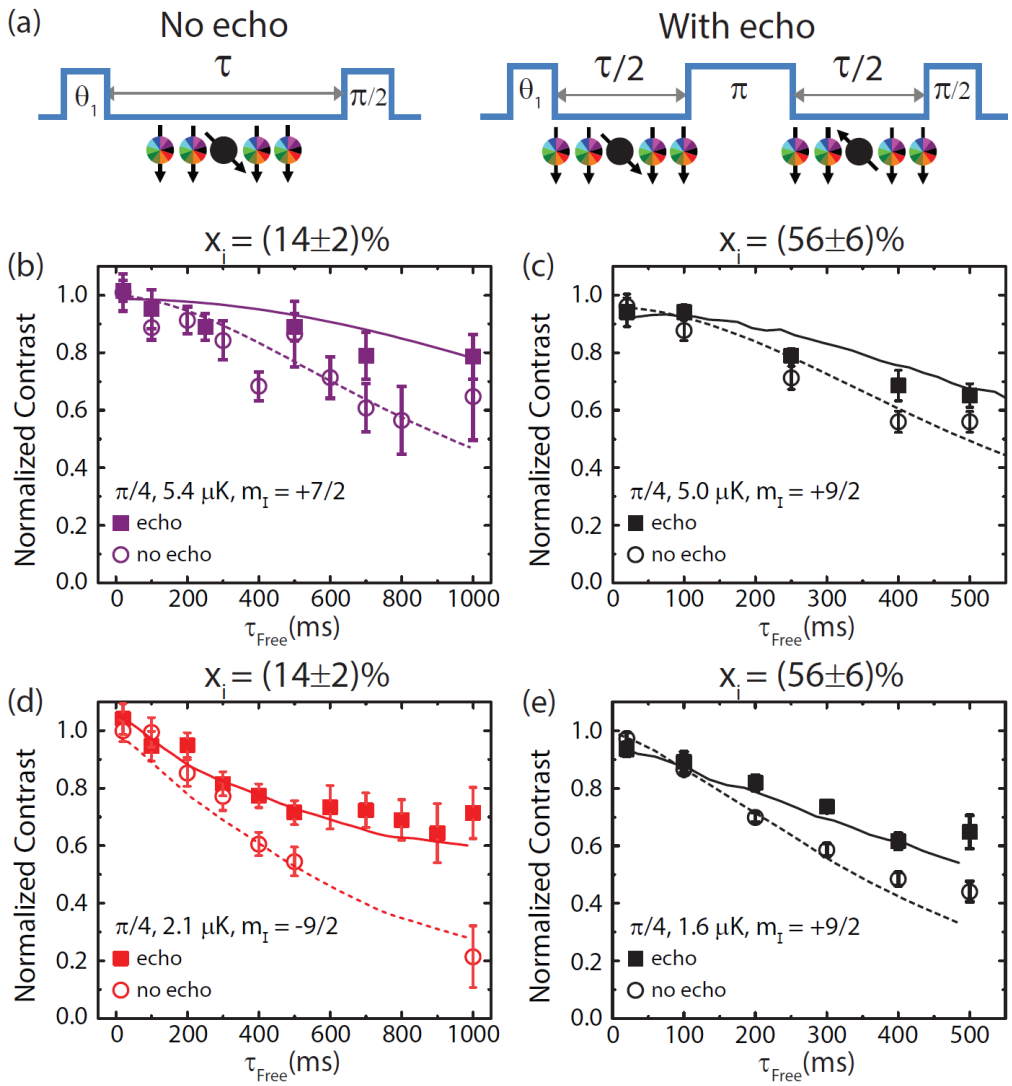

Figure 6.6: Evolution of orbital coherence in nuclear spin-mixed samples. **(a)** (Left panel) Ramsey sequence with varying θ_1 and τ; (Right panel) sequence with an echo (π) pulse. The group of circles illustrates the orbital configurations for interrogated atoms (black circles) and spectator atoms (colored circles). (**(b)** and **(d)**) Normalized Ramsey contrast for $\theta_1 = \pi/4$, $x_i = (14 \pm 2)\%$, under $T_R = 5.4\,\mu$K and $2.1\,\mu$K, respectively: measurements with echo (filled symbols) and without echo (empty symbols). (**(c)** and **(e)**) Normalized contrast for $\theta_1 = \pi/4$, $x_i = (56 \pm 6)\%$, under $T_R = 5.0\,\mu$K and $1.6\,\mu$K, respectively. The solid and dashed lines show theory calculations with echo and without echo, respectively, using a two-orbital model with independently determined parameters (based on measurements shown in Fig. 6.4 and previous studies, see Table 6.1). In this model, the spectators act as an effective inhomogeneous magnetic field causing dephasing to the interrogated atoms. Without mode changing collisions the dephasing is static and removable by echo; with mode changing collisions it is assumed and confirmed experimentally that echo does not remove the time-dependent dephasing. The theory uses a single fitting parameter for the mode-changing processes for all plots. Error bars represent 1σ standard error multiplied by $\sqrt{\chi^2_{reduced}}$.

S1) without any variation of the pre-determined parameters, demonstrating a firm understanding of the system dynamics.

6.8 Conclusions

The experimental exploration of exotic SU($\mathcal{N}$) physics is just starting. The unique capability of precision laser spectroscopy has so far allowed us to explore Ising orbital magnetism at relatively high temperatures. We expect to explore the full Hamiltonian including the exchange interactions by controlling the atomic density, temperature and the magnetic field to engineer various spin-spin and spin-orbital dynamics. This will allow us to push the frontier of emergent many-body quantum physics at increasingly high temperatures, as well as the study of time-resolved dynamics in the SU($\mathcal{N}$) Kondo lattice and Kugel-Khomskii models [92, 127, 128] in the quantum gas regime.

Chapter 7

Spin-Orbit Coupling with Interactions

7.1 Introduction

Spin-orbit coupling (SOC) links a particle's velocity to its quantum mechanical spin and is essential for numerous complex condensed matter phenomena including topological insulators and Majorana fermions. Engineering SOC in cold atom systems therefore allows us to study such materials within the clean environment associated with these systems.

In this work we experimentally explore SOC that occurs naturally within a one-dimensional optical lattice clock when tunneling is allowed. Previous studies of SOC and topological states with alkali atoms has been highly successful for the case of non-interacting systems [129, 130, 131, 132, 133]. However, the detrimental effects of spontaneous emission and heating [134, 135] have limited the study of SOC with interactions in alkali atoms to initial studies in a bulk gas [136, 137], in a lattice modulated BEC [138, 139], and with two particles in a lattice[140]. Encoding the effective spin degree of freedom in the long-lived electronic clock states significantly reduces the detrimental effects of dissipation. We can take advantage of this feature to study the interplay between SOC and the strong collective interactions in an optical lattice clock (OLC). Some of the physics we explore is described in a theory proposal [135], although experimental work naturally follows its own lead.

In our one-dimensional OLC many-body effects arise from the cooperation and competition between p-wave and s-wave interactions (as discussed in chapters 5 and 6), along with single-particle SOC dynamics. The spin-motion coupling we engineer in the OLC primarily affects how spins

interact with each other, without any thermalization effects in the lattice. This unique condition sets up an effective spin system that provides a simpler view of the complex interplay between SOC and many-body interactions. Meanwhile, it grants us immediate access to quantum magnetism at μK motional temperatures.

The many-body dynamics are described by a collective XXZ spin model [15, 141], which contains both exchange (s- and p-wave) and Ising (p-wave) terms. The dynamics of collective XXZ models have largely been studied theoretically in condensed matter physics, for example in the context of superconductivity through the Anderson pseudospin mapping [142], which identifies Cooper pairs and holes as the two components of an effective pseudospin. Only limited experimental studies have been conducted so far, and they have been restricted mainly to weak quenches [143]. The ultra-narrow clock transition in our OLC enables the preparation, control, and spectroscopic resolution of the dynamics in a broad parameter space, including quenches over a large dynamic range.

SOC with strong interactions between a pair of atoms has been realized in a lattice [140]. Here, we instead use a large atom number, N, to tune the strength of the interactions to enter a strong, collective interacting regime well beyond single-particle SOC dynamics. We observe that both s-wave and p-wave interactions induce precession of the collective magnetization. Furthermore, the exchange interactions compete with the SOC-induced dephasing and promote spin alignment and locking. Similar interaction-induced spin locking effects have been observed in other trapped gas experiments [144, 145], and were recently shown to play a crucial role in the stabilization of time crystal phases in trapped ions [146] and impurity centers in diamond [147]. In those cases, however, dephasing arose from spatial inhomogeneities, in contrast to our system where dephasing is a direct consequence of an intrinsic modification of the band structure by SOC.

7.1.1 Chapter Outline

The outline of this chapter is as follows. We will start by reviewing the characterization of the trapping potential in section 7.2 for the case where the two beams forming the lattice have

different powers. We will then review the band structure of the atoms in a lattice in section 7.3, which is important when considering the lineshape when tunneling is allowed in the lattice. We will then discuss the spin-orbit coupling further in section 7.4 and the relation to synthetic gauge fields in section 7.5. The experimental details will then be discussed in section 7.6 and we will show the single particle effects of SOC in our optical lattice clock. We will look at the effects of tunneling on the axial sidebands in section 7.7 and the signatures of Band relaxation that we can see from the sidebands in section 7.8. The effects of tunneling on the carrier transition are discussed in section 7.9 and how the observations can be explained using the band structure of the atoms in the lattice. We will show that these features lead to the ability to select atoms with specific quasimomentum and observe Bloch oscillations for a tilted lattice in section 7.10. By selecting different quasimomentum groups we can Rabi flop the atoms in order to determine the chiral Bloch vector angles in section 7.11, which are the eigenstates of the spin-orbit coupled Hamiltonian.

We will then move on to discuss further dynamics using Ramsey spectroscopy. We will start with the single particle Ramsey contrast in section 7.12 for different tunneling rates before increasing the atom number to introduce the collective interactions in section 7.13. We will then look at the frequency shifts in section 7.14 and compare them to those studied previously, in chapter 6, with zero tunneling rate.

7.2 Atoms trapped in a periodic potential

For the case of a vertical one-dimensional lattice the gravitational energy shift between neighboring lattice sites (~ 1 kHz) lifts the degeneracy between adjacent potential wells which strongly inhibits tunneling [148]. In this case here where we want to study the effects of tunneling we therefore move from a vertical lattice to a horizontal lattice configuration. We will consider the case of an unbalanced lattice where the power of both beams that form the lattice can be different.

The trapping potential near the waist of a one-dimensional lattice that is travelling along the

$\hat{z}$ direction can be written as

$$U(z,r) = -\left[U_{const} + U_z \cos^2(kz)\right] e^{-2r^2/\omega_0^2} \tag{7.1}$$

with

$$U_z = \frac{4\alpha\sqrt{P_1 P_2}}{\pi c \epsilon_0 \omega_0^2} \tag{7.2}$$

$$U_{const} = \alpha\frac{P_1 + P_2 - 2\sqrt{P_1 P_2}}{\pi c \epsilon_0 \omega_0^2} \tag{7.3}$$

where $k = 2\pi/\lambda$ where λ is the lattice wavelength, c is the speed of light, and ϵ_0 is the permittivity of free space. $P_1(P_2)$ is the ingoing (reflected) lattice power, and $\alpha = \alpha(\lambda)$ is the wavelength dependent a.c. polarizability, r is the transverse distance from the trap center and ω_0 is the lattice beam waist. To find solutions to this equation we can Taylor expand the cosine and exponential terms keeping terms up to the fourth spatial power to give

$$U(z,r) \approx U_z\left(-1 + k^2 z^2 + \frac{1}{3}k^4 z^4\right) + (U_z + U_{const})\left(\frac{2r^2}{\omega^2} - \frac{2k^2 r^2 z^2}{\omega_0^2}\right). \tag{7.4}$$

In the axial direction the potential is approximated as a one-dimensional harmonic oscillator with a quartic distortion and in the radial direction we just have a harmonic oscillator. The $r^2 z^2$ term in Eq. 7.4 is an axial radial coupling term.

The harmonic approximation to the trapping frequencies of the lattice can be found by equating the harmonic terms in Eq. 7.4 to the energies of a harmonic oscillator. For example in the axial direction

$$k^2 U_z z^2 = \frac{1}{2} M \omega_z^2 z^2 \tag{7.5}$$

$$\Rightarrow \nu_z = \frac{1}{2\pi}\sqrt{\frac{2k^2 U_z}{M}} \tag{7.6}$$

with $\nu_{rec} = h/(2M\lambda_L^2)$ the recoil frequency. Similarly, the radial trapping frequency is found to be

$$\nu_R = \frac{1}{2\pi}\sqrt{\frac{4(U_z + U_{const})}{m\omega_0^2}}. \tag{7.7}$$

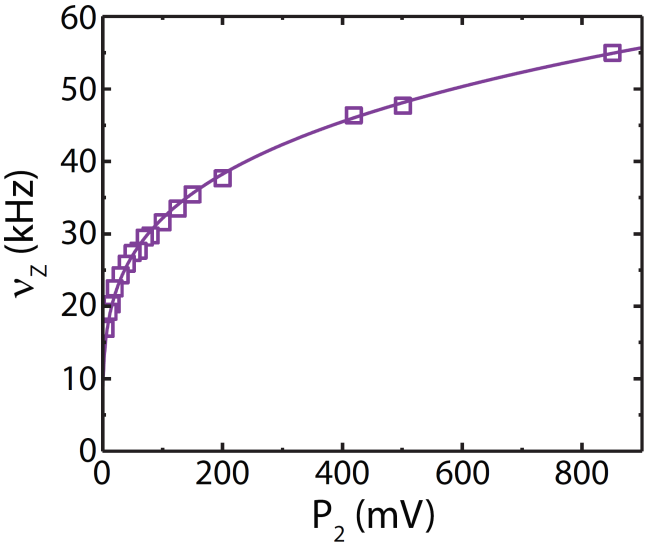

Figure 7.1: Axial trapping frequency, ν_z, against retro-reflected power P_2, which is measured using a photodiode. The data (purple, squares) is fitted with a $P_2^{1/4}$ curve (purple line) as given in Eq. 7.8.

Figure 7.1 shows that experimentally by just lowering the retro-reflected power, P_2, the axial trapping frequency decreases $\propto P_2^{1/4}$ as expected from Eq. 7.6. Inserting the values of U_{const} and U_z into Eq. 7.6 and Eq. 7.7 gives

$$\nu_z = \frac{1}{2\pi\omega_0\lambda_L}\sqrt{\frac{32\pi\alpha\sqrt{P_1P_2}}{c\epsilon_0 M}} \tag{7.8}$$

$$\nu_R = \frac{1}{2\pi\omega_0^2}\sqrt{\frac{4\alpha\left(P_1+P_2+2\sqrt{P_1P_2}\right)}{\pi c\epsilon_0 M}} \tag{7.9}$$

where we can see that for a balanced lattice these equations reduce to the more familiar equations [7]

$$\nu_z = \frac{1}{2\pi\omega_0\lambda_L}\sqrt{\frac{32\pi\alpha P}{c\epsilon_0 M}} \tag{7.10}$$

$$\nu_R = \frac{1}{2\pi\omega_0^2}\sqrt{\frac{16\alpha P}{\pi c\epsilon_0 M}} \tag{7.11}$$

In our experiment we want to be able to keep the radial confinement approximately constant whilst changing the tunneling rate. The axial confinement is due to the interference term between the the two counter propagating laser beams that are making the lattice ($\propto \sqrt{P_1P_2}$). On the other

hand the radial confinement is present even in a dipole trap. We can therefore have tunneling and strong radial confinement by changing the power of only one of the lattice beams. Experimentally this can be done by double passing the retro-reflected lattice beam through an acousto optical modulator (AOM).

7.3 Lattice Band Structure

In order to derive the coupling matrix which describes the motion of particles in a lattice we start with the Schrödinger equation for a particle with a wavefunction $\psi_n(z)$ in a periodic potential given by $V(z) = V_0 \sin^2(kz)$

$$-\frac{\hbar^2}{2M}\frac{d^2}{dz^2}\psi_n(z) + V(z)\psi_n(z) = E_n\psi_n(z), \tag{7.12}$$

where E_n is the particle energy eigenvalue, with n the energy band index. Bloch's theorem tells us that the eigenfunction of a particle in a periodic potential can be written as $\psi_{nq}(z) = e^{iqz}U_{nq}(z)$, where q is the quasimomentum and $U_{nq}(z)$ is a periodic function with the same periodicity as $V(z)$. Inserting this solution into the Schrödinger equation of Eq. 7.12 gives us

$$-\frac{\hbar^2}{2M}\left[\frac{d^2}{dz^2} + 2iq\frac{d}{dz} - q^2\right]U_{nq}(z) + V(z)\psi_n(z) = E_n\psi_n(z). \tag{7.13}$$

We can write the periodic functions as a Fourier series

$$U_{nq}(z) = \sum_{l=-\infty}^{\infty} a_l e^{2iklz}, \tag{7.14}$$

where a_l is the amplitude of the traveling wave forming the lattice, and k is the wavevector of the light forming the lattice. The equation now becomes

$$\frac{\hbar^2}{2M}\sum_{l=-\infty}^{\infty} a_l(q+2kl)^2 e^{2iklz} + \sum_{l=-\infty}^{\infty} V(z)a_l e^{2iklz} = E_n\sum_{l=-\infty}^{\infty} a_l e^{2iklz}. \tag{7.15}$$

Using the exponential definition of a sine function we can rewrite the lattice potential as

$$V(z) = V_0\sin^2(kz) = -\frac{V_0}{4}\left[e^{2ikz} + e^{-2ikz} - 2\right], \tag{7.16}$$

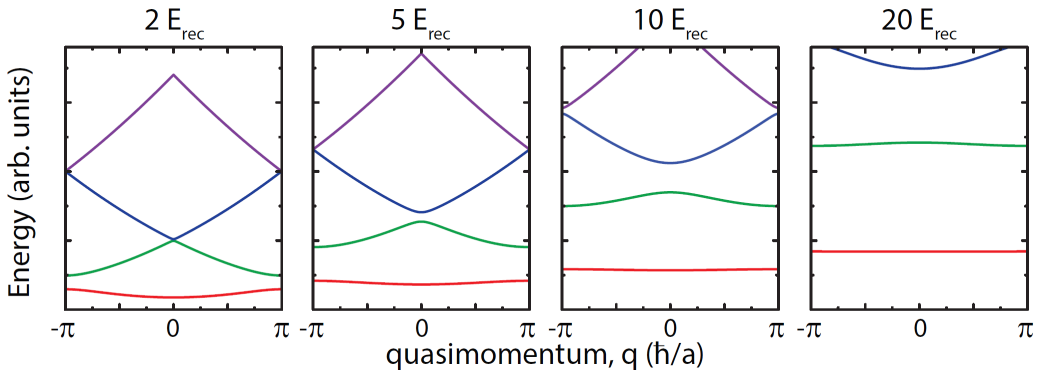

Figure 7.2: Lattice Band structure for increasing lattice depth. The four lowest bands are shown. The energy width of each band is proportional to the tunneling rate which increase with decreasing depth.

inserting this into Eq. 7.15 and considering all terms with $e^{2ikl z}$ we get the following recurrence relation

$$\frac{\hbar^2}{2M} a_l (q + 2kl)^2 - \frac{V_0}{4} \left[a_{l-1} + a_{l+1} \right] + \frac{V_0}{2} = E_n a_l, \tag{7.17}$$

which can be written as an infinite square matrix with quasimomentum dependent eigenvalues $E_n(q)$. To solve for the eigenenergies we need to truncate the matrix which can be written as

$$\begin{bmatrix} \frac{\hbar^2}{2m}(q-2kl)^2 + \frac{V_0}{2} & -\frac{V_0}{4} & 0 & \dots & 0 \\ -\frac{V_0}{4} & \ddots & -\frac{V_0}{4} & \dots & \vdots \\ 0 & \ddots & \frac{\hbar^2}{2m}(q)^2 + \frac{V_0}{2} & \ddots & 0 \\ \vdots & \ddots & -\frac{V_0}{4} & \ddots & -\frac{V_0}{4} \\ 0 & \dots & 0 & -\frac{V_0}{4} & \frac{\hbar^2}{2m}(q+2kl)^2 + \frac{V_0}{2} \end{bmatrix} \tag{7.18}$$

The lowest eigenenergy solutions to this matrix are shown in Fig. 7.2 for different lattice depths as a function of quasimomentum. These solutions are the band structure of the atoms in the lattice where the width of each band is $4J$, with J the tunneling rate.

7.4 Coupling the spin and the orbit

As mentioned in the introduction spin-orbit coupling occurs naturally in a one-dimensional optical lattice clock during clock spectroscopy when tunneling is allowed. When an atom in the

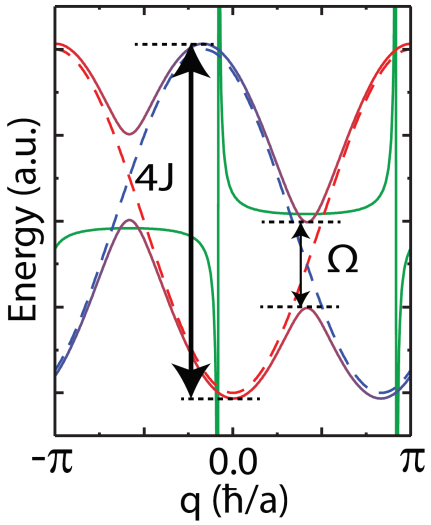

Figure 7.3: Spin-orbit coupled band structure (solid, bichromatic) from the coupling of the bare clock state $|g, q\rangle_0$ (red, dashed) and the momentum-shifted clock state $|e, q + \phi\rangle_0$ (blue, dashed). The band splitting is given by the Rabi frequency, Ω, and has a bandwidth $4J$ with J the tunneling rate. The collective density of states (green, solid) shows divergences around $q \sim 0$ and $q \sim \pi$.

ground state, g, with quasimomentum, q, and ground band 0, which we denote $|g, q\rangle_0$, absorbs a clock laser photon it receives a momentum kick and ends up in $|e, q + \phi\rangle_0$. The momentum kick is given by

$$\phi = \frac{2\pi\hbar}{\lambda_c}\frac{a}{\hbar} = \pi\frac{\lambda_L}{\lambda_c} \approx \frac{7\pi}{6} \tag{7.19}$$

in units of $\hbar/a$, with $a = \lambda_L/2$ the lattice spacing. For convenience we are now going to perform a gauge transformation on the band structure of the lattice trapped atoms described in section 7.3. In the tight-binding limit these bands can be approximated as sinusiodal functions $E_0(q) = -2\hbar J\cos(q)$. These bands are transformed such that $|g, q\rangle_0 \rightarrow |g, q\rangle_0$ remains unchanged and $|e, q\rangle_0 \rightarrow |e, q + \phi\rangle_0$ meaning that all transitions in quasimomentum space now seem to conserve quasimomentum.

Figure 7.3 shows the gauge transformed clock states under the rotating wave approximation with clock laser detuning $\delta = 0$. The ground band of the ground clock state $|g, q\rangle_0$ (red, dashed) and the ground band of the gauge transformed excited clock state $|e, q + \phi\rangle_0$ (blue, dashed) become coupled when the clock laser is on, forming spin-orbit coupled bands (solid, bichromatic). The band

splitting is given by the Rabi frequency Ω and the bandwidth is $4J$.

The probability of a transition between the two bands at a specific q is determined by the joint transition density of states. The joint density of states (green, solid) diverge around $q \sim 0$ and $q \sim \pi$ which is the location of the saddle points in the energy difference between the two band dispersion curves. These divergence points in the density of states of a crystalline lattice are called Van Hove singularities (VHSs) and are well known from optical absorption spectra in solids and scanning tunneling microscopy [149, 150].

The resulting Hamiltonian can be diagonalized in quasimomentum space using this gauge transformation. The transformed spin-orbit coupled Hamiltonian is given by

$$\hat{H}_{SOC}/\hbar = -\sum_{i=1}^{N} \mathbf{B}_{SOC}(q_i, \mathbf{n}_{\mathbf{r}_i}, \Omega, \delta) \cdot \hat{\mathbf{S}}_i, \tag{7.20}$$

where the components of $\mathbf{S}$ are the spin-1/2 angular momentum operators $\hat{S}^{X,Y,Z}$ for the two clock states. $\mathbf{B}_{SOC}(q_i, \mathbf{n}_{\mathbf{r}_i}, \Omega, \delta)$ is an effective quasimomentum-dependent magnetic field given by

$$\begin{aligned} \mathbf{B}_{SOC}(q_i, \mathbf{n}_{\mathbf{r}_i}, \Omega, \delta) &= \left[0, B^Y_{n_z}(\Omega), B^Z_{n_z}(q, \delta)\right] \\ &= [0, \Omega, (E_{n_z}(q) - E_{n_z}(q+\phi))/\hbar + \delta] \end{aligned} \tag{7.21}$$

7.5 Connections to synthetic gauge fields

To connect our system to related works on synthetic gauge field we can treat the clock transition as a synthetic dimension as shown in Fig. 7.4. The clock laser with Rabi frequency Ω excites atoms from $|g\rangle \rightarrow |e\rangle$ along the synthetic dimension. This causes a change in momentum of the atom absorbing the photon of ϕ (see Eq. 7.19). Each lattice site experiences the clock laser with a different phase and this excitation in the synthetic dimension can be thought of as a complex site dependent tunneling rate in a synthetic dimension. In the real dimension of the lattice, the atoms can tunnel between the different lattice sites with a tunneling rate J. In the case of an atom following a closed trajectory about a single plaquette with the path $|g, n\rangle \rightarrow |e, n\rangle \rightarrow |e, n-1\rangle \rightarrow |g, n-1\rangle \rightarrow |g, n\rangle$, will accumulate a phase ϕ which resembles the flux experienced by a charged particle in the presence of an external magnetic field.

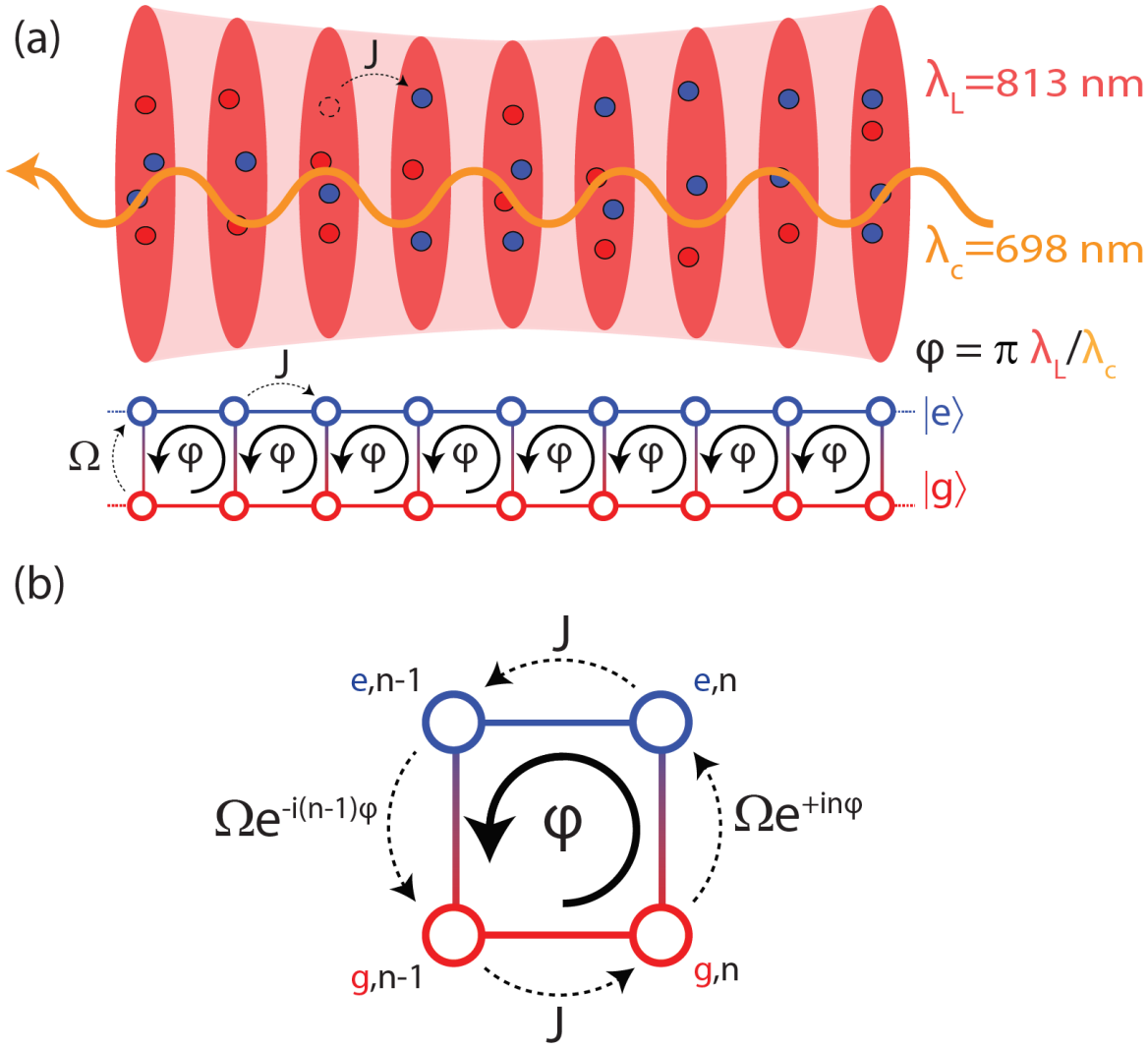

Figure 7.4: Connecting our experiment to work on synthetic gauge fields. **(a)** We can treat the $|g\rangle$ and $|e\rangle$ clock states as a synthetic dimension. Together with the real space dimension of the lattice site, these two dimensions form plaquettes and can be thought of as a two-dimensional synthetic lattice which the atoms are confined to. **(b)** A single plaquette demonstrating the synthetic gauge field. After traversing around the plaquette the atom picks up a phase ϕ. The atoms tunnel in the real space dimension by tunneling with rate J. The clock laser, with Rabi frequency Ω, imprints a site dependent phase on the atoms which can be thought of as a complex site dependent tunneling rate along the synthetic dimension.

7.6 Experimental Setup

In this experiment up to 1.5×10^4 nuclear spin-polarized atoms are cooled to $\sim 2\,\mu$K and loaded into a one-dimensional horizontal lattice aligned along the $\hat{z}$ axis. The lattice is formed using a high power ($P_1 \approx 3$ W) incoming beam and a variable retro-reflected beam. Although the basic setup for these different experiments is the same with a strong incoming beam and a weak retroreflected beam the actual experimental setup was improved between the earlier set of experiments [151] and the experiments studying interactions [89].

First we will briefly describe the initial setup. The initial lattice setup involved free space coupling the 813 nm Ti:sapphire light to the chamber which was thought to be the best approach fro maximum power at the atoms. The lattice is focused and gives both an astigmatic and elliptically shaped beam with waists of $40\,\mu$m and $50\,\mu$m in the two directions. After passing through the chamber, the lattice passes through a polarizing beam splitter (PBS) before being collimated and passes through one or two non-polarizing beam splitters (NPBS) with reflection:transmission of $90:10$ and $50:50$ before passing through a $\lambda/4$ waveplate and then being retro reflected. The NPBSs give an overall maximum power of up to ~ 50 mW that is used for the retro beam and the waveplate combined with the PBS gives us the fine control of the power.

For studying interactions with SOC it is necessary to be able to change the lattice depth during each sequence. For this reason the Ti:sapphire breadboard layout is modified to the setup shown in Fig. 7.5 which allows the power to be fiber-coupled to up to two fibers to the experiment. The acousto-optical modulator (AOM) allows us to servo the intensity of the lattice. In this experiment we only use one fiber but the setup allows for flexibility in future experiments. The simple fiber output near the experiment is shown in Fig. 7.6, where the beam is focused and combined with the MOT beams using a dichroic. This fiber-coupled setup gives us the advantage that any day-to-day pointing stability from the Ti:sapphire laser is not converted to a pointing stability for a lattice and instead the fiber coupling just needs to be optimized. The fiber output also has the advantage that it cleans up the beam shape and we are able to get a symmetric

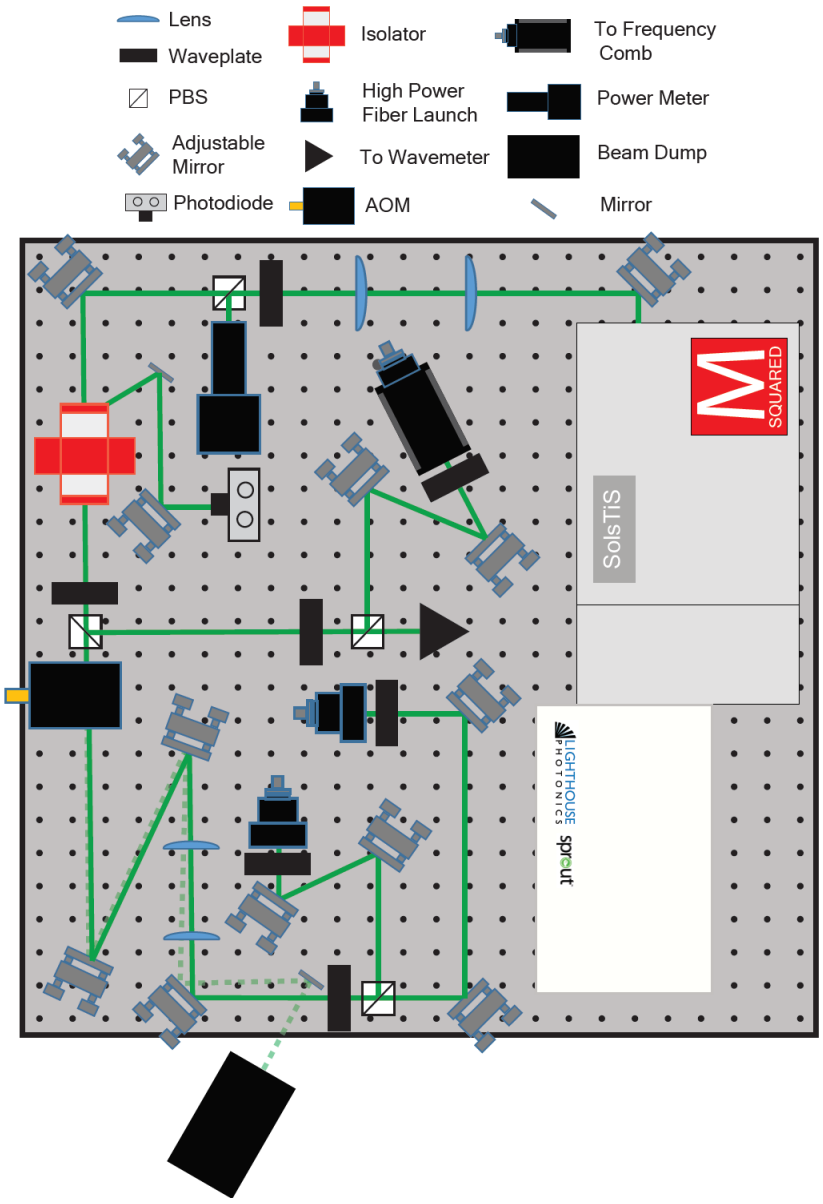

Figure 7.5: Lattice laser setup. The Ti:Sapphire laser (M-squared, SolsTis) is pumped using an 18 W pump laser (Lighthouse Photonics, Sprout) to give up to 6 W of light at 813 nm. The beam is collimated using cylindrical lenses and all the power can be dumped into a power meter or sent to the experiment. The beam to the experiment then passes through an optical isolator before being split between two paths. One of these paths sends a small amount of light to the wavemeter and the frequency comb (for locking). The other path sends light to the lattice with the option of sending light through two different fibers to the vertical or horizontal lattice. The retro reflected lattice light passes through the rejection port of the isolator and is monitored/servoed using a photodiode.

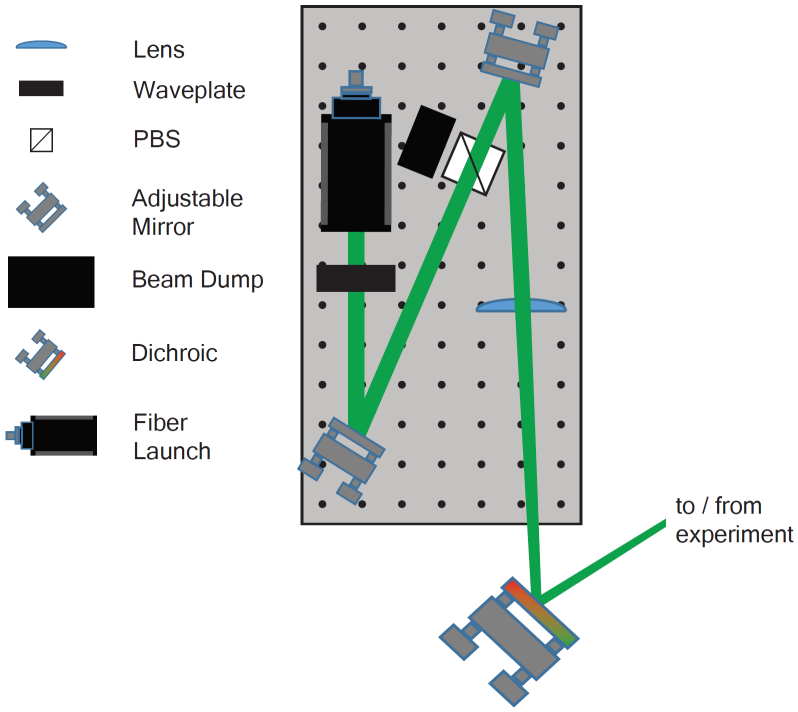

Figure 7.6: The experimental layout of the ingoing horizontal lattice mezzanine. The 813 nm light is outcoupled from a fiber before being focused by a lens onto the atoms. The beam enters the chamber along one of the MOT beams (H_1 axis) and is combined using a 2" dichroic.

Gaussian beam profile with a waist of 40 μm.

The retro-reflection setup for the horizontal lattice is shown in Fig. 7.7. The power of the incoming lattice is monitored using a photodiode which is used to feedback the lattice power to the AOM shown in Fig. 7.5 to servo the lattice. Two AOMs are used in the retro path to dynamically control the retro-reflected intensity. Two AOMs are needed in order to not cause a frequency change in the retro-reflected beam which would mean that no lattice is formed. The first AOM in the setup uses the +1 order and the second AOM uses the −1 order for this reason. A $\lambda/4$ waveplate is used to set the maximum retro-reflected power of the lattice and the power of the retro-reflected light is monitored using a separate photodiode. The retro-reflected light then passes through the chamber and back through the fiber launch shown in Fig. 7.6 and back to the breadboard shown in Fig.7.5 where the power can also be monitored using the rejection port of the optical isolator.

The clock laser beam is combined with the retro-reflected lattice beam using a dichroic. Both

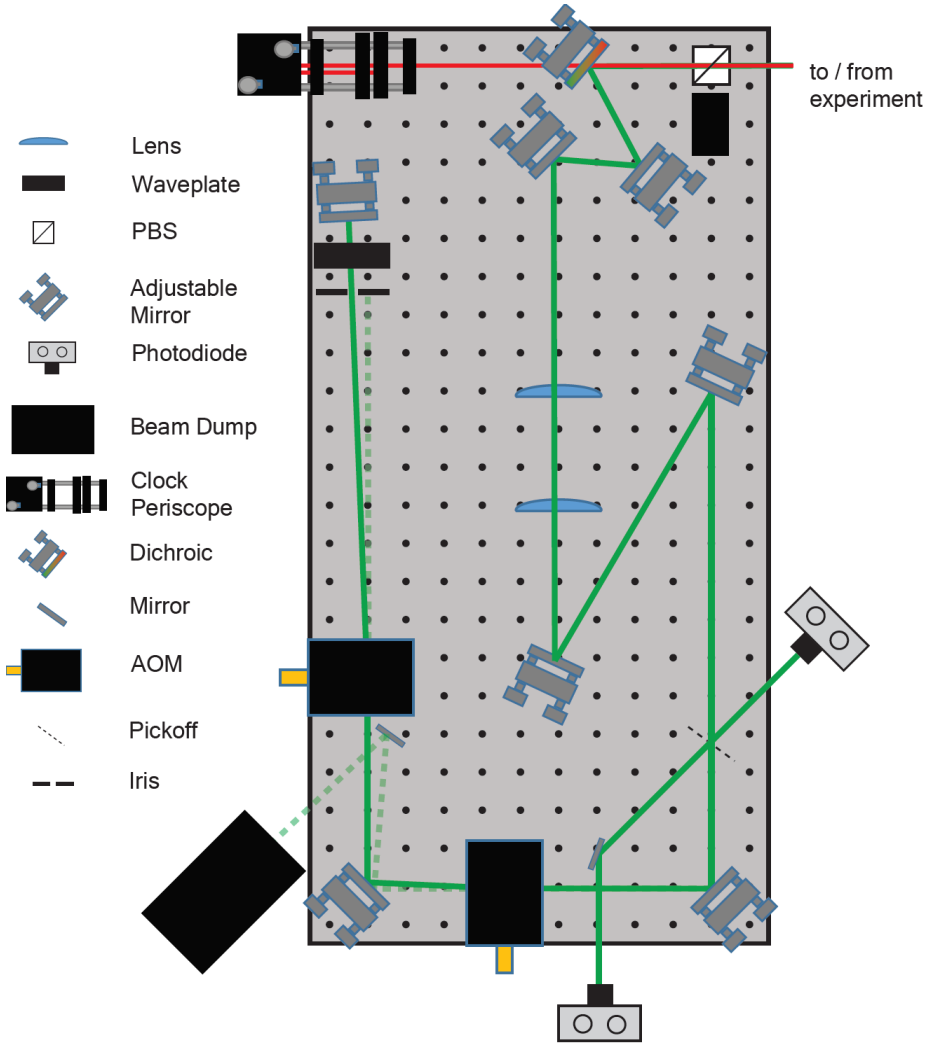

Figure 7.7: The setup of the retro reflected path of the horizontal lattice. After the incoming lattice beam passes through the chamber the following setup is used to control the power of the retro reflected lattice beam. A pickoff monitors both the incoming lattice intensity and the retroreflected lattice intensity. Two AOMs are used in order to keep the frequency of the retro reflected lattice beam the same at the atoms with each AOM using a different diffraction order. An iris and a mirror are used to remove the zeroth orders of the AOMs. The clock laser travels through a periscope from the main experimental table up to the mezzanine shown here. The zeroth order of the clock light is retroreflected for fiber phase noise cancellation and the -1 order of the clock beam is combined with the lattice using a dichroic.

beams are combined with the MOT beams using a small half inch mirror. A dichroic cannot be used in this case because we want the red 689 nm MOT beams to be transmitted and the 698 nm clock laser needs to be reflected into the chamber. To maximize the power a mirror is therefore used and the lattice is offset horizontally from the red MOT beam with both overlapping at the atoms.

7.7 Sideband Structure and Band Selection

A typical coarse scan of the atoms across resonace by changing the frequency of the clock laser is shown in Fig. 7.8 for $U_z/E_{rec} = 30.5$. From this scan we can observe a strong narrow central carrier peak and several sideband transitions. At typical operating temperatures the majority of the atoms are prepared in the ground band (0) of the ground state, g, which we denote $|g\rangle_0$. The central peak is referred to as the carrier transition and represents atoms undergoing a transition from $|g\rangle_0 \rightarrow |e\rangle_0$ where the position of the peaks can be understood due to the band structure of atoms in the lattice.

The sideband transitions are suppressed by the Lamb-Dicke parameter and are caused by transitions between different bands. The blue detuned sideband transition corresponds to the transition $|g\rangle_0 \rightarrow |e\rangle_1$ and a smaller transition is seen at even higher positive detunings corresponding to $|g\rangle_0 \rightarrow |e\rangle_2$. The red detuned sideband corresponds to the transition $|g\rangle_1 \rightarrow |e\rangle_0$ where the population of $|g\rangle_1$ depends on the temperature of the atoms. The ratio between the red and blue sidebands can therefore be used to determine the temperature of the atoms in the lattice [152].

With these carrier and sideband transitions corresponding to different band transitions we can then use these to experimentally prepare atoms in different bands of the lattice. For example we can excite atoms using a clock laser detuned to the blue sideband, remove all remaining ground state atoms using the blue probe beam and we are left with only atoms in the first excited band $|e\rangle_1$. Figure 7.9 shows a sideband scan for atoms in $|e\rangle_0$ and Fig. 7.10 shows a sideband scan for atoms in $|e\rangle_1$ (solid) and for reference a scan for atoms in $|e\rangle_0$ is also shown (dashed line). We can see that the red sidebands for atoms prepared in different bands are offset from each other

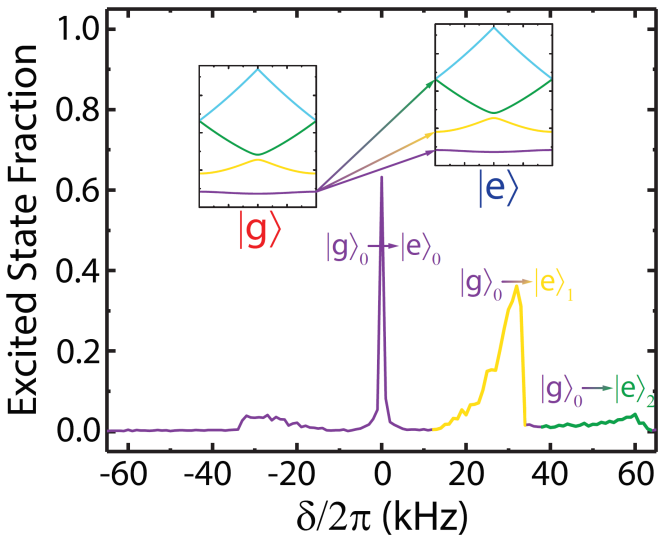

Figure 7.8: Sideband scan from the ground state. At our temperatures the majority of atoms are in the ground band. The transitions from the $|g\rangle_0$ state are shown in the inset using the band structure of the $|g\rangle$ and $|e\rangle$ bands. The carrier transition is dominated by the $|g\rangle_0 \rightarrow |e\rangle_0$ transition, the sideband from $|g\rangle_0 \rightarrow |e\rangle_1$ (yellow, solid) is blue-detuned and the $|g\rangle_0 \rightarrow |e\rangle_2$ sideband (green, solid) can also be seen. Atoms that are not initially in the ground band are detected as a red-detuned sideband with atoms transitioning from $|g\rangle_1 \rightarrow |e\rangle_0$.

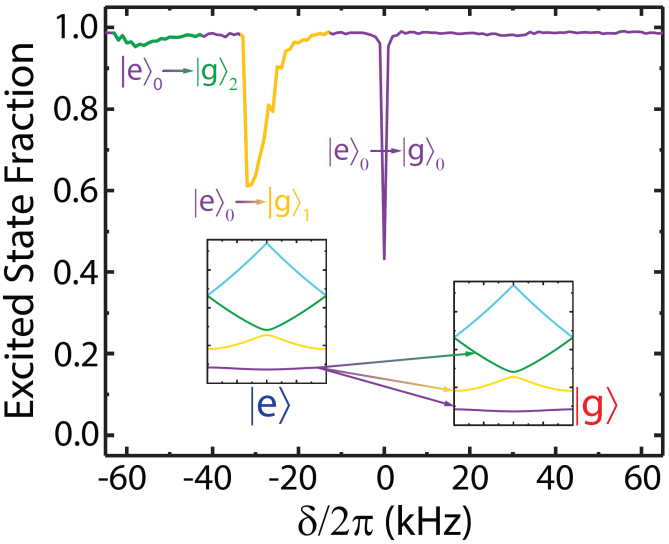

Figure 7.9: Sideband Scan from the excited state ground band. A π-pulse initializes atoms in $|e\rangle_0$ with the transitions from $|e\rangle_0$ shown in the inset using the band structure of the $|e\rangle$ and $|g\rangle$ bands. The carrier transition is dominated by the $|e\rangle_0 \rightarrow |g\rangle_0$ transition, the sideband from $|e\rangle_0 \rightarrow |g\rangle_1$ (yellow, solid) and the $|e\rangle_0 \rightarrow |g\rangle_2$ sideband (green, solid) can be seen on the left. The sideband on the right is decreased from Fig. 7.8 due to the initial π-pulse preparation.

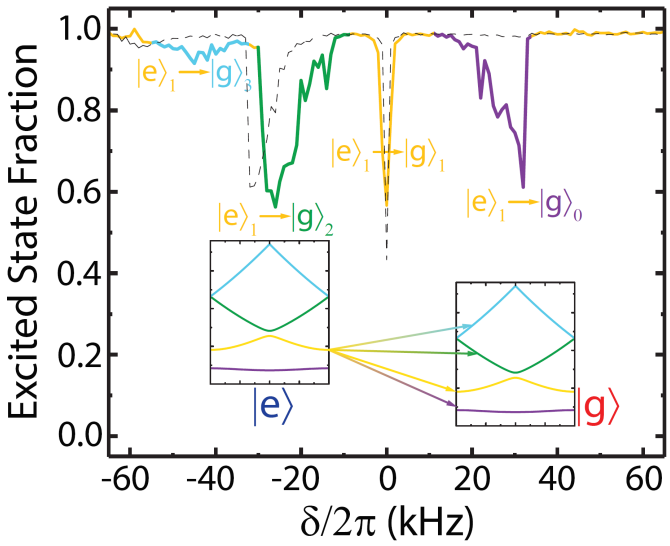

Figure 7.10: Sideband scan from the excited state 1^{st} excited band. A strong clock pulse detuned to the blue sideband initializes atoms in $|e\rangle_1$. The transitions from $|e\rangle_1$ are shown in the inset using the band structure of the $|e\rangle$ and $|g\rangle$ bands. The carrier transition is dominated by the $|e\rangle_1 \rightarrow |g\rangle_1$ transition, the sidebands from transitions from $|e\rangle_1 \rightarrow |g\rangle_2$ (green, solid), $|e\rangle_1 \rightarrow |g\rangle_0$ sideband (purple, solid), and $|e\rangle_1 \rightarrow |g\rangle_3$ sideband (cyan, solid) can all be seen. For comparison the sideband scan from Fig. 7.9 is also shown (black, dashed).

by a lattice recoil, E_{rec}, and this is due to the anharmonicity of the lattice. This anharmonicity of the lattice axial bands makes transitions from $|e\rangle_0 \rightarrow |g\rangle_1$ to be different from transitions from $|e\rangle_1 \rightarrow |g\rangle_2$. For the case of atoms in the 1^{st} excited band shown here, the red detuned transition corresponds to the $|e\rangle_1 \rightarrow |g\rangle_2$ transition, the carrier to $|e\rangle_1 \rightarrow |g\rangle_1$ transition and the blue detuned transition to $|e\rangle_1 \rightarrow |g\rangle_0$.

We can see that the sidebands are smeared out towards the carrier transition and this is due to the radial-axial coupling within the lattice. Experimentally we can see this coupling by exciting atoms from the blue sideband using different clock laser detunings within the sideband. By preparing atoms in $|e\rangle_1$, and removing all other atoms, using different excitation detunings the difference between the different selections can be seen most clearly by then measuring the radial temperature of the atoms in $|e\rangle_1$. An example of this is shown in Fig. 7.11. For atoms excited at the peak of the blue detuned sideband we see a lower radial temperature compared to atoms excited closer to the carrier frequency.

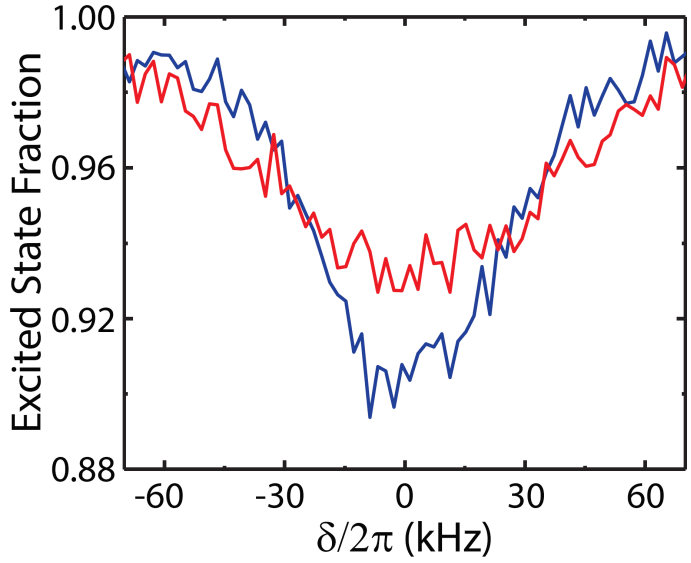

Figure 7.11: By exciting atoms on the blue detuned sideband we can select different radial groups of atoms. The blue line is the case when atoms are excited at the peak of the blue detuned sideband giving a temperature of 2.5 μK. The red line is when atoms are selected from the blue detuned sideband, but at a frequency closer to the carrier frequency giving a temperature of 6.4 μK

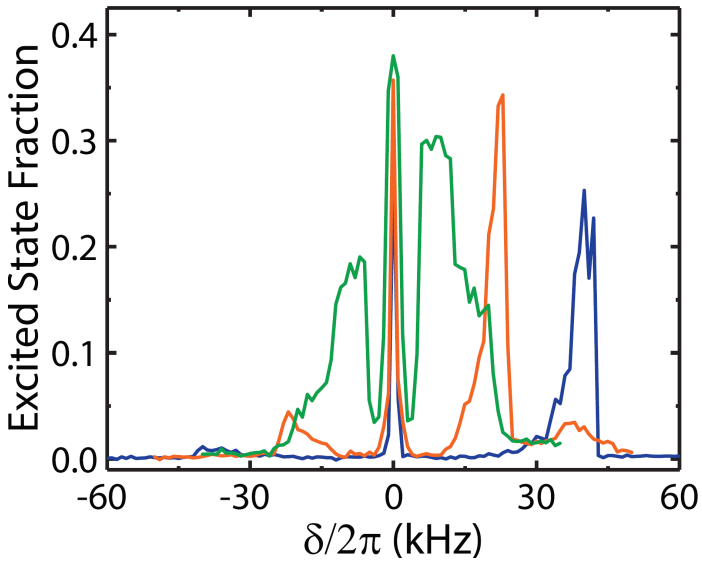

Figure 7.12: Three different sideband scans at lattice depths $U_z/E_{rec} = 5.5$ (green), $U_z/E_{rec} = 17.4$ (red), and $U_z/E_{rec} = 43.9$(blue). As the lattice depth decrease the sideband scans gets closer to an axial Doppler scan.

By lowering the lattice depth the sidebands move towards the carrier. Figure 7.12 shows the

effects of lowering the retro-reflected lattice power P_2 on the sideband structure. For lower lattice depths the sidebands merge together to form a gaussian distribution of atoms.

7.8 Band Relaxation

During the course of these experiments it was discovered that sometimes when the atoms were being prepared in the first excited band $|e\rangle_1$ band relaxation was observed. This was observed both in the splitting of the carrier transition (see section 7.9) and the location of the sideband transitions for different axial bands (see section 7.7). At first this was thought to be due to the ramping of the lattice but the amount of relaxation was found to be independent of the ramping time and also found to occur without any ramping taking place.

It was found that this band relaxation is due to s-wave collisions between atoms in $|g\rangle_0$ and atoms in $|e\rangle_1$ (Fig. 7.13). In both Fig. 7.13(a) and (b) a sideband scan for atoms in $|e\rangle_0$ (blue, dashed) and $|e\rangle_1$ (red, dashed) are shown. If the atoms in $|g\rangle$ are removed straight after band selection, as in Fig. 7.13 (b) to $|e\rangle_1$ then no band relaxation is observed. If however the atoms in $|g\rangle_0$ are not removed straight away and are held in the lattice with the $|e\rangle_1$ atoms before being removed then band relaxation is clearly seen in Fig. 7.13(a).

7.9 Carrier Transition and Band Mapping

For $J = 0$ the excited state fraction, p_e, for detuning, δ, is described by the function

$$p_e(\delta) = \frac{|\Omega_{eg}|^2}{|\Omega_{eg}|^2 + [\delta - \omega_z(n_e - n_g)]^2} \sin^2\left(\frac{t}{2}\sqrt{|\Omega_{eg}|^2 + [\delta - \omega_z(n_e - n_g)]^2}\right) \tag{7.22}$$

For the case of $J \neq 0$ we need to take into account the changing density of states. To do this we can convolve the lineshape given above with the joint transition density of states as a function of δ, which is given by

$$D(\delta) = \begin{cases} \frac{1}{\sqrt{[4J\sin(\phi/2)]^2 - \delta^2}} & -|4J\sin(\phi/2)| \leq \delta \leq |4J\sin(\phi/2)| \\ 0 & \text{otherwise} \end{cases} \tag{7.23}$$

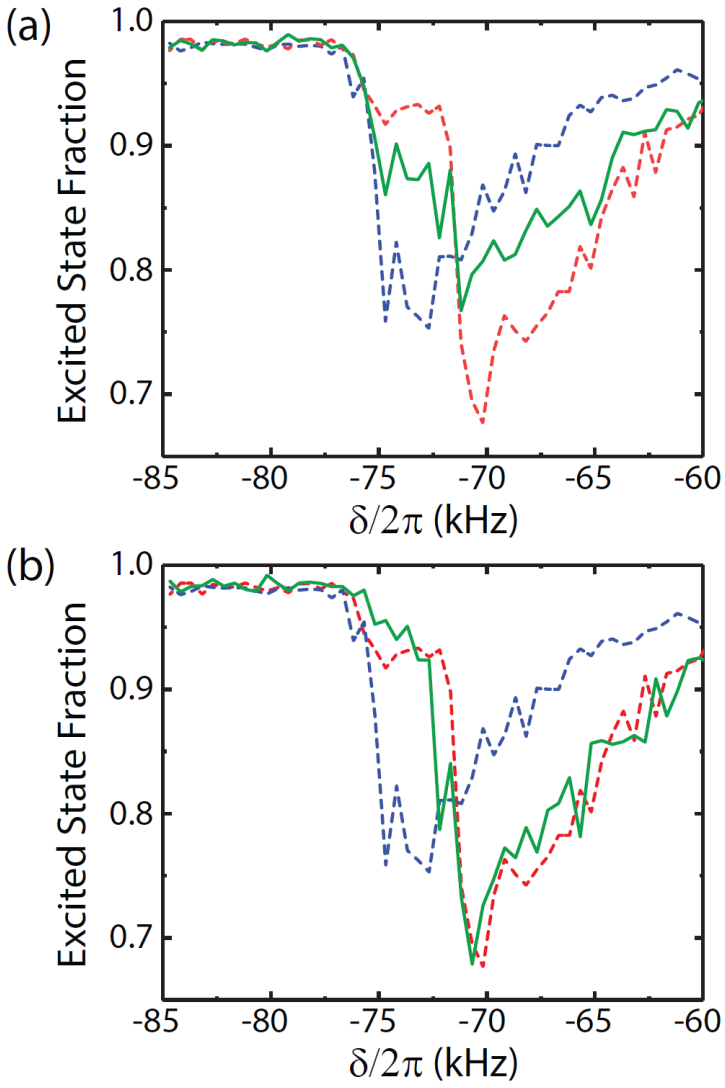

Figure 7.13: Band relaxation caused by s-wave collisions. The red and blue traces, in both plots, show the red detuned sideband for the $|e\rangle_1$ and $|e\rangle_0$ bands respectively. **(a)** Atoms are excited to $|e\rangle_1$ and are held for 200 ms before removing atoms in $|g\rangle_0$ and scanning the sideband (green trace). Atoms can be seen to be present in both $|e\rangle_1$ and $|e\rangle_0$ due to band relaxation caused by the presence of ground state atoms during the hold time. **(b)** Atoms are excited to $|e\rangle_1$ and the ground state atoms are removed before holding for 200 ms and then scanning the sideband (green trace). Atoms can be seen to be present in only $|e\rangle_1$ and no band relaxation is observed.

The convolution can be solved numerically and Fig. 7.14 shows the resulting convolutions for different tunneling rates using a 160 ms π-pulse. For $J/(2\pi) = 0$ Hz the convolution gives the normal Rabi lineshape given in Eq. 7.22. As J increases the lineshapes broadens and two peaks appears. These two peaks arise due to the divergences in the density of states shown in Fig. 7.3, also known as Van Hove Singularities.

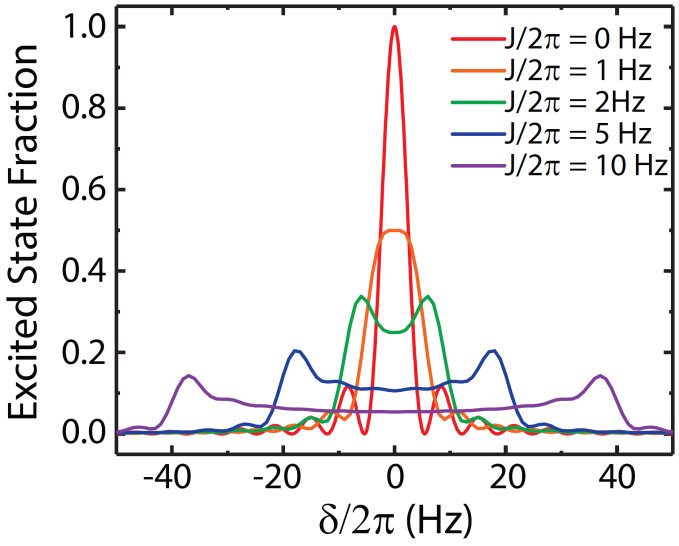

Figure 7.14: The theoretical carrier transition for different tunneling rates and a 160 ms π-pulse. The solutions are numerically integrated convolutions of the joint transitional density of states and the sinc^2 Rabi lineshape.

A comparison between data and a theory prediction is shown in Fig. 7.15 for a 5 ms π-pulse and a tunneling rate $J/(2\pi) = 87$ Hz. The π-pulse is set using a high lattice ($J = 0$ Hz) before lowering the lattice depth and scanning the detuning of the clock laser δ and the excitation fraction is measured in the usual way. We can see that the theory agrees well with the experimental data. Figure 7.16 shows the effect of changing the π-pulse time on the carrier transition. For longer (weaker) pulses the splitting of the Van Hove Singularities is still visible spectroscopically. As the strength of the pulse is increased the splitting is no longer visible anymore. The reason for this is that the Fourier limited linewidth is increasing and becomes larger than the Van Hove splitting.

The results of changing the pulse area are shown in Fig. 7.17 for the carrier transition in the

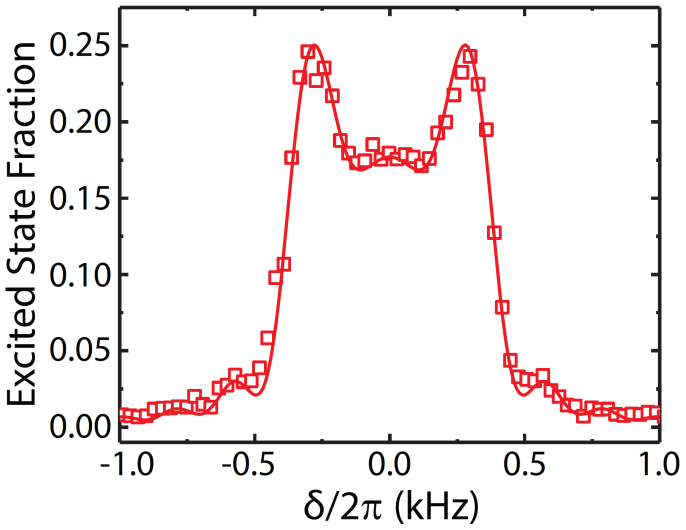

Figure 7.15: Carrier transition in the ground band $|g\rangle_0 \rightarrow |e\rangle_0$ with a comparison of the measured lineshape (red, squares) for a 5 ms π-pulse with $J/(2\pi) = 87$ Hz. The theory prediction (red, solid line) is from the convolution of the joint transitional density of states and the sinc^2 Rabi lineshape. The overall amplitude has been scaled by 0.9 for better theory-experiment agreement.

first excited band $|e\rangle_1 \rightarrow |g\rangle_1$. Two different pulse areas are shown including a π-pulse (red lines)

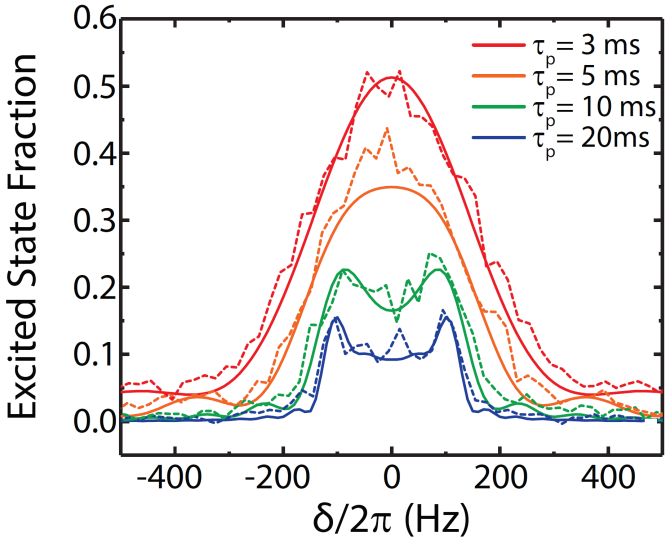

Figure 7.16: Carrier transition in the ground band, $|g\rangle_0 \rightarrow |e\rangle_0$, for $J/(2\pi) = 30$ Hz with different Rabi frequencies. The data is shown as dashed lines and the theory is solid lines for π-pulse times of 3 ms (red), 5 ms (orange), 10 ms (green), and 20 ms (blue). Each theory line has been scaled by an overall amplitude which is the same for each.

and a 3π-pulse (blue lines) where the experimental data (dashed) agrees well with the theory lines (solid). It should be noted that for other pulse areas the amplitude scaling does not agree [151]

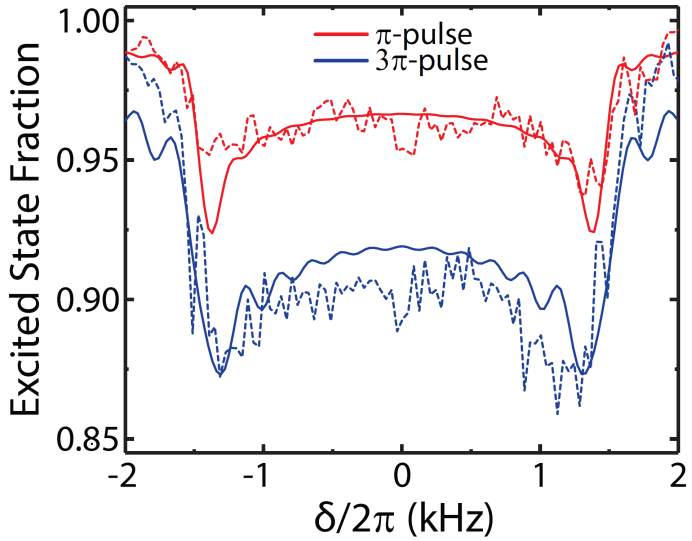

Figure 7.17: Carrier transition in the first excited band, $|e\rangle_1 \rightarrow |g\rangle_1$, for different pulse areas with data shown as dashed lines and theory as solid lines and $J/(2\pi) = 370$ Hz. The π-pulse (red) and 3π-pulse (blue) agree well with theory lines.

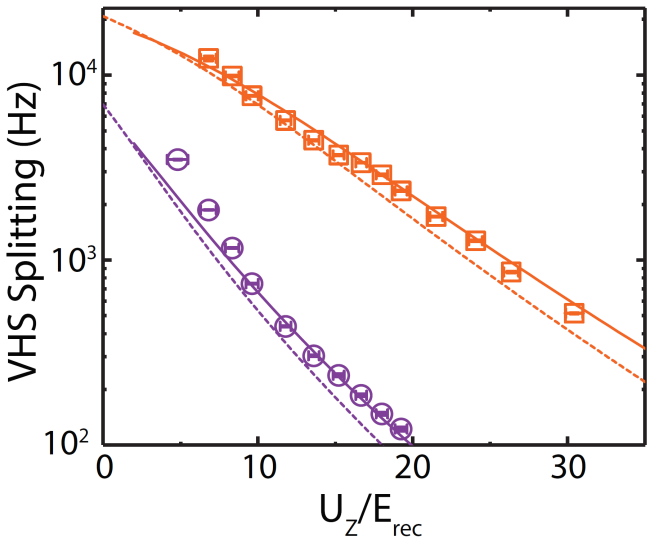

Figure 7.18: Carrier transition splitting for different lattice depths for the $|g\rangle_0 \rightarrow |e\rangle_0$ transition (purple, circles) and the $|e\rangle_1 \rightarrow |g\rangle_1$ transition (orange, squares). The splitting is extracted using fits from a convolution of a lorentzian lineshape and the density of states and the lattice depth is extracted from the sideband scan.

7.10 Quasimomentum selection and Bloch Oscillations

From previous sections we have found that the splitting of the lineshape corresponds to different quasimomenta at different detunings. Therefore, just as the spectroscopically resolved sidebands enable band preparation, the quasimomentum dependence of the clock transition frequency enables the selective preparation and subsequent manipulation of atoms with particular quasimomenta. Following initialization in the $|g\rangle_0$ state, a clock pulse with Rabi frequency $\Omega < 2\Delta$, where $\Delta = 4J|\sin(\phi/2)|$ is the largest momentum-induced detuning from the bare clock transition frequency, is applied to the carrier transition with a clock laser detuning $\delta^* \leq \Delta$. Only atoms with quasimomenta in a window centered around $q^* \approx \arccos(\delta^*/\Delta)$ and with a width bounded by $2\pi\Omega/\Delta$ will be excited to $|e\rangle_0$. Atoms outside this window will be left in $|g\rangle$ and a strong 5 ms pulse of 461 nm light removes them from the lattice. Following a variable hold time, a second π-pulse

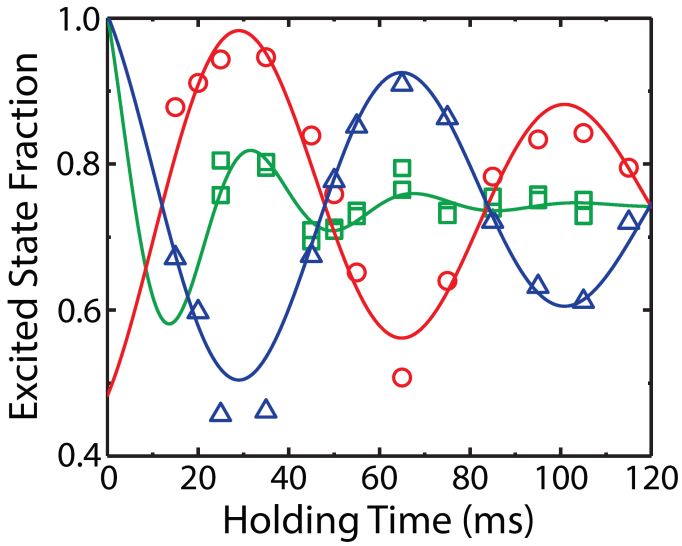

Figure 7.19: The excited state fraction of the Van Hove Singularities (VHSs) versus holding time with fits is shown for a tilted lattice. When only atoms from the left VHS are excited ($q \sim 0$), the left VHS peak height (red, circles) and the right VHS (blue, triangles) oscillate with time. When atoms are excited at the center of the lineshape the VHS peak heights (green, squares) oscillate twice as fast as when $q \sim 0$ atoms are initially prepared. In both case we see the oscillations amplitude decrease with time due to diffusion of quasimomentum and after long times all quasimomentum are occupied.

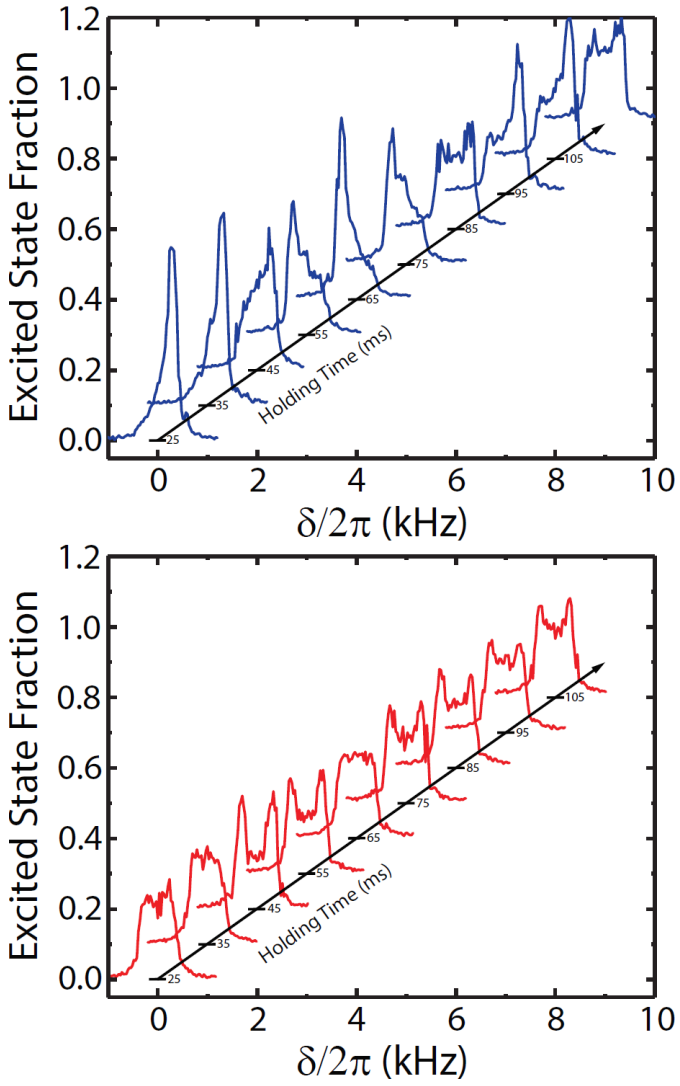

Figure 7.20: With a tilt in the lattice the quasimomentum selection of atoms undergoes Bloch oscillations. A range of quasimomentum can be selected by applying a π-pulse to the line splitting. Shown above are for atoms selected from the left Van Hove singularity (top) and in the center of the lineshape (bottom) and then removing any atoms that are not excited to the excited state.

can be used to measure the new lineshape. If the lattice is tilted with respect to gravity then the atoms will undergo Bloch oscillations during the hold time, with their quasimomenta evolving as

$$q(t) = q_0 + \nu_B t \tag{7.24}$$

where q_0 is the initial quasimomentum of the atom and the value $q(t)$ is restricted to the first Brillouin zone. The Bloch oscillation frequency ν_B is given by

$$\nu_B = \frac{mg\lambda_L \sin(\theta_L)}{4\pi\hbar} \tag{7.25}$$

with g the acceleration due to gravity and θ_L is the angle of the lattice tilt measured from the horizontal.

Figures 7.19 shows how the excitation fraction of the VHSs change with time when undergoing Bloch oscillations. When δ^* is detuned to the left VHS the excitation fraction of the left VHS (red, circles) and right VHS (blue, triangles) can be seen to oscillate with a period of 70 ms indicating a Bloch oscillation frequency of 14 Hz and a lattice tilt $\theta_L = 16$ mRad. When the atoms are excited in the center of the lineshape, $\delta/(2\pi) = 0$, the Bloch Oscillations appear to be twice as fast (green, squares). The reason for this is that when atoms are excited in the center of the lineshape the solution of q^* from above has two solutions. This leads to two groups of atoms being excited and running through quasimomentum space giving the appearance of the oscillations being twice as fast. The complete lineshape data from which this data is extracted is shown in Fig. 7.20 for the case of atoms excited on the left VHS (blue, solid lines) and excitation at the center of the lineshape (red, solid lines).

7.11 Chiral Bloch Vector

The eigenstates of the Hamiltonian $\hat{H}_{SOC}$ (Eq. 7.20) can be described by Bloch vectors in the $\hat{Y} - \hat{Z}$ plane of the Bloch sphere (see Fig. 7.21). They point along the direction of the quasimomentum dependent dependent magnetic field $\mathbf{B}_{SOC}(q_i, \mathbf{n}_{\mathbf{r}_i}, \Omega, \delta)$ with their orientation specified

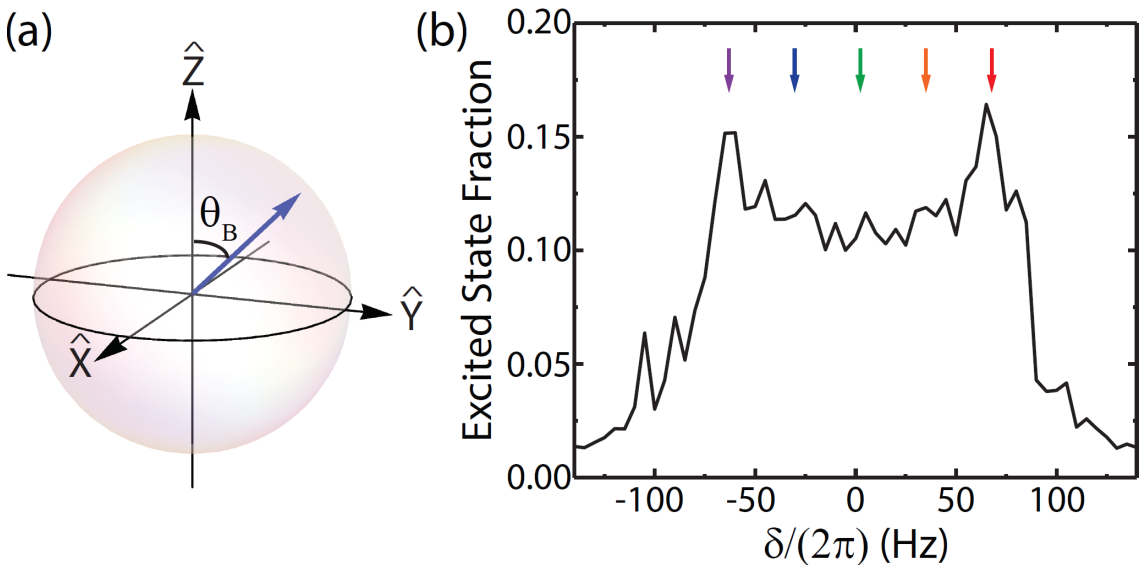

Figure 7.21: **(a)** Chiral Bloch vector on the Bloch spher points in the $\hat{Y}$-$\hat{Z}$ plane at an angle of θ_B with respect to the $\hat{Z}$ axis in the direction of the quasimomentum dependent magnetic field, $\mathbf{B}_{SOC}(q_i, \mathbf{n}_{\mathbf{r}_i}, \Omega, \delta)$. This magnetic field causes a rotation of the Bloch vector around this direction. **(b)** The tunneling rate is set to $J/(2\pi) \sim 16$ Hz and a 50 ms π-pulse is used to select atoms with different q by setting the clock laser detuning to those indicated by the arrows.

by the chiral Bloch vector angle, θ_B, with respect to the $\hat{Z}$ axis and is given by

$$\theta_B = \arctan\left[\frac{\Omega}{(E_{n_z}(q) - E_{n_z}(q+\phi))/\hbar + \delta}\right] \tag{7.26}$$

where the q dependence of θ_B is a manifestation of chiral spin-momentum locking [135, 153]. In the description of the system as a synthetic gauge field the chiral Bloch vector angle is directly connected to the topological nature of chiral edge modes of the two-dimensional Hofstadter model [154, 153]. Coupling multiple nuclear spin states with our synthetic gauge fields should enable the realization of topological bands and exotic phases in higher dimensions.

We can characterize the q dependence of the chiral Bloch vector angle using the same quasi-momentum selection technique that was used to observe Bloch oscillations in Section 7.10. For these measurements the lattice tilt was adjusted to minimize the Bloch oscillation frequency $\nu_B \leq 3$ Hz such that the motion is not dominated by Bloch oscillations. In order to extract a chiral angle we therefore need to determine the effective detuning $\delta_{eff} = \delta + (E_{n_z}(q) - E_{n_z}(q+\phi))/\hbar$ which is

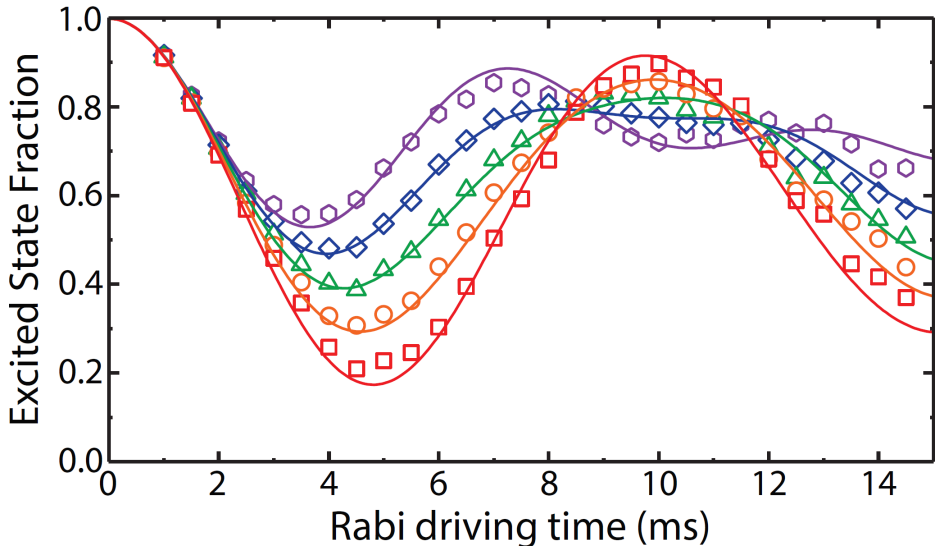

Figure 7.22: Rabi flopping of different quasimomenta. The line splitting is set to 125 Hz ($J/(2\pi) \sim 16$ Hz) and quasimomenta are selected with five equally spaced detunings, red→purple data $\delta/(2\pi) = \{-62.5, -31.25, 0, 31.25, 62.5\}$ Hz using a 50 ms π-pulse. Each q-selection then undergoes Rabi flopping with the clock laser detuned to the right VHS, $\delta/(2\pi) = +62.5$ Hz and a 5 ms π-pulse. The shapes are data and the lines are theory fits.

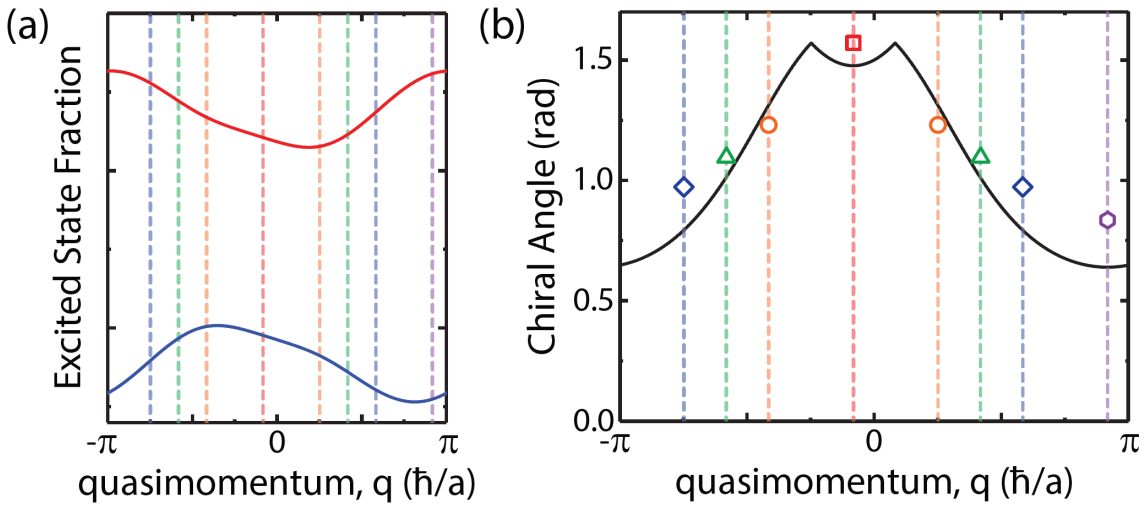

Figure 7.23: **(a)**Spin-orbit coupled band structure during the Rabi flopping, showing the q selection regions as dashed lines corresponding to the colors in Fig. 7.22. **(b)** The extracted Chiral angles for the different q-selections by fitting the data in Fig. 7.22. The black solid line is a theory fit using Eq. 7.26.

made up of the normal laser detuning δ and the additional detuning brought about by tunneling. We can therefore perform a Rabi flopping measurement on our selected quasimomenta and extract an effective detuning.

For this measurement the tunneling rate is set to $J/(2\pi) \sim 16$ Hz and five separate experiments are performed. In each case atoms are prepared in $|e\rangle_0$ using a weak 50 ms π-pulse ($\Omega = 2\pi \times 10$ Hz) and all remaining $|g\rangle$ atoms are removed. For the five experiments, atoms are selected with a clock laser detuning of $\delta/(2\pi) = \{-62.5, -31.25, 0, 31.25, 62.5\}$ Hz as indicated in Fig. 7.21 and thus selecting different quasimomenta groups. Each of these quasimomenta then undergo Rabi flopping as a second pulse with $\Omega = 2\pi \times 100$ Hz is applied with $\delta/(2\pi) = 62.5$ Hz. The resulting Rabi flopping data are shown in Fig. 7.22 where the colors correspond to the q-selection detunings shown in Fig. 7.21.

From this data we can fit each individual curve with a cosine fitting function

$$fit_{Chiral} = A + B\frac{\Omega^2}{\Omega^2 + \delta_{eff}^2}\cos\left[\sqrt{\Omega^2 + \delta_{eff}^2}t\right] \tag{7.27}$$

where A is a constant, $B = B(t)$ is a time varying exponential envelope common to all curves, and we set $\Omega = 2\pi \times 100$ Hz. From these fits we therefore extract the effective detuning δ_{eff} and use this to calculate the chiral angle by

$$\theta_B = \arcsin\left[\frac{\Omega}{\sqrt{\Omega^2 + \delta_{eff}^2}}\right] \tag{7.28}$$

The extracted chiral angles are shown in Fig. 7.23 plotted aginst the theory prediction of Eq. 7.26 alongside the band structure during Rabi flopping. We should note that the theory line assumes only a single value of q is initially selected but a range of q values around the central value are experimentally excited, thus the theory fit is not ideal. The theory lines shown in Fig. 7.22 include the different values of q.

7.12 Ramsey Spectroscopy with SOC

To observe the dynamics of our spin-orbit coupled system we can perform Ramsey spectroscopy. Ramsey Spectroscopy for a single group of non-interacting atoms was discussed in section

6.3, now we can consider the case of Ramsey spectroscopy when SOC is included. An initial pulse with a strong Rabi frequency, and hence short pulse time and large spectral bandwidth, of area θ_1 and $\delta = 0$ excites all atoms into a coherent superposition of clock states that are then allowed to freely evolve during τ. Although the clock laser is off during this period, the atoms accumulate a phase in the rotating frame of the laser and thereby retain the imprinted optical phase. As a result, the atoms continue to experience the SOC induced effective magnetic field $\mathbf{B}_{SOC}(q_i, \mathbf{n}_{\mathbf{r}_i}, \Omega{=}0, \delta{=}0)$ throughout the dark time τ. One observable we measure using this procedure is the Ramsey fringe contrast, defined as $\mathcal{C} = 2\sqrt{\left\langle \hat{S}^X \right\rangle^2 + \left\langle \hat{S}^Y \right\rangle^2}/N$, which is the length of the projection of the collective magnetization in the $\hat{X} - \hat{Y}$ plane of the Bloch sphere. Here $\hat{\mathbf{S}} = \left[\hat{S}^X, \hat{S}^Y, \hat{S}^Z\right]$ are collective spin operators with $\hat{S}^{\{X,Y,Z\}} = \sum_{i=1}^{N} \hat{S}_i^{\{X,Y,Z\}}$.

The concentration of atoms at the two Van Hove singularities allows us to qualitatively understand the ensuing dynamics as arising mainly from these two groups of atoms, with quasimomenta $q \sim 0$ and $q \sim \pi$, and corresponding detunings of $\delta_{\pm}$, respectively. Figure 7.24 depicts the Bloch sphere visualization of Ramsey spectroscopy for the case when the two groups are non-interacting

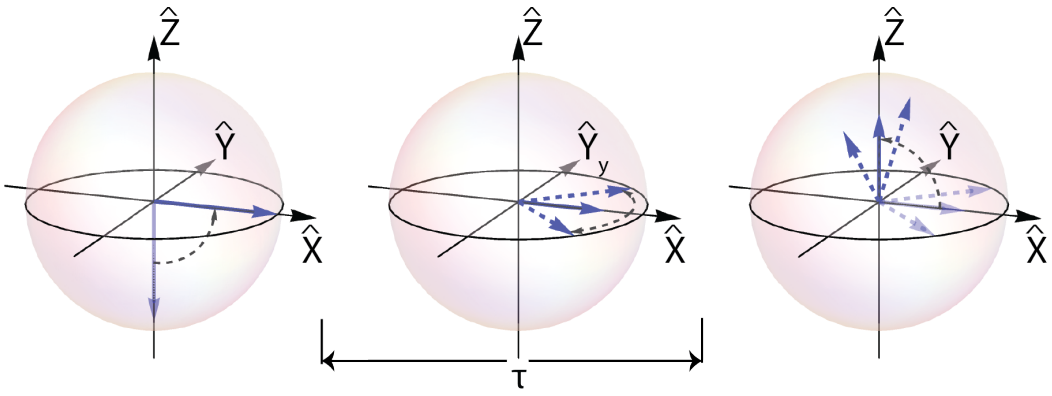

Figure 7.24: Ramsey Spectroscopy with SOC for two groups of atoms with $q \sim 0$ and $q \sim \pi$. An initial strong $\pi/2$ pulse creates a superposition of $|g\rangle$ and $|e\rangle$. During the dark time τ the atom evolves around the Bloch sphere at a rate proportional to the detuning between the laser and the atom resonance. A second $\pi/2$ pulse projects the atoms into the population of $|g\rangle$ and $|e\rangle$

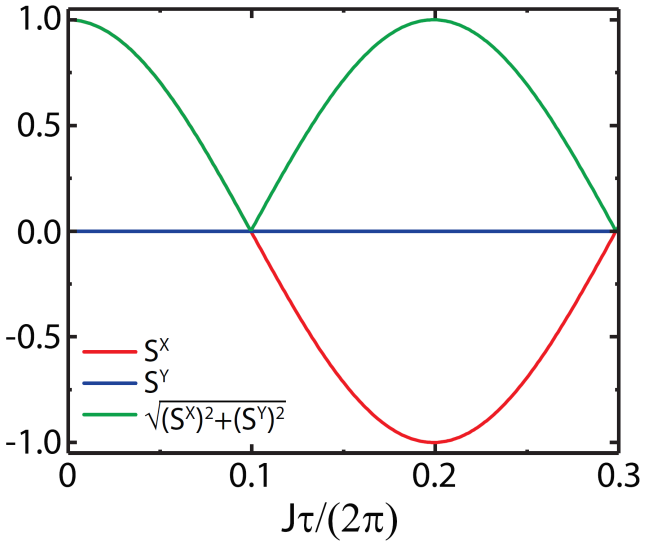

Figure 7.25: Normalized collective Bloch vector components and contrast for Ramsey spectroscopy with 2-atom groups. S^Y remains zero for all times as the Y components for the two groups of atoms cancel. S^X oscillates as the two Bloch vectors rotate around the Bloch sphere leading to a contrast that varies between zero and one.

and for $\theta_1 = \pi/2$. For a variable evolution time τ, the atoms with opposite detunings $\delta_\pm$ evolve around the equator of the Bloch sphere in opposite directions (dashed blue arrows). Consequently, the length of the collective spin vector (solid blue arrow) changes, but the vector direction remains parallel or anti-parallel to $\hat{X}$.

Mathematically we know that the rate of precession of the Bloch vector is proportional to the detuning. As we set the laser detuning $\delta = 0$ we know that the extra detuning is coming from the band structure such that $\delta_{eff} = \delta + \Delta E_n(q) = \Delta E_n(q)$. For the case of our model of two groups of atoms at $q \sim 0$ and $q \sim \pi$ the components of the Bloch vector are given by

$$S^X_{\text{2-atom}} = \sin(\theta_1)\frac{1}{2}\left(\cos\left[\delta_{eff}\tau\right] + \cos\left[\delta_{eff}\tau\right]\right) \tag{7.29}$$

$$S^Y_{\text{2-atom}} = \sin(\theta_1)\frac{1}{2}\left(\sin\left[\delta_{eff}\tau\right] + \sin\left[\delta_{eff}\tau\right]\right) = 0 \tag{7.30}$$

As the initial pulse is around S^Y the atom groups with opposite detunings evolve symmetrically from the $\hat{X}$ axis in opposite directions and the S^Y components from each group of atoms cancel to give a collective $S^Y_{\text{2-atom}} = 0$ at all times. The $S^X_{\text{2-atom}}$ component evolves in time and is shown in

Fig. 7.25 for $\theta_1 = \pi/2$ (red, solid). The contrast (green, solid) starts off at 1 and tends towards zero as $J\tau/(2\pi)$ increases. The contrast then revives and goes back to full scale. We can understand these zeroes of the contrast as the two groups of atoms accumulating a phase difference of π leading to the length of the collective Bloch vector to be zero ($\mathcal{C} = 0$).

Representative contrast curve measurements are shown in Fig. 7.26 for tunneling rates $J_1/(2\pi) =$ 3.2 Hz (green triangles) and $J_2/(2\pi) = 17.6$ Hz (blue circles) as a function of τ. This data was taken in the non-interacting regime by using a small number of atoms ($N < 500$). The collapses and revivals in the contrast can be readily understood from the simple model of the two atom groups. The detuning, $\delta_\pm \approx \pm 4J$ determines the precession rate around the Bloch sphere and we thus expect the contrast to collapse and revive with a periodicity proportional to $1/J$. Figure 7.26 also shows the contrast data with the x-axis scaled as a function of $J\tau/(2\pi)$, illustrating that the contrast curves for different J values then collapse onto a single curve.

An obvious feature of the observed contrast evolution is the long term decay, which is not captured by the simple two-group approximation. While the joint density of states is the largest at the Van Hove Singularities, all q values are in fact populated, with atoms contributing at detunings in-between $\delta_\pm$. Integrating over the contributions from all q the components of the collective Bloch vector and contrast are given by

$$S^X_{\text{All q}} = \sin(\theta_1)\frac{1}{2\pi}\int_{-\pi}^{\pi}\cos\left[\Delta E_n(q)\tau\right]dq = \sin(\theta_1)\mathcal{J}_0\left[4J\tau\sin\left(\phi/2\right)\right] \tag{7.31}$$

$$S^Y_{\text{All q}} = \sin(\theta_1)\frac{1}{2\pi}\int_{-\pi}^{\pi}\sin\left[\Delta E_n(q)\tau\right]dq = 0 \tag{7.32}$$

$$\mathcal{C} = \sqrt{(S^X_{\text{All q}})^2 + (S^Y_{\text{All q}})^2} = \sin(\theta_1)|\mathcal{J}_0\left[4J\tau\sin\left(\phi/2\right)\right]| \tag{7.33}$$

where $\mathcal{J}_0$ is a zeroth order Bessel function of the first kind, as shown in Fig. 7.26.

To validate that the collapses, revivals, and overall decay in contrast are due to $\mathbf{B}_{SOC}(q_i, \mathbf{n}_{\mathbf{r}_i}, \Omega, \delta)$, we can remove its effect by adding a spin echo pulse to the Ramsey sequence. Any dephasing from the static SOC-induced effective magnetic field during the first $\tau/2$ period of free evolution will re-phase during the second $\tau/2$ free evolution period, due to the π echo pulse, which flips the sign of

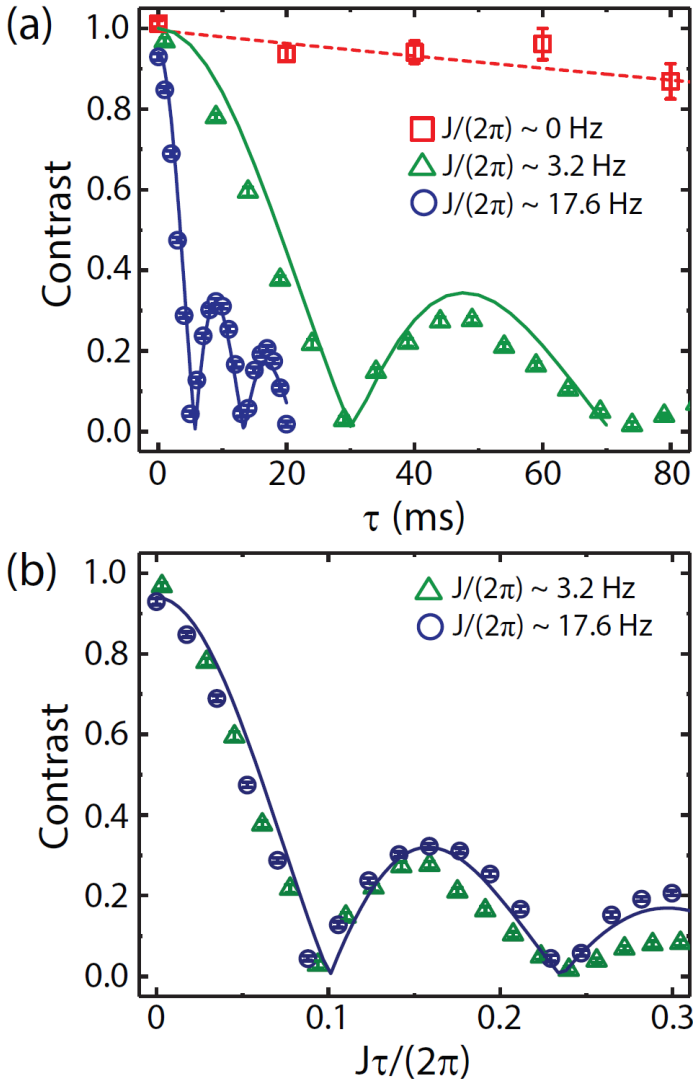

Figure 7.26: **(a)** Ramsey Spectroscopy with SOC for different tunneling rates as a function of dark time, τ. The data shows an oscillation with a magnitude given by a Bessel shaped oscillation. **(b)** The data for different, finite, tunneling rates scales to the same curve when scaled to $J\tau$. The solid lines are theory curves, and the dashed line is an exponential fit with a decay constant of 0.6 s, and the error bars are 1σ confidence intervals.

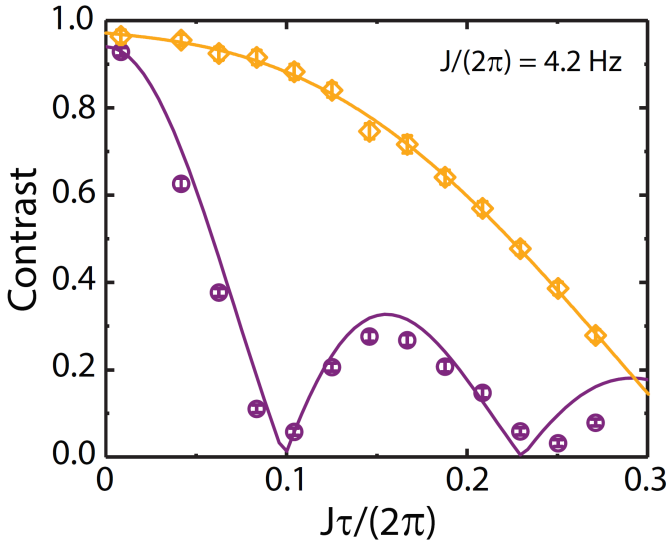

Figure 7.27: Ramsey spectroscopy with a spin-echo pulse. A spin echo pulse (orange, diamonds) removes the static dephasing caused by SOC for a Ramsey sequence for the same J (purple circles, theory is solid purple line). The spin-echo data is a fit $\propto e^{-(\tau/\tau_d)^3}$.

phase accumulation. Figure 7.27 shows the effect of spin echo (orange diamonds) for $J/(2\pi) = 4.2$ Hz. The spin echo eliminates the collapses and revivals from the Ramsey fringe contrast (purple circles), and prolongs the overall contrast decay. However, the observed decay in contrast at long times is still fast compared to the contrast decay time for $J = 0$ (~ 1 s). Contrast decays under spin echo for different values of J are shown in Fig. 7.28. The spin echo decays do not collapse to a single curve when the free evolution time is scaled to $J\tau/(2\pi)$, indicating that the additional dephasing does not scale linearly with J, and that quasimomentum is not conserved at large τ. It is this additional dephasing that results in the suppression of the revivals in contrast at lower tunneling rates as shown in Fig. 7.26 (green triangles).

For $J > 1$ Hz, the SOC-induced dephasing dominates over all other dephasing mechanisms in our clock. While our Hamiltonian accounts for the static dephasing, a systematic investigation of the relevant range of J reveals that the spin echo data has an additional decay with the functional form of $\propto e^{-(\tau/\tau_d)^3}$ as shown in Fig. 7.27. This form of spin echo decay is well known from NMR and solid-state spin defect experiments [155, 156], where the dephasing is the result of a slow,

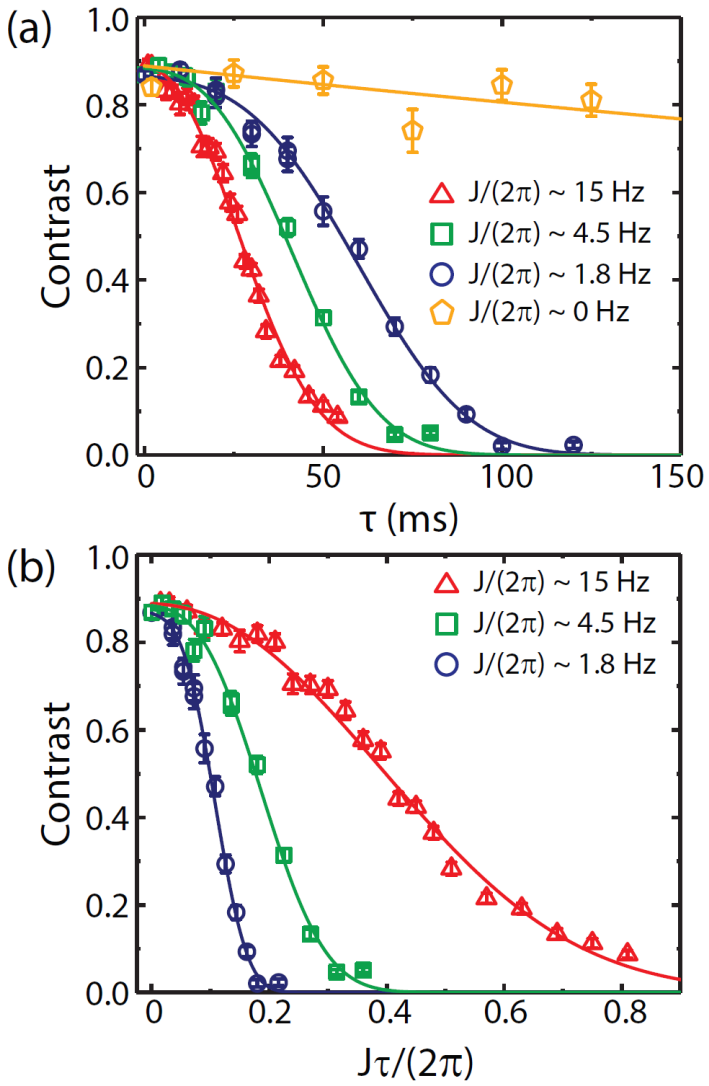

Figure 7.28: **(a)** Spin echo decay of contrast for four different J values as a function of τ **(b)** Same data as in **(a)** (for non-zero J) as a function of $J\tau$. All $J > 0$ curves decay as $\propto e^{-(\tau/\tau_d)^3}$, where τ_d is a nonlinear function of J, implying an extra diffusive dephasing, and do not collapse to a single curve when the free precession time is rescaled to $J\tau$. For $J = 0$ the echo data decays $\propto e^{-(\tau/\tau_{d_0})}$. All error bars are from individual contrast fits, and all solid lines for the $J > 0$ ($J = 0$) echo data are fits $\propto e^{-(\tau/\tau_d)^3}$ ($e^{-(\tau/\tau_{d_0})}$).

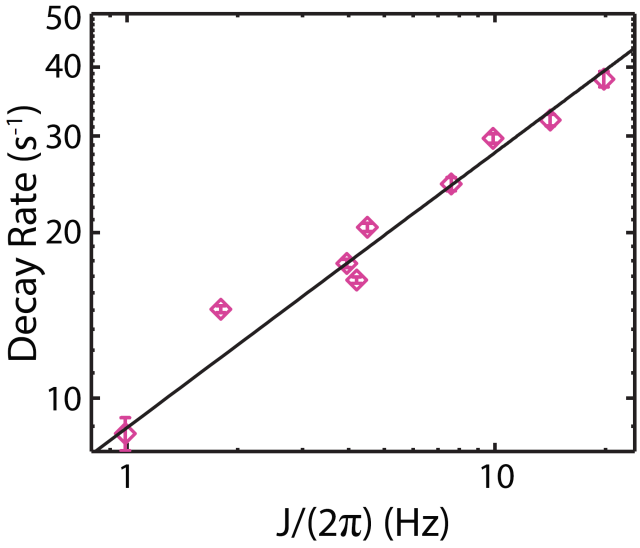

Figure 7.29: A log-log plot of the decay rates $(1/\tau_d)$ as a function of J for different lattice depths show a J dependence consistent with a $1/\tau_d \propto J^{1/2}$. The error bars come from fits of τ_d and the solid line is a best fit curve using $1/\tau_d \propto J^{1/2}$.

random diffusion of magnetic field with time. In our case this corresponds to a diffusion of the SOC effective magnetic field $\mathbf{B}_{SOC}(q)$, indicating that the quasimomentum is not conserved at large τ. The extracted decay rate $(1/\tau_d)$ for different J is shown in Fig. 7.29. The scaling is consistent with $1/\tau_d \propto J^{1/2}$. We observe the same scaling of decay rate with J for the Ramsey sequences, and include this decay in our theory model as an empirical parameter. The most likely mechanism for this empirically observed diffusion of $\mathbf{B}_{SOC}$ is the coupling of axial motion to the thermally populated radial modes. The spatial inhomogeneity in J across the lattice due to the finite Rayleigh range of the lattice beams may also contribute.

We can also use the quasimomentum selection techniques discussed above in section 7.10 to show that the zeroes in the Ramsey contrast are due to the cancellation of the different VHSs. The data in Fig. 7.30 (orange, squares) shows the Ramsey contrast in the case where atoms are selected preferentially from one of the VHSs. For comparison the case without quasimomentum selection is also shown (purple, circles). We can see that for the case of quasimomentum selection we no longer get any zeroes in the contrast and the contrast remains finite.

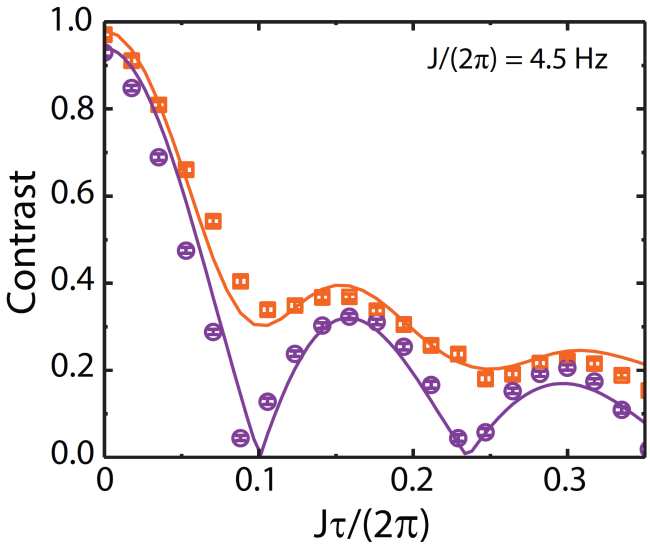

Figure 7.30: Ramsey spectroscopy with q-selection. Atoms are preferentially selected from the right VHS and the other atoms are removed (orange, squares). For comparison the contrast curve for the same tunneling rate is shown without quasimomentum selection (purple, circles).

7.13 Ramsey Spectroscopy with SOC and Interactions

Having characterized the single particle Ramsey dynamics under SOC, we introduce interactions by increasing the atomic density. As shown in Figs. 7.31 and 7.32, signatures of strong spin interactions start to emerge as N increases. The blue circles are the case of no interactions ($N < 500$) and red squares are the case where we introduce interactions by increasing the atom number by more than an order of magnitude ($N \sim 1 \times 10^4$). We observe in Fig. 7.31 that for an initial Ramsey pulse $\theta_1 = \pi/4$, an increase in atomic density qualitatively alters the dynamics, suppressing the collapses in contrast observed for the low density case. For $\theta_1 = \pi/2$ we observe that interactions shift the zeroes of the contrast compared to the non-interacting case (Fig. 7.32), and by further increasing the density and reducing the tunneling rate, we see that the first collapse of the contrast can be suppressed altogether. We note that for $J = 0$ the contrast decay has been previously seen to be highly sensitive to the initial Ramsey pulse area and no contrast revival with interactions has been observed [15, 141].

In order to quantitatively understand the complex interplay between interactions and SOC,

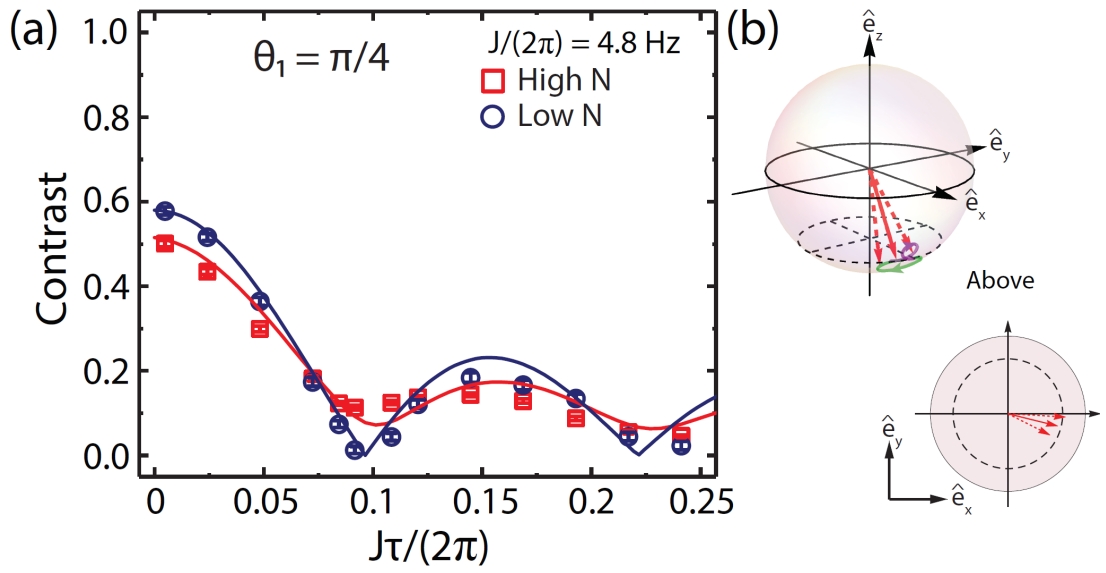

Figure 7.31: **(a)** Ramsey spectroscopy with interactions for an initial pulse of area $\theta_1 = \pi/4$. Without interactions (blue, circles) the overall amplitude is reduced from the $\theta_1 = \pi/2$ case because of the $\sin(\theta_1)$ amplitude of the contrast. With interactions (red, squares) the contrast no longer goes to zero due to the rotation caused by the exchange interactions. **(b)** On the Bloch sphere, as the VHSs (dashed arrows) rotate around the Bloch sphere they become distinguishable and exchange interactions induce rotations shown as purple and green trajectories. For $\theta_1 = \pi/4$ this rotation leads to the Bloch vectors for the two VHSs being of unequal length in the $\hat{X} - \hat{Y}$ plane so that the collective spin vector (solid arrow) remains finite.

we consider the spin model that has previously been successfully used to understand many-body interactions in optical lattice clocks [15, 141]. During these measurements all atoms are initially prepared in the $|g\rangle$ spin state, and each atom occupies a single motional mode in the lattice. The initial mode distribution is preserved during clock interrogation as the collision energy is insufficient to alter the motional eigenstates. Since the motional degrees of freedom are frozen, we can treat the single-particle modes as corresponding lattice sites spanning an energy space. Thus, s-wave and p-wave contact interactions are mapped into non-local, infinite-range collective interactions between the electronic pseudospins in the energy-space lattice [15]. The Hamiltonian for our system, including interactions, then becomes $\hat{H} = \hat{H}_{SOC} + \hat{H}_{\text{int}}$, with $\hat{H}_{\text{int}}$ given by,

$$\hat{H}_{\text{int}}/\hbar = \frac{\chi^+}{L}\left(\hat{S}^Z\right)^2 + \frac{C^+}{L}(N)\,\hat{S}^Z + \frac{\xi^+}{L}\hat{\mathbf{S}}\cdot\hat{\mathbf{S}}. \tag{7.34}$$

The spin couplings $\chi^+ = (V_{gg} + V_{ee} - 2V_{eg})/2$, $C^+ = (V_{ee} - V_{gg})/2$, and $\xi^+ = \left(V_{eg} - U_{eg}^-\right)/2$

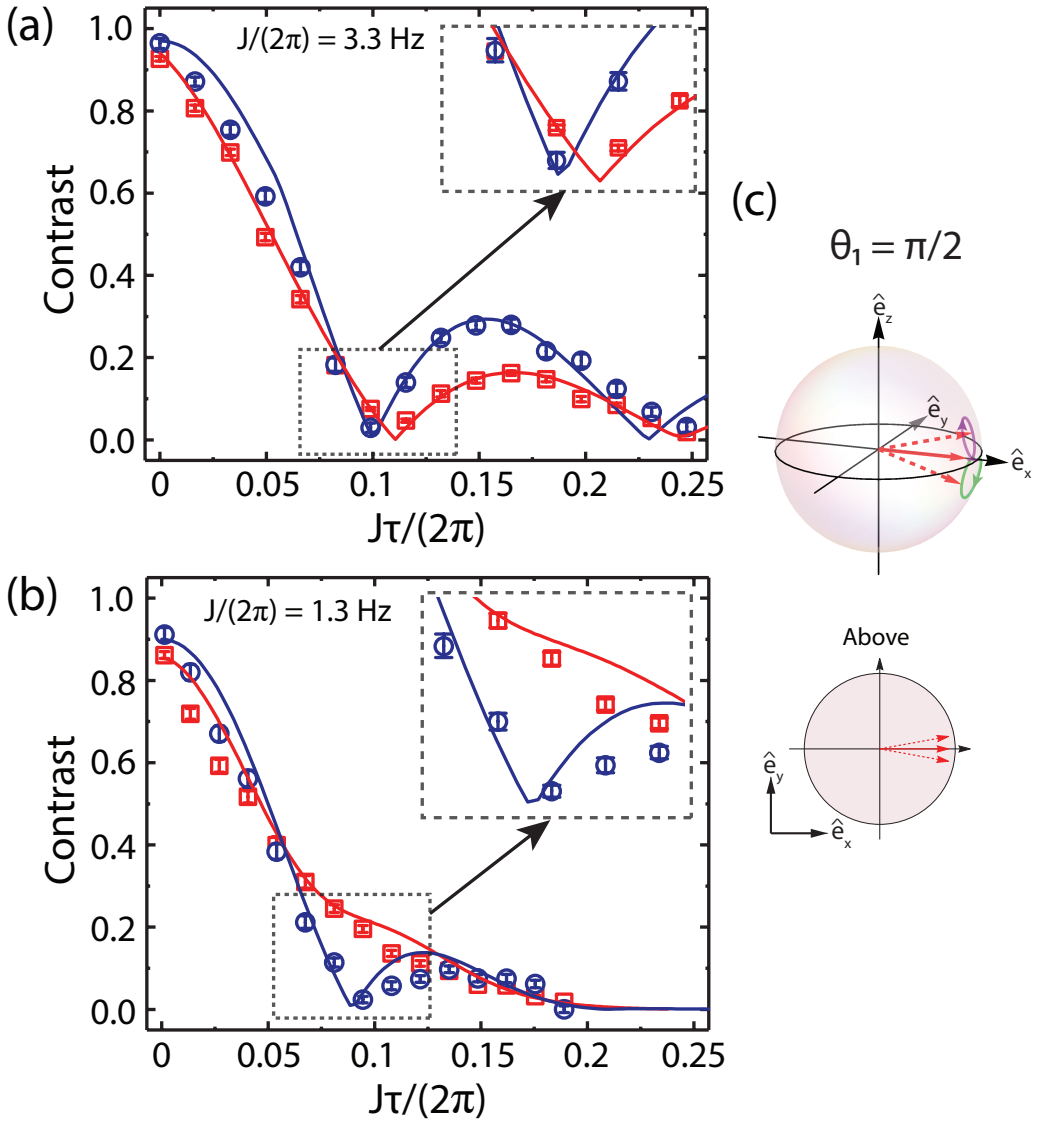

Figure 7.32: Contrast curves for $\theta_1 = \pi/2$. **(a)** $J > |N\xi^+/L| = 3.5$ Hz and the interactions cause the zero in the contrast to be pushed to larger $J\tau$. **(b)** $J \sim |N\xi^+/L| = 5.6$ Hz and interactions prevent static dephasing and the contrast approaches zero only at long times. Solid lines are theory including atom loss and diffusive dephasing (see Fig. 7.28). **(c)** On the Bloch sphere for $\theta_1 = \pi/2$ the exchange induced rotation is symmetric and the two Bloch vectors are the same length in the $\hat{X} - \hat{Y}$ plane and are shown as green and purple trajectories on the Bloch sphere.

depend on $V_{\alpha\beta}$ and $U^{-}_{\alpha\beta}$ which are the p-wave and s-wave mean interaction parameters, respectively. L is the number of lattice sites, and thus N/L represents the mean number of atoms per site. Due to the temperature of the atoms in the lattice being $> 1\mu$K the s-wave and p-wave interactions are similar in magnitude (see Fig. 7.33).

The term proportional to ξ^{+} encapsulates the exchange interaction process mediated by both s-wave and p-wave collisions. For the nuclear spin-polarized identical fermions initially prepared in the lattice, and in the absence of SOC, this term becomes a constant of motion and is thus irrelevant to the dynamics. However, when $J \neq 0$, the effective q-dependent SOC magnetic field $\mathbf{B}_{SOC}(q_i, \mathbf{n}_{\mathbf{r}_i}, 0, \delta)$ causes the initially spin polarized atoms to dephase with respect to each other, thereby introducing exchange interactions between them, which directly compete with the single-particle SOC dynamics.

The p-wave interaction terms proportional to χ^{+} and C^{+} generate a collective Ising Hamiltonian which commutes with $\hat{\mathbf{S}}^2$ and have previously, in the absence of SOC, been shown to induce many-body spin dynamics [15] for any superposition of e and g. These terms are unchanged in the presence of SOC, and have a negligible effect on the spin contrast for the experimental conditions and timescales we study here.

Throughout this work, we find that the explored experimental timescales are in a regime where the mean field approximation is valid. In this approximation the interaction terms can be treated as an additional time-dependent magnetic field generated by the collective spin vector, $\mathbf{B}_{\text{int}}$. This allows us to factor out a collective spin operator from $\hat{H}_{\text{int}}$ as given in Eq. 7.34 in order to arrive at the mean field Hamiltonian including both interactions and SOC:

$$\hat{H}^{\text{MF}}/\hbar = -\sum_{i=1}^{N} \mathbf{B}_{SOC}(q_i, \mathbf{n}_{\mathbf{r}_i}, \Omega, \delta) \cdot \hat{\mathbf{S}}_i + \sum_{i=1}^{N} \mathbf{B}_{\text{int}} \cdot \hat{\mathbf{S}}_i, \tag{7.35}$$

where $\mathbf{B}_{\text{int}} = \left[\frac{2\xi^{+}}{L}\left\langle \hat{S}^X \right\rangle, \frac{2\xi^{+}}{L}\left\langle \hat{S}^Y \right\rangle, \left(2\frac{\xi^{+}+\chi^{+}}{L}\right)\left\langle \hat{S}^Z \right\rangle + N\frac{C^{+}}{L}\right]$. The $\hat{X}$ and $\hat{Y}$ components can be written together as a collective, evolving, transverse magnetic field, $\frac{2\xi^{+}}{L}\langle \hat{\mathbf{S}}^{\perp}(t)\rangle$ around which individual atom Bloch vectors rotate. This term competes with the single particle dephasing term, $\mathbf{B}_{SOC}(q_i, \mathbf{n}_{\mathbf{r}_i}, \Omega, \delta)$, and forces the pseudo-spins to remain aligned, causing interaction dependent

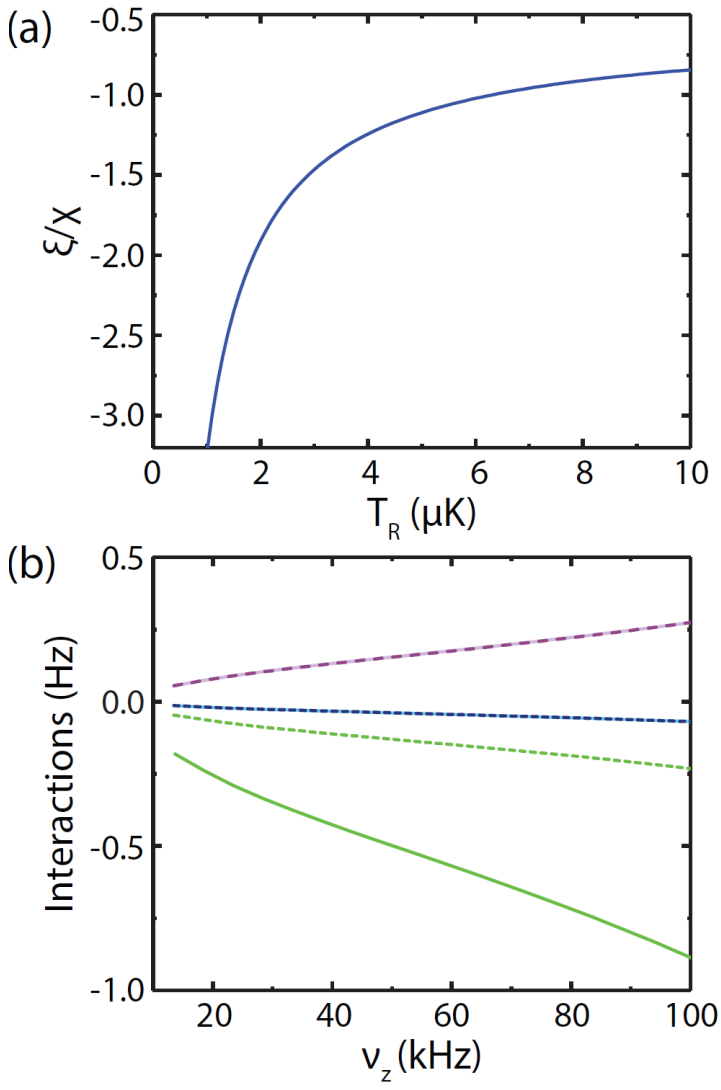

Figure 7.33: Dependence of interactions on temperature and lattice depth. **(a)** Under current experimental temperatures the exchange interactions (ξ^+) are of the same order as the Ising interactions (χ^+). **(b)** Interaction strengths at $T = 1\mu$K (solid lines) and $T = 10\mu$K (dashed lines) for the interaction parameters χ^+ (purple), ξ^+ (green), and C^+ (Blue) at different lattice depths. The strong dependence of the exchange interactions on temperature is due to the s-wave contribution. The p-wave interactions which enter C and χ^+ are independent of temperature.

changes to the contrast. The $\hat{Z}$ component of the interaction magnetic field is a constant of motion and gives rise to a collective precession of the Bloch vectors at a rate $N\left(\frac{C^+}{L} - \frac{\chi^+ + \xi^+}{L}\cos\theta_1\right)$, where $\langle \hat{S}^Z \rangle = -N/2\cos\theta_1$. When the tunneling rate J is zero, all the terms proportional to ξ^+ in $\hat{H}^{MF}$ will not affect the contrast or frequency shift.

The competition between the interaction-induced transverse magnetic field and the static SOC dephasing is shown schematically in Fig. 7.31 and Fig. 7.32 under the simple two-group approximation for $\theta_1 = \pi/4$ and $\theta_1 = \pi/2$, respectively. For $\theta_1 = \pi/4$, the collective rotation differentially changes the projected length of the individual Bloch vectors on the transverse plane, generating a net $|\langle \hat{S}^Y(t) \rangle| > 0$. As a result, when the vectors are π out of phase, they no longer completely cancel, leaving a finite contrast at all times, as opposed to the complete collapse observed for the non-interacting case where $|\langle \hat{S}^Y(t) \rangle| = 0$. This is apparent in the data shown in Fig. 7.31, where the contrast remains finite for the interacting case (red circles, $N\xi^+/L = -2.0$ Hz, $N\chi^+/L = 1.2$ Hz).

For $\theta_1 = \pi/2$, due to symmetry, the rotation of the Bloch vectors on the Bloch sphere (red, dashed arrows in Fig. 7.32) around the collective spin vector (red, solid arrow) does not change the relative transverse length of the vectors – which imposes $|\langle \hat{S}^Y(t) \rangle| = 0$. The effects of interactions are shown in Fig. 7.32 for varying strengths of interactions ($N\xi^+/L$) compared to J. When the interactions are still small compared to the tunneling ($J > |N\xi^+/L|$, with $N\xi^+/L = -3.5$ Hz and $N\chi^+/L = 1.3$ Hz) (Fig. 7.32, (a)), they cause no qualitative change to $\mathcal{C}$ compared to the non-interacting case, except for a weak rephasing of the spins that slightly delays the contrast collapse and decreases the revival amplitude. This is manifested as an interaction-induced shift of the time of the first contrast zero, $\propto N^2(\xi^+)^2/L^2J^2$.

If J is decreased such that $J \sim |N\xi^+/L|$, then the exchange interactions produce a qualitatively different behavior, as shown in Fig. 7.32(b). For $J/(2\pi) = 1.3$ Hz, the non-interacting case (blue circles) shows the characteristic collapse and revival. In contrast, the interacting case (with $N\xi^+/L = -5.6$ Hz, $N\chi^+/L = 3.4$ Hz), shows no collapse whatsoever, instead exhibiting only a monotonic decay with $J\tau$. The suppression of the collapse and revivals is a result of the exchange-

induced rephasing of the spins. Ideally, this type of spin locking would preserve the coherence indefinitely, as can been seen directly from the interacting Hamiltonian (7.34), where for large ξ^+ the initial state is an eigenstate. Indeed, long-term synchronization has been previously observed in other cold atom experiments [144] with dominant s-wave interactions. In our OLC we also need to account for competing mechanisms.

One important decoherence mechanism is atom loss due to inelastic two-body $e-e$ p-wave collisions [87, 122], which becomes particularly relevant for a large N. The effect of the losses on the contrast, however, is largely compensated when the contrast is normalized by the total atom number, as we do throughout this work. The most relevant contribution to decoherence for the current experiment is the single-particle diffusive dephasing observed in Fig. 7.28. Its effect on the contrast can already be seen in the non-interacting case (blue circles) and is exacerbated when operating at the low tunneling rates required to enter the $J \sim |N\xi^+/L|$ regime. We anticipate that quasimomentum conservation, and signatures of spin-locking at longer times, will be achievable in a 3D optical lattice, where coupling to the thermally populated radial modes would be eliminated.

7.14 Frequency Shift

To complete our full characterization of the spin system and to disentangle the interaction dynamics from decoherence, we also study the effects of interactions on the phase accumulated by the collective spin vector during the free precession time τ, $\tan(\Delta\nu 2\pi\tau) = \left\langle \hat{S}^Y \right\rangle / \left\langle \hat{S}^X \right\rangle$. In optical lattice clocks this is traditionally described by a density-dependent frequency shift [15, 16] ($\Delta\nu$).

For $J = 0$ (no SOC), ξ^+ is a constant of motion, and the density shift arises entirely from the Ising p-wave interactions. In Fig. 7.34 a density shift measurement without SOC shows a clear linear dependence on the fraction of the atoms in the excited clock state (also shown on the Bloch sphere), fully consistent with previous studies [15, 141]. These works were all performed in the regime $J = 0$, where $\Delta\nu$ has been well characterized and found to be independent of the dark time between the Ramsey pulses. In this work the measured shift in the absence of SOC agrees with the

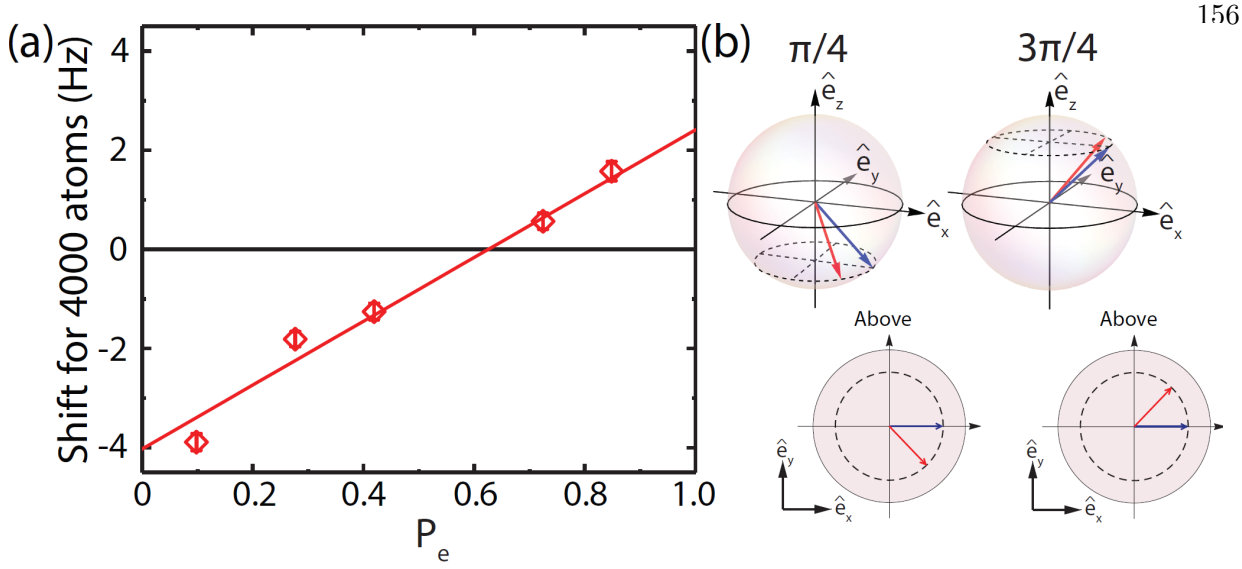

Figure 7.34: **(a)** With $J = 0$ (no SOC) atoms interact via p-wave collisions only, leading to a frequency shift linearly dependent on excitation fraction, P_e. **(b)** On the Bloch sphere for $\theta_1 < \pi/2$ the collective vector for atoms with interactions (red) rotates to give a negative phase shift with respect to the non-interacting (blue) vector. For $\theta_1 > \pi/2$ the interactions lead to a positive shift.

prediction from the mean-field Hamiltonian (Eq. 7.35) $\Delta\nu_{J=0} = N\left(\frac{C^+}{L} - \frac{\chi^+}{L}\cos\theta_1\right)$, where the shift depends linearly on the fraction of atoms in the excited clock state ($P_e = (1 - \cos\theta_1)/2$).

In contrast, interactions in the presence of SOC give rise to a frequency shift that is dependent on the dark time between the Ramsey pulses (Fig. 7.35(a)). From this data the frequency shift extrapolated to zero excitation fraction is seen to diverge when the single-particle contrast decays to zero (see Fig. 7.35(b)).

For $J > 0$ (with SOC), the situation becomes more complicated. To develop an intuitive understanding, we return again to the two atom-group model, where a simple analytic expression can be derived to first order in interactions

$$\Delta\nu = \Delta\nu_{J=0} - \frac{N\xi^+}{L}\cos(\theta_1)\left(1 - \frac{\tan(4J\tau)}{4J\tau}\right). \tag{7.36}$$

The same exchange term that produces the time-dependent collective transverse field responsible for modifying the contrast dynamics also results in a frequency shift. This term diverges when $\cos(4J\tau) = 0$, which physically corresponds to the case when the two non-interacting atom group

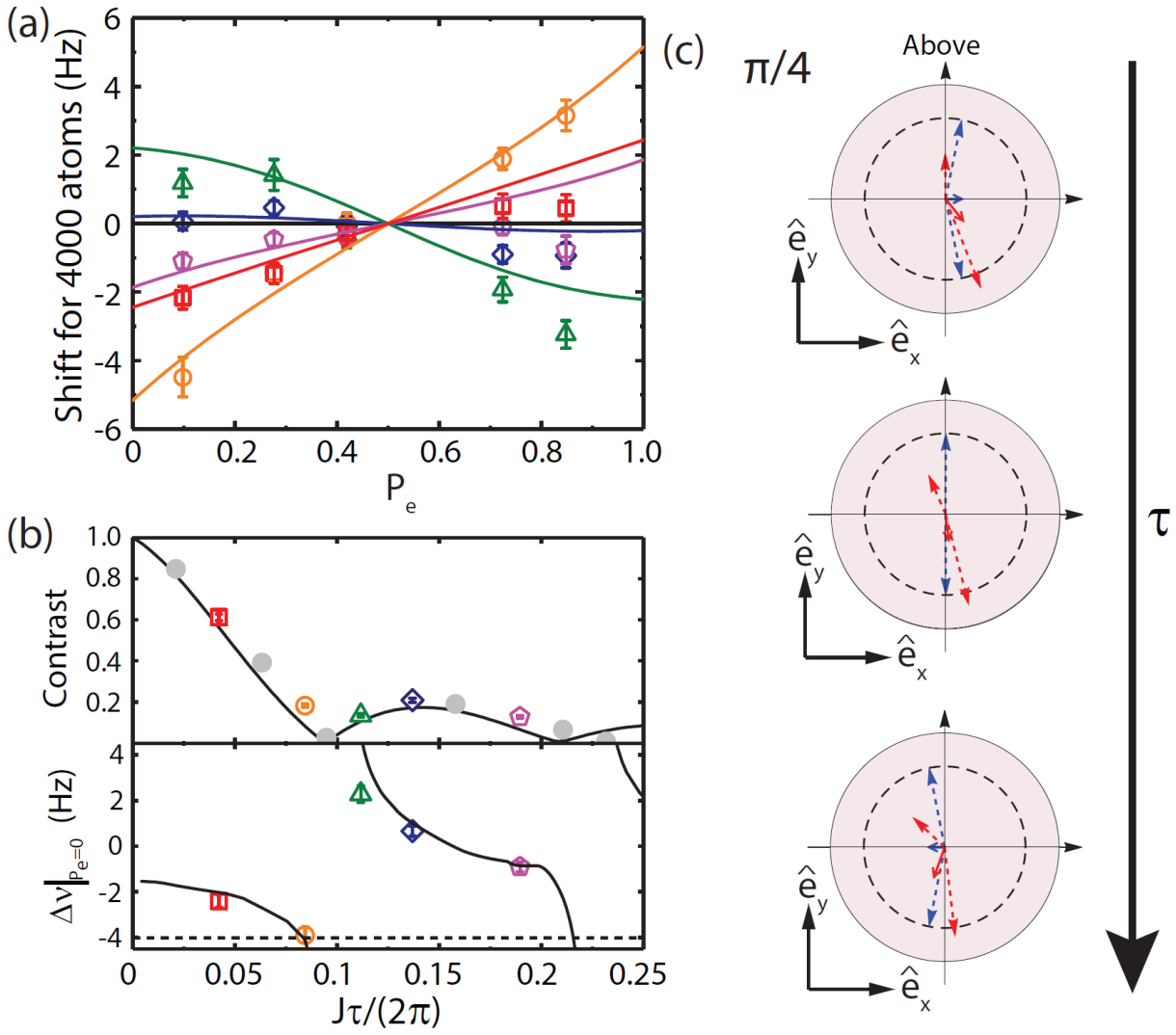

Figure 7.35: **(a)** Density shifts for $J/(2\pi) = 2.2$ Hz (with SOC) for different $J\tau$ measured by varying τ, as indicated in panel **(b)**. The magnitude and sign of the density shift can be seen to vary with time. **(b)** The non-interacting contrast curve, including additional grey contrast data, and the $\Delta\nu\big|_{P_e=0}$ density shift for 4000 atoms corresponding to the data in **(a)** including theory curves for $J > 0$ (solid, black) and $J = 0$ (dashed, black). **(c)** The divergence can be understood by considering the Bloch vectors for the different VHSs (dashed arrows) with τ. As the contrast goes through zero for no interactions (blue), the SOC induced exchange interactions (red) prevent the collective spin vector (red, solid arrow) from going to zero. As the non-interacting collective spin vector (blue, solid) goes through zero it changes sign, causing a change in sign of the slope of the density shift. All error bars are 1σ confidence intervals.

vectors are π radians out of phase on the Bloch sphere, as illustrated in Fig. 7.35(c). When the spins rephase and the contrast becomes finite again, the exchange-induced shift diminishes. It completely turns off in the two atom-group approximation when the spins re-align. However, for the experimentally relevant case of a thermally populated band with all q values participating, the density shift will change in magnitude with time but will not disappear completely, since the spins do not completely rephase.

The experimentally measured dependence of the SOC density shift on τ at a finite tunneling rate of $J/(2\pi) = 2.2$ Hz is shown in Fig. 7.35(a)-(b) for $N\xi^+/L = -2.7$ Hz and $N\chi^+/L = 1.6$ Hz. The observed shift is not entirely linear in excitation fraction, indicating that the interactions can no longer be described by first order perturbation theory, and higher order corrections are required. Figure 7.35(b) compares the contrast to the extrapolated density shift for zero excitation fraction $\left(\Delta\nu\Big|_{P_e=0}\right)$ for the same data as in Fig. 7.35(c). The extracted quantity $\Delta\nu\Big|_{P_e=0}$ shows a divergence around the zero of the contrast, consistent with Eq. 7.36. The highly non-trivial functional form of the density shift indicates that SOC induced exchange interactions will be a major factor in optical lattice clocks if the effects of tunneling are not suppressed. However, the experimentally observed density shift and contrast, which encapsulate the magnetization dynamics, can be well described by theory. This agreement highlights the fact that for the experimentally relevant timescales, the complex interplay between SOC and many-body dynamics can be understood and explored precisely.

7.15 Conclusions

In conclusion, we have explored the emergence of complex dynamics with interacting fermions under engineered spin-orbit coupling in a Sr optical lattice clock. The many-body dynamics are fully characterized by a collective XXZ Hamiltonian aside from extra dephasing arising from non-conserved quasimomenta. In the future we plan to suppress this dephasing by using more sophisticated pulse sequences[155] or by employing a 3D optical lattice [6], where the p- wave interactions would also be suppressed. The lower temperatures associated with loading a Fermi-degenerate gas

in a 3D lattice geometry will also enable the study of SOC in higher dimensions, precise control of the SOC phase [157, 140] ϕ, and exploration of a new strongly interacting regime where the collective XXZ model is no longer applicable, and where richer exotic behaviors including topological superfluids[158] and Kondo correlated metallic phases can emerge[159].

Chapter 8

Conclusions and Outlook

The work that is presented in this thesis will be useful for future generations of clocks based on 3D lattice geometries. These clocks are cooled to degeneracy by allowing multiple nuclear spin states to be present, making the SU($\mathcal{N}$) interactions discussed in chapter 6 relevant. Initial studies of these SU($\mathcal{N}$) symmetric interactions have taken place in a 3D lattice[124] with these measurements of few body interactions improving upon the precision of the measured scattering parameters measured in chapter 6. The close agreement between the values measured in these two studies confirms the validity of the numerical expressions that were used to determine some of these scattering parameters.

As these 3D optical lattice clocks move towards Mott and band insulator states [19] the long range interactions between atoms studied in chapter 4 between atoms on different lattice sites will become the leading density dependent interaction. The spin-orbit coupling discussed in chapter 7 will also become important as the excited state atomic lifetime in these 3D lattice clocks is reduced due to Raman scattering of atoms from $^3P_0$ to $^3P_1$. Experimental schemes using lower lattice depths may therefore be necessary to take full advantage of the full ~ 160 s lifetime of the excited clock state.

As mentioned in the introduction, our Sr1 clock experiment has been working successfully for more than ten years. The future plans of the experiment mean that it is necessary to upgrade the experimental vacuum chamber to allow for more flexibility with future experiments as well as a better vacuum lifetime. The new chamber design is shown in Fig. 8.1. It consists of a two-chamber

design where one chamber will be used for the MOTs and the other will be the science chamber. This two-chamber design along with the commercial Zeeman slower from AOSense allow us to avoid the use of a heated window, which avoids the uncertainty associated with the BBR shift from this heated window. The atoms will be optically transported between the two chambers and the atoms can then be cooled to degeneracy before being transported to within an optical cavity where the atoms will be trapped within either a 2D or 3D optical lattice.

The multi chamber design allows the preparation of atoms whilst measurements of the atoms are taking place. The only deadtime associated with the measurement will be due to the time it takes to move the atoms from the cooling region in the center of the science chamber to the cavity. It is predicted the deadtime will be as short as 25 ms. The cavity, with high finesse at 689 nm, will be used to create one of the lattice dimensions of the lattice and will be used to create a spin-squeezed clock.

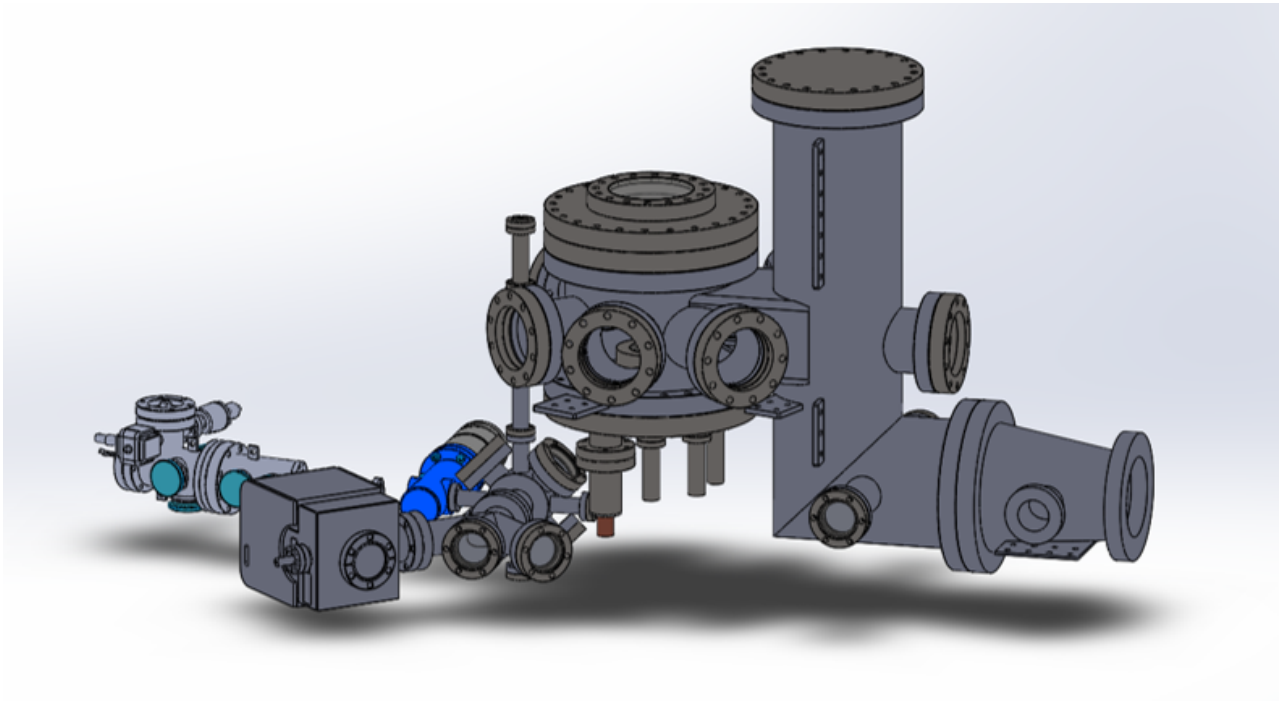

Figure 8.1: The future experimental vacuum chamber design will allow for semi-continuous measurements of degenerately cooled atoms inside a cavity. The cavity will be used to study spin-squeezing of atomic clocks.

Bibliography

[1] I. Shaw. Ancient Egyptian Technology and Innovation. Bloomsbury Egyptology. Bloomsbury, London, (2012).

[2] F. G. Major. The Quantum Beat. Springer, Berlin, (2007).

[3] M. A. Lombardi, T. P. Heavner, and S. R. Jefferts. NIST primary frequency standards and the realization of the SI second. NCSLI Measure, **2**:74–89, (2007).

[4] B. J. Bloom. Building a Better Atomic Clock. PhD thesis, University of Colorado, (2014).

[5] A. D. Ludlow, M. M. Boyd, J. Ye, E. Peik, and P. O. Schmidt. Optical atomic clocks. Rev. Mod. Phys., **87**:637–701, (2015).

[6] S. L. Campbell, R. B. Hutson, G. E. Marti, A. Goban, N. Darkwah Oppong, R. L. McNally, L. Sonderhouse, J. M. Robinson, W. Zhang, B. J. Bloom, and J. Ye. A Fermi-degenerate three-dimensional optical lattice clock. Science, **358**:90–94, (2017).

[7] M. J. Martin. Quantum Metrology and Many-Body Physics: Pushing the Frontier of the Optical Lattice Clock. PhD thesis, University of Colorado, (2013).

[8] M. M. Boyd. High Precision Spectroscopy of Strontium in an Optical Lattice: Towards a New Standard for Frequency and Time. PhD thesis, University of Colorado, (2007).

[9] N. Poli, R. E. Drullinger, G. Ferrari, J. Léonard, F. Sorrentino, and G. M. Tino. Cooling and trapping of ultracold strontium isotopic mixtures. Phys. Rev. A, **71**:061403, (2005).

[10] F. Buchinger, R. Corriveau, E. B. Ramsay, D. Berdichevsky, and D. W. L. Sprung. Influence of the n=50 shell closure on mean square charge radii of strontium. Phys. Rev. C, **32**:2058–2066, (1985).

[11] H. Jürgen Kluge and Hatto Sauter. Levelcrossing experiments in the first excited1p1 states of the alkaline earths. Z. Phys., **270**:295–309, (1974).

[12] I. Courtillot, A. Quessada-Vial, A. Brusch, D. Kolker, G. D. Rovera, and P. Lemonde. Accurate spectroscopy of Sr atoms. Eur. Phys. J. D, **33**:161–171, (2005).

[13] G. zu Putlitz. Bestimmung des elektrischen kernquadrupolmomentes des ungeraden stabilen strontium-87-kerns. Zeitschrift für Physik, **175**:543–552, (1963).

[14] E. D. Black. An introduction to Pound-Drever-Hall laser frequency stabilization. Am. J. Phys., **69**:79–87, (2001).

[15] M. J. Martin, M. Bishof, M. D. Swallows, X. Zhang, C. Benko, J. von Stecher, A. V. Gorshkov, A. M. Rey, and J. Ye. A quantum many-body spin system in an optical lattice clock. Science, **341**:632–636, (2013).

[16] N. D. Lemke, J. von Stecher, J. A. Sherman, A. M. Rey, C. W. Oates, and A. D. Ludlow. p-wave cold collisions in an optical lattice clock. Phys. Rev. Lett., **107**:103902, (2011).

[17] A. D. Ludlow, N. D. Lemke, J. A. Sherman, C. W. Oates, G. Quéméner, J. von Stecher, and A. M. Rey. Cold-collision-shift cancellation and inelastic scattering in a Yb optical lattice clock. Phys. Rev. A, **84**:052724, (2011).

[18] M. D. Swallows, M. J. Martin, M. Bishof, C. Benko, Y. Lin, S. Blatt, A. M. Rey, and J. Ye. Operating a ^{87}Sr optical lattice clock with high precision and at high density. IEEE T. Ultrason. Ferr., **59**:416–425, (2012).

[19] R. B. Hutson et al. Prospects for an optical lattice clock in the Mott and band insulating regimes. (to be published).

[20] J. Lodewyck, M. Zawada, L. Lorini, M. Gurov, and P. Lemonde. Observation and cancellation of a perturbing dc stark shift in strontium optical lattice clocks. IEEE T. Ultrason. Ferr., **59**:411–415, (2012).

[21] B. J. Bloom, T. L. Nicholson, J. R. Williams, S. L. Campbell, M. Bishof, X. Zhang, W. Zhang, S. L. Bromley, and J. Ye. A new generation of atomic clocks: Accuracy and stability at the 10^{-18} level. Nature, **506**:71–75, (2014).

[22] T. L. Nicholson. A new record in atomic clock performance. PhD thesis, University of Colorado, (2015).

[23] K. Beloy, N. Hinkley, N. B. Phillips, J. A. Sherman, M. Schioppo, J. Lehman, A. Feldman, L. M. Hanssen, C. W. Oates, and A. D. Ludlow. Atomic clock with 1×10^{-18} room-temperature blackbody stark uncertainty. Phys. Rev. Lett., **113**:260801, (2014).

[24] T. Middelmann, S. Falke, C. Lisdat, and U. Sterr. High accuracy correction of blackbody radiation shift in an optical lattice clock. Phys. Rev. Lett., **109**:263004, (2012).

[25] M. S. Safronova, S. G. Porsev, U. I. Safronova, M. G. Kozlov, and C. W. Clark. Blackbody-radiation shift in the sr optical atomic clock. Phys. Rev. A, **87**:012509, (2013).

[26] S. G. Porsev, A. D. Ludlow, M. M. Boyd, and J. Ye. Determination of Sr properties for a high-accuracy optical clock. Phys. Rev. A, **78**:032508, (2008).

[27] S. Falke, M. Misera, U. Sterr, and C. Lisdat. Delivering pulsed and phase stable light to atoms of an optical clock. App. Phys. B, **107**:301–311, (2012).

[28] K. Gibble. Scattering of cold-atom coherences by hot atoms: Frequency shifts from background-gas collisions. Phys. Rev. Lett., **110**:180802, (2013).

[29] M. Gross and S. Haroche. Superradiance: An essay on the theory of collective spontaneous emission. Phys. Rep., **93**:301–396, (1982).

[30] A. V. Andreev, V. I. Emel'yanov, and Y. A. Il'inskii. Collective spontaneous emission (Dicke superradiance). Sov. Phys. Usp., **23**:493–514, (1980).

[31] R. H. Dicke. Coherence in spontaneous radiation processes. Phys. Rev., **93**:99–110, (1954).

[32] H. J. Kimble. The quantum internet. Nature, **453**:1023–1030, (2008).

[33] N. Skribanowitz, I. P. Herman, J. C. MacGillivray, and M. S. Feld. Observation of Dicke superradiance in optically pumped HF gas. Phys. Rev. Lett., **30**:309–312, (1973).

[34] D. Pavolini, A. Crubellier, P. Pillet, L. Cabaret, and S. Liberman. Experimental evidence for subradiance. Phys. Rev. Lett., **54**:1917–1920, (1985).

[35] T. Wang, S. F. Yelin, R. Côté, E. E. Eyler, S. M. Farooqi, P. L. Gould, M. Koštrun, D. Tong, and D. Vrinceanu. Superradiance in ultracold Rydberg gases. Phys. Rev. A, **75**:033802, (2007).

[36] R. Friedberg and S. R. Hartmann. Superradiant stability in specially shaped small samples. Opt. Commun., **10**:298–301, (1974).

[37] R. Friedberg and S. R. Hartmann. Temporal evolution of superradiance in a small sphere. Phys. Rev. A, **10**:1728–1739, (1974).

[38] G. S. Agarwal, R. Saxena, L. M. Narducci, D. H. Feng, and R. Gilmore. Analytical solution for the spectrum of resonance fluorescence of a cooperative system of two atoms and the existence of additional sidebands. Phys. Rev. A, **21**:257–259, (1980).

[39] M. Lewenstein and K. Rzazewski. Collective radiation and the near-zone field. J. Phys. A: Math. Gen., **13**:743–756, (1980).

[40] H. Steudel and T. Richter. Radiation properties of a continuously pumped two-atom system. Ann. Phys., **490**:122–136, (1978).

[41] K. Rzażewski and W. Żakowicz. Initial value problem for two oscillators interacting with electromagnetic field. J. Math. Phys., **21**:378–388, (1980).

[42] J. Ruostekoski and J. Javanainen. Quantum field theory of cooperative atom response: Low light intensity. Phys. Rev. A, **55**:513–526, (1997).

[43] M. O. Scully. Collective Lamb shift in single photon dicke superradiance. Phys. Rev. Lett., **102**:143601, (2009).

[44] R. H. Lehmberg. Radiation from an N-atom system. I. General formalism. Phys. Rev. A, **2**:883–888, (1970).

[45] D. F. V. James. Frequency shifts in spontaneous emission from two interacting atoms. Phys. Rev. A, **47**:1336–1346, (1993).

[46] J. Keaveney, A. Sargsyan, U. Krohn, I. G. Hughes, D. Sarkisyan, and C. S. Adams. Cooperative lamb shift in an atomic vapor layer of nanometer thickness. Phys. Rev. Lett., **108**:173601, (2012).

[47] Z. Meir, O. Schwartz, E. Shahmoon, D. Oron, and R. Ozeri. Cooperative lamb shift in a mesoscopic atomic array. Phys. Rev. Lett., **113**:193002, (2014).

[48] S. Jennewein, Y. R. P. Sortais, J.-J. Greffet, and A. Browaeys. Propagation of light through small clouds of cold interacting atoms. Phys. Rev. A, **94**:053828, (2016).

[49] S. Jennewein, M. Besbes, N. J. Schilder, S. D. Jenkins, C. Sauvan, J. Ruostekoski, J.-J. Greffet, Y. R. P. Sortais, and A. Browaeys. Coherent scattering of near-resonant light by a dense microscopic cold atomic cloud. Phys. Rev. Lett., **116**:233601, (2016).

[50] S. D. Jenkins, J. Ruostekoski, J. Javanainen, R. Bourgain, S. Jennewein, Y. R. P. Sortais, and A. Browaeys. Optical resonance shifts in the fluorescence of thermal and cold atomic gases. Phys. Rev. Lett., **116**:183601, (2016).

[51] R. Röhlsberger, K. Schlage, B. Sahoo, S. Couet, and R. Rüffer. Collective lamb shift in single-photon superradiance. Science, **328**:1248–1251, (2010).

[52] S. Balik, A. L. Win, M. D. Havey, I. M. Sokolov, and D. V. Kupriyanov. Near-resonance light scattering from a high-density ultracold atomic ^{87}Rb gas. Phys. Rev. A, **87**:053817, (2013).

[53] M. Chalony, R. Pierrat, D. Delande, and D. Wilkowski. Coherent flash of light emitted by a cold atomic cloud. Phys. Rev. A, **84**:011401, (2011).

[54] C. C. Kwong, T. Yang, M. S. Pramod, K. Pandey, D. Delande, R. Pierrat, and D. Wilkowski. Cooperative emission of a coherent superflash of light. Phys. Rev. Lett., **113**:223601, (2014).

[55] W. Guerin, M. O. Araújo, and R. Kaiser. Subradiance in a large cloud of cold atoms. Phys. Rev. Lett., **116**:083601, (2016).

[56] G. Labeyrie, F. de Tomasi, J.-C. Bernard, C. A. Müller, C. Miniatura, and R. Kaiser. Coherent backscattering of light by cold atoms. Phys. Rev. Lett., **83**:5266–5269, (1999).

[57] P. Kulatunga, S. Sukenik, S. Balik, M. D. Havey, D. V. Kupriyanov, and I. M. Sokolov. Measurement of correlated multiple light scattering in ultracold atomic ^{85}Rb. Phys. Rev. A, **68**:033816, (2003).

[58] P. de Vries, D. V. van Coevorden, and A. Lagendijk. Point scatterers for classical waves. Rev. Mod. Phys., **70**:447–466, (1998).

[59] M. C. W. van Rossum and Th. M. Nieuwenhuizen. Multiple scattering of classical waves: microscopy, mesoscopy, and diffusion. Rev. Mod. Phys., **71**:313–371, (1999).

[60] T. Walker, D. Sesko, and C. Wieman. Collective behaviour of optically trapped neutral atoms. Phys. Rev. Lett., **64**:408–411, (1990).

[61] R. Heidemann, U. Raitzsch, V. Bendkowsky, B. Butscher, R. Löw, L. Santos, and T. Pfau. Evidence for coherent collective Rydberg excitation in the strong blockade regime. Phys. Rev. Lett., **99**:163601, (2007).

[62] M. D. Lukin, M. Fleischhauer, R. Cote, L. M. Duan, D. Jaksch, J. I. Cirac, and P. Zoller. Dipole blockade and quantum information processing in mesoscopic atomic ensembles. Phys. Rev. Lett., **87**:037901, (2001).

[63] M. Saffman, T. G. Walker, and K. Mølmer. Quantum information with Rydberg atoms. Rev. Mod. Phys., **82**:2313–2363, (2010).

[64] T. Lahaye, C. Menotti, L. Santos, M. Lewenstein, and T. Pfau. The physics of dipolar bosonic quantum gases. Rep. Prog. Phys., **72**:126401, (2009).

[65] R. Löw, H. Weimer, J. Nipper, J. B. Balewski, B. Butscher, H. P. Bchler, and T. Pfau. An experimental and theoretical guide to strongly interacting Rydberg gases. J. Phys. B:At. Mol. Opt. Phys., **45**:113001, (2012).

[66] T. Peyronel, O. Firstenberg, Q.-Y. Liang, S. Hofferberth, A. V. Gorshkov, T. Pohl, M. D. Lukin, and V. Vuletic. Quantum nonlinear optics with single photons enabled by strongly interacting atoms. Nature, **488**:57–60, (2012).

[67] S. Ravets, H. Laubuhn, D. Barredo, L. Beguin, T. Lahaye, and A. Browaeys. Coherent dipole-dipole coupling between two single rydberg atoms at an electrically-tuned förster resonance. Nature Phys., **10**:914–917, (2014).

[68] G. Günter, H. Schempp, M. Robert-de Saint-Vincent, V. Gavryusev, S. Helmrich, C. S. Hofmann, S. Whitlock, and M. Weidemüller. Observing the dynamics of dipole-mediated energy transport by interaction-enhanced imaging. Science, **342**:954–956, (2013).

[69] D. E. Chang, J. Ye, and M. D. Lukin. Controlling dipole-dipole frequency shifts in a lattice-based optical atomic clock. Phys. Rev. A, **69**:023810, (2004).

[70] M. Kuś and K. Wódkiewicz. Two-atom resonance fluorescence. Phys. Rev. A, **23**:853–857, (1981).

[71] W. Żakowicz. Superradiant decay of a small spherical system of harmonic oscillators. Phys. Rev. A, **17**:343–352, (1978).

[72] R. T. Sutherland and F. Robicheaux. Coherent forward broadening in cold atom clouds. Phys. Rev. A, **93**:023407, (2016).

[73] T. L. Nicholson, S. L. Campbell, R. B. Hutson, G. E. Marti, B. J. Bloom, R. L. McNally, W. Zhang, M. D. Barrett, M. S. Safronova, G. F. Strouse, W. L. Tew, and J. Ye. Systematic evaluation of an atomic clock at 2×10^{-18} total uncertainty. Nat. Commun., **6**:6896, (2015).

[74] I. Ushijima, M. Takamoto, M. Das, T. Ohkubo, and H. Katori. Cryogenic optical lattice clocks. Nat Photon, **9**:185–189, (2015).

[75] B. Olmos, D. Yu, Y. Singh, F. Schreck, K. Bongs, and I. Lesanovsky. Long-range interacting many-body systems with alkaline-earth-metal atoms. Phys. Rev. Lett., **110**:143602, (2013).

[76] H. P. Specht, C. Nolleke, A. Reiserer, M. Uphoff, E. Figueroa, S. Ritter, and G. Rempe. A single-atom quantum memory. Nature, **473**:190–193, (2011).

[77] T. Ido, T. H. Loftus, M. M. Boyd, A. D. Ludlow, K. W. Holman, and J. Ye. Precision spectroscopy and density-dependent frequency shifts in ultracold Sr. Phys. Rev. Lett., **94**:153001, (2005).

[78] X. Xu, T. H. Loftus, J. L. Hall, A. Gallagher, and J. Ye. Cooling and trapping of atomic strontium. J. Opt. Soc. Am. B, **20**:968–976, (2003).

[79] A. Lagendijk and B. A. Van Tiggelen. Resonant multiple scattering of light. Phys. Rep., **270**:143–215, (1996).

[80] L. Allen and J. H. Eberly. Optical Resonance and Two-Level Atoms. Dover Books on Physics. Dover Publications, New York, (1987).

[81] W. Heitler. The Quantum Theory of Radiation. Oxford University Press, London, (1954).

[82] B. Zhu, J. Cooper, J. Ye, and A. M. Rey. Light scattering from dense cold atomic media. Phys. Rev. A, **94**:023612, (2016).

[83] B. Zhu. Many-body physics in long-range interacting quantum systems. PhD thesis, University of Colorado, (2017).

[84] J. Javanainen, J. Ruostekoski, Y. Li, and S.-M. Yoo. Shifts of a resonance line in a dense atomic sample. Phys. Rev. Lett., **112**:113603, (2014).

[85] R. Friedberg, S.R. Hartmann, and J.T. Manassah. Frequency shifts in emission and absorption by resonant systems ot two-level atoms. Phys. Rep., **7**:101 – 179, (1973).

[86] P. S. Julienne. Cold binary atomic collisions in a light field. J. Res. Natl. Inst. Stand. Technol., **101**:487 – 503, (1996).

[87] A. M. Rey, A. V. Gorshkov, C. V. Kraus, M. J. Martin, M. Bishof, M. D. Swallows, X. Zhang, C. Benko, J. Ye, N.D. Lemke, and A. D. Ludlow. Probing many-body interactions in an optical lattice clock. Ann. Phys., **340**:311–351, (2014).

[88] A. Auerbach. Interacting Electrons and Quantum Magnetism. Dover Books on Physics. Springer, Berlin, (1998).

[89] S. L. Bromley, S. Kolkowitz, T. Bothwell, D. Kedar, A. Safavi-Naini, M. L. Wall, C. Salomon, A. M. Rey, and J. Ye. Dynamics of interacting fermions under spin-orbit coupling in an optical lattice clock. Nat. Phys., **14**:399–404, (2018).

[90] M. M. Boyd, T. Zelevinsky, A. D. Ludlow, S. M. Foreman, S. Blatt, T. Ido, and J. Ye. Optical atomic coherence at the 1-second time scale. Science, **314**:1430–1433, (2006).

[91] M. M. Boyd, T. Zelevinsky, A. D. Ludlow, S. Blatt, T. Zanon-Willette, S. M. Foreman, and J. Ye. Nuclear spin effects in optical lattice clocks. Phys. Rev. A, **76**:022510, (2007).

[92] A. V. Gorshkov, M. Hermele, V. Gurarie, C. Xu, P. S. Julienne, J. Ye, P. Zoller, E. Demler, M. D. Lukin, and A. M. Rey. Two-orbital SU(N) magnetism with ultracold alkaline-earth atoms. Nat. Phys., **6**:289–295, (2010).

[93] M. A. Cazalilla, A. F. Ho, and M. Ueda. Ultracold gases of ytterbium: ferromagnetism and Mott states in an SU(6) Fermi system. New J. Phys., **11**:103033, (2009).

[94] C. Wu, J.-P. Hu, and S.-C. Zhang. Exact SO(5) symmetry in the spin-3/2 fermionic system. Phys. Rev. Lett., **91**:186402, (2003).

[95] M. Hermele, V. Gurarie, and A. M. Rey. Mott insulators of ultracold fermionic alkaline earth atoms: Underconstrained magnetism and chiral spin liquid. Phys. Rev. Lett., **103**:135301, (2009).

[96] A. J. Daley, M. M. Boyd, J. Ye, and P. Zoller. Quantum computing with alkaline-earth-metal atoms. Phys. Rev. Lett., **101**:170504, (2008).

[97] A. V. Gorshkov, A. M. Rey, A. J. Daley, M. M. Boyd, J. Ye, P. Zoller, and M. D. Lukin. Alkaline-earth-metal atoms as few-qubit quantum registers. Phys. Rev. Lett., **102**:110503, (2009).

[98] A. J. Daley. Quantum computing and quantum simulation with group-II atoms. Quantum Information Processing, **10**:865–884, (2011).

[99] I. Reichenbach and I. H. Deutsch. Sideband cooling while preserving coherences in the nuclear spin state in group-II-like atoms. Phys. Rev. Lett., **99**:123001, (2007).

[100] D. Banerjee, M. Bögli, M. Dalmonte, E. Rico, P. Stebler, U.-J. Wiese, and P. Zoller. Atomic quantum simulation of U(N) and SU(N) non-abelian lattice gauge theories. Phys. Rev. Lett., **110**:125303, (2013).

[101] Y. Tokura and N. Nagaosa. Orbital physics in transition-metal oxides. Science, **288**:462–468, (2000).

[102] X. G. Wen, F. Wilczek, and A. Zee. Chiral spin states and superconductivity. Phys. Rev. B, **39**:11413–11423, (1989).

[103] S. Kraft, F. Vogt, O. Appel, F. Riehle, and U. Sterr. Bose-Einstein condensation of alkaline earth atoms: ^{40}Ca. Phys. Rev. Lett., **103**:130401, (2009).

[104] S. Stellmer, F. Schreck, and T. C. Killian. Degenerate Quantum Gases Of Strontium, chapter 1, pages 1–80.

[105] Y. Takasu, K. Maki, K. Komori, T. Takano, K. Honda, M. Kumakura, T. Yabuzaki, and Y. Takahashi. Spin-singlet Bose-Einstein condensation of two-electron atoms. Phys. Rev. Lett., **91**:040404, (2003).

[106] S. Stellmer, R. Grimm, and F. Schreck. Detection and manipulation of nuclear spin states in fermionic strontium. Phys. Rev. A, **84**:043611, (2011).

[107] S. Blatt, T. L. Nicholson, B. J. Bloom, J. R. Williams, J. W. Thomsen, P. S. Julienne, and J. Ye. Measurement of optical feshbach resonances in an ideal gas. Phys. Rev. Lett., **107**:073202, (2011).

[108] R. Yamazaki, S. Taie, S. Sugawa, and Y. Takahashi. Submicron spatial modulation of an interatomic interaction in a Bose-Einstein condensate. Phys. Rev. Lett., **105**:050405, (2010).

[109] F. Scazza, C. Hofrichter, M. Höfer, P. C. De Groot, I. Bloch, and S. Fölling. Observation of two-orbital spin-exchange interactions with ultracold SU(N)-symmetric fermions. Nat. Phys., **501**:779–784, (2014).

[110] G. Cappellini, M. Mancini, G. Pagano, P. Lombardi, L. Livi, M. Siciliani de Cumis, P. Cancio, M. Pizzocaro, D. Calonico, F. Levi, C. Sias, J. Catani, M. Inguscio, and L. Fallani. Direct observation of coherent interorbital spin-exchange dynamics. Phys. Rev. Lett., **113**:120402, (2014).

[111] S. Taie, R. Yamazaki, S. Sugawa, and Y. Takahashi. An SU(6) mott insulator of an atomic Fermi gas realized by large-spin pomeranchuk cooling. Nat. Phys., **8**:825–830, (2012).

[112] G. Pagano, M. Mancini, G. Cappellini, P. Lombardi, F. Schfer, H. Hu, X.-J. Liu, J. Catani, C. Sias, M. Inguscio, and L. Fallani. A one-dimensional liquid of fermions with tunable spin. Nat. Phys., **10**:198–201, (2014).

[113] Y. N. Martinez de Escobar, P. G. Mickelson, P. Pellegrini, S. B. Nagel, A. Traverso, M. Yan, R. Côté, and T. C. Killian. Two-photon photoassociative spectroscopy of ultracold ^{88}Sr. Phys. Rev. A, **78**:062708, (2008).

[114] A. Stein, H. Knockel, and E. Tiemann. The s+s asymptote of Sr studied by fourier-transform spectroscopy. Eur. Phys. J. D, **57**:171–177, (2010).

[115] N. Hinkley, J. A. Sherman, N. B. Phillips, M. Schioppo, N. D. Lemke, K. Beloy, M. Pizzocaro, C. W. Oates, and A. D. Ludlow. An atomic clock with 10^{18} instability. Science, **341**:1215–1218, (2013).

[116] T. L. Nicholson, M. J. Martin, J. R. Williams, B. J. Bloom, M. Bishof, M. D. Swallows, S. L. Campbell, and J. Ye. Comparison of two independent Sr optical clocks with 1×10^{-17} stability at 10^3 s. Phys. Rev. Lett., **109**:230801, (2012).

[117] A. P. Koller, M. Beverland, A. V. Gorshkov, and A. M. Rey. Beyond the spin model approximation for ramsey spectroscopy. Phys. Rev. Lett., **112**:123001, (2014).

[118] B. Yan, S. A. Moses, B. Gadway, J. P. Covey, K. R. A. Hazzard, A. M. Rey, D. S. Jin, and J. Ye. Observation of dipolar spin-exchange interactions with lattice-confined polar molecules. Nature, **501**:521–525, (2013).

[119] R. Islam, C. Senko, W. C. Campbell, S. Korenblit, J. Smith, A. Lee, E. E. Edwards, C.-C. J. Wang, J. K. Freericks, and C. Monroe. Emergence and frustration of magnetism with variable-range interactions in a quantum simulator. Science, **340**:583–587, (2013).

[120] K. I. Kugel and D. I. Khomskii. The jahn-teller effect and magnetism: transition metal compounds. Sov. Phys. Usp., **25**:231–256, (1982).

[121] P. Corboz, M. Lajkó, A. M. Läuchli, K. Penc, and F. Mila. Spin-orbital quantum liquid on the honeycomb lattice. Phys. Rev. X, **2**:041013, (2012).

[122] M. Bishof, M. J. Martin, M. D. Swallows, C. Benko, Y. Lin, G. Quéméner, A. M. Rey, and J. Ye. Inelastic collisions and density-dependent excitation suppression in a ^{87}Sr optical lattice clock. Phys. Rev. A, **84**:052716, (2011).

[123] Z. Idziaszek and P. S. Julienne. Universal rate constants for reactive collisions of ultracold molecules. Phys. Rev. Lett., **104**:113202, (2010).

[124] A. Goban, R. B. Hutson, G. E. Marti, S. L. Campbell, M. A. Perlin, P. S. Julienne, J. P. D'Incao, A. M. Rey, and J. Ye. Emergence of multi-body interactions in few-atom sites of a fermionic lattice clock. arxiv, 1803.11282, (2018).

[125] K. R. A. Hazzard, M. van den Worm, M. Foss-Feig, S. R. Manmana, E. G. Dalla Torre, T. Pfau, M. Kastner, and A. M. Rey. Quantum correlations and entanglement in far-from-equilibrium spin systems. Phys. Rev. A, **90**:063622, (2014).

[126] K. R. A. Hazzard, B. Gadway, M. Foss-Feig, B. Yan, S. A. Moses, J. P. Covey, N. Y. Yao, M. D. Lukin, J. Ye, D. S. Jin, and A. M. Rey. Many-body dynamics of dipolar molecules in an optical lattice. Phys. Rev. Lett., **113**:195302, (2014).

[127] M. Foss-Feig, M. Hermele, and A. M. Rey. Probing the kondo lattice model with alkaline-earth-metal atoms. Phys. Rev. A, **81**:051603, (2010).

[128] M. Hermele and V. Gurarie. Topological liquids and valence cluster states in two-dimensional SU(N) magnets. Phys. Rev. B, **84**:174441, (2011).

[129] H. Zhai. Degenerate quantum gases with spin–orbit coupling: a review. Rep. Prog. Phys., **78**:026001, (2015).

[130] N. Goldman, G. Juzeliūnas, P. Öhberg, and I.B. Spielman. Light-induced gauge fields for ultracold atoms. Rep. Prog. Phys., **77**:126401, (2014).

[131] A. Celi, P. Massignan, J. Ruseckas, N. Goldman, I. B. Spielman, G. Juzeliūnas, and M. Lewenstein. Synthetic gauge fields in synthetic dimensions. Phys. Rev. Lett., **112**:043001, (2014).

[132] V. Galitski and I. B. Spielman. Spin-orbit coupling in quantum gases. Nature, **494**:49–54, (2013).

[133] N. Goldman, J. Dalibard, M. Aidelsburger, and N. R. Cooper. Periodically driven quantum matter: The case of resonant modulations. Phys. Rev. A, **91**:033632, (2015).

[134] J. Dalibard, F. Gerbier, G. Juzeliūnas, and P. Öhberg. Colloquium: Artificial gauge potentials for neutral atoms. Rev. Mod. Phys., **83**:1523–1543, (2011).

[135] M. L. Wall, A. P. Koller, S. Li, X. Zhang, N. R. Cooper, J. Ye, and A. M. Rey. Synthetic spin-orbit coupling in an optical lattice clock. Phys. Rev. Lett., **116**:035301, (2016).

[136] Y.-J. Lin, K. Jimnez-Garca, and I. B. Spielman. Spin-orbit-coupled Bose-Einstein condensates. Nature, **471**:49–54, (2011).

[137] Z. Fu, L. Huang, Z. Meng, P. Wang, X.-J. Liu, H. Pu, H. Hu, and J. Zhang. Radio-frequency spectroscopy of a strongly interacting spin-orbit-coupled Fermi gas. Phys. Rev. A, **87**:053619, (2013).

[138] L. C. Ha, C. V. Anderson B. M. Clark, L. W. Parker, and C. Chin. Roton-maxon excitation spectrum of Bose condensates in a shaken lattice. Phys. Rev. Lett., **114**:055301, (2015).

[139] J. Huang W. Burchesky S. Shteynas B. Top F. Jamison A.O. Li, J. R. Lee and W. Ketterle. A stripe phase with supersolid properties in spin-orbit-coupled Bose-Einstein condensates. Nature, **543**:91–94, (2017).

[140] M. E. Tai, A. Lukin, M. Risploi, R. Schittko, T. Menke, D. Borgnia, P. M. Preiss, F. Grusdt, A. M. Kaufman, and M. Greiner. Microscopy of the interacting Harper-Hofstadter model in the few-body limit. Nature, **546**:519–523, (2017).

[141] X. Zhang, M. Bishof, S. L. Bromley, C. V. Kraus, M. S. Safronova, P. Zoller, A. M. Rey, and J. Ye. Spectroscopic observation of SU(N)-symmetric interactions in Sr orbital magnetism. Science, **345**:1467–1473, (2014).

[142] P. W. Anderson. Random-phase approximation in the theory of superconductivity. Phys. Rev., **112**:1900–1916, (1958).

[143] R. Matsunaga, N. Tsuji, H. Fujita, A. Sugioka, K. Makise, Y. Uzawa, H. Terai, Z. Wang, H. Aoki, and R. Shimano. Light-induced collective pseudospin precession resonating with Higgs mode in a superconductor. Science, **345**:1145–1149, (2014).

[144] C. Deutsch, F. Ramirez-Martinez, C. Lacroûte, F. Reinhard, T. Schneider, J. N. Fuchs, F. Piéchon, F. Laloë, J. Reichel, and P. Rosenbusch. Spin self-rephasing and very long coherence times in a trapped atomic ensemble. Phys. Rev. Lett., **105**:020401, (2010).

[145] X. Du, L. Luo, B. Clancy, and J. E. Thomas. Observation of anomalous spin segregation in a trapped Fermi gas. Phys. Rev. Lett., **101**:150401, (2008).

[146] J. Zhang, P. W. Hess, A. Kyprianidis, P. Becker, A. Lee, J. Smith, G. Pagano, I. D. Potirniche, A. C. Potter, A. Vishwanath, N. Y. Yao, and C. Monroe. Observation of a discrete time crystal. Nature, **543**:217–220, (2017).

[147] S. Choi, J. Choi, R. Landig, G. Kucsko, H. Y. Zhou, J. Isoya, F. Jelezko, S. Onoda, H. Sumiya, V. Khemani, C. von Keyserlingk, N. Y. Yao, E. Demler, and M. D. Lukin. Observation of discrete time-crystalline order in a disordered dipolar many-body system. Nature, **543**:221–225, (2017).

[148] P. Lemonde and P. Wolf. Optical lattice clock with atoms confined in a shallow trap. Phys. Rev. A, **72**:033409, (2005).

[149] L. Van Hove. The occurrence of singularities in the elastic frequency distribution of a crystal. Phys. Rev., **89**:1189–1193, (1953).

[150] P. Kim, T. W. Odom, J.-L. Huang, and C. M. Lieber. Electronic density of states of atomically resolved single-walled carbon nanotubes: Van Hove singularities and end states. Phys. Rev. Lett., **82**:1225–1228, (1999).

[151] S. Kolkowitz, S. L. Bromley, T. Bothwell, M. L. Wall, G. E. Marti, A. P. Koller, X. Zhang, A. M. Rey, and J. Ye. Spin-orbit-coupled fermions in an optical lattice clock. Nature, **542**:66–70, (2017).

[152] S. Blatt, J. W. Thomsen, G. K. Campbell, A. D. Ludlow, M. D. Swallows, M. J. Martin, M. M. Boyd, and J. Ye. Rabi spectroscopy and excitation inhomogeneity in a one-dimensional optical lattice clock. Phys. Rev. A, **80**:052703, (2009).

[153] D. Hügel and B. Paredes. Chiral ladders and the edges of quantum hall insulators. Phys. Rev. A, **89**:023619, (2014).

[154] M. Atala, M. Aidelsburger, M. Lohse, J. T. Barreiro, B. Paredes, and I. Bloch. Observation of chiral currents with ultracold atoms in bosonic ladders. Nat. Phys, **10**:588–593, (2014).

[155] G. de Lange, Z. H. Wang, D. Ristè, V. V. Dobrovitski, and R. Hanson. Universal dynamical decoupling of a single solid-state spin from a spin bath. Science, **330**:60–63, (2010).

[156] C. P. Slichter. Principles of Magnetic Resonance. Springer, Berlin, (1996).

[157] L. F. Livi, G. Cappellini, M. Diem, L. Franchi, C. Clivati, M. Frittelli, F. Levi, D. Calonico, J. Catani, M. Inguscio, and L. Fallani. Synthetic dimensions and spin-orbit coupling with an optical clock transition. Phys. Rev. Lett., **117**:220401.

[158] X.-. Qi and S.-C. Zhang. Topological insulators and superconductors. Rev. Mod. Phys., **83**:1057–1110, (2011).

[159] L. Isaev, J. Schachenmayer, and A. M. Rey. Spin-orbit-coupled correlated metal phase in Kondo lattices: An implementation with alkaline-earth atoms. Phys. Rev. Lett., **117**:135302, (2016).

Appendix A

Atom Number Calibration

A.1 Quantum Projection Noise

As discussed in section 1.4, binomial statistics tells us that the standard deviation of the measured excitation fraction is given by

$$\sigma_{QPN} = \sqrt{\frac{p_e(1-p_e)}{N}} \tag{A.1}$$

where N is the number of atoms measured and p is the mean excitation fraction. We can therefore use this as a calibration of our atom number. The atom number that we measure will be proportional to the voltage, V_{PMT}, that we measure using a photomultiplier tube (PMT) and we can therefore rewrite our standard deviation of the measured excitation fraction as

$$\sigma_{QPN} = \sqrt{\frac{p_e(1-p_e)}{N}} \equiv \sqrt{\frac{p_e(1-p_e)}{a_{QPN}V_{PMT}}} \tag{A.2}$$

where a_{QPN} is a conversion factor between measured voltage and atom number that we wish to determine for our atom number calibration.

However, during our measurements we are also susceptible to other noise such as electronic noise that we need to take into account. When we measure the excitation fraction we do this by measuring three independent voltages to give the excitation fraction

$$p_e = \frac{V_{Exc} - V_{Bgnd}}{V_{Gnd} + V_{Exc} - 2V_{Bgnd}} = \frac{V_{Exc} - V_{Bgnd}}{V_{PMT}} \tag{A.3}$$

where V_{Exc} is the PMT voltage from the excited state atom number, V_{Gnd} is the PMT voltage from the ground state atom number, and V_{Bgnd} is the background voltage of the PMT. If we assume

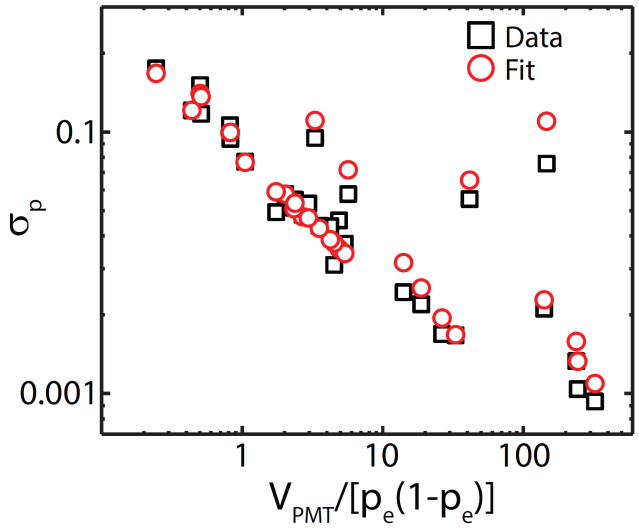

Figure A.1: Measurement of the standard deviation of the excitation fraction, σ_p, versus $V_{PMT}/(p_e(1-p_e))$ where V_{PMT} is the voltage measured using a PMT from atomic fluorescence proportional to the atoms number N. Both the atom number and excitation fraction are varied systematically to obtain the data (black, squares) and the data is fit (red, circles) with Eq. A.7 to extract the conversion factor between measured voltage and atom number $a_{QPN} = 16,800$

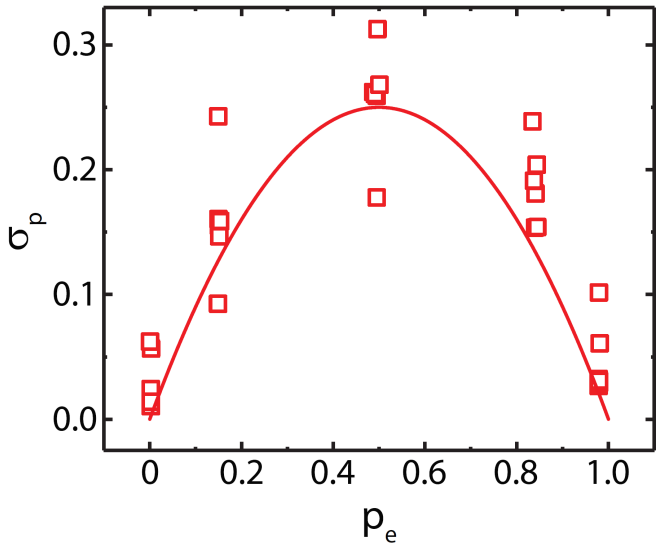

Figure A.2: When the data in Fig. A.1 is scaled using the calibrated atom number, it can be seen that the data agrees well with the predicted $p_e(1-p_e)$ theoretical curve.

that each of these measurements contains electronic noise each with standard deviation δC which is shared by V_{Exc}, V_{Gnd}, and V_{Bgnd} then the standard deviation from electronic noise is given by

$$\sigma_{electronic} = \sqrt{\left(\frac{\partial p}{\partial V_{Exc}}\right)^2 (\delta C)^2 + \left(\frac{\partial p}{\partial V_{Gnd}}\right)^2 (\delta C)^2 + \left(\frac{\partial p}{\partial V_{Bgnd}}\right)^2 (\delta C)^2} \tag{A.4}$$

$$= |\delta C| \sqrt{\left(\frac{1-p}{V_{PMT}}\right)^2 + \left(\frac{-p}{V_{PMT}}\right)^2 + \left(\frac{-1+2p}{V_{PMT}}\right)^2} \tag{A.5}$$

$$= \frac{|\delta C|}{V_{PMT}} \sqrt{2 - 6p + 6p^2} \tag{A.6}$$

Combining this result with the standard deviation from QPN we get the total standard deviation to be

$$\sigma_{QPN+electronic} = \sqrt{\frac{p(1-p)}{a_{QPN} V_{PMT}} + \left(\frac{|\delta C|}{V_{PMT}}\right)^2 (2 - 6p + 6p^2)} \tag{A.7}$$

Experimentally these measurements can be made by changing both the atom number and the excitation fraction in a systematic way. An example measurement is shown in Fig. A.1 and A.2. In this case a π pulse of 1 ms was calibrated and then both the length of the blue MOT loading time was changed, to change the atom number, for five different pulse times ranging from 0 ms to 1 ms were used to measure the standard deviations of the excitation fraction and gives an atom number calibration of $(16,800 \pm 1,100)\,\text{atoms}/V_{PMT}$

A.2 Transfer Efficiencies

This method of calculating the atom number depends upon knowing the number of atoms loaded into the blue MOT and then calculating the transfer efficiencies for the different cooling stages. To estimate the number of atoms in the blue MOT we can observe the fluorescence emitted during the MOT. We know that the $^1S_0 - ^1P_1$ cooling transition is almost closed with a small leakage rate to the $^1D_2$ where some atoms end up in the metastable $^3P_2$ state. The branching ratios are well known such that measurements of the blue MOT lifetime, in the absence of repumps, can therefore be used to extract an effective saturation parameter for the blue MOT beams. This gives us a measurement of how long the atoms spend in the $^1P_1$ state and thus how many photons are

emitted per atom. The saturation parameter is given in terms of the measured MOT lifetime, τ, by [78]

$$S_0 = \frac{1 + 4\left(\frac{\Delta}{\Gamma}\right)^2}{\tau/\tau_0 - 1} \tag{A.8}$$

where $\tau_0 = 0.00156$, and $S_0 = 0.37$ in our most recent measurement.

The excited state fraction can be written as

$$p_e = \frac{1}{2}\left(\frac{s}{1 + s + 4\Delta^2/\Gamma^2}\right) \tag{A.9}$$

When we are measuring the fluorescence from the blue MOT we are using a detector that only measures a fraction of the solid angle f_{SA}. The number of photons emitted per atom is $A\rho_{exc}$ where $A = 32$ MHz$/2\pi$ where the number of atoms in the blue MOT is given by

$$N_{blueMOT} = \frac{\text{number of photons detected}}{f_{SA} A \rho_{exc}} \tag{A.10}$$

where we also use the fact that our detector, along with our SRS preamp, has a calibrated signal of 104 nW per Volt at 461 nm. The latest measurement was taken under the same configuration as discussed in section A.1 giving an atom number of $(15,500 \pm 1000)\,\text{atoms}/V_{PMT}$ where both independent measurements agree within error bars.

This measurement gives us the number of atoms in the blue MOT. To calculate the number of atoms in the red MOT we need to calculate the number of atoms transferred to the broadband red MOT. The probe beam that we use is too small compared to the blue MOT so in order to measure the transfer efficiency from the blue MOT we need to use the blue MOT beams instead. It is very easy to saturate the PMT in this case so the voltage needs to be turned down considerably compared to our usual measurement of atoms in the lattice or red MOT. Once the transfer efficiency to the broadband red MOT is measured, the usual blue probe beam is used to measure each of the other transfer stages. In the case of a dense ^{88}Sr single frequency red MOT the density can get high enough that collective effects need to be taken into account and waiting for a longer time of flight will give an increase fluorescence signal.